An Electrochemical and Spectroelectrochemical Investigation of Binuclear Transition Metal Complexes

Marie Elliot

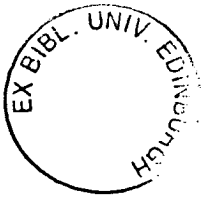

PhD Thesis – The University of Edinburgh – 2001

Declaration

Except where specific reference is made to other sources, the work contained in this thesis is the original work of the author. It has not been submitted, in whole or in part, for any other degree.

Marie Elliot

Acknowledgements

I would like to thank the following people who have helped me in the past three years in numerous ways. Firstly (and most importantly) Lesley Yellowlees for her excellent supervision throughout my PhD and for her ceaseless support, enthusiasm and energy which proved to be very infectious. Thanks also go to the members of the Yellowlees group, past (Alan and Xiao Ming) and present (Ken and Lorna), without whom life in the lab would've been a lot less enjoyable. In particular I'd like to thank Ken for his help during the final hurdle, he never let me down once. I should also thank him for the numerous meals he cooked – but to be fair I did usually leave him little present at the end of the night!

Thanks also have to go to the crystallography section, that is Bob, Simon, Steve, Bob and Andy for laughing at the size of my crystals, but being able to solve the structure regardless. Also to the technical staff, in particular Donald for letting me use the IR spectrometer until silly hours of the morning, and also to the guys in the mechanical and electrical workshop for their speedy repair jobs on the electrodes and the glass-blower, well, for blowing glass. Thanks to 'mass spec Sally' for teaching me how to use the spectrometer.

A big thank you goes to Neil Connelly and his group down in Bristol and Enzo Alessio and his group in Trieste for sending me the compounds, the analysis of which formed a large part of this work.

I'd also like to thank my friends and family – without your support I never would've made it. Especially to Mandy, who has been going through the hell that is thesis writing with me – its nice to have someone who is thinking exactly the same as you for company, and to Mary – poor Mary – who has had to live (or not as the case may be) with both of us. It must've been hell. I also have to say sorry to all of the friends I haven't phoned in ages - Janet, Janice and Gillian I promise I'll be in touch soon. A million thanks to the old Thursday night crew – them were the days. Finally, thanks also to Tony, for being there for me, even when you weren't here!

Abstract

Three different types of mixed-valence complexes are studied in this thesis, namely, homonuclear d^4/d^5, heteronuclear d^5/d^6 and homonuclear d^5/d^6 binuclear metallic species.

The electrochemical syntheses of the mononuclear complexes, $[OsCl_5(N\text{-cypy})]^{-/2-}$ (N = 2, 3, 4; cypy = cyanopyridine), and the asymmetrical homonuclear complexes, $[Cl_5Os(N\text{-cypy})OsCl_5]^{n-}$ (N = 3, 4; n = 4, 5, 6) are reported.

The mononuclear cyanopyridine complexes produce two isomeric forms, the cyanopyridine can be bound though either the pyridine nitrogen or the cyano nitrogen. Electrochemical investigations confirm that the isomer bound through the pyridine nitrogen is most stable. The X-ray crystal structure of this isomer for 3- and 4-cypy is reported. The complexes have also been investigated using UV/Vis spectroelectrochemistry. The mononuclear complexes have been found to be very similar electronically. That is, the exact position of the cyano moiety has little effect on the overall electronic nature of the complex. This is in accordance with these ligands being principally σ-donating ligands.

The binuclear complexes of 3- and 4-cypy have also been synthesised and investigated electrochemically. The redox chemistry of the binuclear complex differs from the mononuclear compounds. This is indicative of some communication between the two metal centres. K_c for the 4-cypy complex was found to be 17000 and for 3-cypy to be 1100. Thus the degree of communication is larger for 4-cypy compared to 3-cypy, in agreement with results published previously using these ligands, with different metal fragments. These complexes are described as Class II mixed-valence complexes.

The heteronuclear cyanide bridged mixed-valence complexes $[(NH_3)_5Ru(\mu\text{-}NC)Mn(CO)(\eta^2\text{-dppm})_2]^{n+}$ (**1**), $[cis\text{-}(NH_3)_5Ru(\mu\text{-}NC)Mn(CO)_2(\eta^2\text{-}$

dppm)(P{OEt}$_3$)]$^{n+}$ (**2**) and [*trans*-(NH$_3$)$_5$Ru(μ-NC)Mn(CO)$_2$(η^2-dppm)(P{OEt}$_3$)]$^{n+}$ (**3**) (dppm =$Ph_2PCH_2PPh_2$; n = 2, 3, 4) have also been investigated. Electrochemical and spectroelectrochemical (UV/Vis and IR) investigations show that the n = 2/3 redox couple is primarily based on the ruthenium metal centre and the n = 3/4 redox couple on the manganese. The half-wave potential of the redox process based on the ruthenium centre remained fairly constant, while the half-wave potential of the redox process based on the manganese centre was found to vary with both the number and the position of the carbonyl groups. An electronic change at the ruthenium centre resulted in a shift in the position of the carbonyl bands in the IR spectrum, illustrating that there is some communication between the two metal centres.

Finally, also investigated are homonuclear mixed-valence complexes containing $RuCl_4$(DMSO) fragments bridged by a variety of organic ligands (L). The mononuclear complexes [$RuCl_4$(DMSO)L], where L = pyrazine, pyrimidine and bipyridine, were investigated electrochemically and spectroelectrochemically. Both the solvent and the nature of the counterion were found to have an effect on the electronic nature of the complex under study. Upon reduction, the weakly bound DMSO ligand was easily replaced by a solvent molecule, this ligand substitution reaction could be suppressed at temperatures of 233 K and below.

The binuclear complexes with L = pyrazine, pyrimidine, bipyridine, BPA, and BPE, (BPA = 1,2-bis(4-pyridyl)ethane; BPE = *trans*-1,2-bis(4-pyridyl)ethylene) were investigated. Two reversible reduction redox couples were only observed when the bridging ligand was pyrazine, indicating that the amount of communication between the two metal centres is greatest here. This was also confirmed by UV/Vis spectroelectrochemistry. An IVCT transition was observed in this mixed-valence complex, the band position of which was found to correlate with Gutmanns acceptor number. K_c for the pyrazine-bridged mixed-valence species was found to be 10^2 indicating that it is a Class II compound.

Table of Contents

Abbreviations

AN	acceptor number (Gutmann scale)
bipy	bipyridine
BPA	1,2-bis(4-pyridyl)ethane
BPE	trans-1,2-bis(4-pyridyl)ethylene
bznl	benzonitrile
Cp	cyclopentadienyl
CT	charge transfer
cypy	cyanopyridine
DCM	dichloromethane
DMF	N,N-dimethylformamide
DMSO	dimethyl sulfoxide
DN	donor number (Gutmann scale)
dppe	$Ph_2PCH_2CH_2PPh_2$
dppm	$Ph_2PCH_2PPh_2$
E	potential
$E_{½}$	half-wave potential
E_p	peak potential
EPR	electron paramagnetic resonance
HOMO	highest occupied molecular orbital
i_p	peak current
IR	infrared
IVCT	intervalence charge transfer
K_c	comproportionation constant
LMCT	ligand to metal charge transfer
LUMO	lowest unoccupied molecular orbital
MLCT	metal to ligand charge transfer
NMR	nuclear magnetic resonance
OTE	optical transparent electrode
OTTLE	optically transparent thin layer electrode
Ph	phenyl

phen	phenanthrolene
py	pyridine
pym	pyrimidine
pyz	pyrazine
SCE	standard calomel electrode
SOMO	semi-occupied molecular orbital
TBA	tetrabutylammonium
TCNE	tetracyanoethylene
TCNQ	tetracyanoquinodimethane
THF	tetrahydrofuran
TLC	thin layer chromatography
UV	ultraviolet
Vis	visible

List of Figures

CHAPTER ONE :

Introduction

1 Introduction

1.1 Mixed-valence Complexes

Mixed-valence complexes have two (or more) metal centres which are linked together either by direct bonding or *via* a bridging ligand. These metal centres have a different number of electrons. The odd electron can be localised on one metal centre, or delocalised by some extent over all the metal centres. The properties of these complexes are rarely just the sum of the two constituent metal ions, and often dramatic changes in the physical properties of the system are observed. The main reason for the interest in this type of complex is that they allow the study of the most fundamental process in chemistry, electron-transfer. This process can be studied under controlled intramolecular conditions, that is, across a fixed distance, between fragments whose properties are known and through bridges whose conformations and electronic characteristics are well defined.

Consider the case where a metal centre M and its one-electron oxidised product M^+ are linked together. The bridge, which may range from an organic bridging ligand to a single atom or even nothing as in a M-M bond, has a large influence on the coupling between the metal centres. If it is assumed that the distance between the two metal centres, r, is moderate, and the electronic coupling between them, H_{AB}, is small and the constituents of the metal coordination spheres are identical and finally, that one of the metal sites is labelled so that the left- and right-hand sites are distinguishable, then the following conclusions can be drawn. The metal-ligand bond lengths and force constants will differ for M and M^+. In addition, if the complex is in solution, the solvation of the two sites will also be different. As a result, electron-transfer between the two centres will have an activation barrier. That is, on the transfer of the electron (induced by the absorption of light), a M^+ with the inner and outer sphere of a M ion will be created, as will a M with the coordination sphere of a M^+, thus it is a high energy state. Nuclear arrangement will then take place to give the final product (this is much slower than electronic motion – Franck-Condon principle). This is illustrated in Figure 1.1. Optical electron-transfer will occur when

the incident light is of the correct energy, $E_{op} = h\nu$. This absorption of light is termed an intervalence charge transfer (IVCT) absorption.

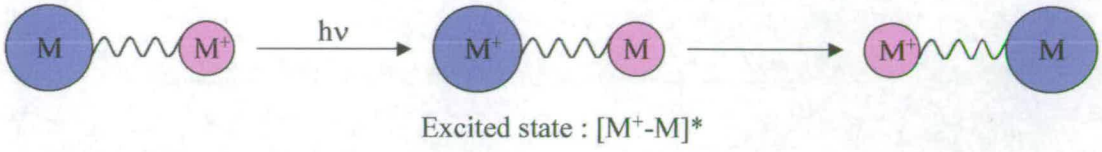

Figure 1.1 Optical electron-transfer process in a symmetrical binuclear mixed-valence complex where the circles represent the whole metal-ligand coordination sphere (including secondary sphere solvent interactions).

Mixed-valence complexes can be divided into three classes (proposed by MB Robin and P Day[1]) which reflect the differences in the strength of interaction between the metals.

In Class I compounds the odd electron is fully localised. That is, there are no detectable interactions between the two metal centres. Only the properties of the isolated mononuclear complexes (M and M^+) are observed. The reason for there being no interaction is varied, but may be due to the metal separation being too large, or the metal environments being very different, as for example in Pb_3O_4 which contains the two common oxidation states Pb(IV) and Pb(II).

The other extreme is Class III compounds. This is where the odd electron is fully delocalised. The interaction between the metal centres is so great that the properties of the isolated metal ions are absent and only new properties characteristic of the unit $(M\text{-}M)^+$ exist. The metal ions are in identical coordination environments and are therefore crystallographically equivalent. An example of a Class III mixed-valence compound is Ag_2F which contains sheets of metal-metal bonded Ag atoms with a positive charge and is a bronze coloured conductor.

Class II compounds have a weak interaction between the metal centres. Their properties are slightly altered from that of the individual ions and they may also exhibit additional properties which are not associated with the individual ions. Compounds of this class tend to have almost identical ligand fields, but are

crystallographically distinguishable. One classic example of this type of compound is Prussian Blue.

1.1.1 Analysis of Mixed-Valence Complexes

The most useful method of analysis of these mixed-valence compounds so far has proved to be electronic spectroscopy. The assignment of bands in an absorption spectrum is however notoriously difficult. The following section attempts to aid in this band assignment.

Electronic Spectroscopy

Three main types of electronic transitions are usually considered. These are categorised as 'metal based', charge transfer, or 'ligand based' in origin.[2]

'Metal based' (or d-d) transitions

These bands arise due to the excitation of an electron from one d-orbital on a central metal atom to another d-orbital. For example, in the case of an octahedral complex with a d^1 configuration, following absorption of light of the correct frequency the electron can be excited from the t_{2g} orbital to the e_g orbital as outlined in Figure 1.2.

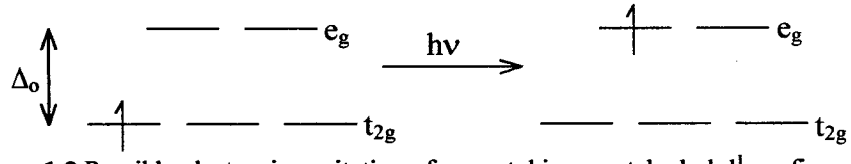

Figure 1.2 Possible electronic excitation of an metal in an octahedral d^1 configuration.

This type of absorption tends to occur in the near-IR or visible region of the electronic spectrum and is characteristically weak. The intensity of a band is measured by the extinction coefficient, ε, which is calculated according to Equation 1.1

$$\varepsilon = A / cl \qquad \text{where } A = \text{absorbance}, \; c = \text{concentration in mol dm}^{-3}, \; l = \text{path length of cell in cm} \qquad \textbf{Equation 1.1}$$

A typical extinction coefficient for a d-d transition is of the order of 1–10 M^{-1} cm^{-1}. The intensity of a band in electronic spectroscopy is governed by the probability of that transition occurring. Metal-based transitions are formally forbidden in a strict octahedral environment (thus the extinction coefficient is small) due to Laportes rule which states that $\Delta l = \pm 1$. These transitions are independent of the nature of the solvent.

Charge transfer transitions

Absorption bands due to charge transfer transitions involve the transfer of an electron from a molecular orbital based mainly on the metal to one based mainly on the ligand (MLCT) or vice versa (LMCT). They are usually observed at the blue end of the spectrum or in the UV region. Nearly all of these charge transfer transitions are fully allowed and as such they tend to be very intense, that is ε is of the order 10^3-10^4 M^{-1} cm^{-1}.

MLCT and LMCT transitions can be distinguished from each other by contrasting the behaviour of the energy of the band upon oxidation or reduction. If an absorption occurs due to a MLCT transition, then oxidation of the metal centre will move the band to higher energy and vice versa for a LMCT. The energy of these bands are dependent on the nature of the solvent since the dipole of the excited state is different to that of the ground state and as such the orientation of the solvent molecules will be different in each. Since it is assumed that the electronic transition is a Frank-Condon type of transition, it will take place much faster than nuclear rearrangement. Depending on the solvent used and the change of dipole, the excited state may be either stabilised or destabilised, that is, the absorption band will move to lower or higher energy respectively.

'Ligand based' or Intraligand transitions

Some ligands have low lying empty orbitals which are usually anti-bonding in character. An electronic transition can occur from an occupied orbital localised on the ligand to this low lying orbital, this band is termed an intraligand transition.

These transitions usually occur in the high energy region of the spectrum, the UV region, and are fully allowed with an extinction coefficient of the order 10^3-10^6 M^{-1} cm^{-1}. The energy of these transitions depends on the nature of the metal centre since the metal–ligand bond will involve the occupied ligand based orbital, hence the position of the band will be sensitive to the oxidation state of the metal. Generally, when the metal centre is oxidised the transition will move to lower energy.

The intensity of a band in electronic spectroscopy is determined largely from selection rules, with more intense bands arising from transitions which are both spin and orbitally allowed. The spin selection rule states that $\Delta S = 0$, for example, a singlet cannot undergo a transition to a triplet. This selection rule can be relaxed due to spin-orbit coupling, thus in heavy atoms (where this phenomenon is more prominent) spin-forbidden bands are often significant features. The Laporte selection rule states that transitions between states of the same parity are forbidden, or in other words, $\Delta l = \pm 1$. For example d-d transitions are forbidden, but s-p and p-d transitions would be allowed. The most intense absorption bands arise when the electronic transition is accompanied by a large change in dipole moment.

In addition to the transitions discussed above, mixed-valence complexes of Class II or Class III exhibit low energy absorption(s) in their electronic spectrum. In Class II complexes, this transition has been termed an intervalence charge transfer (IVCT) transition and occurs due to the electron-transfer from one metal centre to another (see Figure 1.1). As mentioned above, this generates a M^+ ion in the co-ordination environment of a M and vice versa. The excited species then reverts back to the ground state configuration by vibrational relaxation. The bands which arise from this transition tend to be fairly weak with $\varepsilon \approx 10\text{-}10^3$ $mol^{-1}cm^{-1}dm^3$. They are usually broad and the band halfwidth, $\Delta\nu_{½}$, for symmetrical complexes is usually around 5000 cm^{-1} and should be a function of the band maximum, ν_{max}, according to Equation 1.2.

$$\Delta\nu_{½} = [2310\nu_{max}]^{½}\ cm^{-1} \qquad \textbf{Equation 1.2}$$

In addition, the band position should be solvent dependent. The potential energy diagram for a Class II symmetrical mixed-valence complex is shown in Figure 1.3.

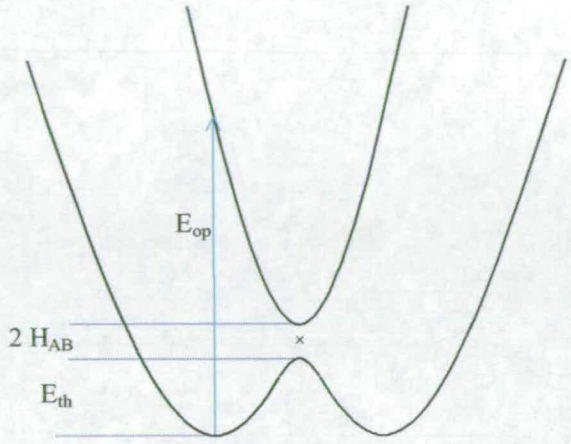

Figure 1.3 Potential energy versus nuclear configuration for a Class II symmetrical mixed-valence complex.

If the nuclear motion is harmonic and $E_{th} = \Delta G^*$, the energy of the IVCT band, E_{op}, is related to the free energy of activation, ΔG^*, by Equation 1.3

$$E_{op} = \lambda = 4\,\Delta G^* \qquad \textbf{Equation 1.3}$$

where $E_{op} = E_{in} + E_{out}$ **Equation 1.4**

E_{in} is related to a Franck-Condon term and E_{out} is associated with the reorganisation of the solvent molecules around the metal centres following electron-transfer. According to Marcus-Hush theory, the term E_{out} may be expressed as in Equation 1.5.

$$E_{out} = e^2\,(1/2a_1 + 1/2a_2 - 1/r)\,(1/D_{op} - 1/D_s) \qquad \textbf{Equation 1.5}$$

where $a_{1,2}$ = radii of the two co-ordination spheres
r = metal-metal distance in Å
D_{op} = optical dielectric constant of solvent
D_s = static dielectric constant of solvent

The energy of the intervalence charge transfer is therefore dependent on the solvent used. A plot of ν_{max} versus $1/D_{op} - 1/D_s$ should produce a straight line.[3, 4,5]

In Class III complexes, this low energy band is often wrongly termed an intervalence transition. Since in this type of complex the metal centres are strongly interacting,

each metal centre should be considered as having averaged valency. It is necessary therefore to invoke a molecular orbital approach, in which the low energy bands arise due to transitions within this molecular orbital framework and are best described as $\pi \rightarrow \pi^*$ type transitions. That is, the odd electron is promoted from an orbital delocalised over the whole metal-ligand-metal system to a higher energy orbital which is likewise delocalised. This transition is allowed, therefore the bands tend to be much more intense, and also have a smaller band half-width (*i.e.* does not fit Equation 1.2). The bands should show no solvent dependence since both metal centres have the same charge and co-ordination environment.

From the above discussion it is apparent that by examination of the low energy region of the electronic spectrum the class of the mixed-valence binuclear complex can be determined.

Electrochemistry

Often, the most relevant equilibrium for mixed-valence complexes is that for comproportionation (see Equation 1.6 for a M(II) and M(III) system) since the mixed-valence species is only present when this equilibrium is favourable.

$$\text{(II-II)} + \text{(III-III)} \rightleftharpoons 2\ \text{(III-II)} \qquad \textbf{Equation 1.6}$$

The equilibrium constant for this reaction is termed the comproportionation constant and is written K_c. K_c can range from 4, (the statistical value) in complexes where the redox processes are inseparable, to $>10^{13}$ in strongly coupled Class III systems.[6] At the statistical value of four, the mixture will contain 25% of the II-II and 25% of the III-III species and 50% of the III-II species thus, provided the characteristic spectral features of the II-II and III-III species are known, information regarding the mixed-valence species may be extracted.[7]

One of the most obvious indications of metal-metal interaction (*i.e.* delocalisation) is a separation of the two metal centred redox potentials for metals which are in apparent identical chemical environments. If the separation between the two couples

is sufficiently large, K_c can be calculated directly from the electrochemistry of the complex. This is much more difficult as the potential between the two redox couples decreases, and hence K_c approaches it statistical value of four. Equation 1.7 shows how K_c is related to the electrode potentials.[8] This value is most accurate for ΔE values of 250mV and above.

$$\log K_c = 16.9 (E_1^0 - E_2^0) \qquad \textbf{Equation 1.7}$$

where E_i^0 = Standard potential of step i which is approximately $E_{½}$ for that step (in V)

These are the two main methods used here to determine the extent of communication between the binuclear complexes studied. In order to highlight the other techniques which might also be used, there follows a brief review of the Creutz-Taube ion.

1.1.2 The Creutz-Taube Ion

One of the first, and most important, mixed-valence complex studied is the Creutz-Taube ion shown below (Figure 1.4) which formally contains Ru(II) and Ru(III). The classification of this mixed-valence compound has been the subject of debate for many years, whether it should be defined as Class II, trapped valence (Ru^{II}/Ru^{III}) or Class III, delocalised valence ($Ru^{2.5}/Ru^{2.5}$). The delocalisation of the odd electron being possible *via* the pyrazine π^* orbitals.

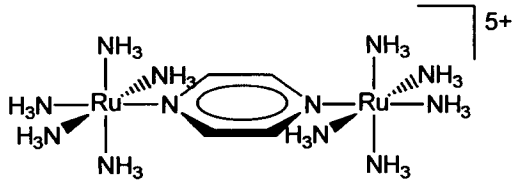

Figure 1.4 Structure of the Creutz-Taube ion.

This ion was first synthesised in 1969 following the observation that the basicity of pyrazine was enhanced when complexed to ruthenium(II) and so perhaps another metal ion could be complexed to the free nitrogen to produce a binuclear complex.[9] The complex was originally synthesised with an overall charge of 4+ and was found to exhibit two well-defined one-electron oxidations with a difference in half-wave potential of 360 mV (determined by potentiometric titration). This corresponds to a K_c value of 3×10^6.

The 5+ ion was isolated and the electronic spectrum was recorded and compared with the 4+ and 6+ species. One band was observed in the visible region at 565 nm compared to a band at 547 nm in the 4+ species. This was attributed to the $t_{2g} \rightarrow \pi^*$ transition. It was only when this investigation was extended to the near-IR region that an exciting discovery was made. A band was observed at 1570 nm which was not present in either the 4+ or 6+ species, this was assigned to the IVCT transition [2,3] $\rightarrow$ [3,2]*. The explanation given for this was, that energy is required for this transition because the 3+ and 2+ ions in the final state will be in environments (*e.g.* bond lengths, solvation) appropriate to 2+ and 3+ ion respectively. Here, it was acknowledged that although electron-transfer was expected to be fast, the ion was

described as having non-equivalent ruthenium atoms, that is, Class II.[9] It was noted in a later paper by the authors that the IVCT transition did not exhibit the solvent effect predicted by Hush, and although shifts were observed, they were only one tenth of that predicted.[10]

Following the publication of this initial report, a large number of investigations into this ion and its analogues ensued. There have been many studies of different salts of this ion, involving electronic, photoelectron, infrared, Raman, resonance Raman, Mössbauer, and electron spin resonance spectroscopy and magnetic measurements. Most of these investigations have favoured the delocalised picture, however, a definitive answer to the question of assignment as Class II or Class III has not been given. It is acknowledged that this complex lies close the Class II/III borderline.[11]

The majority of the conflict in assigning the Creutz-Taube ion as Class II or Class III arises due to the different time-scale of the techniques used to study the electron-transfer reaction. As mentioned above, on the basis of the electronic spectroscopy, the Creutz-Taube ion was assigned as Class II. Contrary to this, early proton NMR studies showed that at room temperature only two types of ammine protons were observed, that is, those *cis* and *trans* to the pyrazine.[12] Thus implying that the complex has delocalised valence. However, given the time-scale of this experiment (10^{-8} sec) compared to the expected rate of electron-transfer, this does not provide significant evidence for its Class assignment.

Mössbauer spectroscopy concluded that equal concentrations of Ru(II) and Ru(III) exist.[13] However, this was performed in the solid state, at 4 K and is therefore not comparable to the majority of studies which have been carried out in solution at room temperature. Solid state IR studies proved to be consistent with either the delocalised or localised description as these only involved the study of the ammine function.[10] Later, an IR spectroelectrochemical technique was employed to study the solution near-mid IR spectrum.[14] This showed the spectral features of the 5+ ion to be intermediate of the 4+ and 6+ ions, thus indicating that on the vibrational time-scale (10^{-11}-10^{-13} sec) in solution the complex is valence delocalised, hence Class III.

Theoretical calculations have also been carried out on this ion.[15,16] In the most recent of these papers, calculations were performed using the symmetric crystallographic geometry and also using a plausible asymmetric geometry based on the crystal structures of the corresponding 4+ and 6+ ions. The results for both of these models showed strong mixing of the two Ru $4d_{xz}$ orbitals with one π^* orbital on the pyrazine bridging ligand. When the bond lengths were changed from the symmetric to the asymmetric model, the ruthenium centres remained extensively mixed through the π^* orbital and the charges on the ruthenium ions were found to be nearly identical. This provides evidence for delocalised valence.

It would be foolish to enter into a discussion about every technique which has been used in the study of this ion, but these examples clearly show the complexity of the problem presented in trying to decide the level of electron delocalisation in this ion. An extensive collaborative paper in which a large number of techniques were used was published and although this was not wholly conclusive, the weight of evidence was found to lie in favour of the delocalised valence description.[17] It was deemed possible that the Creutz-Taube ion is Class III on a long time-scale (*e.g.* crystallographic, NMR) but Class II on a short time-scale (*e.g.* photoelectron).

The aims of this thesis are to study three distinct types of mixed-valence complexes, i) homonuclear asymmetrical d^4/d^5, ii) heteronuclear cyanide bridged d^5/d^6 and iii) homonuclear d^5/d^6.

The homonuclear d^4/d^5 complexes feature the $OsCl_5$ fragment bridged by the cyanopyridine series of ligands. The variation of the level of metal-metal communication with the position of the cyano group of the bridging ligand will be studied and compared to similar complexes based on the $Ru(NH_3)_5$ fragment.

The heteronuclear d^5/d^6 complexes to be studied involve a combination of the classical metal fragment, $Ru(NH_3)_5$, and an organometallic fragment, namely

$[Mn(CO)_2(L\text{-}L)L]$ (where L-L is a diphosphine and L a phosphine), bridged by a cyanide ligand.

The homonuclear d^5/d^6 complexes to be investigated involve the replacement of the ammine ligands of the Creutz-Taube ion by strong σ-donor, π-donor chloride ligands to assess the effect this has on the amount of delocalisation in the mixed-valence complex. The metal fragment here is *trans*-$RuCl_4DMSO$. The bridging ligand is also varied to study the effect this has on metal-metal communication.

CHAPTER TWO :

Experimental Techniques

2 Experimental Techniques

2.1 Introduction

Throughout the course of this work a number of electrochemical and spectroelectrochemical techniques have been used. This chapter gives an outline of the various techniques employed and discusses the advantages and disadvantages of each.

2.2 Electrochemical Techniques

Electrochemical studies were performed using a DELL 466DL personal computer with General Purpose Electrochemical System (GPES) Version 4.5 software connected to an Autolab system containing a PSTAT20 potentiostat.

All of the electrochemical techniques considered here require a three electrode configuration, namely a working electrode, a reference electrode and a counter (auxiliary) electrode. A potential difference is applied between the working electrode and the reference electrode and the current is monitored between the working electrode and the counter electrode.

The form of the working electrode depends on the electrochemical technique being used. In organic media (as used here), platinum electrodes are generally employed since they are stable over a wide potential range. The micro-working electrode used here is a platinum disc of 0.5 mm diameter.

The reference electrode, as its name suggests, maintains a constant reference potential throughout the experiment. It must satisfy the following conditions.(i) It must have a reversible couple which obeys the Nernst equation; (ii) this couple must occur at a potential that is invariant with respect to temperature and time; (iii) the internal resistance of this component should be high compared to the other electrodes. This helps to prevent current flowing to the reference electrode, which

leaves it unpolarised and hence stable; (iv) it must not cause contamination of the test solution or be contaminated itself. In order to prevent this a salt bridge is generally employed. The reference electrode used here is Ag/AgCl in a solution of 0.45 M $[N^nBu_4][BF_4]$ and 0.05 M $[N^nBu_4]Cl$ in DCM, against which the ferrocinium/ferrocene couple was measured at +0.55 V.

The counter electrode used for electrochemical experiments in organic media is constructed of an inert material such as platinum and should have a much larger surface area than the working electrode. The counter electrode used here is a platinum rod.

Sample stability and solubility dictate the choice of solvent. Other features of the solvent also taken into consideration for its use as an electrochemical solvent are a useable potential range, a suitably high dielectric constant, an accessible temperature range, a low viscosity and an ease of purification. If the solvent has donor or coordinating properties these should also be borne in mind.

Supporting electrolyte is present in a solvent system in order to increase conductivity of the solution. In the experiments discussed here the electrolyte concentration varies between 0.1 and 0.5 M depending on the solvent. This increased conductivity results in a decrease in the resistance between the working electrode and counter electrode and reduces the uncompensated solution resistance between the working electrode and the reference electrode. The vast excess of electrolyte ions compared to sample ions results in the structure of the double layer adjacent to the working electrode being largely determined by the electrolyte ions. Also migration of the sample species between the working electrode and the counter electrode is eliminated as a mode of mass transport.

The cell employed depends on the technique being used. A typical cell for conventional electrochemistry (cyclic voltammetry, differential pulse etc.) is shown in Figure 2.1.

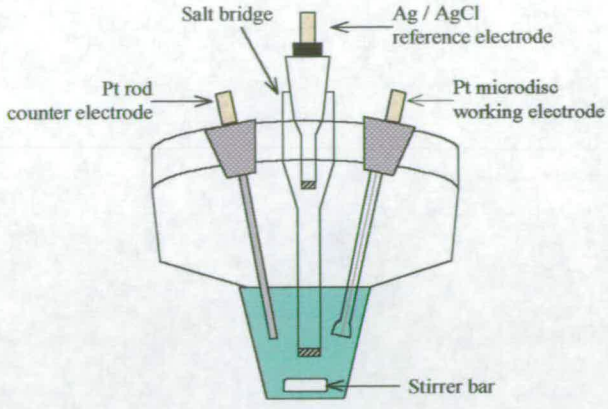

Figure 2.1 Schematic representation of the three electrode cell used for cyclic voltammetry and differential pulse voltammetry.

2.2.1 Cyclic voltammetry

Cyclic voltammetry uses stationary electrodes in an unstirred solution. In this work a platinum microdisc was employed as the working electrode and a platinum rod as the counter electrode. The large amount of electrolyte present in the test solution results in negligible mass transport of the sample species by either migration or convection. As a result, diffusion is the only means of mass transport of the sample to the solution/working electrode interface.

The potential of the working electrode is ramped linearly with time between two or three potentials. This gives rise to the triangular wave form shown in Figure 2.2. The potential is ramped from the starting potential, E_1, to E_2 where the potential is then switched in the opposite direction until it reaches E_3 and then finally back to the starting potential to complete the cycle. The scan rate, ν, for this is typically between 0.02 and 0.5 Vs^{-1}. All cyclic voltammograms shown in the following chapters have been recorded using a scan rate of 0.1 Vs^{-1} unless otherwise stated. The current, i, which flows at the working electrode is measured as a function of the potential of the working electrode, E.

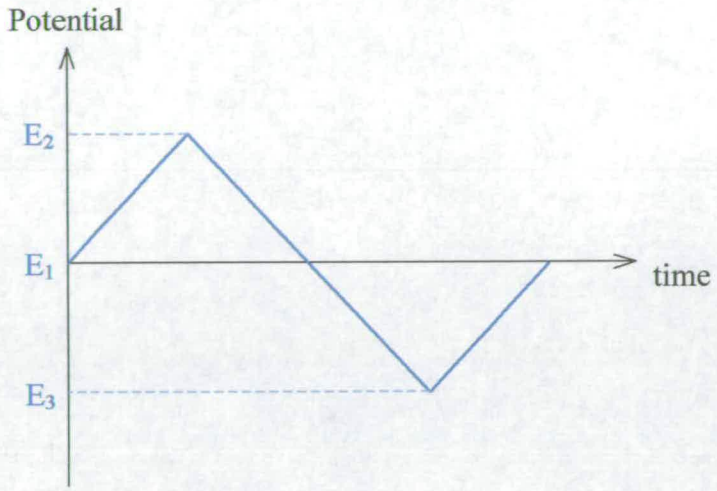

Figure 2.2 Triangular wave form of cyclic voltammetry.

An electroactive species which exhibits electron-transfer at an electrode falls into one of four classes:

(i) Reversible: where electron-transfer is more rapid than diffusion of the species to the electrode.

(ii) Quasi-Reversible: where the rate of electron-transfer and diffusion are similar.

(iii) Irreversible: where the rate of electron-transfer is slower than diffusion to the electrode surface.

(iv) Partially-Reversible: where an irreversible chemical reaction follows a reversible or quasi-reversible electron-transfer.

A typical cyclic voltammogram for a reversible electron-transfer reaction is shown in Figure 2.3, this is a profile of a species which is being oxidised. The current response takes the form of two asymmetric peaks. Two factors contribute to the shape of these curves, that is, the electron-transfer rate and the diffusion rate. As the potential is swept positive (or negative if the process is a reduction) a current is produced when the electroactive species begins to be oxidised (or reduced) at the electrode. By convention this current is considered positive if the process is a oxidation (or negative if it is a reduction). This electron-transfer rate increases rapidly with increasing E, depleting the concentration of unreacted species at the electrode surface. When this depletion is large enough, the current reaches a peak and the

electron-transfer becomes diffusion controlled. Finally it reaches a constant level where the electroactive species travels from the bulk solution to the surface of the electrode where it reacts immediately. The potential ramp is reversed at the switching potential (E_2 in Figure 2.2). When the oxidised species at the electrode surface is re-reduced a return peak is observed at a more negative potential than for the forward peak. The shape of this peak is governed by similar electron-transfer and diffusion rate factors as discussed above for the oxidation process.

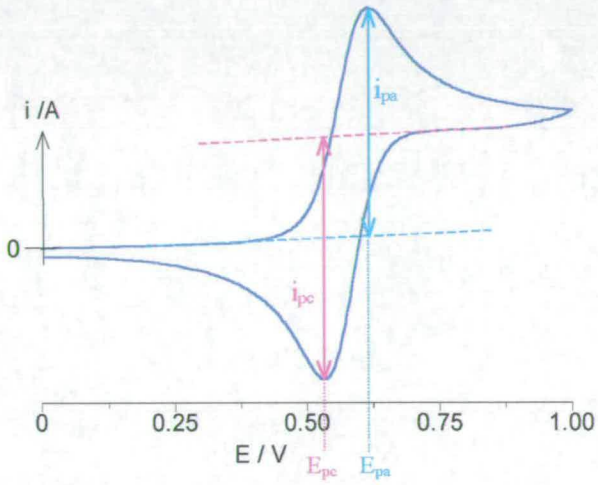

Figure 2.3 Cyclic voltammogram (of ferrocene in 0.4 M $[N^nBu_4][BF_4]$ /DCM) illustrating the important parameters in this technique.

The parameters obtained from a cyclic voltammogram can be used to determine the nature of a particular charge transfer reaction. The parameters which are most important in this respect are the anodic and cathodic peak currents and potentials, that is, i_{pa}, i_{pc}, E_{pa} and E_{pc} respectively. These are shown in Figure 2.3. The average potential of E_{pa} and E_{pc} is the half-wave potential, $E_{½}$, for the redox process under investgation. For a fully reversible electron-transfer reaction E_{pa}-E_{pc} = 59 mV and i_{pa}/i_{pc} = 1.0 at 298 K.

2.2.2 Stirred Voltammetry

In order to determine whether a redox process is an oxidation or a reduction stirred voltammetry must be used. This experiment involves the application of a single, slow (0.02 Vs^{-1}), linear potential ramp at the working electrode in a uniformly stirred

solution. Electron-transfer at the electrode is governed by convection and diffusion. A cathodic current flow indicates a reduction, while an anodic current flow indicates an oxidation.

2.2.3 Differential pulse voltammetry

Differential pulse voltammetry uses stationary electrodes in an unstirred solution, but unlike cyclic voltammetry where the potential is ramped linearly with time, here the potential is applied in pulses. The excitation signal used in this process is outlined in Figure 2.4. The current is measured twice in each step, once just before the pulse is applied (i_1) and then a second just before the pulse is removed (i_2). These two current values are averaged and plotted against the potential, this gives a bell shaped voltammogram (see Figure 2.5).

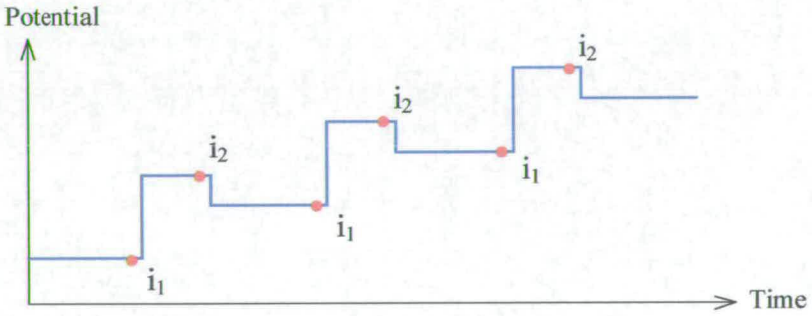

Figure 2.4 Waveform of differential pulse voltammetry. The red dots indicate the time at which the current is measured.

In fact, this type of voltammogram is essentially the result of differentiating the direct current voltammogram. Peak potentials are very similar to the half-wave potential measured in cyclic voltammetry. Due to the shape of differential pulse voltammograms (see Figure 2.5), increased resolution is achieved compared to cyclic voltammetry. This technique is most successfully used to study multi-component samples.

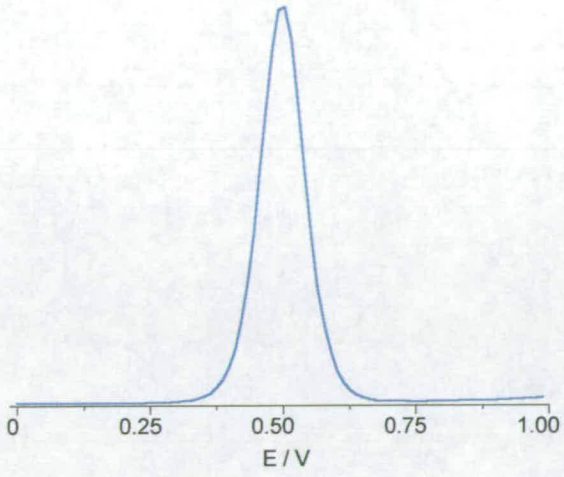

Figure 2.5 Differential pulse voltammogram of ferrocene in 0.4 M $[N^nBu_4][BF_4]$ / DCM.

2.2.4 Bulk Electrolysis – Coulometry – Electrosynthesis

There are two types of electrolysis, potentiostatic, where the potential is fixed and the current is monitored with time, and galvanostatic, where a chosen current is forced to flow through the cell. Potentiostatic electrolysis was used throughout this work. This electrochemical technique requires a different cell set up which is shown in Figure 2.6 and is commonly know as an H-cell.

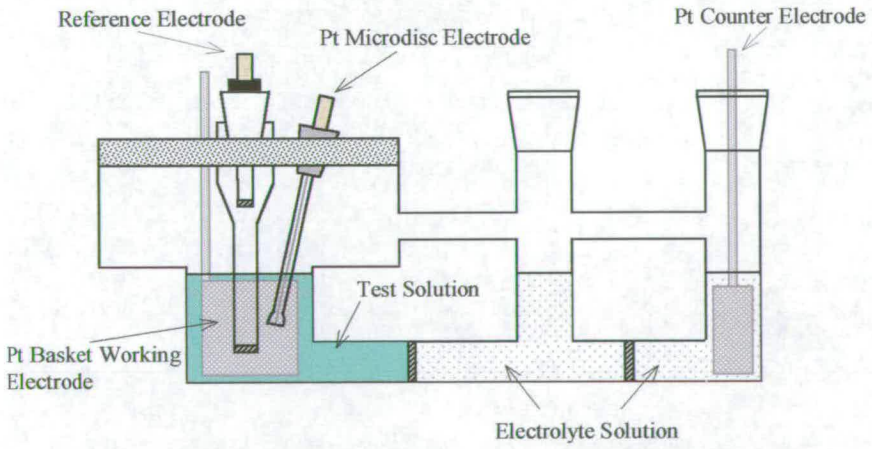

Figure 2.6 H-type cell used for potentiostatic electrolysis.

In bulk electrolysis a chosen potential is applied at a large working electrode (a platinum basket electrode was employed here) and the complete sample of electroactive species is reduced or oxidised in the stirred solution. The reference

electrode is placed in the centre of the basket electrode and a platinum microdisc electrode is also present in this compartment to facilitate the study of the redox properties of the electroactive species and the electrolysis products. In order to avoid the counter electrode reversing the electron-transfer process, it is placed in a compartment separated from the working electrode by a glass frit. This also prevents the contamination of the test solution with any counter electrode products which may be produced during the electrolysis.

In order for electron-transfer to be fully achieved at the working electrode the potential applied must be at least 60 mV more positive of the $E_{½}$ for an oxidation (or more negative for a reduction). The current which flows can be measured and its integral, charge, Q can be calculated. Assuming 100% efficiency, this charge can be related to the amount of material and hence the number of electrons involved in the electron-transfer step can be calculated using Equation 2.1.

$$n = \frac{QM}{FW}$$ **Equation 2.1**

where Q = total charge passed
M = Molecular weight of electroactive species
F = Faraday Constant
W = weight of sample used

Following complete reduction or oxidation the product can then be investigated using the platinum microdisc electrode and the processes outlined above.

2.3 Spectroelectrochemical Techniques

Spectroelectrochemical experiments have long been important tools in the investigation of organic and inorganic compounds. This experiment is particularly helpful in the characterisation of short-lived reaction intermediates and when redox reaction products are unstable.

To date, the most used solution spectroscopic technique combined with the electrochemical experiment is UV/visible detection, due to the simplicity of this experimental set-up and the decreased number of problematic conditions. To a much lesser extent, IR detection has been used. The main use of this technique is in the study of electrode surface reactions, a solid-state investigation. The principal reason for this is that the strong absorption of IR radiation by the solvent can interfere with the absorption by the redox active species. Only careful selection of solvent and IR handle (on the redox active species) can overcome this problem. Using IR spectroscopy as a detection method is desirable since considerable detail regarding the molecular structure of products and intermediates of the redox reaction can be obtained.

2.3.1 UV/Vis spectroelectrochemistry

All spectra were recorded on a λ-9 spectrophotometer (Perkin Elmer) controlled by a Datalink PC running UV WinLab software (version 2.70.01).

Using the cell shown in Figure 2.7, the products of a bulk electrolysis experiment can be monitored *in situ* by electronic UV/Vis absorption spectroscopy. The optically transparent thin layer electrode (OTTLE.) cell consists of a platinum/rhodium gauze working electrode fitted into a quartz cell with a path length of 0.5 mm. A quartz extension is fitted to the cell which acts as a reservoir for the sample solution. To complete the conventional three electrode system a platinum wire counter electrode and a Ag/AgCl reference electrode are placed into this reservoir, both electrodes being separated from the sample solution by porous frits.

The cell assembly is then placed into a PTFE block which is placed in the spectrometer. Control of the temperature is achieved by passing dry, pre-cooled nitrogen between the inner pair of quartz windows of the cell. The temperature is monitored using a thermocouple connected to a digital thermometer. To prevent the inner pair of quartz windows from fogging, room temperature, dry nitrogen is passed between the inner and outer quartz windows and the sample chamber of the spectrometer is flushed with nitrogen.

Bulk electrolysis is performed as above and the spectrum recorded every five minutes. Once complete the potential is switched to regenerate the starting material. If the electron-transfer process is reversible the spectrum of the starting material will be unchanged.

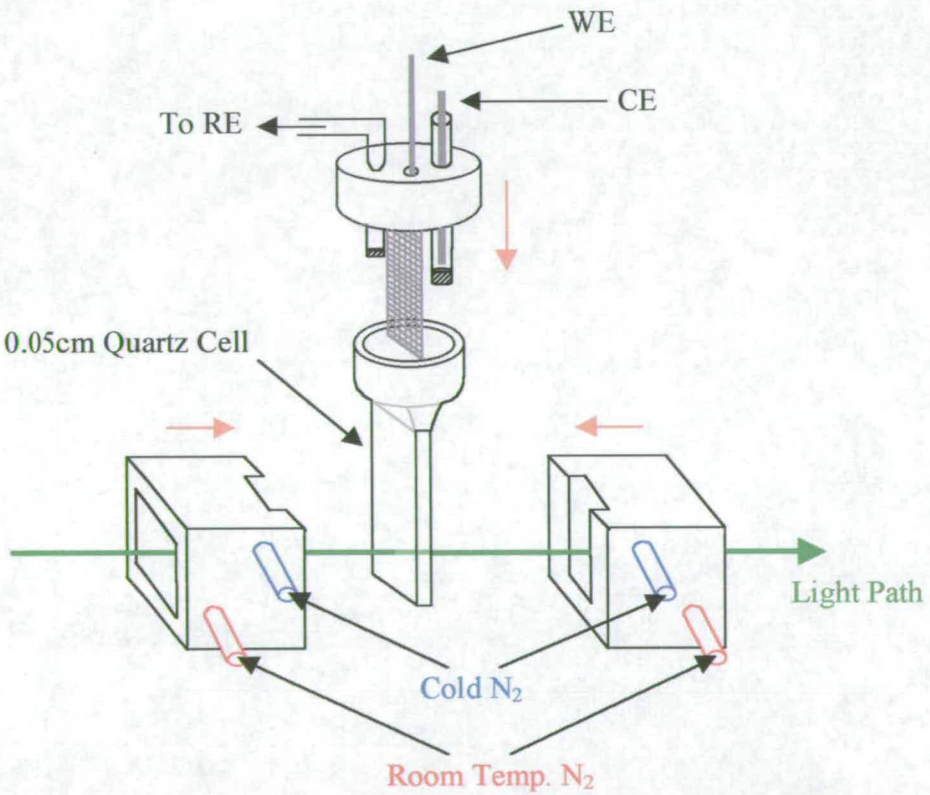

Figure 2.7 Schematic diagram of the experimental set-up used for UV/Vis spectroelectrochemistry.

2.3.2 IR spectroelectrochemistry

All spectra were recorded on a FTIR 2000 spectrometer (Perkin Elmer). Data was manipulated using the UV WinLab software (version 2.70.01).

2.3.2.1 Cell Design

There are two principal IR spectroelectrochemical cell designs which have thus far been employed for solution studies. These are external reflectance[18], and transmission cells.[19] External reflectance cells need more advanced IR spectrometers (with additional optical components) and also have other disadvantages. Transmission cells on the other hand can be used in conventional IR spectrometers,[20] for this reason it was decided that this type of cell would be used.

A transmittance cell and the UV/Visible spectroelectrochemical cell (discussed previously) are both known as optically transparent thin-layer electrochemical (OTTLE) cells. The IR transmittance cell is based on a 'sandwich' type design in which an optically transparent electrode (OTE) is positioned between two IR-transparent windows. The cell was made using equipment available in the laboratory. The material of choice for the windows was KBr. In order to create a cavity between the two windows, into which the OTE would fit, some aluminium sheet was cut into a U shape. The pieces were then glued together using Araldite, shown in Figure 2.8.

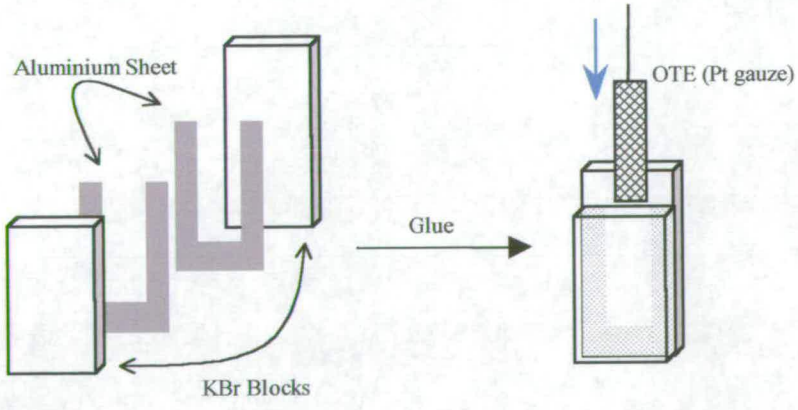

Figure 2.8 Step one in the construction of an OTTLE cell for IR spectroelectrochemistry.

The next step was to create a reservoir around the top of the cell to allow the addition of the counter and reference electrodes, completing the three electrode configuration

(Figure 2.9). This was achieved by gluing glass slides (cut to fit) around the top of the KBr blocks.

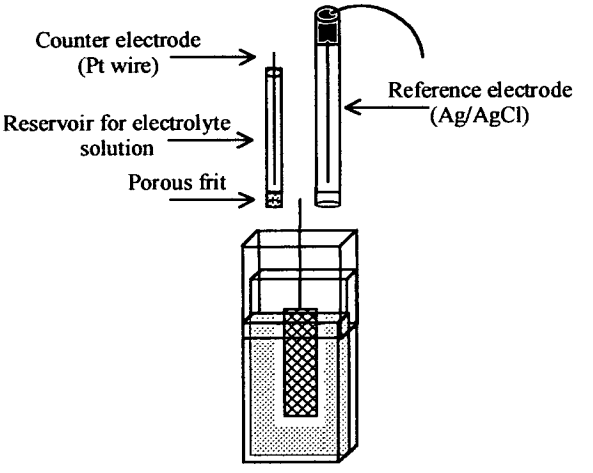

Figure 2.9 Diagram of the OTTLE cell constructed.

The main disadvantage of this design is the glue. Solvents are known to attack glue, hence it is prone to springing leaks when used a number of times. Obviously, leaks can be repaired, but a much better design would avoid the need for glue all together. One such design is shown in Figure 2.10.

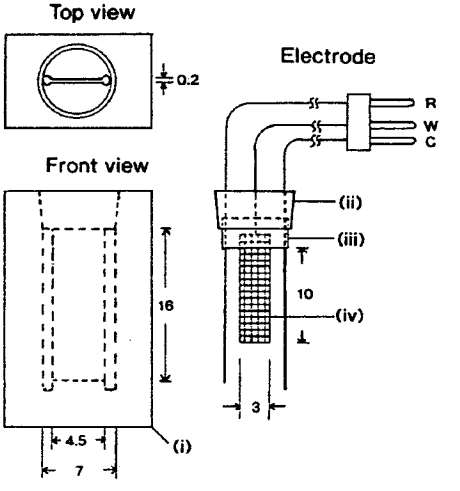

Figure 2.10 Schematic illustration of KBr cell chamber: (i) KBr cell body, (ii) Teflon cell cap, (iii) Tefzel film, (iv) platinum working electrode gauze; W, working electrode; C, counter electrode; R, silver wire pseudo-reference electrode.[21]

This is sculpted from a single block of KBr. Ultrasonic machining is used to create a cavity in the centre, into which an OTE can fit. A larger cavity is made at the top for

the remaining electrodes to be added to the set-up. This cell and the design of the cell lid, allows the exclusion of air from the sample, hence reducing the risk of decomposition due to arial effects. A disadvantage of this set-up compared to the one used here is the fact that the counter electrode is not isolated from the bulk solution. While this may be satisfactory when analysing compounds with easily accessible redox potentials (±0.3 V) and when only one redox couple is to be investigated, it will become a problem in all other cases.

2.3.2.2 Cell Application

Following the construction of this cell, in order to test its function, the IR spectroelectrochemistry of tetracyanoquinodimethane (TCNQ) was investigated. The structure of this compound is shown in Figure 2.11. This particular compound was chosen because it has been studied by this method previously,[22,23] has accessible redox potentials and the redox products are known to be stable at room temperature on the experimental time-scale.

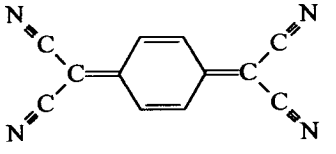

Figure 2.11 Structure of TCNQ

The cyclic voltammetry of this compound is shown in Figure 2.12. The compound has two fully reversible one-electron reductions at +0.345 V and –0.230 V. The half-wave potentials of TCNQ have been reported previously as +0.202 V and –0.332 V (referenced to the SCE electrode).[24] The ratio of peak currents was found to be close to unity for both processes, an indication that the electron-transfer processes are chemically reversible.

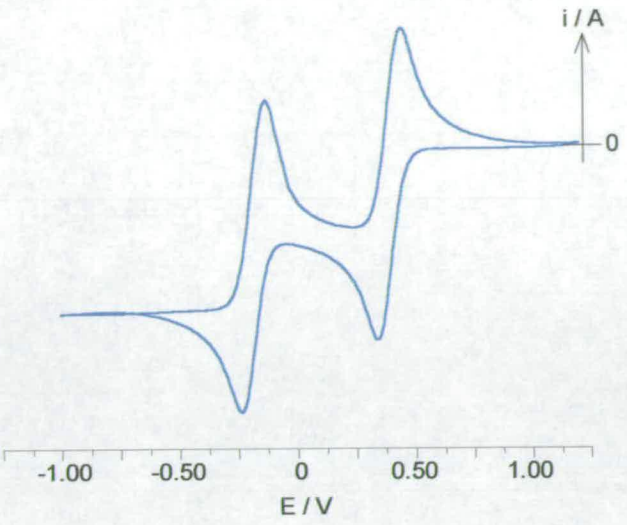

Figure 2.12 Cyclic voltammogram of TCNQ in 0.4 M $[N^nBu_4][BF_4]$ / DCM at 293 K.

Upon dissolution of TCNQ in air, the solution quickly changes colour from orange to green. This colour change occurs because upon contact with the oxygen in the air, the compound is being reduced by one electron (the half-wave potential for the reduction is quite positive). This was confirmed when the stirred voltammogram of a solution that had not been exposed to air was compared to one that had. The stirred voltammogram of the orange solution (TCNQ) showed two reductions, while that of the green solution ($TCNQ^-$) showed one reduction and one oxidation.

This reduction of the compound could not be avoided during the assembly of the cell. Thus, the starting material for the *insitu* IR experiment was the monoanionic species ($TCNQ^-$). During the experiment, the potential was set at a level which would induce oxidation (+0.7 V) to produce the uncharged species (TCNQ). IR spectra were recorded during this process approximately every five minutes. The potential was then switched to 0.0 V to induce a one-electron reduction to regenerate the monoanionic species to determine the reversibility of the couple.

One of the aims for this cell was to be able to carry out *insitu* analysis at reduced temperatures. For this, dry, pre-cooled nitrogen was passed directly into the chamber of the IR spectrometer. This allowed the sample to be cooled to at least 233 K. The sample chamber was flushed with nitrogen to minimise fogging, but this will only

become a significant problem in the IR experiment if H_2O has active vibrational modes in the region under investigation.

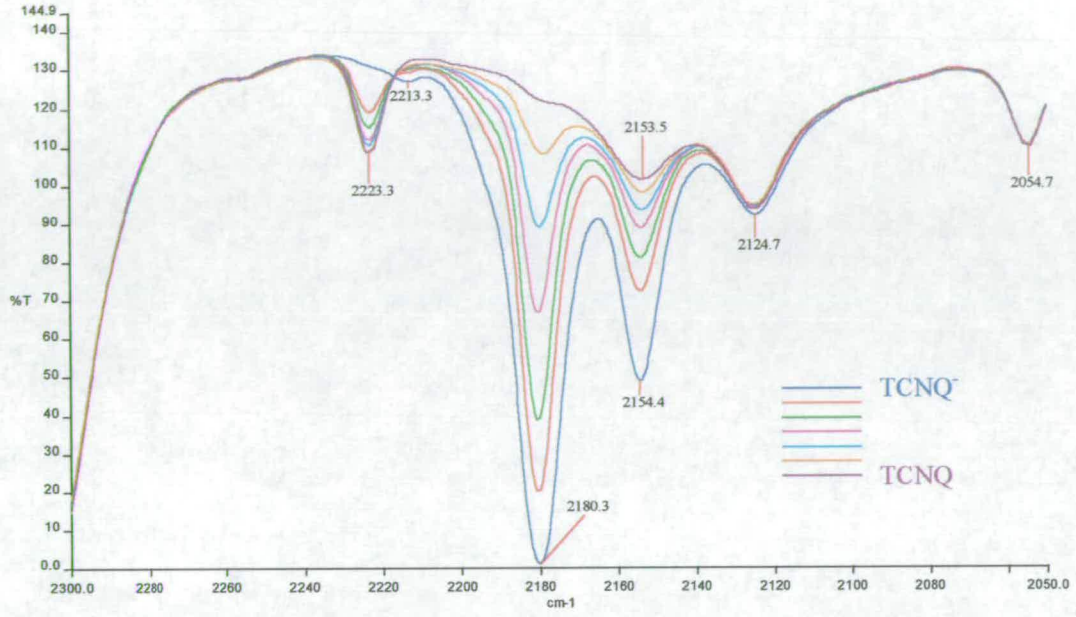

Figure 2.13 IR Spectroelectrochemistry of $TCNQ^-$ in 0.4 M $[N^nBu_4][BF_4]$ / DCM at 263 K. E_{app} = +0.70 V.

Figure 2.13 shows the IR spectroelectrochemistry of this compound. Only the CN region is given since this was the working region with the chosen solvent/electrolyte system. TCNQ is planar and has a D_{2h} symmetry element. Therefore, TCNQ and its anions, if they are also planar, should have two IR active CN stretching modes.[22] For neutral TCNQ the modes are thought to be coincident and have been reported previously at 2228 cm^{-1}.[25] This band is observed here at 2223 cm^{-1}. In the spectrum of $TCNQ^-$ studied previously, two individual bands were observed at 2182 and 2156 cm^{-1}.[22] In this work these bands were observed at 2180 and 2154 cm^{-1}. The work performed previously has always been reported as difference spectra. It can be seen from this work here that this is not necessary, and in fact an accurate isosbestic point is observed at 2217 cm^{-1}.

Upon reduction from TCNQ to $TCNQ^-$ the CN bands move to lower energy. Previous MO calculations on the similar complex TCNE have shown that upon reduction the electron goes into an orbital which is anti-bonding with respect to the

CN bonds. TCNQ is thought to be similar[22] and indeed these results support this assumption. The CN bands move to lower energy on reduction, this implies that the CN bond is being weakened, an explanation for this would be that the additional electron density is being delocalised onto the CN π^* orbitals.

The results found here are in good agreement with those reported previously and show that the cell constructed can be used to perform IR spectroelectrochemical experiments.

CHAPTER THREE :

Electrosynthesis of Binuclear Osmium Complexes Bridged by the Cyanopyridine Series

3 Electrosynthesis of Binuclear Osmium Complexes Bridged by the Cyanopyridine Series

3.1 Introduction

Redox induced substitution reactions are widely used in the synthesis of transition metal complexes. These reactions can be either chemically or electrochemically induced. Electrochemical methods are extremely important, and unrivalled, when investigating the mechanisms of electron-transfer reactions. For preparative purposes however, both methods are usually employed – each having its own merits.

The electrochemical method of choice is controlled potential electrolysis. It gives a wide range of accessible potentials and is very precise (±1 mV); this is very important especially if the starting material has two closely spaced redox processes. This technique can be coupled with voltammetric methods (*e.g.* cyclic voltammetry) which allow the redox process to be monitored throughout the electrogeneration process. The main disadvantage of this technique, with respect to synthesis, is the presence of supporting electrolyte. This is usually present in large excess over the desired product, and often they have similar solubilities, which make separation of the product species from the supporting electrolyte very difficult.

Obviously when chemical oxidants or reductants are employed, there is no need for a supporting electrolyte to be added, therefore the separation problem is avoided. This is the major advantage. Other advantages include fast reaction times (especially at low temperatures) and larger-scale reactions. Low polarity solvents can be used with this method, these solvents are usually non-coordinating and seldom displace ligands from the redox product, and so chemical stability is increased. The limiting factor in the use of chemical methods is that, a chemical redox agent in a particular solvent has a fixed formal potential, therefore in order to provide a range of different redox strengths, a range of reagents is required.[26] A further disadvantage of chemical reducing/oxidising agents is their possible inclusion in the final product.

Both of these methods have been used here in the synthesis of substituted chloro-osmium complexes. The reduction of $[OsCl_6]^{2-}$ in the presence of a π-accepting ligand gives rise to the following reaction.[27]

$$[OsCl_6]^{2-} + e^- \rightleftharpoons [OsCl_6]^{3-} \xrightarrow{L} [OsCl_5L]^{2-} + Cl^-$$

The π-accepting nature of the incoming ligand, L, is necessary to stabilise the electron rich $(OsCl_5)^{2-}$ moiety. However L need not be a strong π-acceptor ligand, species such as pyridine or acetonitrile (which can be thought of as σ-only donors) stabilise $[OsCl_5L]^{2-}$ compared to $[OsCl_6]^{3-}$.

Provided the ligand is added in a stoichiometric amount, the new species $[OsCl_5L]^{2-}$ will be exclusively formed. If the ligand, L, has a second uncoordinated site which is also capable of π-accepting then, by adding and reducing another molar equivalent of $[OsCl_6]^{2-}$, a new binuclear complex can be formed, as outlined below.

$$[OsCl_6]^{2-} + e^- \rightleftharpoons [OsCl_6]^{3-} \xrightarrow{[OsCl_5L]^{2-}} [Cl_5OsLOsCl_5]^{4-} + Cl^-$$

The ligands, L, investigated in this chapter are 2-, 3- and 4-cyanopyridine :

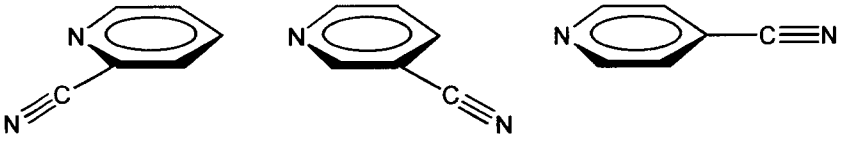

Comparison of these binuclear complexes to the 'Creutz-Taube ion' (mentioned previously), shows that (i) the terminal ammine ligands have been replaced by chloride ligands. Exchange of the σ-only donor NH_3 groups on the metal centre by the strongly π-donating Cl^- ligands results in the stabilisation of the M(III/IV) oxidation states, thus bringing this redox step to within the solvent window. This allows study of the unusual III/IV (d^4, d^5) mixed-valence complex. (ii) The ruthenium metal centre is changed to an osmium centre. These complexes were prepared by the electro-reduction of the hexachlorometallate. However preparation

of binuclear compounds by this route is only possible for osmium since, the reduction of $[RuCl_6]^{2-}$ results in the following rapid reaction:

$$2[RuCl_6]^{2-} + 2e^- \rightleftharpoons 2[RuCl_6]^{3-} \longrightarrow [Ru_2Cl_9]^{3-} + 3Cl^-$$

(iii) the bridging pyrazine ligand is replaced with the asymmetric cyanopyridine ligand. This renders the two metal centres chemically non-identical giving them an inherent difference in $E_{½}$ thus, making them easier to study.

This chapter details the synthesis of these compounds, the characterisation of the binuclear complexes, and the study of how the symmetry of the bridging ligand affects the ability of the two osmium metal centres to communicate with each other.

3.2 Synthesis

Dichloromethane was stored over KOH for at least two weeks, then freshly distilled from P_2O_5 under an atmosphere of nitrogen prior to use. All other solvents were used as supplied. 4- and 3-cyanopyridine (Aldrich) were purified by vacuum sublimation and stored in a drying cabinet.

3.2.1 Preparation of starting material $[N^nBu_4]_2[OsCl_6]$

$[NH_4]_2[OsCl_6]$ (0.5707 g, 1.30×10^{-3} mol) was dissolved in 1 M hydrochloric acid (60 cm^3). To this tetrabutylammonium hydroxide solution (40% by weight) was added dropwise until no further precipitation occurred. The resulting yellow solid was isolated by filtration. It was then dissolved in dichloromethane and the solution dried over anhydrous $MgSO_4$. The product was recovered by reducing the volume of dichloromethane to a minimum then addition of chloroform to form fine crystals. The solid was then dried *in vacuo* at 70 °C for 48 hrs. Yield – 85% **CHN Anal** : Found : C, 43.49; H, 8.43; N, 3.12; $OsCl_6N_2C_{32}H_{72}$ requires : C, 43.29; H, 8.17; N, 3.16.

3.2.2 Electrochemical synthesis

The voltammetric experiments were carried out using the three electrode configuration described in chapter 2.2. Redox potentials and peak-to-peak values are reported for a scan rate of 100 mVs^{-1}. Bulk electrolysis experiments were performed using platinum mesh electrodes as working and counter electrodes. The inert electrolyte used in all electrochemical experiments was tetrabutlyammonium tetrafluoroborate ($[N^nBu_4][BF_4]$ or $TBA[BF_4]$) which was synthesised in the lab. All solutions were bubbled with nitrogen or argon prior to study.

3.2.2.1 Preparation of $[TBA]_2[OsCl_5(L)]$ where L=2-, 3-, 4-cyanopyridine

To an H-type cell containing 0.3 M $[TBA]BF_4$ in dichloromethane, $[TBA]_2[OsCl_6]$ (30 mg, 3.38×10^{-5} mol) and L (3.6 mg, 3.46×10^{-5} mol) were added. The yellow solution was then electrogenerated at –0.67 V until complete electrolysis (zero

current). This was accompanied by a colour change (yellow to deep pink when L = 4-cypy; yellow to brown when L = 3- and 2-cypy). Voltammetric techniques were run before and after electrolysis to investigate the new mononuclear complexes.

3.2.2.2 Preparation of $[TBA]_2[OsCl_5(L)]$ where L=2-, 3-, 4-cyanopyridine -10 fold excess of L

To an H-type cell containing 0.3 M $[TBA]BF_4$ in dichloromethane, $[TBA]_2[OsCl_6]$ (30 mg, 3.38×10^{-5} mol) and L (35.2 mg, 33.81×10^{-5} mol) were added. The solution was electrogenerated at –0.67 V until complete electrolysis (zero current). A colour change (as described above) was observed. Voltammetric techniques were run before and after electrolysis to investigate the new mononuclear complexes.

3.2.2.3 Preparation of $[TBA]_4[Cl_5Os(L)OsCl_5]$ where L=3-, 4-cyanopyridine

To an H-type cell containing 0.4 M $[TBA]BF_4$ in dichloromethane, $[TBA]_2[OsCl_6]$ (23.0 mg, 2.59×10^{-5} mol) and L (2.7 mg, 0.483 cm^3 of a 0.054 M solution, 2.59×10^{-5} mol) were added. The solution was then electrogenerated at -0.67 V until complete electrolysis (zero current). A colour change was observed. To this, $[TBA]_2[OsCl_6]$ (23.0 mg, 2.59×10^{-5} mol) was added and again the solution was electrogenerated at -0.67 V until electrolysis was complete. A colour change (deep pink to purple when L = 4-cypy; brown to brown/red when L = 3-cypy) was observed. Finally, the solution was electrogenerated at +0.175 V to generate the mixed-valence species. Voltammetric and UV/Vis spectroscopic techniques were run at all stages of the reaction to investigate the species present.

3.2.2.4 Preparation of $[TBA]_4[Cl_5Os(L)OsCl_5]$ where L=3-, 4-cyanopyridine 2:1

To an H-type cell containing 0.4 M $[TBA]BF_4$ in dichloromethane, $[TBA]_2[OsCl_6]$ (63.1 mg, 7.11×10^{-5} mol) and L (3.7mg, 3.55×10^{-5} mol) were added . The solution was electrogenerated at –0.67 V until complete electrolysis. Voltammetric techniques were run at each stage of the reaction.

3.2.2.5 Separation of $[TBA]_4[Cl_5Os(L)OsCl_5]$ where L=3-, 4-cyanopyridine

The solutions from preps 3.2.2.3 and 3.2.2.4 were reduced in volume by blowing nitrogen over them. The product was then separated from the inert electrolyte by chromatography on a silica gel 60 column. The silica gel 60 was stirred with ethyl acetate while bubbling with nitrogen for at least 10 minutes. The column was then poured and kept under nitrogen. The reaction mixture was loaded on, and the column flushed with ethyl acetate (pushed through with N_2) until no more electrolyte was observed in the eluent. The solvent was then changed to degassed propan-2-ol which gave a pink coloured band. Ethanol was used next, this gave a brown band and then finally methanol which also gave a brown band. These bands were collected in separate schlenk tubes and the solvents were removed under vacuum. Differential pulse voltammetry identified the pink band as mononuclear complex. When the ethanol and methanol were removed, sticky solids remained (purple in colour for 4-cyanopyridine and red/brown for 3-cyanopyridine). This was identified by differential pulse voltammetry as the binuclear complex. All attempts at isolating a solid for elemental analysis or X-ray crystal structure analysis failed. Complexes could be stored under nitrogen at –26 °C for an infinite time. If exposed to air the binuclear complex slowly decomposed to a brown solid (approx. 1 day).

3.2.3 Chemical Synthesis

Cobaltocene (Aldrich) was sublimed under vacuum prior to use. $[NO]BF_4$ (Aldrich) was used as supplied.

3.2.3.1 Preparation of $[TBA][OsCl_5(4\text{-cypy})]$

$[TBA]_2[OsCl_6]$ (37.7 mg, 4.2×10^{-5} mol) and 4-cyanopyridine (5.3 mg, 5.1×10^{-5} mol) were dissolved in dichloromethane (10 cm^3) and the solution was degassed then kept under nitrogen using standard schlenk techniques. To this an excess of cobaltocene (15 mg, 7.9×10^{-5} mol) was added and the solution stirred for 5 minutes. Excess cobaltocene was filtered off using a canular filter. $[NO]BF_4$ (14 mg, 1.2×10^{-4} mol) was added and the solution stirred for a further 5 minutes. Excess $[NO]BF_4$ was then filtered off and the yellow product separated using a preparative TLC plate eluted

with dichloromethane. The product was recrystallised by dissolving in a minimum of dichloromethane and allowing ether to slowly diffuse into this. This yielded brown plate crystals, suitable for X-ray diffraction studies.

Crystal data

Data was collected on a Bruker AXS SMART diffractometer equipped with a CCD area detector, Oxford Cryosystems cryostream and graphite monochromated Mo-K_α radiation using ϕ and ω scans in the range $1.76 \leq \theta \leq 26.50$ °. The crystal was a brown plate of dimensions 0.28×0.18×0.05 mm. Of a total of 11573 reflections collected, 5765 were found to be independent. The final difference map extrema were 2.343 and –1.795 e $Å^{-3}$ with a final R of 3.47% for 4391 parameters. An absorption correction was applied using the method of Blessing (T_{min} = 0.385, T_{max} = 0.801).

Table 3.1 Crystallographic data for $[N^nBu_4][OsCl_5(p\text{-}NC_5H_4CN)]$.

Empirical formula	$C_{22}H_{40}Cl_5N_3Os$	γ / °	106.780(2)
Formula weight	714.02	Volume / $Å^3$	1427.6(5)
Crystal system	Triclinic	Z	2
Space group	P-1	Temperature	150(2) K
a / Å	11.214(2)	Wavelength / Å	0.71073
b / Å	11.460(2)	Density calc. / Mg m^{-3}	1.661
c / Å	13.378(3)	μ(Mo-K_α) / mm^{-1}	4.949
α / °	112.341(2)	$R_1[F>4\sigma F]$	0.0347
β / °	101.414(2)	wR_2 (all data)	0.0733

Larger preparations were also carried out. For these, the preparative TLC step was replaced by a silica gel 60 column. The silica gel in DCM was stirred and degassed for at least 10 minutes prior to use. The product was loaded on and DCM used as the eluent, this produces a very slow moving yellow band. The solvent was then changed to degassed ethyl acetate, this gave a bright yellow band which was collected in a schlenk. The solvent was removed *in vacuo* and the product recrystallised as above.

3.2.3.2 Preparation of [TBA][$OsCl_5$(3-cypy)]

$[TBA]_2[OsCl_6]$ (43.7 mg, 4.9×10^{-5} mol) and 3-cyanopyridine (15 mg, 1.44×10^{-4} mol) were dissolved in dichloromethane (10 cm^3) and the solution was degassed then kept under nitrogen using standard schlenk techniques. To this an excess of cobaltocene (13 mg, 6.9×10^{-5} mol) was added and the solution stirred for 5 minutes. Excess cobaltocene was filtered off using a canular filter. $[NO]BF_4$ (18 mg, 1.54×10^{-4} mol) was added and the solution stirred for a further 5 minutes. Excess $[NO]BF_4$ was then filtered off and the yellow product separated using a preparative TLC plate eluted with dichloromethane. The product was recrystallised by dissolving in a minimum of dichloromethane and layering with ether. After storage at –26 °C for approximately one week, this yielded yellow block crystals which were suitable for X-ray diffraction studies.

Crystal data

Data was collected on a Stoe Stadi4 diffractometer equipped with Oxford Cryosystems cryostream and graphite monochromated Mo-K_α radiation using ω-θ scans and the learnt-profile method in the range $2.54 \leq \theta \leq 25.09$ °. The crystal was a yellow block of dimensions 0.31×0.23×0.12 mm. Of a total of 5227 reflections collected, 5147 were found to be independent. The final difference map extrema were 0.562 and –0.604 e $Å^{-3}$ with a final R of 3.05% for 4531 parameters. An optimised numerical absorption correction based on face indices was applied (T_{min} = 0.394, T_{max} = 0.583).

Table 3.2 Crystallographic data for $[N^nBu_4][OsCl_5(m\text{-}NC_5H_4CN)]$.

Empirical formula	$C_{22}H_{40}Cl_5N_3Os$	γ / °	90.407(13)
Formula weight	714.02	Volume / $Å^3$	1453.2(5)
Crystal system	Triclinic	Z	2
Space group	P-1	Temperature	220(2) K
a / Å	11.262(2)	Wavelength / Å	0.71073
b / Å	11.767(2)	Density calc. / Mg m^{-3}	1.632
c / Å	12.736(3)	μ(Mo-K_α) / mm^{-1}	4.862
α / °	112.992(10)	R_1[F>4σF]	0.0305
β / °	108.836(10)	wR_2 (all data)	0.0594

For larger preparations, the same column as that explained above (section 3.2.3.1) was used.

3.2.3.3 Preparation of TBA[$OsCl_5$(pyz)]

$[TBA]_2[OsCl_6]$ (52.1 mg; 5.9×10^{-5} mol) and pyrazine (6.0 mg; 7.5×10^{-5} mol) were dissolved in DMC (10 cm^3) and the solution was degassed then kept under nitrogen using standard schlenk techniques. To this an excess of cobaltocene (32.1 mg; 1.70×10^{-4}) was added and the solution stirred for 5 minutes. Excess cobaltocene was filtered off using a canular filter. $[NO]BF_4$ (20.2 mg; 1.73×10^{-4} mol) was then added and the solution stirred for a further 5 minutes. Excess $[NO]BF_4$ was then filtered off and the yellow product separated using a preparative TLC plate eluted with DCM. The product was recrystallised by dissolving in a minimum of DCM and allowing ether to slowly diffuse into this solution. This yielded yellow block crystals suitable for X-ray diffraction studies. **CHN Anal** : Found : C, 35.39; H, 6.10; N, 5.87; $OsCl_5N_3C_{20}H_{40}$ requires : C, 34.81; H, 5.84; N, 6.09.

Crystal data

Data was collected on a Stoe Stadi4 diffractometer equipped with Oxford Cryosystems cryostream and graphite monochromated Mo-K_α radiation using ω-θ scans and the learnt-profile method in the range $2.62 \leq \theta \leq 25.07$ °. The crystal was a yellow block of dimensions 0.35×0.27×0.12 mm. Of a total of 5749 reflections collected, 4985 were found to be independent. The final difference map extrema were 2.034 and –1.400 e $Å^{-3}$ with a final R of 5.80% for 3045 parameters. An absorption correction based on azimuthal measurements was applied (T_{min} = 0.307, T_{max} = 1.00).

Table 3.3 Crystallographic data for $[N^nBu_4][OsCl_5(N_2C_4H_4)]$.

Empirical formula	$C_{20}H_{40}Cl_5N_3Os$	γ / °	90
Formula weight	690.00	Volume / $Å^3$	2822.6(15)
Crystal system	Monoclinic	Z	4
Space group	P2(1)/c	Temperature	220(2) K
a / Å	10.761(3)	Wavelength / Å	0.71073
b / Å	32.755(13)	Density calc. / Mg m^{-3}	1.624
c / Å	8.659(2)	μ(Mo-K_α) / mm^{-1}	5.003
α / °	90	R_1[F>4σF]	0.0580
β / °	112.36(2)	wR_2 (all data)	0.1199

3.2.3.4 Preparation of TBA[$OsCl_5$(2-cypy)]

$[TBA]_2[OsCl_6]$ (51.5 mg, 5.8×10^{-5} mol) and 2-cyanopyridine (15.0 mg, 1.4×10^{-4} mol) were dissolved in dichloromethane (5 cm^3) and the solution was degassed then kept under nitrogen using standard schlenk techniques. To this an excess of cobaltocene (15.6 mg, 8.2×10^{-5} mol) was added and the solution stirred for 5 minutes. Excess cobaltocene was filtered off using a canular filter. $[NO]BF_4$ (10.2 mg, 8.7×10^{-5} mol) was added and the solution stirred for a further 5 minutes. Excess $[NO]BF_4$ was then filtered off and the yellow product separated using a preparative TLC plate eluted with dichloromethane. The product was recrystallised by redissolving the resultant yellow oil in dichloromethane. After storage at –26 °C for approximately two weeks, this solution yielded orange block crystals which were suitable for X-ray diffraction studies.

Crystal data

Data was collected on a Stoe Stadi4 diffractometer equipped with Oxford Cryosystems cryostream and graphite monochromated Mo-K_α radiation using ω-θ scans in the range $2.56 \leq \theta \leq 25.06$ °. The crystal was a orange block of dimensions 0.19×0.19×0.12 mm. Of a total of 6248 reflections collected, 4959 were found to be independent. The final difference map extrema were 1.588 and –0.811 e $Å^{-3}$ with a final R of 5.92% for 2898 parameters. An absorption correction based on azimuthal measurements was applied (T_{min} = 0.217, T_{max} = 0.254).

Table 3.4 Crystallographic data for $[N^nBu_4][OsCl_4(\eta^2\text{-}N_2C_5H_4CONH)]$.

Empirical formula	$C_{22}H_{41}Cl_4N_3OOs$	γ / °	90
Formula weight	695.58	Volume / $Å^3$	5604.9(18)
Crystal system	Orthorhombic	Z	8
Space group	Pbca	Temperature	123(2) K
a / Å	18.090(3)	Wavelength / Å	0.71073
b / Å	16.779(3)	Density calc. / Mg m^{-3}	1.649
c / Å	18.466(3)	μ(Mo-K_α) / mm^{-1}	4.950
α / °	90	R_1[F>4σF]	0.0592
β / °	90	wR_2 (all data)	0.1198

3.2.3.5 Preparation of $[TBA]_4[Cl_5Os(4\text{-cypy})OsCl_5]$

$TBA_2(OsCl_6)$ (103.5 mg, 1.17×10^{-4} mol) and 4-cyanopyridine (6.1 mg, 5.9×10^{-4} mol) were added to dichloromethane (20 cm^3) which was degassed and kept under nitrogen using standard schlenk techniques. An excess of cobaltocene (23.7 mg, 1.25×10^{-4} mol) was added and the solution stirred for approximately 15 minutes. The excess cobaltocene was removed by canular filtration. The volume of solution was reduced under vacuum and the pink solution loaded onto a silical gel 60 column with dichloromethane. The column was then performed as outlined above in 3.2.2.5. Ethyl acetate gave a yellow band. Propan-2-ol gave a pink band, differential pulse voltammetry of the pink solid identified it as $[OsCl_5(4\text{-cypy})]^{2-}$. A sticky purple solid was the result of the two brown bands collected from ethanol and methanol, identified by differential pulse voltammetry as $[Cl_5Os(4\text{-cypy})OsCl_5]^{4-}$.

3.3 Results and Discussion

3.3.1 4-Cyanopyridine Bridged Complex

As discussed previously, one of the main advantages of electrosynthesis over chemical synthesis is that the progress of the redox reaction can be followed using cyclic voltammetry and differential pulse voltammetry.

The cyclic voltammogram of $[OsCl_6]^{2-}$ in DCM at room temperature is shown in Figure 3.1. This shows a reversible one-electron reduction ($E_{½}$ = -0.57 V; ΔE = 80 mV), and a fully reversible one-electron oxidation ($E_{½}$ = +1.37 V; ΔE = 75 mV) .The number of electrons involved in each process was confirmed using bulk electrolysis. Both processes are electrochemically reversible as indicated by the linear i_p versus $\nu^{½}$ response and the insensitivity of E_p to the scan rate. However, the reduction process is not chemically reversible since the ratio of peak currents (i_{pa}/i_{pc}) was found to be 0.79. The oxidation step on the other hand has a peak current ratio of 1.0 indicating that this process is chemically reversible. These values reported here were recorded at a scan rate of 0.1 Vs^{-1} where the $E_{½}$ of ferrocene under the same conditions was measured at +0.55 V (ΔE = 80 mV).

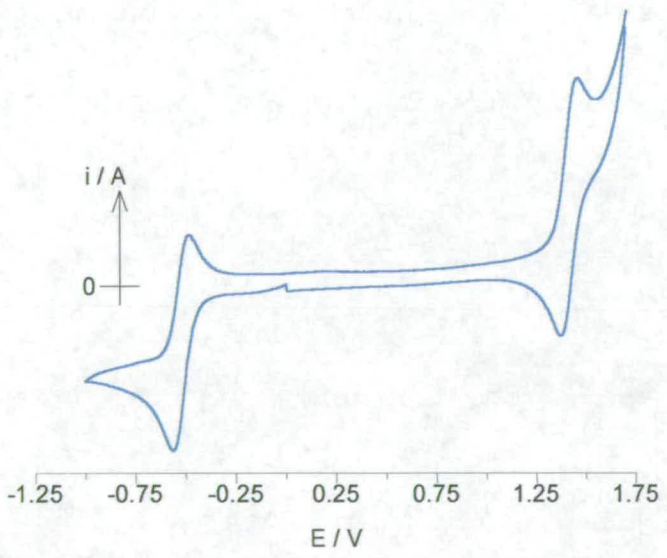

Figure 3.1 Cyclic voltammogram of $[OsCl_6]^{2-}$ in 0.4 M $[N^nBu_4][BF_4]$ / DCM at 290 K.

4-cyanopyridine (one molar equivalent) is then added to the cell and the Os(IV) is reduced using bulk electrolysis to Os(III). The cyclic voltammograms of these steps are shown in Figure 3.2.

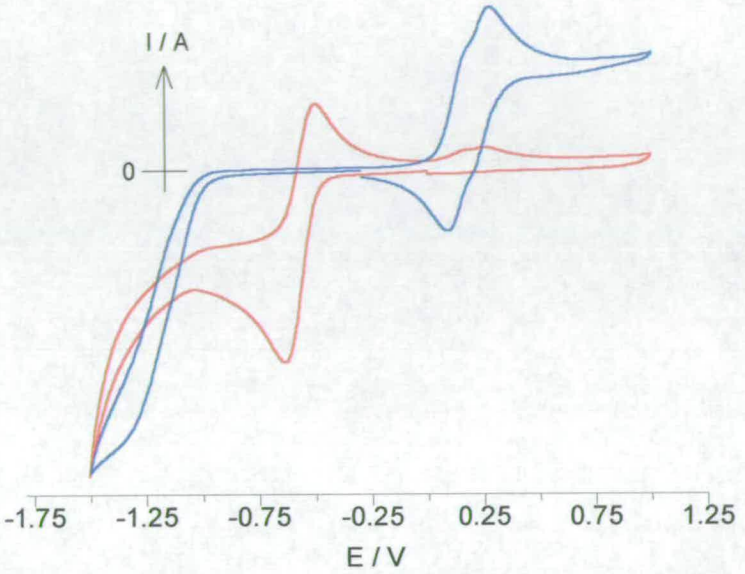

Figure 3.2 Cyclic voltammogram of $[OsCl_6]^{2-}$ + 4-cyanopyridine (red) and $[OsCl_5(4\text{-cypy})]^{2-}$ (blue) in 0.3 M $[N^nBu_4][BF_4]$ / DCM at 290 K.

Following the addition of 4-cyanopyridine, the cyclic voltammogram (red line) of the reaction mixture has not altered greatly (from pure $[OsCl_6]^{2-}$ in Figure 3.1) since 4-cyanopyridine does not have a rich electrochemistry (it does have a reduction but this is at too negative a potential to be seen within this solvent/electrolyte window). However, the reduction of the $[OsCl_6]^{2-}$ is now obviously partially reversible. Following reduction, a chemical reaction can occur between the osmium centre and the ligand, thus the reoxidation peak for $[OsCl_6]^{3-}$ is smaller. On closer inspection of the positive potential region, a new wave may be observed growing in (daughter peak) at approximately +0.2 V which is due to the mononuclear complex formed, namely $[OsCl_5(4\text{-cypy})]^{2-}$.

The cyclic voltammogram following complete reduction (blue line) clearly shows no more $[OsCl_6]^{2-}$ exists in the reaction mix, and the presence of two new species (E_{pa} = +0.27 V; E_{pc} = +0.11 V) whose half-wave potentials are similar but distinguishable, both of which have the formula $[OsCl_5(4\text{-cypy})]^{2-}$. These processes are both fully

reversible (linear i_p versus $\nu^{1/2}$ response; ratio of peak currents of 1.0). The observation of two redox processes with similar potentials can be explained by considering the asymmetry of 4-cyanopyridine. This ligand when coordinated to a metal centre will give rise to two isomers, (i) bound through the ring nitrogen or (ii) bound through the nitrogen of the cyano group. The electronic effects of these two donor atoms are very similar hence, the half-wave potentials of the metal complexes are almost overlapping. The presence of two compounds is more obvious if the more sensitive technique, differential pulse voltammetry is used (Figure 3.3).

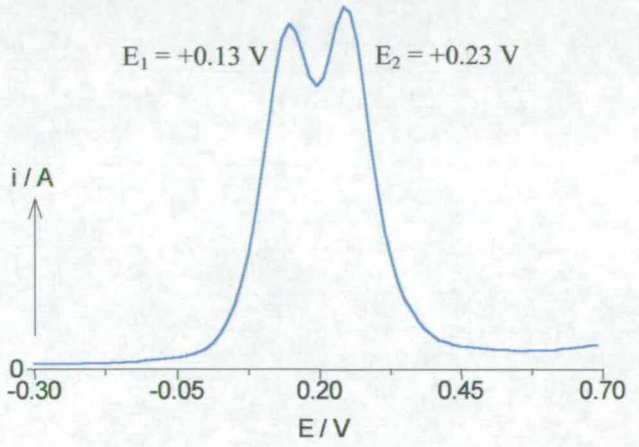

Figure 3.3 Differential pulse voltammogram of $[OsCl_5(4\text{-cypy})]^{2-}$ in 0.3 M $[N^nBu_4][BF_4]$ / DCM at 290 K.

In order to identify which peak corresponds to each isomer, two systems were investigated which mimic the different coordination sites of 4-cyanopyridine. Namely, $[TBA]_2[OsCl_5(py)]$ which represents the isomer with the ligand bound through the ring nitrogen, and $[TBA]_2[OsCl_5(bznl)]$, (bznl = benzonitrile) which is analogous to the isomer with the ligand bound through the nitrogen of the cyano group. The cyclic voltammograms of these monomeric species are given Figure 3.4. The half wave potential of the complex with pyridine (-0.01 V) is lower, or at more negative potentials, than that of the benzonitrile complex (+0.17 V). This suggests that for the 4-cyanopyridine complex, the isomer with the lower half wave potential will be due to the ring bound form and hence, the other to the cyano bound form.

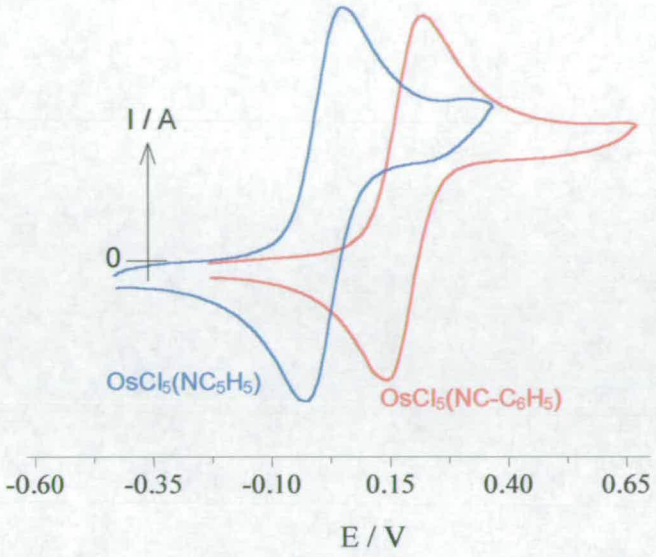

Figure 3.4 Cyclic voltammogram of $[OsCl_5(NC_5H_5]^{2-}$ (blue) and $[OsCl_5(NC\text{-}C_6H_5]^{2-}$ (red) in 0.3 M $[N^nBu_4][BF_4]$ / DCM at 290 K.

To further investigate this prediction a modelling program (CAChe 3.2) was used. An electron density calculation was performed on 4-cyanopyridine, this produced the electron density map shown in Figure 3.5. When studying M(III)/(IV) redox processes, the effect of the π-acceptor capability of the ligands on the stability of the complexes is considered small, hence it is thought the main contributing factor is the σ-donor effect.

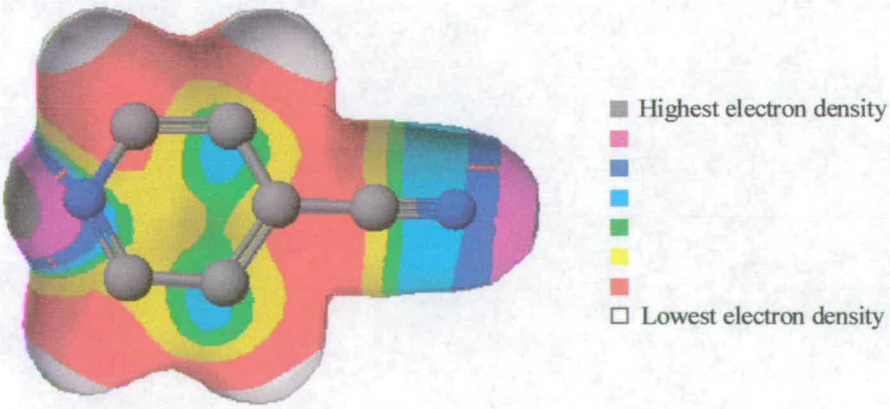

Figure 3.5 Electron density map of 4-cyanopyridine as calculated by CAChe 3.2

Figure 3.5 shows that both nitrogen atoms are electron rich compared to the remainder of the molecule. Detailed study of the electron density calculation reveals there is a greater amount of electron density on the ring nitrogen compared to the nitrogen of the cyano group (the values given were 5.06 and 5.02 respectively) *i.e.* the ring nitrogen is more basic than the cyano nitrogen. Thus the ring nitrogen is a better σ-donor, this would make the Os(III) complex more easy to oxidise than that bound through the cyano group, hence $[OsCl_5(\underline{N}C_5H_4CN)]^{2-}$ will have the lower Os(III)/Os(IV) half-wave potential.

The differential pulse voltammogram shown in Figure 3.3 was performed immediately following the complete reduction of $[OsCl_6]^{2-}$. This shows that initially the two isomers are formed in equal amounts (the two peaks are equal in area). However, when left at room temperature under Argon, a change in the differential pulse voltammogram was observed with time (Figure 3.6). An isomerisation reaction is taking place, the cyano-nitrogen bound species is converting to the ring bound species. Eventually, after approximately two days, complete conversion to the more thermally stable isomer namely, $[OsCl_5(\underline{N}C_5H_4CN)]^{2-}$ is observed.

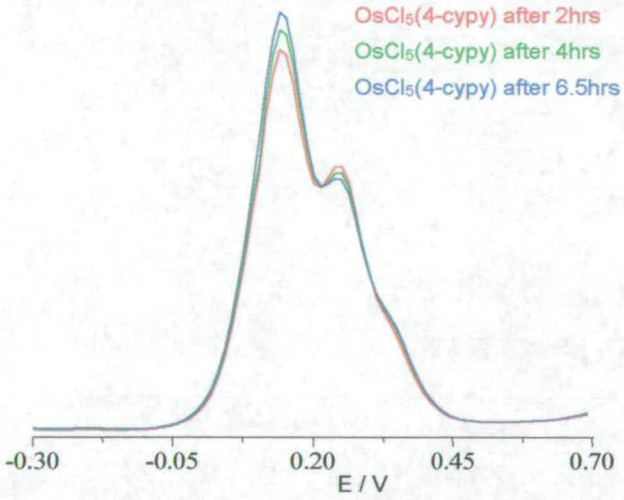

Figure 3.6 Differential pulse voltammograms following conversion of $[OsCl_5(4\text{-cypy})]^{2-}$ to stable isomer.

The complex TBA[$OsCl_5$(4-cypy)] has also been synthesised chemically.[28] Crystals suitable for X-ray analysis were grown and the resulting structure is shown in Figure

3.7. Interesting bond lengths and angles are shown in Table 3.5. Note that it was only possible to isolate and structurally characterise the pyridine-bound isomer. The cyano-bound isomer has never been isolated from this reaction, which is another indication of the stability of the ring-bound form. An electrochemical study of a solution of the pyridine-bound isomer reveals a redox process at +0.14 V confirming the assignment of the lower half-wave potential process in Figure 3.3 to the compound $[OsCl_5(p\text{-}\underline{N}C_5H_4CN)]^{1-}$.

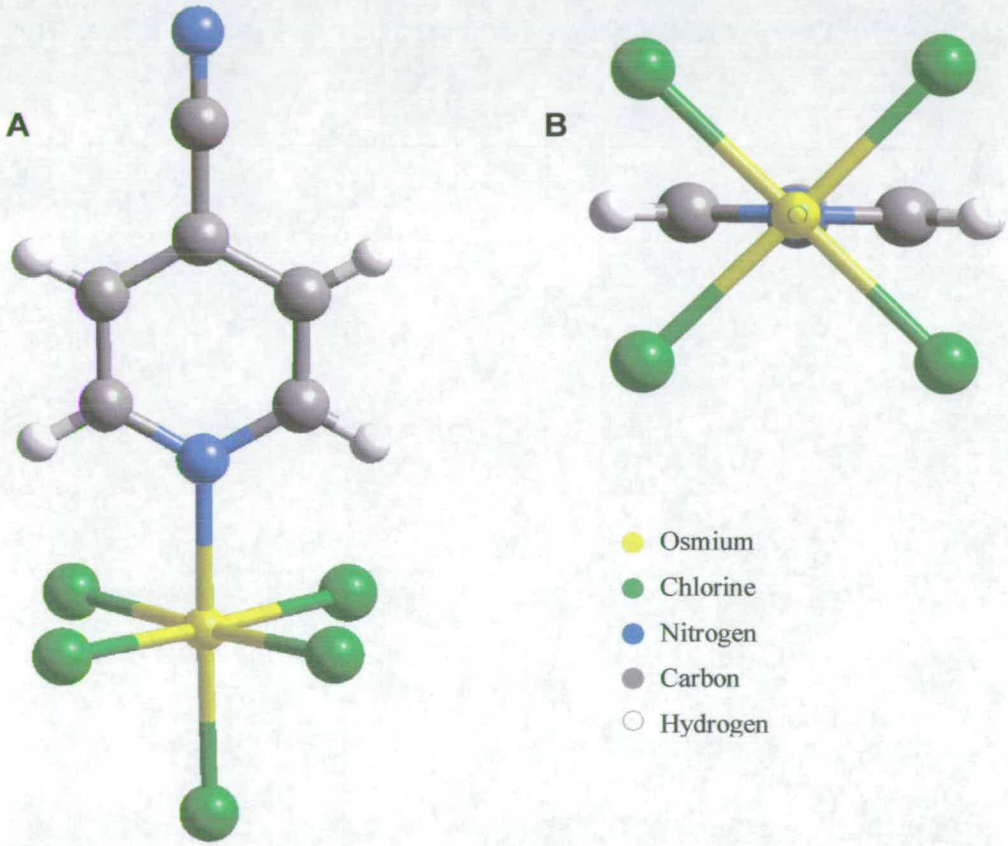

Figure 3.7 Crystal structure of TBA[$OsCl_5$(4-cypy)]. **A** shows the complete structure and **B** shows the orientation of the ring by viewing along the Cl-Os-N bonds.

Table 3.5 Selected bond lengths (Å) and angles (°) for $[N^nBu_4][OsCl_5(p\text{-}\underline{N}C_5H_4CN)]$.

Os(1) – N(1)	2.129(4)	N(1) – Os(1) – Cl(1)	179.87(13)
Os(1) – Cl(1)	2.3088(15)	N(1) – Os(1) – Cl(2-5)	87.82-88.92(12)
Os(1) – Cl(2-5)	2.3218-2.3349(15)	C(2) – N(1) – Os(1)	120.8(5)
C(7) – N(8)	1.144(7)	C(6) – N(1) – Os(1)	120.5(5)
C(7) – C(4)	1.430(8)		

Also synthesised in this work was the compound TBA[$OsCl_5$(pyz)] its crystal structure is shown in Figure 3.8 for comparison. Interesting bond angles and bond lengths are shown in Table 3.6.

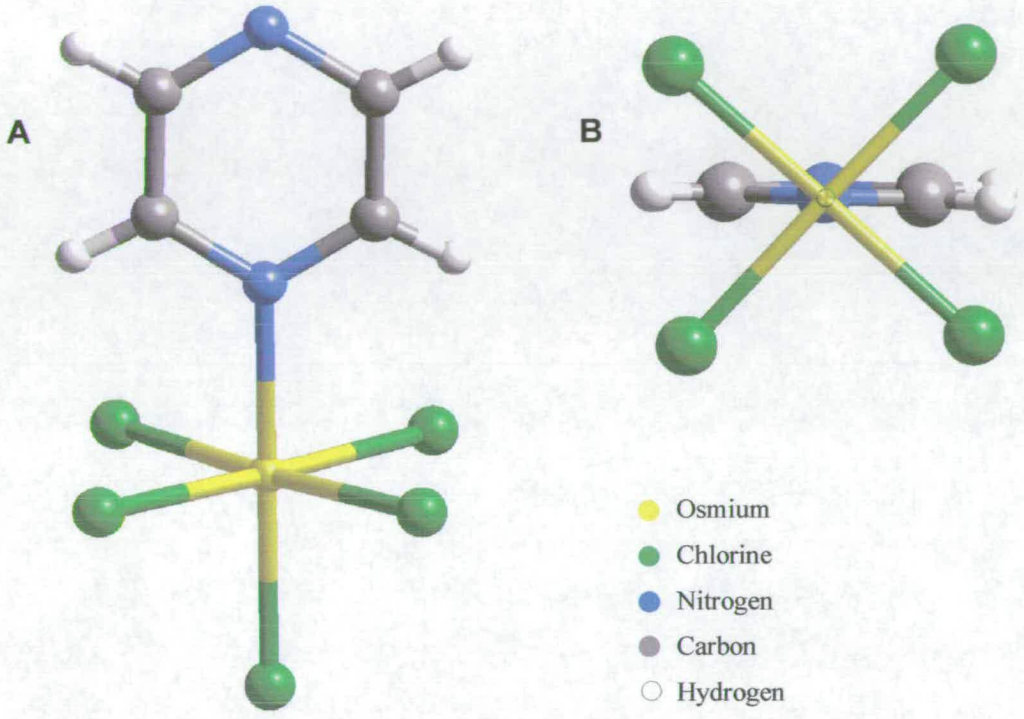

Figure 3.8 Crystal structure of TBA[$OsCl_5$(pyz)]. **A** shows the complete structure and **B** shows the orientation of the ring by viewing along the Cl-Os-N bonds.

Table 3.6 Selected bond lengths (Å) and angles (°) for [N^nBu_4][$OsCl_5(N_2C_4H_4)$].

Os(1) – N(1)	2.102(9)	N(1) – Os(1) – Cl(8)	178.6(3)
Os(1) – Cl(8)	2.306(3)	N(1) – Os(1) – Cl(4-7)	88.1-90.2(3)
Os(1) – Cl(4-7)	2.319-2.332(3)	C(2) – N(1) – Os(1)	121.5(8)
		C(6) – N(1) – Os(1)	123.9(8)

If these two structures are compared the bond lengths and angles around the osmium centre are not significantly different (when errors are considered). Thus, no information regarding the electronic nature of the osmium centre can be extracted from this comparison.

In general, the OsCl bond, which is *trans* to the 4-cyanopyridine (or pyrazine) ligand, is shorter then the four remaining equatorial OsCl bonds, as predicted by the *trans* influence. The ring is orientated such that the steric interaction with the equatorial chloride ligands is minimised. All other parameters are as expected for a structure of this type.

When a one-to-one equivalent of metal to ligand are reacted in the electrosynthesis experiment a 50:50 ratio of isomers is initially produced. This is the statistical distribution expected. The species then slowly converts to the most stable isomer over two days. To investigate the effect of having a higher ligand to metal ratio, the electrolysis of $[OsCl_6]^{2-}$ was carried out in the presence of a ten fold excess of 4-cyanopyridine. Here, initially the isomers were formed in a 2:1 ratio (ring bound : cyano-nitrogen bound) and after only 5 hours the conversion to the ring-bound isomer was complete. This shows the strong preference for the formation of the ring-bound isomer indicating its increased stability compared to the cyano bound isomer.

A UV/Visible spectroelectrochemical experiment was performed of the reversible Os(III)/Os(IV) redox process in $[OsCl_5(4\text{-cypy})]^-$. The results are shown below in Figure 3.9. The spectrum of the Os(IV) species is dominated by an intense band at 26750 cm^{-1} (ε = 4200 M^{-1} cm^{-1}) which is assigned as a LMCT transition, namely, Cl^- $\rightarrow$ Os(IV) $d\pi$. A corresponding spin-forbidden transition occurs at 23400 cm^{-1} (ε = 900 M^{-1} cm^{-1}). The most probable assignment of the band at 34000 cm^{-1} (ε = 2100 M^{-1} cm^{-1}) is an intraligand, $\pi \rightarrow \pi^*$ transition since this band does not collapse upon reduction to the Os(III) species.

In general, the OsCl bond, which is *trans* to the 4-cyanopyridine (or pyrazine) ligand, is shorter then the four remaining equatorial OsCl bonds, as predicted by the *trans* influence. The ring is orientated such that the steric interaction with the equatorial chloride ligands is minimised. All other parameters are as expected for a structure of this type.

When a one-to-one equivalent of metal to ligand are reacted in the electrosynthesis experiment a 50:50 ratio of isomers is initially produced. This is the statistical distribution expected. The species then slowly converts to the most stable isomer over two days. To investigate the effect of having a higher ligand to metal ratio, the electrolysis of $[OsCl_6]^{2-}$ was carried out in the presence of a ten fold excess of 4-cyanopyridine. Here, initially the isomers were formed in a 2:1 ratio (ring bound : cyano-nitrogen bound) and after only 5 hours the conversion to the ring-bound isomer was complete. This shows the strong preference for the formation of the ring-bound isomer indicating its increased stability compared to the cyano bound isomer.

A UV/Visible spectroelectrochemical experiment was performed on the reversible Os(III)/Os(IV) redox process in $[OsCl_5(4\text{-cypy})]^-$. The results are shown below in Figure 3.9. The spectrum of the Os(IV) species is dominated by an intense band at 26750 cm^{-1} ($\varepsilon = 4200\ M^{-1}\ cm^{-1}$) which is assigned as a LMCT transition, namely, $Cl^- \rightarrow$ Os(IV) $d\pi$. A corresponding spin-forbidden transition occurs at 23400 cm^{-1} ($\varepsilon = 900\ M^{-1}\ cm^{-1}$). The most probable assignment of the band at 34000 cm^{-1} ($\varepsilon = 2100\ M^{-1}\ cm^{-1}$) is an intraligand, $\pi \rightarrow \pi^*$ transition since this band does not collapse upon reduction to the Os(III) species.

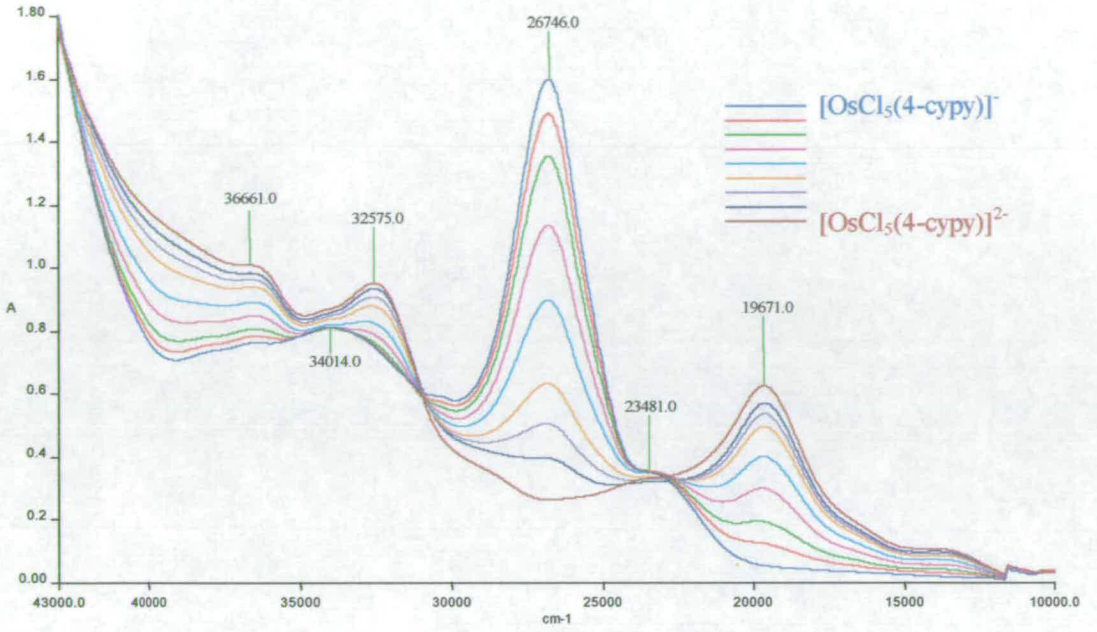

Figure 3.9 UV/Vis Spectroelectrochemistry of $[OsCl_5(4\text{-cypy})]^-$ in 0.4 M $[N^nBu_4][BF_4]$ / DCM at 253 K. E_{app} = -0.13 V.

The spectrum of the Os(III) species shows an absorption at 19650 cm^{-1} (ε = 1600 M^{-1} cm^{-1}) which has been assigned as a MLCT, namely Os(III) $d\pi \rightarrow \pi^*$(4-cypy). The band at 32600 cm^{-1} (ε = 2500 M^{-1} cm^{-1}) has been assigned as a $Cl^- \rightarrow$ Os(III) $d\pi$ LMCT transition, this has moved to higher energy upon reduction to Os(III) as expected due to the increased electron density on the metal centre. Higher energy shoulders and bands are probably, in part, due to intra-ligand transitions. An additional band is observed in the near-IR region, this is shown in Figure 3.10. The spectra shown in this figure are difference spectra since this absorption occurs on top of an absorption by the solvent (DCM).

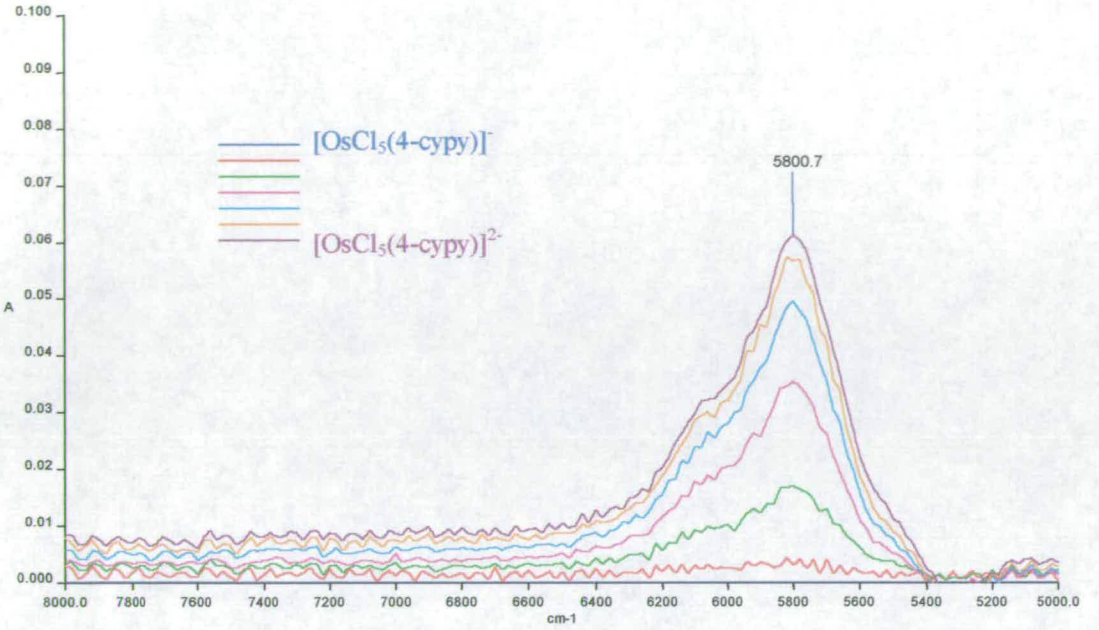

Figure 3.10 Difference spectra of the near-IR region spectra calculated by subtracting the spectrum of $[OsCl_5(4\text{-cypy})]^-$ from those recorded during the one electron reduction of $[OsCl_5(4\text{-cypy})]^-$.

The band at 5800 cm^{-1} (ε = 150 M^{-1} cm^{-1}) is assigned as a d-d transition. Usually this would be due to an excitation from the dπ orbital to a dσ orbital, however, in these osmium complexes the dπ-dσ gap is too large. Thus, transitions between these orbitals will occur in the visible region and most likely be masked by the more intense CT transitions. In complexes such as these the possibility arises for transitions within the metal-based non-degenerate dπ orbitals, these transitions occur at low energy and are weak. Thus the band is assigned as a d$\pi \rightarrow$ dπ transition.

It is thought that upon reduction and re-oxidation of $[OsCl_5(4\text{-cypy})]^-$ some conversion between the two isomers is taking place. As a result, the isosbestic points observed during this experiment (at approximately 23000 and 30800 cm^{-1}) are not as clear as they should be. It is believed that the majority of the complex will be in the ring bound form, however, band positions may be affected by the presence of the cyano-bound isomer.

It has been noted previously, that following formation of the mononuclear complex, $[(NH_3)_5Ru(pyz)]^{2+}$, the basicity of the non-coordinated nitrogen was increased.[29]

CAChe 3.2 was used to predict whether this was also the case when an $[OsCl_5]^{2-}$ fragment was coordinated to the ring nitrogen of 4-cyanopyridine (Figure 3.11). The electron density map shows clearly that the area of grey over the nitrogen of the cyano group is greater than that in Figure 3.5 above; that is, the electron density on the nitrogen atom of the cyano group is considerably greater if the 4-cyanopyridine is bound to a $(OsCl_5)^{2-}$ fragment than in the free 4-cyanopyridine. Thus the basicity of the uncoordinated N atom in $[OsCl_5(\underline{N}C_5H_4CN)]^{1-}$ is increased compared to NC_5H_4CN in a similar way to that noted by Ford *et al.*[29] for $[(NH_3)_5Ru(pyz)]^{2+}$.

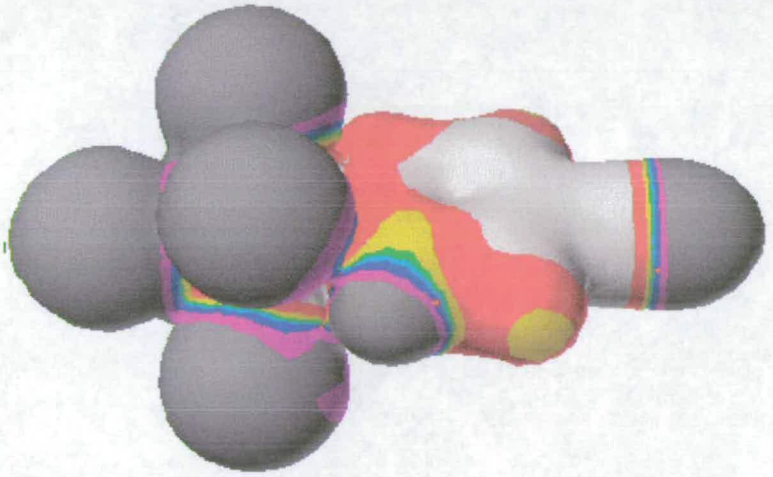

Figure 3.11 Electron density map of $[OsCl_5(\underline{N}C_5H_4CN)]^-$ as calculated by CAChe 3.2

The next step in the electrosynthesis experiment, having synthesised the mononuclear complex, $[OsCl_5(4\text{-cypy})]^{2-}$, is to add a molar equivalent of $[OsCl_6]^{2-}$. Following complete reduction of this second mole equivalent of $[OsCl_6]^{2-}$ a new species is observed. The cyclic voltammograms of these steps are shown in Figure 3.12. It can be seen clearly from the cyclic voltammogram following the complete reduction (blue line) that there is no $[OsCl_6]^{2-}$ present in solution, and the new species has two oxidation peaks with a larger separation than those of the mononuclear complexes. The two oxidation processes at +0.08 V and +0.33 V are attributed to the binuclear species, $[Cl_5Os(4\text{-cypy})OsCl_5]^{4-}$.

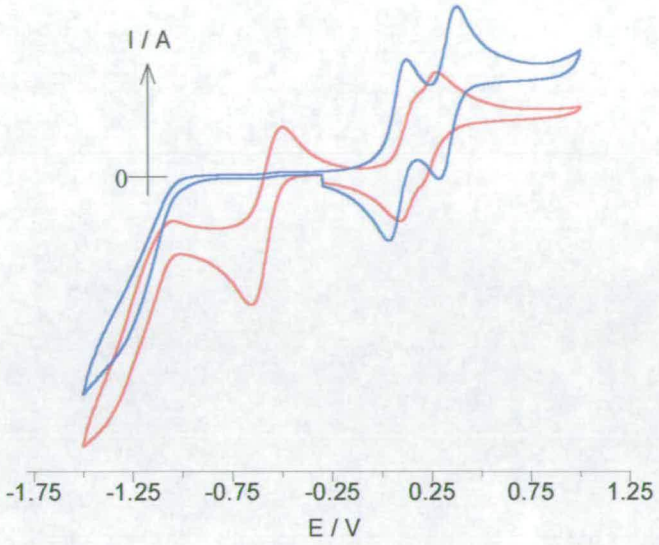

Figure 3.12 Cyclic voltammogram of $[OsCl_6]^{2-}$ + $[OsCl_5(4\text{-cypy})]^{2-}$ (red) and $[Cl_5Os(4\text{-cypy})OsCl_5]^{4-}$ (blue) in 0.3 M $[N^nBu_4][BF_4]$ / DCM at 290 K.

Continuation of the argument presented for assignment of the redox potentials to the individual isomers of the mononuclear species suggests that the half-wave potential measured at +0.08 V involves the osmium centre attached to the pyridine nitrogen of the 4-cyanopyridine bridging ligand. The further process at +0.33 V is attributed to the osmium centre bound through the cyano-nitrogen of the bridging ligand.

The differential pulse voltammogram of the mononuclear and the binuclear species are shown in Figure 3.13, where the difference between the oxidation potentials becomes very apparent. The intensities of the two differential pulse waves for the binuclear species are very similar and do not change with time, unlike the mononuclear species response. This is the expected behaviour for the oxidation of one osmium centre of the binuclear compound followed by oxidation of the second osmium centre, thus confirming the formation of the binuclear species and its indefinite stability.

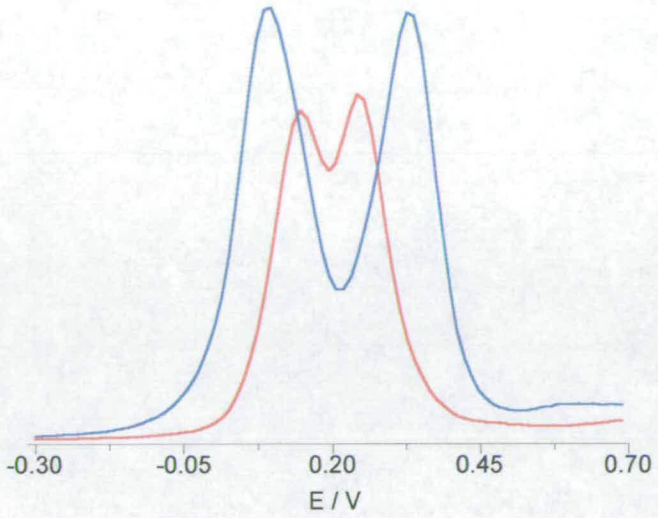

Figure 3.13 Differential pulse voltammogram of $[OsCl_5(4\text{-cypy})]^{2-}$ (red line) and $[Cl_5Os(4\text{-cypy})OsCl_5]^{4-}$ (blue line) in 0.3 M $[N^nBu_4][BF_4]$ / DCM at 290 K.

The first oxidation based on the binuclear complex becomes easier (less positive potential) compared to the mononuclear complexes and the second oxidation becomes more difficult. This phenomenon is often observed when studying binuclear complexes and is indicative of some communication between the metal centres. In the Creutz-Taube ion, even though both metal centres are in chemically identical environments, the successive $Ru^{II/III}$ couples occur at +0.37 and +0.76 V (versus the SHE), a difference of 390 mV,[10] compared to the mononuclear complex which has a half-wave potential of +0.49 V.[30]

The first oxidation is easier with respect to the mononuclear complex due to the addition of an electron rich fragment ($OsCl_5$) to the free nitrogen of the 4-cyanopyridine (or the pyrazine in the Creutz-Taube ion). This additional electron density is communicated through the ligand and, therefore it becomes easier to remove an electron from the system, and hence the oxidation moves to a lower potential. Having taken one electron away from the system, the electron density at one of the metal centres is now greatly reduced. This additional positive charge is then communicated through the bridge to the second metal centre, making it more difficult to remove a second electron from the system, hence the second oxidation moves to a higher potential compared to the mononuclear complex.

Obviously, the binuclear complex $[Cl_5Os(NC_5H_4CN)OsCl_5]^{4-}$ has been prepared in the Os(III)/Os(III) state. Bulk electrolysis at a potential between the two oxidations will generate the mixed-valence Os(III)/Os(IV) species.

Once the desired binuclear compound has been synthesised it is then necessary to separate this species from the inert electrolyte which was added to the solution to improve conductivity. The separation is difficult because the binuclear compound and the electrolyte have similar solubilities, and the only way found to date to separate them is by using a silica gel column. Unfortunately, the binuclear complex is not stable in air in any oxidation state, making this procedure more difficult. In addition, some of the binuclear species reverts back to the mononuclear complex while loaded on the column.

Due to the binuclear complex being unstable in air, characterisation techniques such as elemental analysis could not be performed in order to confirm its formation. A small amount has been isolated, which was used for negative ion electrospray mass spectrometry. Figure 3.14 shows the expected electrospray mass spectra for fragments of $[Cl_5Os(4\text{-cypy})OsCl_5]$ which may be expected to form. The actual mass spectrum obtained is shown in Figure 3.15. The peaks at approximately 419 amu and 540 amu have been expanded to show the isotope distribution more clearly (see Figure 3.16 and Figure 3.17 respectively). The excellent agreement between the isotope distribution of the observed mass spectrum and the predicted spectrum of $Cl_5Os(4\text{-cypy})OsCl_5$ and its fragments, confirms that the binuclear complex has been formed and isolated. To date, crystals suitable for X-ray analysis have proved elusive.

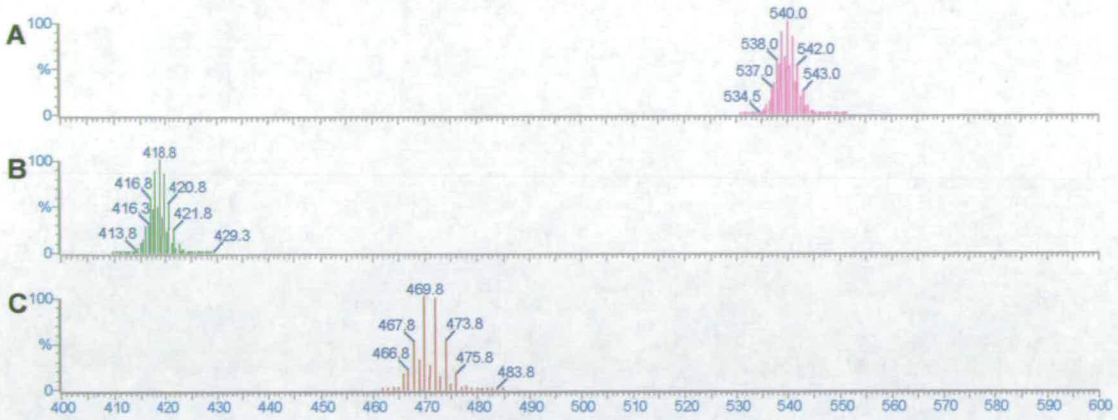

Figure 3.14 Predicted electrospray mass spectrum of **A** $\{Cl_5OsN_2C_6H_4OsCl_5.N(C_4H_9)_4\}^{2-}$, **B** $[Cl_5OsN_2C_6H_4OsCl_5]^{2-}$ and **C** $[OsCl_5N_2C_6H_4]^-$.

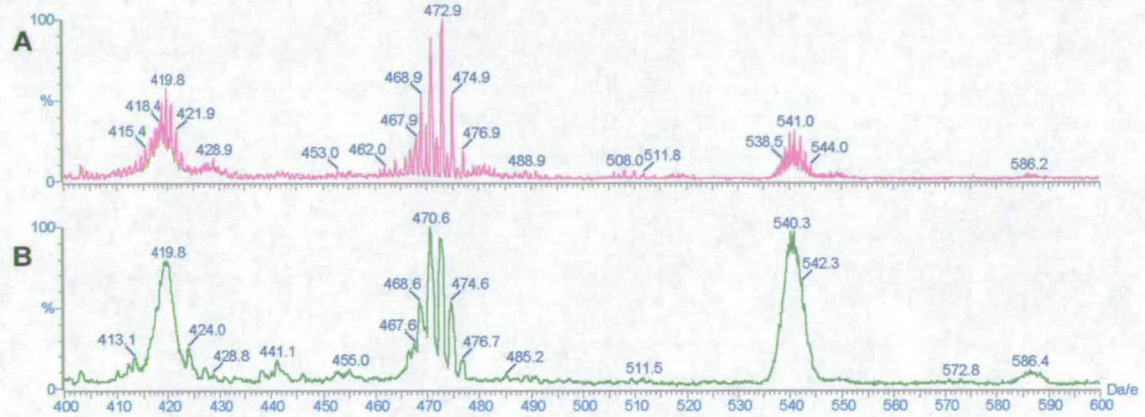

Figure 3.15 Actual mass spectrum of $[Cl_5OsN_2C_6H_4OsCl_5]^{3-}$, **A** at a high resolution and **B** at a lower resolution in DCM.

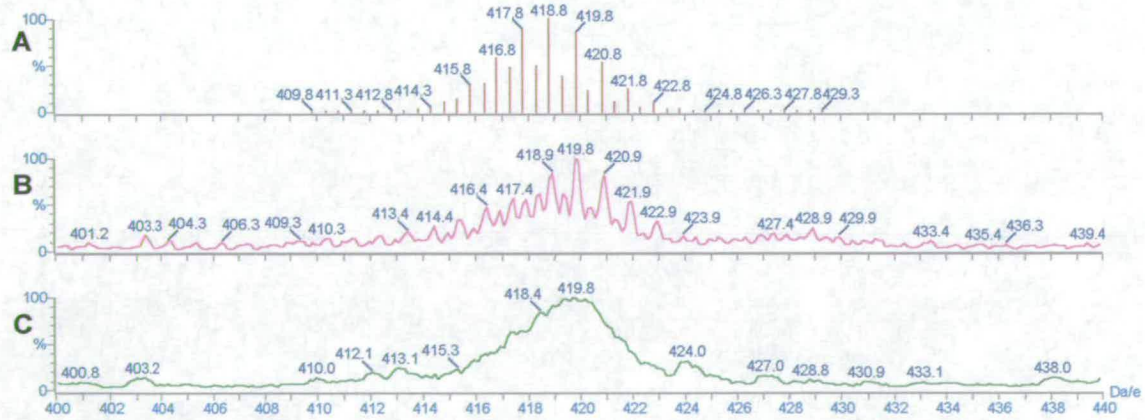

Figure 3.16 Comparison of expected mass spectrum of $[Cl_5OsN_2C_6H_4OsCl_5]^{2-}$ (**A**) and the actual lines observed (**B** and **C**).

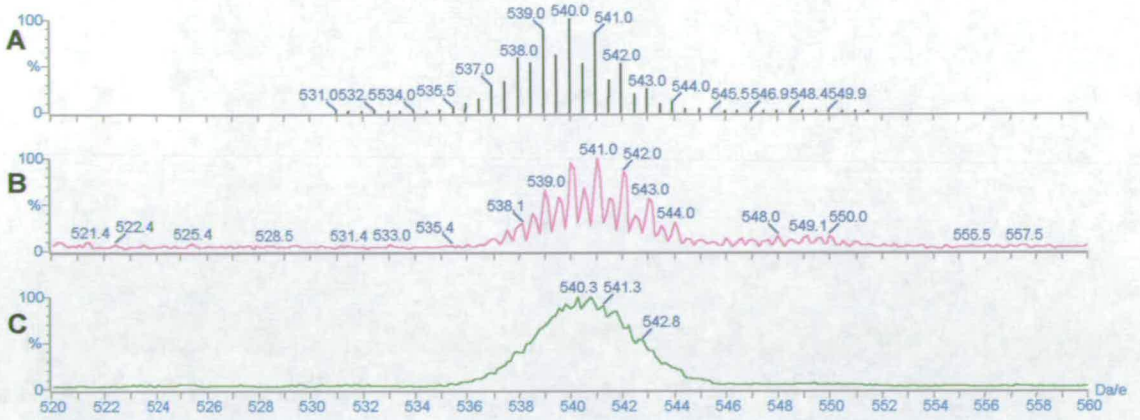

Figure 3.17 Comparison of expected mass spectrum of $\{Cl_5OsN_2C_6H_4OsCl_5.N(C_4H_9)_4\}^{2-}$ (**A**) and the actual lines observed (**B** and **C**).

Table 3.7 shows a summary of the half-wave potentials of complexes obtained during the electrosynthesis of the 4-cyanopyridine bridged complex.

Table 3.7 Half-wave potentials of the 4-cyanopyridine complexes.

Compound	$E_{½}$ / V
$[OsCl_6]^{2-/3-}$	-0.57
$[OsCl_5(p\text{-}\underline{N}C_5H_4CN)]^{2-/-}$	+0.14
$[OsCl_5(p\text{-}\underline{N}CC_5H_4N)]^{2-/-}$	+0.24
$[Cl_5\mathbf{Os}(p\text{-}NC_5H_4CN)OsCl_5]^{4-/3-}$	+0.08
$[Cl_5Os(p\text{-}NC_5H_4CN)\mathbf{Os}Cl_5]^{3-/2-}$	+0.33

The binuclear complex isolated was investigated using electrochemistry and showed the same cyclic voltammogram and differential pulse voltammogram as those found when electrochemically generated, however, a stirred voltammogram showed a reduction process and an oxidation process to be present. Thus indicating that the species is in its mixed-valence form, $[Cl_5Os(4\text{-cypy})OsCl_5]^{3-}$. This complex was then investigated spectroelectrochemically. The spectra recorded during the one electron reduction are shown in Figure 3.18.

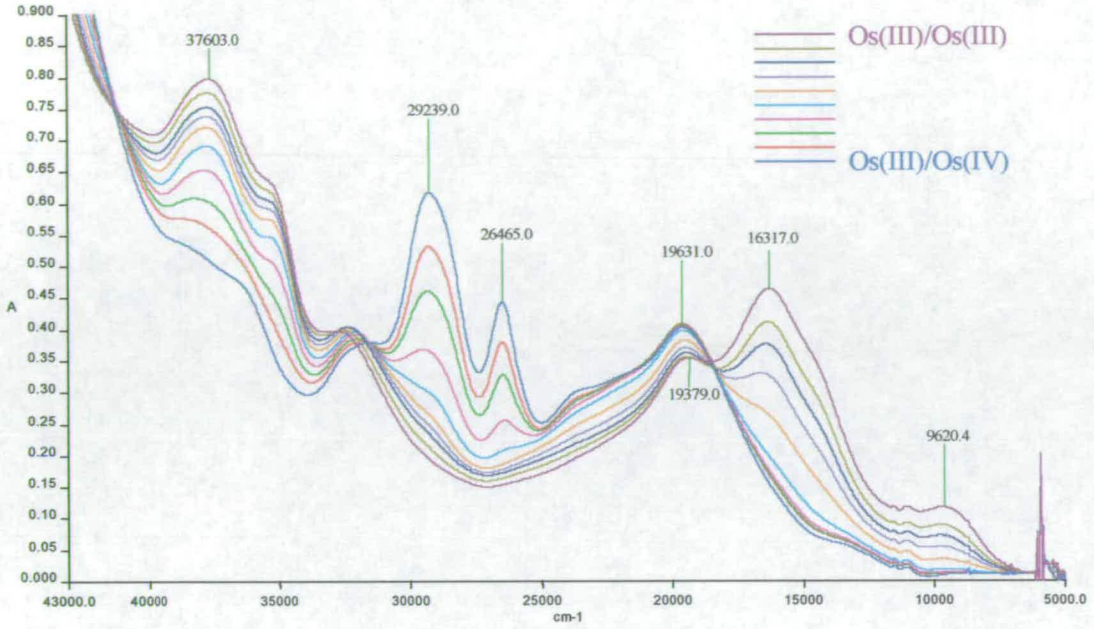

Figure 3.18 UV/Vis spectra recorded during the one-electron reduction of $[Cl_5Os(4\text{-cypy})OsCl_5]^{3-}$ in 0.4 M $[N^nBu_4][BF_4]$ / DCM at 233 K. E_{app} = -0.6 V.

Generally, in symmetrical binuclear complexes, the UV/Vis spectrum of the fully reduced species resembles that of the reduced mononuclear species (see Chapter 5). If the spectrum of the fully reduced binuclear complex is compared to that of the reduced mononuclear complex, namely, $[OsCl_5(p\text{-}\underline{N}C_5H_4CN)]^{2-}$ some similarities are observed. Both contain bands at approximately 19500 cm^{-1} and 32500 cm^{-1} and the band assignment in the binuclear complex will be as that for the mononuclear complex. On the other hand, the spectrum of the binuclear complex contains additional bands which are not present in the mononuclear species. This can be explained by considering the asymmetry of the complex. The expected spectrum of this asymmetrical binuclear complex will be a combination of the spectrum of the pyridine-bound isomer and the spectrum of the cyano-bound isomer. Thus the additional bands in the binuclear species can be attributed to the osmium which is bound to the cyano nitrogen. The band at 16300 cm^{-1} (ε = 3500 M^{-1} cm^{-1}) is assigned as a MLCT transition, namely Os(III) $d\pi \rightarrow \pi^*$(4-cypy).

Three isosbestic points are observed during this reduction, at 41000, 31500 and 18300 cm^{-1}. The accuracy of these points is being lost near the end of the

coulometry. This indicates that the fully reduced species may be unstable under these conditions even at low temperature. However, the spectrum produced upon re-oxidation to the mixed-valence species is almost identical to the starting spectrum. This indicates that the decomposition of the complex is minimal.

The near-IR region of these spectra is shown below (see Figure 3.19). The bands in this region are tentatively assigned as dπ-dπ transitions ($\varepsilon \sim 10^2$ M^{-1} cm^{-1}) which can occur in both the Os(III)/Os(III) and Os(III)/Os(IV) oxidation states.

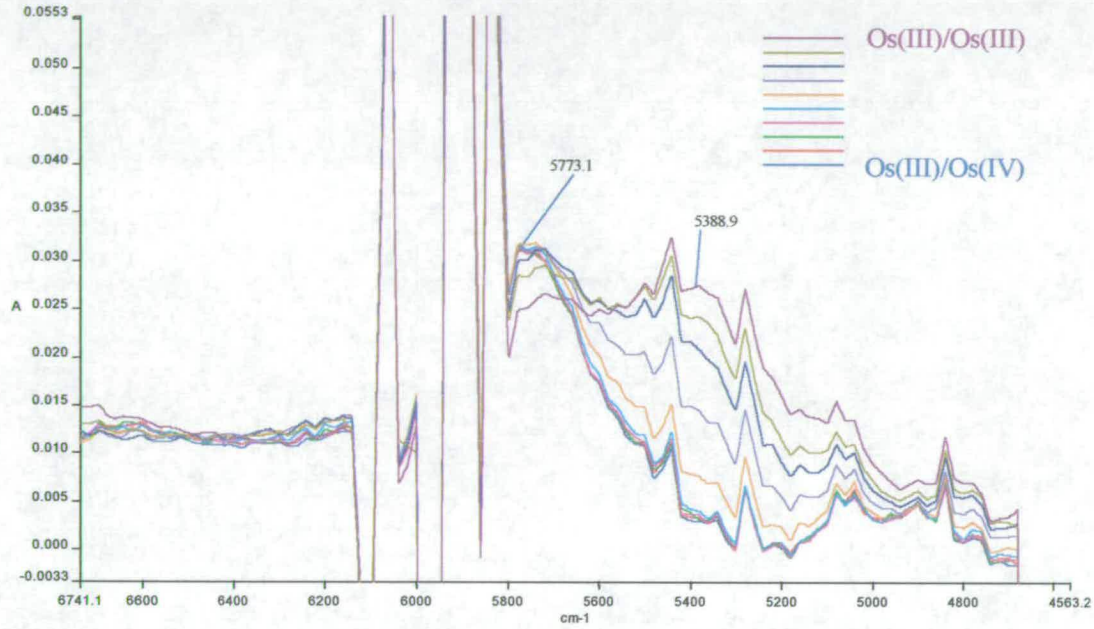

Figure 3.19 Near IR region of the UV/Vis spectra recorded during the one-electron reduction of the complex $[Cl_5Os(4\text{-cypy})OsCl_5]^{3-}$ in 0.4 M $[N^nBu_4][BF_4]$ / DCM at 233 K. E_{app} = -0.6 V.

The spectra recorded during the one-electron oxidation are shown in Figure 3.20 below. Following the investigation of the fully reduced species, the spectrum of the fully oxidised species should resemble that of the mononuclear pyridine-bound Os(IV) species. Any additional bands will be due to transitions mainly within the osmium fragment which is bound to the cyano nitrogen. The bands at 23200 (ε = 2400 M^{-1} cm^{-1}) and 26500 cm^{-1} (ε = 6100 M^{-1} cm^{-1}) are both observed in the spectrum of the pyridine-bound isomer (at 23400 and 26700 cm^{-1}) and are assigned similarly. The additional band at 29100 cm^{-1} (ε = 5500 M^{-1} cm^{-1}) is assigned as a

LMCT transition, namely, $Cl^- \rightarrow Os(IV)$ $d\pi$ transition involving the osmium fragment which is bound to the cyano nitrogen.

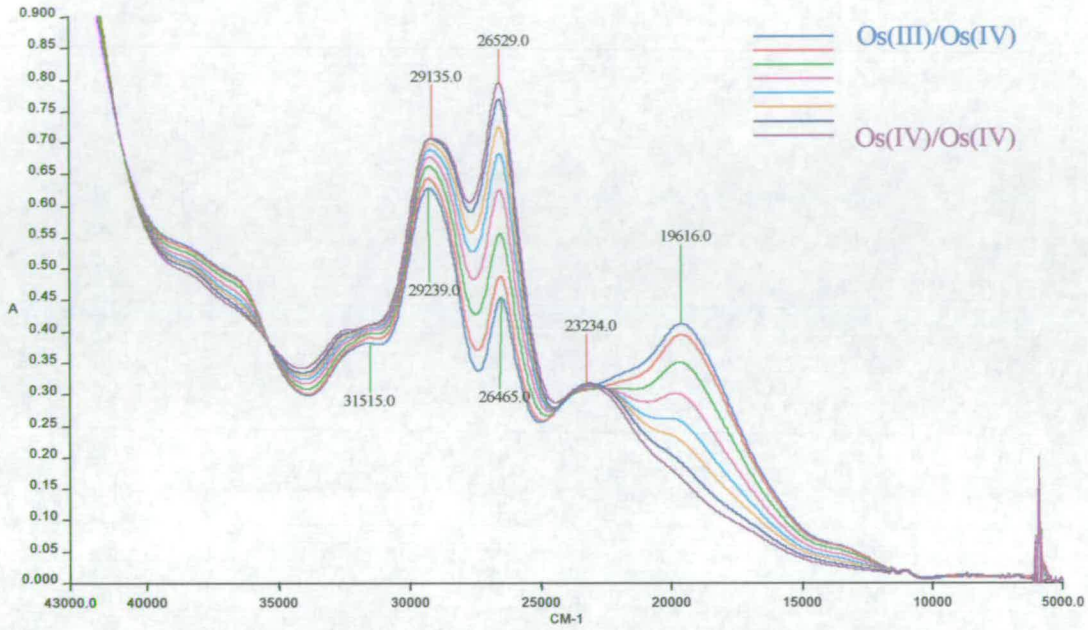

Figure 3.20 UV/Vis spectra recorded the one-electron oxidation of $[Cl_5Os(4\text{-cypy})OsCl_5]^{3-}$ in 0.4 M $[N^nBu_4][BF_4]$ / DCM at 233 K. E_{app} = +0.4 V.

Two isosbestic points are observed during this oxidation, at 35350 and 22550 cm^{-1}. The accuracy of these isosbestic points is lost near the end of the coulometry. This indicates that the fully oxidised species may also be unstable under these conditions even at low temperature. The spectrum produced upon re-reduction to the mixed-valence species is almost identical to the starting spectrum, indicating that the level of decomposition of the complex is minimal.

The near-IR region of the spectra recorded during the oxidation is shown in Figure 3.21. The bands in this region collapse upon formation of the Os(IV)/Os(IV) species.

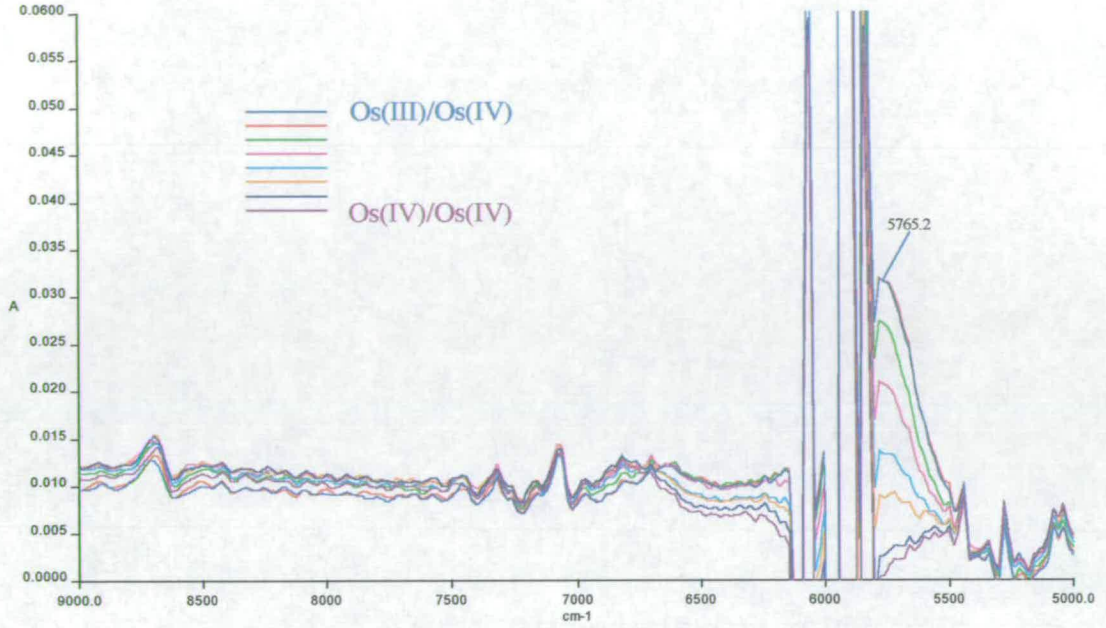

Figure 3.21 Near IR region of the UV/Vis spectra recorded during the one-electron oxidation of $[Cl_5Os(4\text{-cypy})OsCl_5]^{3-}$ in 0.4 M $[N^nBu_4][BF_4]$ / DCM at 233 K. E_{app} = +0.4 V.

The spectrum of the mixed-valence species displays aspects of both the fully reduced and the fully oxidised species but with slightly perturbed features. This has been outlined more clearly in Figure 3.22. One explanation for the appearance of the spectrum could be the disproportionation reaction:

$$2\ \text{Os(IV)/Os(III)} \rightleftharpoons \text{Os(III)/Os(III)} + \text{Os(IV)/Os(IV)}$$

If this were the case, the spectrum observed would be the sum of the fully reduced spectrum and the fully oxidised spectrum divided by two. The software used to control the UV/Vis spectrometer allows this calculation to be performed and the spectrum produced is also shown in Figure 3.22 (red line).

If the actual spectrum of the mixed-valence complex is compared to the spectrum expected for the disproportionation product, then it is obvious that disproportionation does not account for the observed spectrum. Since the spectrum observed is slightly perturbed for those of the constituent ions, then this would imply that the binuclear species is a Class II mixed-valence species. If this is the case, an intervalence charge transfer transition should be observed.

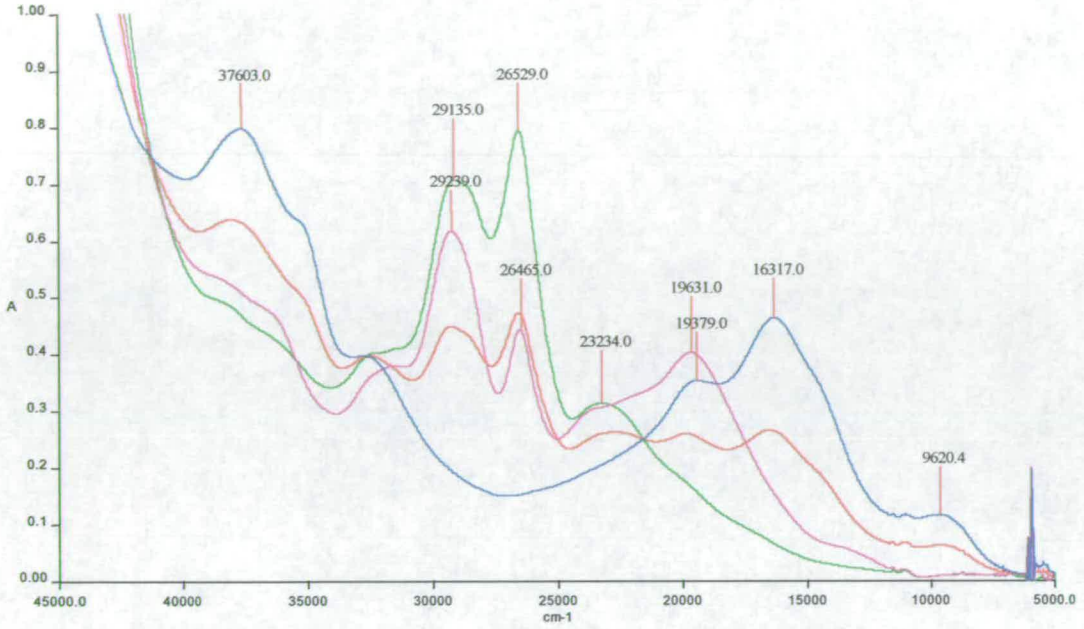

Figure 3.22 UV/Vis spectrum of $[Cl_5Os(4\text{-cypy})OsCl_5]^{4-}$ - blue line; $[Cl_5Os(4\text{-cypy})OsCl_5]^{3-}$ - pink line; $[Cl_5Os(4\text{-cypy})OsCl_5]^{2-}$ - green line in 0.4 M $[N^nBu_4][BF_4]$ / DCM at 233 K and predicted spectrum of the disproportionation reaction product – red line.

The near IR region of the spectrum is complicated by the $d\pi \rightarrow d\pi$ transitions which are characteristic of the Os(III) oxidation state and the band observed at 5750 cm^{-1} is very similar to the band in the mononuclear Os(III) complex. Furthermore, if the IVCT transition occurs at higher energy, it will probably be masked by the numerous CT transitions. It is thus difficult to identify an IVCT transition in this mixed-valence species.

3.3.2 3-Cyanopyridine Bridged Complex

The bridging ligand cyanopyridine has three isomeric forms, 4-cyanopyridine, 3-cyanopyridine and 2-cyanopyridine. This section reports the analogous study to the 4-cyanopyridine (section 3.3.1) using 3-cyanopyridine.

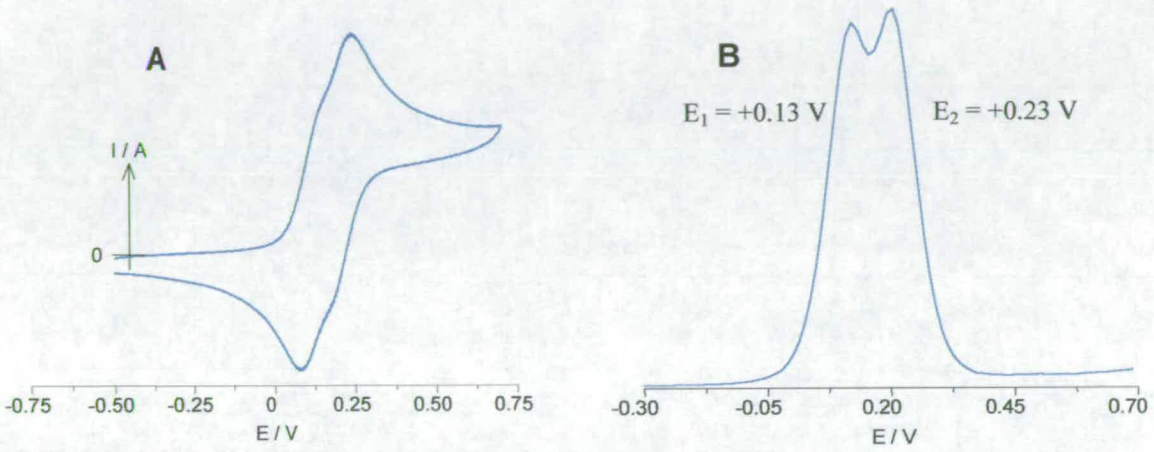

Figure 3.23 A, Cyclic voltammogram and **B,** differential pulse voltammogram of $[OsCl_5(3\text{-cypy})]^{2-}$ in 0.4 M $[N^nBu_4][BF_4]$ / DCM at 290 K.

Figure 3.23 show the cyclic voltammogram and differential pulse voltammogram, respectively, of the product obtained following bulk reduction of $[OsCl_6]^{2-}$ in the presence of a one molar equivalent of 3-cyanopyridine. These voltamograms indicate the presence of two new species (E_{pa} = +0.24 V; E_{pc} = +0.08 V) whose half-wave potentials are similar but distinguishable, both of which have the formula $[OsCl_5(3\text{-cypy})]^{2-}$. These processes are both fully reversible, that is, they show a linear i_p versus $v^{½}$ response and the ratio of peak currents is 1.0.

As in the case of 4-cyanopyridine, there is the possibility of forming two isomers, and indeed these are quite clearly present in approximately a 50:50 ratio. If the reaction mixture is left under argon for a period, a collapse in the band at higher potential and the corresponding growth of the band at lower potential is observed. Thus, the same assignment of these redox processes may be used as that for the mononuclear 4-cyanopyridine compounds. The band at lower potential is due to the isomer in which the ligand is bound through the ring nitrogen, and that at higher potential is due to the cyano-bound form.

$[OsCl_5(3\text{-cypy})]^{1-}$ was synthesised by chemically reducing $[OsCl_6]^{2-}$ with cobaltocene in the presence of 3-cyanopyridine and the product was isolated as yellow needles. The X-ray crystal structure was determined of the pyridine bound isomer and is shown in Figure 3.24. A summary of the interesting bond lengths and angles is given Table 3.8. The cyano-bound isomer has never been isolated from this reaction (as also found for 4-cyanopyridine).

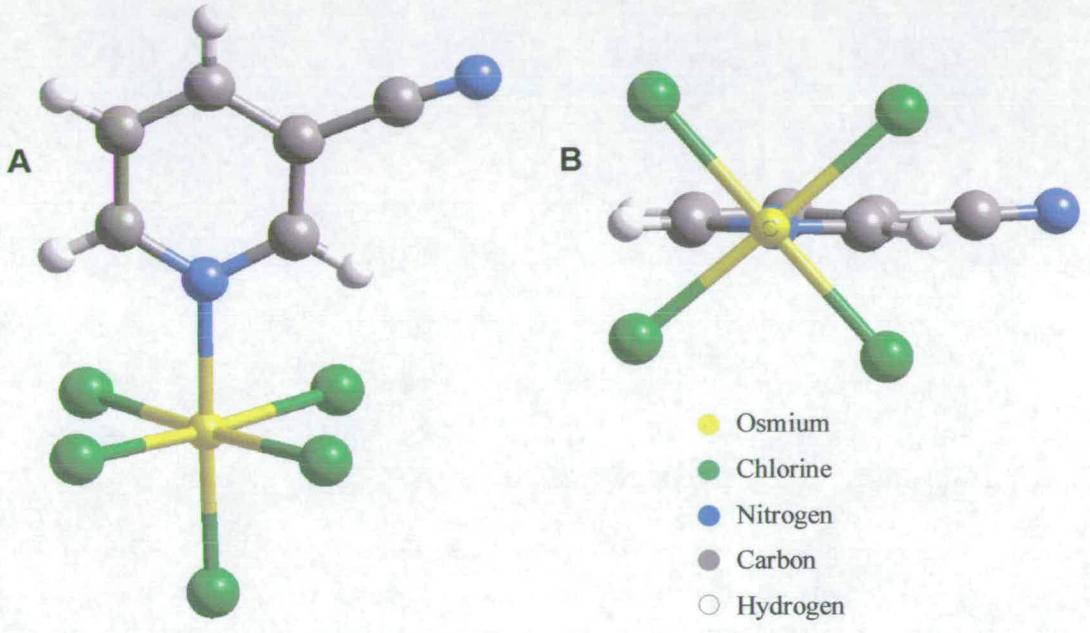

Figure 3.24 Crystal structure of TBA[$OsCl_5$(3-cypy)]. **A** shows the complete structure and **B** shows the orientation of the ring by viewing along the Cl-Os-N bonds.

Table 3.8 Selected bond lengths (Å) and angles (°) for $[N^nBu_4][OsCl_5(m\text{-}NC_5H_4CN)]$.

Os(1) – N(1)	2.138(4)	N(1) – Os(1) – Cl(1)	178.16(11)
Os(1) – Cl(1)	2.2842(16)	N(1) – Os(1) – Cl(2-5)	87.21-88.62(11)
Os(1) – Cl(2-5)	2.3180-2.3423(14)	C(2) – N(1) – Os(1)	119.0(3)
C(7) – N(8)	1.128(7)	C(6) – N(1) – Os(1)	123.1(3)
C(7) – C(3)	1.442(8)		

As found for the 4-cyanopyridine and pyrazine complexes, the OsCl bond which is *trans* to the 3-cyanopyridine ligand is shorter than the four remaining equatorial OsCl bonds, as predicted by the *trans* influence. The ring is orientated such that the steric interaction with the chloride ligands is minimised.

The electrochemistry of the $[OsCl_5(3\text{-cypy})]^{1-}$ isolated was investigated. The cyclic voltammogram obtained showed a fully reversible reduction at +0.12 V confirming the assignment given above. The electrochemical synthesis of the mononuclear complex was repeated using a 10-fold excess of ligand. The product formed was almost exclusively the ring bound form. These results indicate that the pyridine bound isomer is the more stable.

A UV/Visible spectroelectrochemical experiment was performed of the reversible Os(III)/Os(IV) redox process in $[OsCl_5(3\text{-cypy})]^-$. The results are shown below in Figure 3.25. The spectrum of the Os(IV) species is dominated by an intense band at 26950 cm^{-1} (ε = 1800 M^{-1} cm^{-1}) which is assigned as a LMCT transition, namely, Cl^- $\rightarrow$ Os(IV) dπ. A corresponding spin-forbidden transition occurs at 23300 cm^{-1} (ε = 500 M^{-1} cm^{-1}). The most probable assignment of the band 38200 cm^{-1} (ε = 1100 M^{-1} cm^{-1}) is an intraligand, $\pi \rightarrow \pi^*$ transition since this band does not collapse upon reduction to the Os(III) species.

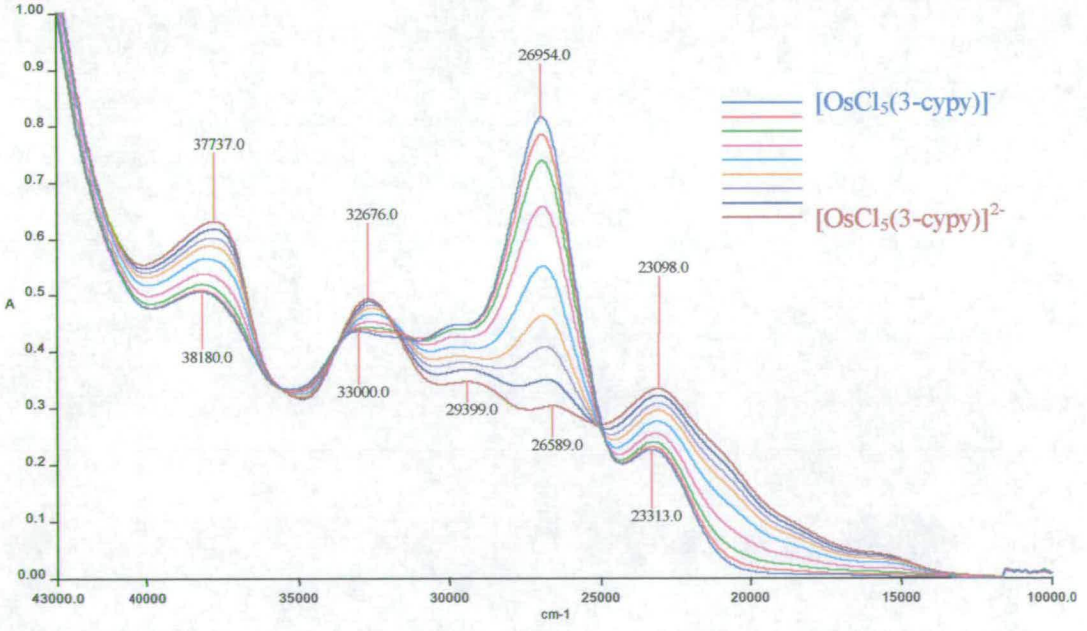

Figure 3.25 UV/Vis Spectroelectrochemistry of $[OsCl_5(3\text{-cypy})]^-$ in 0.4 M $[N^nBu_4][BF_4]$ / DCM at 273 K. E_{app} = -0.20 V.

The spectrum of the Os(III) species shows an absorption at 23100 cm^{-1} (ε = 700 M^{-1} cm^{-1}) which has been assigned as a MLCT, namely Os(III) $d\pi \rightarrow \pi^*$(3-cypy). The band at 32700 cm^{-1} (ε = 1100 M^{-1} cm^{-1}) has been assigned as a $Cl^- \rightarrow$ Os(III) $d\pi$ LMCT transition, this has moved to higher energy upon reduction to Os(III) as expected due to the increased electron density on the metal centre. An additional band is observed in the near-IR region, this is shown in Figure 3.26. The spectra shown in this figure are difference spectra since this absorption occurs on top of an absorption by the solvent (DCM).

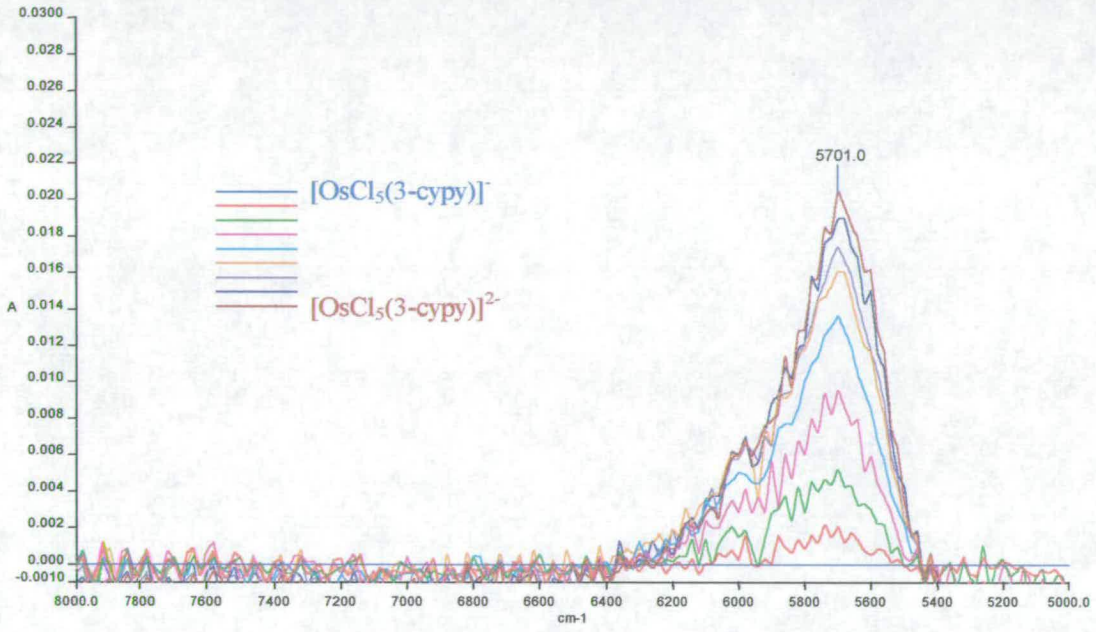

Figure 3.26 Difference spectra of the near-IR region spectra calculated by subtracting the spectrum of $[OsCl_5(3\text{-cypy})]^-$ from those recorded during the one electron reduction of $[OsCl_5(3\text{-cypy})]^-$.

Similar to the 4-cyanopyridine complex, the band in the near infrared region (5700 cm^{-1}; ε = 50 M^{-1} cm^{-1}) is assigned as a $d\pi \rightarrow d\pi$ transition.

It is thought that upon reduction and re-oxidation of $[OsCl_5(3\text{-cypy})]^-$ some conversion between the two isomers is taking place (this was experienced previously with the 4-cyanopyridine complex). As a result, the isosbestic points observed during this experiment (at approximately 25000, 31700, 33600 and 35500 cm^{-1}) are not as clear as they should be. It is believed that the majority of the complex will be in the

ring bound form, however, band positions may be affected by the presence of the cyano-bound isomer.

The next step in the electrochemical experiment is to add a molar equivalent of $[OsCl_6]^{2-}$ and reduce it. The cyclic voltammogram and differential pulse voltammogram obtained following the bulk reduction of the second molar equivalent of $[OsCl_6]^{2-}$ are shown in Figure 3.27. Also shown in Figure 3.27**B** is the differential pulse voltammogram of the isomers of the mononuclear complex for comparison (red line).

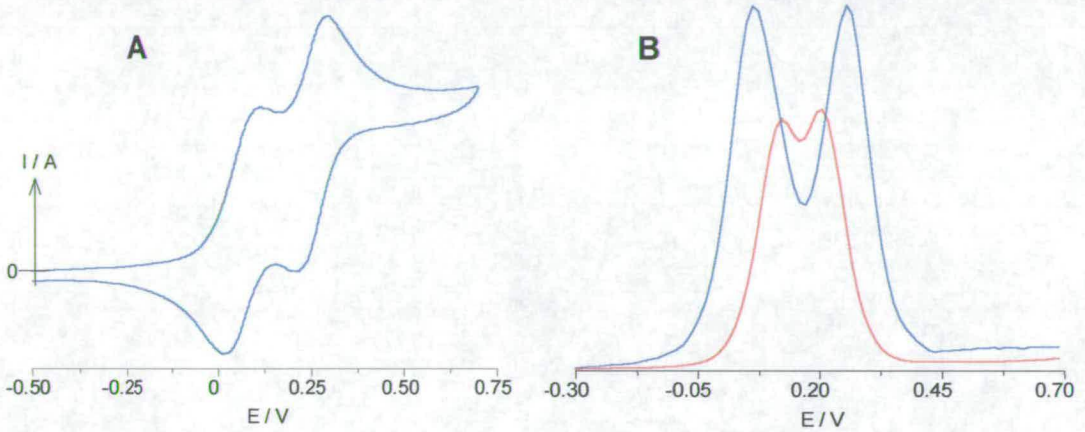

Figure 3.27 A, Cyclic voltammogram of $[Cl_5Os(3\text{-cypy})OsCl_5]^{4-}$ and **B**, differential pulse voltammogram of $[Cl_5Os(3\text{-cypy})OsCl_5]^{4-}$ (blue line) and $[OsCl_5(3\text{-cypy})]^{2-}$ (red line) in 0.4 M $[N^nBu_4][BF_4]$ / DCM at 290 K.

The half-wave potentials for the oxidations of the binuclear complex have a greater separation than the mononuclear complexes. This was also observed using 4-cyanopyridine (*vide supra*), and the same arguments used for the half-wave potentials may be used here. That is, following the correct assignment of the half-wave potentials for the mononuclear complex, it is suggested that the half-wave potential measured at +0.07 V involves the osmium centre attached to the pyridine nitrogen (this is at a lower potential than the corresponding mononuclear species due to the increased electron density caused by the addition of the $(OsCl_5)^{2-}$ fragment to the other side of the bridge). Therefore, the half-wave potential at +0.25 V involves the osmium centre bound to the cyano nitrogen (and is at a more positive potential than the corresponding mononuclear species because an electron has already been

removed from the system and this additional positive charge is communicated through the bridge onto this osmium centre).

Table 3.9 shows a summary of the half-wave potentials of the complexes obtained during the electrosynthesis of the 3-cyanopyridine bridged complex.

Table 3.9 Half-wave potentials of the 3-cyanopyridine complexes.

Compound	$E_{½}$ / V
$[OsCl_6]^{2-/3-}$	-0.57
$[OsCl_5(m\text{-}\underline{N}C_5H_4CN)]^{2-/-}$	+0.12
$[OsCl_5(m\text{-}\underline{N}CC_5H_4N)]^{2-/-}$	+0.20
$[Cl_5\mathbf{Os}(m\text{-}NC_5H_4CN)OsCl_5]^{4-/3-}$	+0.07
$[Cl_5Os(m\text{-}NC_5H_4CN)\mathbf{Os}Cl_5]^{3-/2-}$	+0.25

The binuclear complex, $[Cl_5Os(3\text{-cypy})OsCl_5]^{4-}$ is produced in the Os(III)/Os(III) form. The mixed-valence species can be generated electrochemically by bulk electrolysis at a potential between the two oxidation processes. The same separation problems as experienced for the 4-cyanopyridine complex were encountered for the 3-cyanopyridine complex and to date no suitable crystals for X-ray diffraction studies have been isolated.

From the electrochemistry it can be concluded that the binuclear complex has indeed formed (only this explains the increase in $\Delta E_{½}$ observed following the reduction of the second mole equivalent of $OsCl_6$). However, despite numerous attempts at isolating an electrolyte free sample of the binuclear complex being performed, this was unsuccessful. Therefore further analysis was not permitted.

3.3.3 2-Cyanopyridine Bridged Complex

The electrosynthesis experiment was repeated once more, this time using 2-cyanopyridine as the bridging ligand instead of 4- and 3-cyanopyridine as in Sections 3.3.1 and 3.3.2 respectively.

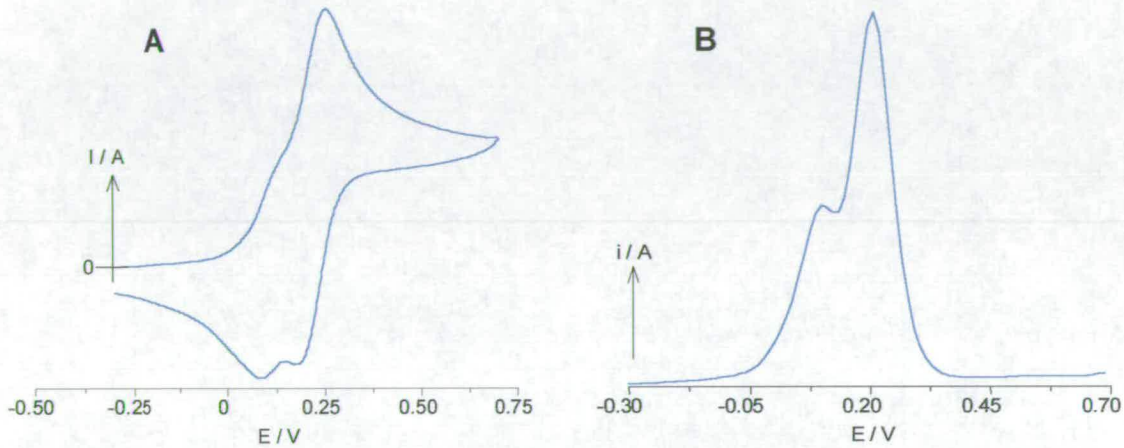

Figure 3.28 A, Cyclic voltammogram and **B,** differential pulse voltammogram of $[OsCl_5(2\text{-cypy})]^{2-}$ in 0.4 M $[N^nBu_4][BF_4]$ / DCM at 290 K.

Figure 3.28 shows the cyclic voltammogram and the differential pulse voltammogram of the product obtained following the reduction of a 1:1 molar solution of $[OsCl_6]^{2-}$ and 2-cyanopyridine. Analogous experiments with 4- and 3-cyanopyridine in place of 2-cyanopyridine resulted in the formation of the two isomers of $[OsCl_5(n\text{-cypy})]^{2-}$. However when a chloride ligand is replaced by 2-cyanopyridine a predominance of one isomer over the other is observed. It is the isomer with the higher half-wave potential which is prevalent. This is in contrast to the other two mononuclear complexes with 3- and 4-cyanopyridine where initially, the isomers were formed in an approximate 50:50 ratio, and then slow conversion to the isomer with the lower potential was observed. This result for the 2-cyanopyridine ligand implies that the isomer bound through the cyano nitrogen is formed preferentially over that bound through the ring nitrogen. One explanation for this is the steric effect of having the cyano group in the 2 position. Obviously this makes the ring nitrogen more sterically crowded, and hence the ligand will prefer to bind through the protruding cyano nitrogen.

If the mixture is allowed to sit in an atmosphere of Argon for a time, some conversion to the lower potential isomer is observed, but it seems that the complex with 2-cyanopyridine is more unstable than those examined previously. The differential pulse voltammogram of the solution having been left over-night shows that some of the complex has converted back to $[OsCl_6]^{2-}$. Of the complex that remains the ratio of isomers is 50:50.

When this reaction is performed in the presence of a ten-fold excess of 2-cyanopyridine, the ratio of isomers produced initially was 1:2 (py bound: CN bound). This is in contrast to the 4- and 3-cyanopyridine complexes investigated where the ring nitrogen bound isomer was formed almost exclusively. These results highlight that steric factors play an important role in the overall stability of the complex when the ligand is 2-cyanopyridine.

The chemical synthesis of the mononuclear 2-cyanopyridine complex was attempted. However, the product isolated from this (Figure 3.29) was not the desired product. Instead, the ligand appears to have been oxidised and is coordinated in a bidentate fashion. Compared to the structures of the 4- and 3-cyanopyridine complexes shown previously, this molecule is under more strain. The angles around the central osmium atom are altered from the octahedral. The N-Os-N angle is 79.2° probably as the result of the formation of a five-membered ring. To compensate for this, the remaining angles in this plane are all greater than 90°, while the pyridine ring of the ligand remains planar. Hydrogen bonds between molecules stabilise this structure.

This result is rather surprising, since ligand oxidation was not found to occur in the mononuclear complexes with 4- or 3-cyanopyridine and highlights that the 2-cyanopyridine complex is unstable. This ligand oxidation probably occurred during the recrystallisation step. No further analysis was carried out on this complex.

Cyanopyridines have been found to be unstable before. Yeh *et al.* [31] when investigating a binuclear complex bridged by 4- and 3-cyanopyridine found that the compounds were unstable with respect to ligand hydrolysis. The complex,

$[(CN)_5Fe(pyCN)Ru(NH_3)_5]^{-1}$ (pyCN = 4- and 3-cyanopyridine) was synthesised and chemically oxidised by one electron to give the mixed-valence state. Following this, a nitrile hydrolysis reaction took place, the final product being $[(CN)_5Fe(pyCONH)Ru(NH_3)_5]$.

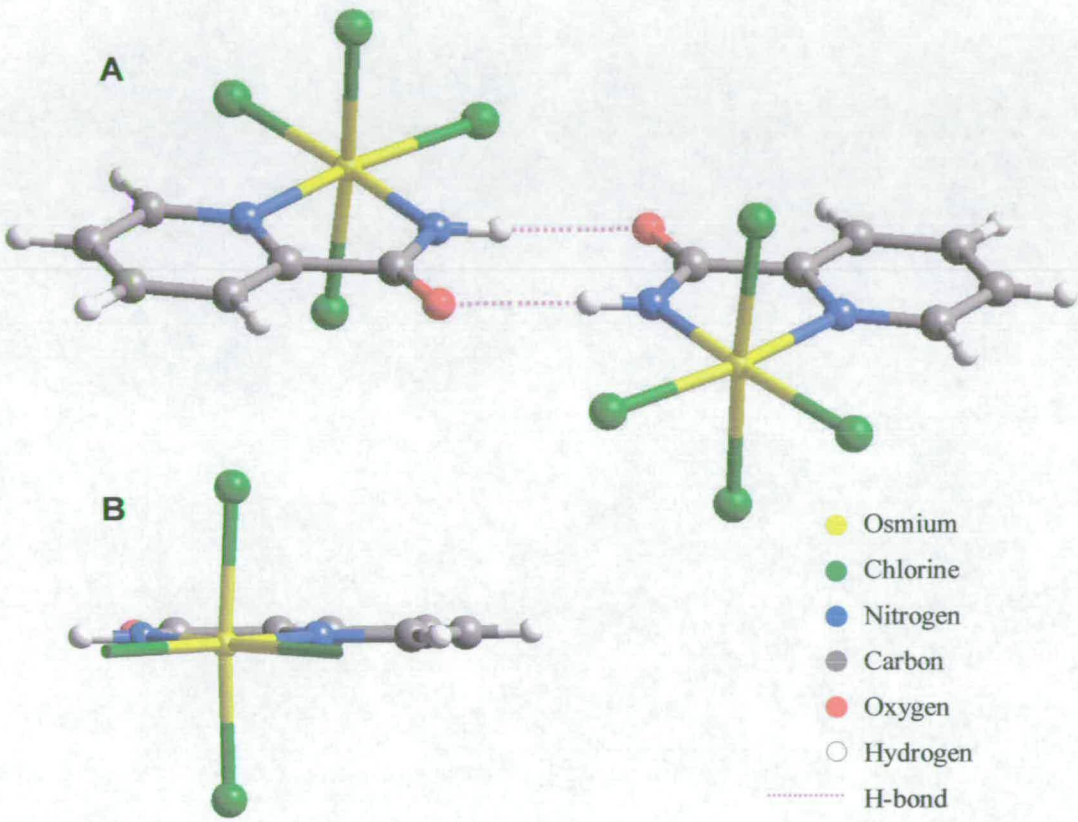

Figure 3.29 Crystal structure of TBA$[OsCl_4(NC_5H_4(CONH)]$. **A** shows the complete structure and the H-bonding between the molecules. **B** shows the orientation of the ring by viewing along the axial plane (as drawn).

Following the formation of the mononuclear complex, a molar equivalent of $[OsCl_6]^{2-}$ was added and then reduced. The differential pulse voltammogram performed immediately after this step is shown in Figure 3.30, which also shows the differential pulse of the mononuclear complex for comparison.

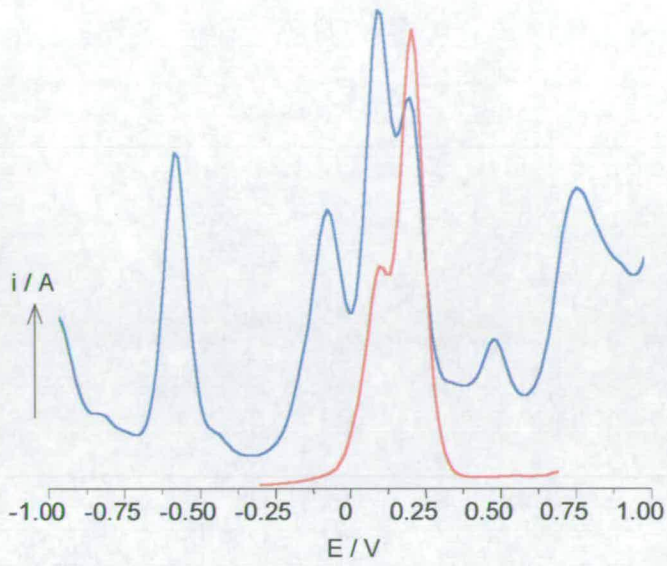

Figure 3.30 Differential pulse voltammogram following the reduction of a molar equivalent of $[OsCl_6]^{2-}$ in the presence of $[OsCl_5(2\text{-cypy})]^{2-}$ (blue line) and, $[OsCl_5(2\text{-cypy})]^{2-}$ (red line) in 0.3 M $[N^nBu_4][BF_4]$ / DCM at 290 K.

It is obvious from these that the binuclear complex does not seem to have been produced since no separation of the half-wave potentials is observed and also the two peaks are not equal in height. A new species seems to be forming with a half-wave potential which is more negative than the mononuclear complex. This product is as yet unidentified.

It has been predicted elsewhere in a study of different systems,[32] that 2-cyanopyridine should allow approximately the same level of communication between the two metal centres as 4-cyanopyridine. Hence, it is expected that upon formation of the binuclear complex the difference between the two half-wave potentials should be approximately equal to that observed with 4-cyanopyridine as the bridging ligand.

In order to ascertain whether it is possible to synthesise the 2-cyanopyridine bridged species, the binuclear complex was modelled using the programme CAChe 3.2. When looking at purely steric effects, taking into consideration the van der waals radii, it seems that formation of the binuclear complex should be possible. It must however be remembered that the osmium centre of $OsCl_5$ unit is electron rich hence,

considerable repulsion is expected between the two pentachloro fragments, perhaps resulting in the formation of the binuclear species being unfavourable. Unfortunately, CAChe 3.2 is not advanced enough to take this into account, a more sophisticated modelling programme would have to be used in order to look at this electronic repulsion effect.

It must be noted that despite an extensive literature search, no evidence of the formation of a binuclear complex bridged by 2-cyanopyridine could be found.

The half-wave potentials for the mononuclear complexes have been highlighted in Table 3.10.

Table 3.10 Half-wave potential of the 2-cyanopyridine complexes.

Compound	$E_{½}$ / V
$[OsCl_6]^{2-/3-}$	-0.57 V
$[OsCl_5(o\text{-}\underline{N}C_5H_4CN)]^{2-/-}$	+0.10 V
$[OsCl_5(o\text{-}\underline{N}CC_5H_4N)]^{2-/-}$	+0.20 V

3.4 Comparison of the cyanopyridines as ligands

3.4.1 Mononuclear complexes

When the electrochemistry of the mononuclear complexes are compared, it is clear that the electronic nature of these three complexes are very similar, thus the exact position of the cyano group on the pyridine ring makes little difference to the redox properties.

If the crystal structure of the complexes with 3- and 4-cyanopyridine are compared, no significant differences in the bond lengths and angles were observed. This is also an indication that the electronic properties are very similar.

On comparison of the UV/Vis spectroelectrochemistry of the 3- and 4-cyanopyridine mononuclear complexes, very few differences are noted. The majority of the similarly assigned bands in the UV/Vis spectra of equally charged species are very close in energy (within 100-200 cm^{-1}). This is another indication that the electronic nature of these complexes is very similar.

The only significant changes in the absorption bands in the 4-cyanopyridine and 3-cyanopyridine complexes are those which involve the π^* energy level of the cyanopyridine ligand. The $\pi \rightarrow \pi^*$ transition in the Os(IV) complex with 4-cyanopyridine is 4000 cm^{-1} lower in energy than the equivalent band in the 3-cyanopyridine complex. This illustrates that there is a large inherent difference in the energy of the frontier orbitals of the cyanopyridine ligands, the HOMO/LUMO gap being much larger for 3-cyanopyridine.

The MLCT (Os $d\pi \rightarrow \pi^*$) in the Os(III) complexes also varies in energy by a large amount (4000 cm^{-1}), being at a lower energy when the ligand is 4-cyanopyridine. This tends to suggest that the overlap between the Os(III) centre and the π^* orbital of 3-cyanopyridine is greater. However, since the π/π^* gap varies between ligands, and

the energy of the LUMO for each ligand is unknown (it would be necessary to measure the reduction potential of the ligand to give an indication of this), no conclusions can be drawn from this.

Generally, LMCT ($Cl^- \rightarrow d\pi$) transitions were observed in both the Os(III) and Os(IV) species, with the transitions in the Os(III) (d^5 electronic configuration) species being at a much higher energy (10000 cm^{-1}). On reduction to Os(III) the energy of the $d\pi$ levels will increase and as a result it will be more difficult to perform this LMCT transition, and hence the absorption will move to a higher energy. Also, in the Os(IV) (d^4 electronic configuration) species, the additional electron (from the ligand) may enter an empty orbital, whereas in the Os(III) (d^5) species the orbital is already singly occupied, this may be another reason for the difference in energy.

The low energy band observed in both mononuclear Os(III) complexes (at ~5700 cm^{-1}) has been assigned as a $d\pi \rightarrow d\pi$ transition (sometimes termed an intra-t_{2g} transition). This type of band has been observed previously[33,34] and can be used as a diagnostic tool for the Os(III) oxidation state. In a communication by Lay *et al.*[34] it was stated that "in general a medium intensity ($\varepsilon \sim 10^2$ M^{-1} cm^{-1}) narrow transition occurs at ~2100 nm, along with other weaker transitions for complexes containing π-acceptor ligands. For those where π-bonding is weak, only weak ($\varepsilon \leq 10$ M^{-1} cm^{-1}) transitions have been observed." Since the extinction coefficient of the 4-cyanopyridine complex is much larger than that of the 3-cyanopyridine complex, this tends to suggest that 4-cyanopyridine is acting as a better π-acceptor.

3.4.2 Binuclear complexes

The formation of the binuclear complex with 4-cyanopyridine was confirmed using electrospray mass spectrometry.

In general, upon formation of the binuclear complex, the splitting between the two peaks in the differential pulse voltammograms (180-250 mV) is increased compared to the splitting due to the two mononuclear isomers (100 mV) and is indicative of some communication between the two metal centres (discussed previously). The potential difference ($\Delta E_{½} = E_1 - E_2$) when 4-cyanopyridine is the bridging ligand is 250 mV, while the complex with 3-cyanopyridine has a $\Delta E_{½}$ of only 180 mV. This corresponds to K_c values of approximately 17000 and 1100 respectively. However, K_c values for asymmetrical complexes must be treated with caution since there is an inherent potential difference in the absence of communication between the two centres (shown by the difference in potentials of the isomers of the mononuclear complexes). Nevertheless, these values do show that there is a greater level of interaction between the osmium centres when they are bridged by 4-cyanopyridine compared to 3-cyanopyridine.

3.5 Conclusions

The mononuclear complexes of 2-, 3- and 4-cyanopyridine have been shown, through (where possible) electrochemical and spectroelectrochemical investigations, to be very similar electronically. That is, the exact position of the cyano moiety has little effect on the overall electronic nature of the complex. This is in accordance with these ligands being principally σ-donating ligands.

In the binuclear complexes, it appears that the bridging ligand 4-cyanopyridine permits a larger degree of communication between the two osmium centres than the 3-cyanopyridine. This is evident in the splitting between the two redox couples (and correspondingly the K_c values), which is larger with 4-cyanopyridine than 3-cyanopyridine.

This phenomenon was also noted by Richardson and Taube in a study of $[\{Ru(NH_3)_5\}_2(\mu\text{-}L)]^{n+}$ (where n = 4, 5, 6 and L = pym, pyz, 3-cypy, 4-cypy amongst others).[32] Here, when the bridging ligand was 4-cyanopyridine the comproportionation constant, K_c, was calculated to be 45000, while that for the 3-cyanopyridine complex was 6370. Thus, the extent of delocalisation is reduced in the latter. Through investigating a number of bridging ligands some guidelines were established for the prediction of the relative degree of metal-metal interaction in related intramolecular redox systems. It was stated that if a metal is bound to the starred position of a neutral alternating hydrocarbon bridging ligand (see Figure 3.31), the strongest metal-metal interaction occurs when the second metal is bound to an unstarred position. Thus, the results reported in this chapter are in accordance with this.

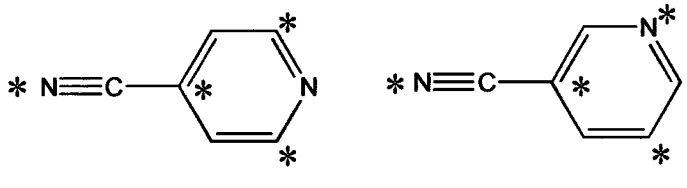

Figure 3.31 Structure of 4-cyanopyridine and 3-cyanopyridine with alternating atoms highlighted.

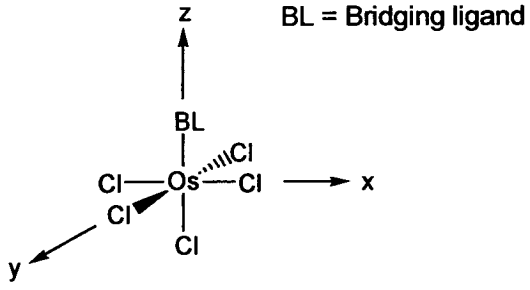

Figure 3.32 Labelling scheme for the molecular fragment $OsCl_5L$.

Upon substitution of the NH_3 ligand for Cl^- ligands the amount of communication between the metal centres is reduced. This can be explained if the molecular orbitals of the osmium centre are considered. Assuming the molecular axes are labelled as shown in Figure 3.32, the d_{xz} and the d_{yz} orbitals will interact with 3 Cl^- ligands (plus the bridging ligand), thus will be destabilised by some extent. The d_{xy} orbital will interact with 4 Cl^- ligands thus will be destabilised by an even larger amount. Therefore the LUMO/SOMO of the complex will be the d_{xy} orbital. In the mixed-valence complex (d^4/d^5) the odd electron will be in the d_{xy} orbital. This orbital has no direct overlap with the orbitals of the bridging ligand thus the reduced level of delocalisation observed experimentally is explained.

Although the chloride ligands have allowed the study of the d^4/d^5 mixed-valence complex, due to the π-donating nature of the chloride ligands and the symmetry of the complexes, the level of communication between the metal centres has been reduced. It is unfortunate that the very rich absorption spectra of these complexes has precluded observation of IVCT transitions and hence a more detailed study of the d^4/d^5 mixed-valence state.

CHAPTER FOUR :

Cyanide Bridged Heteronuclear Mixed-Valence Complexes of Ruthenium and Manganese

4 Cyanide Bridged Heteronuclear Mixed-Valence Complexes of Ruthenium and Manganese

Reported here is an electrochemical and spectroelectrochemical investigation of the heteronuclear complexes shown in Figure 4.1. Two spectroelectrochemical techniques will be used, namely IR and UV/Visible spectroelectrochemistry. All accessible oxidation states will be studied. The carbonyl group(s) will be used as the IR handle in the IR spectroelectrochemical study.

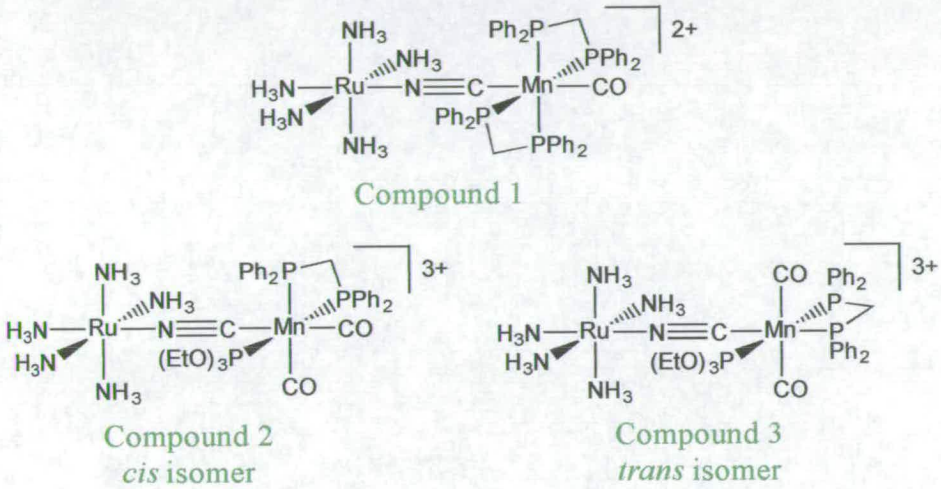

Figure 4.1 Compounds to be studied.

4.1 Introduction

Early studies on mixed-valence compounds focused on the synthesis and investigation of symmetrical homonuclear complexes. Various metal centres were used, the most common containing two ruthenium or two ferrocene nuclei. Unsymmetrical complexes, with respect to the ligand field, were first investigated from 1975. For example, Meyer and co-workers investigated the series $[(NH_3)_5RuLRuCl(bpy)_2]^{4+}$ (L = pyz, 4,4'-bpy, BPE) which formally contains a Ru(II) and a Ru(III) metal centre.[35] They found near-IR intervalence-transfer bands which indicated weak electronic interaction between the two metal centres.

Surprisingly, few studies have been focused on the synthesis of heteronuclear mixed-valence complexes. Early work on heteronuclear mixed-valence compounds primarily involved the combination of a ruthenium pentaammine 2+/3+ fragment and an iron pentacyano 3-/2- unit with a variety of bridging ligands.[36, 37,31] Both of these moieties contain a d^5/d^6 electronic configuration (the iron will be low spin due to the presence of the π-accepting nature of the cyano ligand). These binuclear complexes were found to be best described in terms of valence trapped structures.

Later, this work was also extended to look at a combination of iron, osmium, cobalt and chromium centres with cyanide as the bridging ligand.[38] Here, it was also noted that due to the redox asymmetry of these systems, IVCT bands were shifted to higher energy and often occurred in the visible region. Ligands such as pyrazine also give rise to an intense MLCT in the same energy range, which may obscure the IVCT transition. Thus, pyrazine-type bridging ligands are not ideal for the study of IVCT transitions in heteronuclear complexes. Using cyanide, which is a strong field ligand and therefore is involved in high energy MLCT transitions,[2] avoids these complications. The complexes investigated were found to be weakly interacting.

This realisation afforded an increase in the number of cyanide bridged heteronuclear complexes being investigated. The actual number of studies of their redox and mixed-valence behaviour, however, is still rather small.

4.1.1 Cyanide as a bridging ligand

The molecular orbital diagram for CN^- is shown in Figure 4.2. On bonding to a metal, CN^- will prefer to σ-donate through the carbon atom, since the σ-symmetry orbital (HOMO) has more carbon character than nitrogen and can be considered as a lone pair on the carbon see Figure 4.3. Furthermore, CN^- may also act as weak π-acceptor due to its low energy π* orbitals, which also have more carbon character than nitrogen (see Figure 4.3).

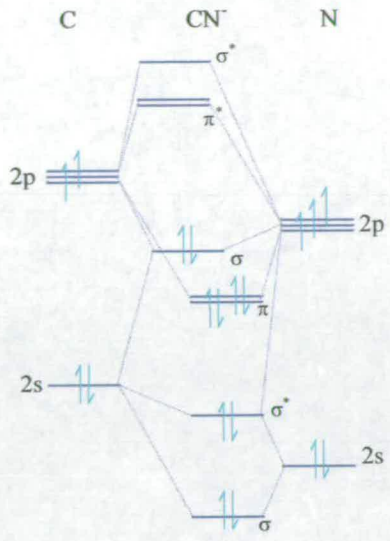

Figure 4.2 Molecular orbital diagram for CN^-.

In order for cyanide to form a bridge between two metal centres, it must donate electrons from the filled σ*-symmetry orbital which is mostly nitrogen in character (that is, the N-lobe protrudes further than the C lobe as shown in Figure 4.3). The overlap between this second metal and the π*-orbital is expected to be smaller than that between the carbon and its coordinated metal (since the lobe of the π*-orbital is smaller on nitrogen). Hence, the π-acceptor capability of the nitrogen will be smaller than that of the carbon. This is shown pictorially in Figure 4.3. These pictures were created using the molecular modelling programme CAChe 3.2.

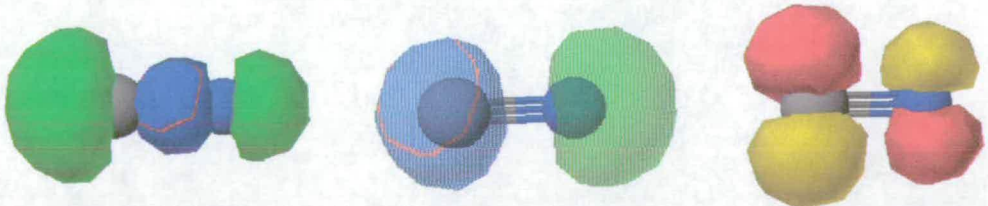

σ-symmetry orbital through which the carbon donates to the metal.

σ*-symmetry orbital through which the nitrogen donates to the metal.

π*-symmetry orbital into which the metal can donate electron density.

Figure 4.3 Pictorial representation of the molecular orbitals of cyanide which are important for bonding to two metal centres. The carbon centre is depicted in grey and the nitrogen in blue.

In an investigation into compounds of the type $[(L\text{-}L)L(OC)_2Mn(\mu\text{-}CN)Mn(CO)_2L'(L'\text{-}L')][PF_6]$ (where L-L and L'-L' are a diphosphine and L and L' a phosphite or a phosphine) which may have *trans,trans; cis,trans; trans,cis* or *cis,cis*

geometries of the carbonyl ligands, led to the conclusion that an N-bound manganese centre is more electron rich than a C-bound analogue.[39] Figure 4.4 shows two of the complexes investigated in this publication.

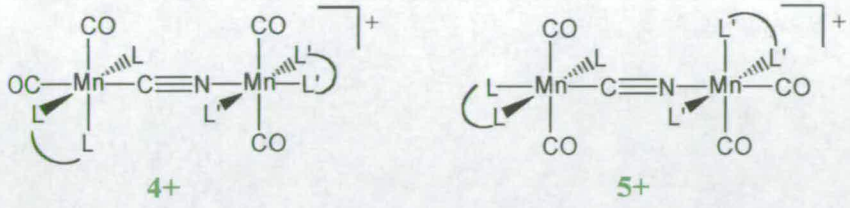

Figure 4.4 Structure of cyanide bridged manganese dicarbonyl complexes.

An IR spectroscopic study showed that the stretching vibrations of the CO moiety for the C-bound *cis* unit of **4+** occurred at 1971 and 1921 cm^{-1} while those of the N-bound *cis* unit of **5+** were 1968 and 1901 cm^{-1}. That is, the carbonyl bonds in the N-bound *cis* unit are weaker than those of the C-bound *cis* unit. This observation implies that there is an increased level of back-bonding into the π^*-orbital of the CO ligands (hence the bond is weaker; CO stretch at lower energy) bound to the manganese centre which is N-bound with respect to CN. This in turn implies that there must be more electron density on this N-bound metal centre compared to its C-bound analogue. This additional electron density can be attributed to a smaller degree of donation from this metal into the π^*-orbital of the CN, which is also attributable to a poorer overlap.

This argument was reinforced during a combined electrochemical and IR investigation. The *trans, trans* complexes show two reversible one-electron oxidation steps. The half-wave potentials of the two oxidation waves show little or no difference on changing the diphosphine ligands. However, the substitution of $P(OPh)_3$ by $P(OEt)_3$ or PEt_3 at the N-bonded manganese centre significantly lowers the half-wave potential of the first oxidation (E_1) (by 150-230 mV) while leaving that of the second (E_2) essentially unchanged (moves 10-30mV). Similarly, replacement of $P(OPh)_3$ by $P(OEt)_3$ or PEt_3 at the C-bonded manganese shifts E_2 (by 117-240) to a more negative value while E_1 remains fairly constant (moves 40-80 mV). The dependence of E_1 on the phosphine ligand bonded to the N-bound manganese centre

and E_2 on that bonded to the C-bound manganese centre implies that the first oxidation E_1, is mainly located on the N-bound manganese and E_2, on the C-bound manganese. Thus, the N-bonded manganese is more electron rich than the C-bonded manganese.

A similar result was found during an investigation into polynuclear, cyano-bridged ruthenium polypyridine complexes.[40] Three complexes were synthesised, $[NC\text{-}Ru^{II}(bipy)_2\text{-}CN\text{-}Ru^{II}(bipy)_2\text{-}CN]^+$, $[NC\text{-}Ru^{II}(bipy)_2\text{-}CN\text{-}Ru^{II}(phen)_2\text{-}CN]^+$ and $[NC\text{-}Ru^{II}(bipy)_2\text{-}CN\text{-}Ru^{II}(bipy)_2\text{-}NC\text{-}Ru^{II}(bipy)_2\text{-}CN]^{2+}$ and their redox, spectroscopic, and photophysical properties studied and compared with those of $Ru(bipy)_2(CN)_2$ and $Ru(phen)_2(CN)_2$. The bonding mode of the CN bridge was determined by the synthetic procedure used and it was assumed that no linkage isomerisation occurred (this was supported by the electrochemical results). By comparing the electrochemistry of the mono- and poly-nuclear complexes, the number of one-electron oxidative processes was found to correspond to the number of ruthenium atoms in the complex. A cathodic shift in the first oxidation potential in the series $Ru(bipy)_2(CN)_2$, $[NC\text{-}Ru^{II}(bipy)_2\text{-}CN\text{-}Ru(bipy)_2\text{-}CN]^+$ and $[NC\text{-}Ru^{II}(bipy)_2\text{-}CN\text{-}Ru^{II}(bipy)_2\text{-}NC\text{-}Ru^{II}(bipy)_2\text{-}CN]^{2+}$ (easiest to oxidise) was observed. Thus, the ruthenium centre is more easily oxidised with a CN-Ru-NC arrangement, than a CN-Ru-CN arrangement, and finally most difficult with a NC-Ru-CN arrangement of the cyanide ligands. Hence, the electron density on an N-bonded ruthenium is greater than that of a C-bonded ruthenium (*i.e.* the π-overlap is poorer).

Structural evidence of the increased π-acceptor capability of the carbon terminus of CN was provided by Zhu and Vahrenkamp in a recent publication.[41] The linkage isomers $(CO)_5Cr\text{-}CN\text{-}Fe(dppe)Cp$ (**2a**) and $(CO)_5Cr\text{-}NC\text{-}Fe(dppe)Cp$ (**2b**) (see Figure 4.5) were prepared and an X-ray crystal structure analysis performed.

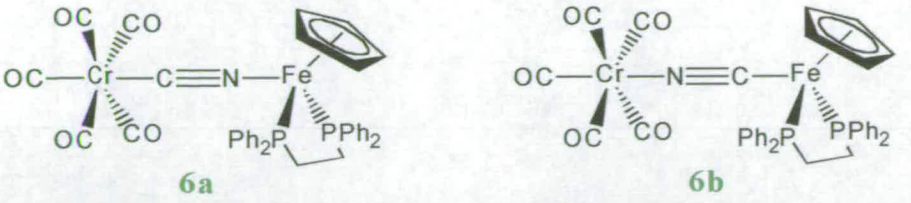

Figure 4.5 Representation of the linkage isomers $(CO)_5Cr$-CN-Fe(dppe)Cp and $(CO)_5Cr$-NC-Fe(dppe)Cp.

These two complexes were found to be isomorphous and so their structures could be represented by a single drawing. The Fe-C bond (1.897(4) Å) in **6b** is shorter than the Fe-N bond (1.934(4) Å) in **6a**, and likewise the Cr-C bond (2.064(5) Å) in **6a** is shorter than the Cr-N bond (2.086(3) Å) in **6b**. Although the changes in bond length are quite small, the fact that the M-C bond is shorter than the M-N bond indicates that the carbon has a larger π-interaction. Further support for this is provided by the angles around the metal-cyanide bond. In both cases, the M-N-C angle deviates more from 180° than the M-C-N angle. This is also attributed to a larger amount of back-bonding with the carbon atom over the nitrogen. This proves that the carbon of cyanide is the better π-acceptor, and hence, a metal bonded here will be electron deficient (more difficult to oxidise) compared to the same metal bonded to the nitrogen terminus.

It has been observed generally that bridging cyanides have higher energy stretching vibrations (ν_{CN}) with respect to those of terminal cyanides.[42, 43, 44] Dows *et al.*[43] explained that the frequency increase observed was associated largely with kinematic coupling *i.e.* the motion of the bridging CN being constrained by the second metal centre. More recently, in a bid to gain some general insight into the factors that affect the stretching frequency of bridging cyanides, Bignozzi *et al.*[45] having investigated a series of binuclear and trinuclear species of the type $[M\text{-}NC\text{-}M'(bipy)_2\text{-}CN\text{-}M]^{6+/4+}$ and $[NC\text{-}M'(bipy)_2\text{-}CN\text{-}M]^{3+/2+}$ (where M = $[Ru(NH_3)_5]^{2+/3+}$ and M'= Ru^{II}, Os^{II}, Re^{I}) came to the following conclusions. The effect of bridge formation on the cyanide stretching frequency was found to be complex. The combined effects of three factors

three factors were found to contribute: (i) kinematic coupling; (ii) back-bonding from the C-bonded metal; (iii) back-bonding from the N-bonded metal.

(i) Kinematic coupling is defined as the simple mechanical constraint on the CN motion imposed by the second metal centre and is expected to always be present. This will shift ν_{CN} to higher energy.

(ii) Before bridge formation, a certain amount of back-bonding from the metal bound to the carbon of the cyanide may be present. (The amount of this back-bonding will be dependent on the nature of the metal and the other ligands present as potential competitors.) On coordination of the second metal centre, charge will be withdrawn from the CN, as a result, the amount of back-bonding is expected to be enhanced (in order to compensate for the loss of electron density). This will have the effect of weakening the CN bond, and so ν_{CN} will move to lower energy with the formation of a bridge.

(iii) Back-bonding to a bridging CN from the N-bound metal is generally not considered (in light of what is already known). However, this effect may become relevant if the C-bound metal centre does not act as a strong π-donor and the N-bound metal is in a low oxidation state with strong donating ligands. In this case, back-bonding into the nitrogen end will weaken the CN bond and ν_{CN} will move to lower energy upon bridge formation.

These effects are thought to operate simultaneously with the magnitude and direction of the shift in ν_{CN} depending on their relative importance.

It is assumed that cyanide can mediate an IVCT transition through delocalisation into the two perpendicular π*-orbitals. In general terms, there is a strong correlation between the number of atoms in a bridging ligand and the degree of interaction, with the interaction decreasing exponentially as the bridging ligand increases in size. Also, strong interaction occurs only with smaller ligands that feature strong π-donor or π-acceptor tendencies.[8] Cyanide of course is a small molecule. However, its π-

accepting capabilities are small, which raises the question of whether it can allow a significant metal-metal interaction.

Cyanide has been known to promote weak interactions in mixed-valence complexes. In a recent publication investigating complexes containing the moiety Cp(dppe)Fe, cyanide was found to act as an effective bridge between the two metallic fragments.[46] The publication was a study of two binuclear compounds, namely $[\{Cp(dppe)Fe\}_2\text{-}\mu\text{-}CN]^{+/2+}$ (**7**) and $[Cp(dppe)Fe\text{-}CN\text{-}Mn(CO)_2(dppm)P(OPh)_3]^{+/2+}$ (**8**), which are shown in Figure 4.6.

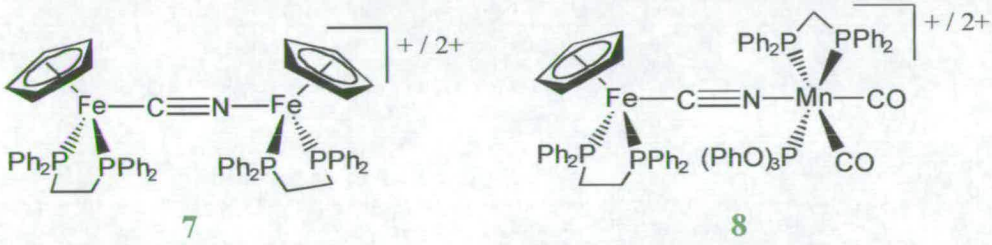

Figure 4.6 Representation of $[\{Cp(dppe)Fe\}_2\text{-}\mu\text{-}CN]^{+/2+}$ (**7**) and $[Cp(dppe)Fe\text{-}CN\text{-}Mn(CO)_2(dppm)P(OPh)_3]^{+/2+}$ (**8**).

An electrochemical study of **7** showed two reversible, one-electron oxidations with a considerable difference between the two half-wave potentials (660 mV).[47] This difference corresponds to a K_c (comproportionation constant) value of 1.4×10^{11} which indicates a stronger interaction between the metallic centres than that experienced in similar ruthenium complexes bridged with several other types of ligands.[48] The K_c value for **8** was calculated to be 3×10^{10}.[47]

However, care must be taken when comparing K_c values for asymmetrical complexes since there will be an inherent difference in the redox potentials in the absence of any metal-metal interaction. In this example, two complexes were used to model each side of the binuclear complex, namely, $[Cp(dppe)Fe\text{-}NCCH_3]^+$ and $[Cp(dppe)FeCNCH_3]^+$, whose half-wave potentials were 0.84 and 1.15 V. The difference is explained by the π-accepting capability of either side of the cyanide ligand as discussed above. Therefore, the calculated numerical value of K_c cannot be used as a reliable measure of metal-metal interactions in asymmetric binuclear

complexes. IVCT band analysis is the only way this metal-metal interaction can be quantified. Hush theory was applied to the IVCT bands observed in these complexes and indicated considerable interaction between the two metal centres, which behave as Class II mixed-valence complexes.[46]

Structural evidence of this interaction between two cyano-bridged metal centres was recently published.[41] This example has been discussed previously, but can now be taken further. The isomers, $(CO)_5$Cr-CN-Fe(dppe)Cp (**6a**) and $(CO)_5$Cr-NC-Fe(dppe)Cp (**6b**) were synthesised and their X-ray crystal structure determined (Figure 4.5). Also reported is the crystal structure of $[(CO)_5$Cr-CN-Fe(dppe)Cp$]^+$ (**6a-ox**), which has been compared to **6a**. As with the comparison of **6a** and **6b**, the differences in bond lengths between **6a** and **6a-ox** are only slight. The Fe-N bond in **6a-ox** is 0.04 Å shorter and the Fe-P and Fe-C(Cp) bonds are, on average, 0.06 Å and 0.03 Å longer than found in **6a**. This corresponds to the location of the positive charge on the iron centre. The Fe-P and Fe-C(Cp) bonds becoming longer due to reduced back-bonding from the iron (since it has less electron density upon oxidation) and the fact that the Fe-N bond becomes shorter illustrates that the cyanide N has no noticeable π-acceptor properties (if it had, upon oxidation, this bond should get longer). On the other side of the binuclear complex, the Cr-C(CN) bond is 0.06 Å shorter and the Cr-C(CO-*trans*) bond is 0.03 Å longer in **6a-ox** than in **6a**. Oxidation at the iron centre has caused a reduced amount of back-bonding from the Cr to the *trans*-CO function *i.e.* the Cr centre has also become more electron deficient. This is due to an increase in the π-acceptor properties of the carbon of cyanide (supported by the shortening of the Cr-C(CN) bond). That is, the loss of electron density on the iron centre is communicated through the cyanide bridge to the chromium centre.

4.1.2 Heteronuclear cyano-bridged complexes

Of the heteronuclear mixed-valence complexes bridged by the cyanide ligand studied, organometallic complexes seem to be the most prevalent. This is in part due to the inertness and ease of preparation of these complexes.

One of the first heteronuclear cyanide-bridged organometallic compounds investigated involved the combination of a $Mn(CO)_2(L\text{-}L)L$ (L-L = dppm, dppe; L=$P(OPh)_3$, PEt_3) and a Fe(Cp)(dppe) fragment.[47] This gave rise to a number of isomers; the carbonyl groups can be *cis* or *trans* and the cyanide can be either C or N bound to the manganese, and also the L-L and L can be altered to produce a series of compounds.

The oxidation of these compounds was studied electrochemically by cyclic voltammetry and chemically by infrared spectroscopy. Generally, two one-electron oxidations were observed, the first affecting the Fe or Mn fragment depending on its position relative to the cyanide bridge and the stereochemistry of the dicarbonyl function. It was noted that when the *cis*-$Mn(CO)_2(L\text{-}L)L$ fragment is oxidised a very rapid isomerisation to the *trans* form is observed.

The ability of the cyanide ligand to mediate charge transfer between the two metal centres was highlighted when the *cis*-dicarbonyl complexes, [Cp(dppe)Fe-CN-$Mn(CO)_2(L\text{-}L)L]^+$ were investigated. The first oxidation (+0.46 to +0.74 V) was found to occur at the iron centre regardless of the coordination mode of the cyanide ligand (this was deemed reasonable due to the high oxidation potential of the *cis*-$Mn(CO)_2$ fragments (+1.2 V) when N-bonded and even higher when C-bonded). When the Fe centre was chemically oxidised to produce the dication an isomerisation reaction took place at the manganese centre. The isomerisation was explained by an intramolecular electron-transfer from the Mn to the Fe through the CN bridge (so effectively the Mn has now been oxidised). The general scheme below was given.

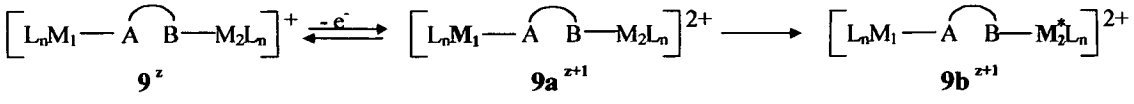

Scheme 4.1 General scheme for isomerisation with electron-transfer. The green type represents the metal centre being oxidised.

If the oxidation potential of the fragment M_1-A is lower than that of M_2-B, then the complex will be oxidised at M_1 first to give $\mathbf{9a}^{z+1}$. However, if the fragment M_2 has another isomeric form, M_2^*, and the oxidation potential of B-M_2^* is lower than that of M_1-A, the isomerisation of $\mathbf{9a}^{z+1}$ to $\mathbf{9b}^{z+1}$ could take place, providing that the bridge A-B allows electron-transfer and that kinetic factors are favourable. The isomerisation process will be faster, the smaller the difference in electron richness (as measured by the redox potentials) of the M_1-A and M_2-B fragments.

There are many more examples of these cyano-bridged heteronuclear complexes containing organometallic fragments reported.[49]

Denning and Laidlaw investigated the combination of both an organometallic fragment and a classical ligand in 1994.[50] The novel complexes studied were $[(\eta^5\text{-}C_5H_5)(PPh_3)M'(\mu\text{-}CN)M(NH_3)_5]^{3+}$ (M = Ru, M' = Ru or Os; M = Os, M' = Ru or Os) and $[(\eta^5\text{-}C_5R_5)(PPh_3)_2Ru(\mu\text{-}CN)Ru(NH_3)_5]^{3+}$ ($C_5R_5 = C_5H_4Me$ or C_5Me_5) using electronic and infrared spectroscopy and cyclic voltammetry for their characterisation.

Generally, the cyclic voltammetry showed an irreversible oxidation at approximately +1.2 V and a near-reversible reduction at around 0.0 V or –0.7 V depending on the metal centre. The electrochemistry of the cyclopentadienylmetal precursor (mononuclear complex) showed an irreversible oxidation between +0.7 and +1.0V.[51] Hence, the irreversible oxidation in the binuclear complex was assigned as oxidation of the $M'(\eta^5\text{-}C_5H_5)(PPh_3)$ organometallic fragment. Thus, the reduction couples are assigned to the pentaammineruthenium centre (at 0.0 V) or the pentaammineosmium centre (at –0.7 V).

The complexes exhibit moderately intense ($\varepsilon_{max} \approx 2000\text{-}4000\ M^{-1}\ cm^{-1}$), broad IVCT transitions in the visible region. This corresponds to Robin-Day Class II behaviour. The IVCT transitions were found to be strongly solvatochromic. However, they did not display direct proportionality to the solvent dielectric function ($1/D_{op} - 1/D_s$) as

predicted by Hush. Previous studies observed pronounced solvatochromic shifts in the electronic spectra of $[Ru(NH_3)_5(C_5H_4N)]^{2+/3+}$ complexes. The origin of this shift comes from the stabilisation of the ammineruthenium(III) centre relative to the ruthenium(II) state through outer-sphere solvent-ammine hydrogen bonding.[52, 53] The IVCT transition energies were instead correlated with the Gutmann[54] donor number (discussed in greater detail in chapter 5.1).

The infrared spectroscopy revealed that, upon binuclear complex formation a large shift in ν_{CN} to lower energy was observed. In light of the Bigozinni *et al.*[45] publication discussed above, this low energy shift was attributed to the strong π-accepting nature of the pentaamminemetal(III) moiety. Upon reduction ν_{CN} moves to higher energy, implying that ν_{CN} is now dominated by the kinematic effect, as expected since pentaammineruthenium(II) is not a π-acceptor.

It is this combination of an organometallic fragment, namely $(Mn(CO)_2(L\text{-}L)L)$ and a classical fragment, $Ru(NH_3)_5$ bridged by the cyanide ligand which will be discussed here. Electrochemical and spectroelectrochemical techniques will be used in their characterisation. As mentioned previously (chapter 2.3), in order to study a compound using IR spectroelectrochemistry, care has to be taken over the choice of solvent and electrolyte. To allow the study of the carbonyl region of the IR spectral range, two solvents were used, tetrahydrofuran (THF) and dichloromethane (DCM) neither of these solvents has significant absorptions in the carbonyl region. The electrolyte used was tetrabutylammonium tetrafluoroborate which also has no significant absorptions in this region.

4.2 Experimental

4.2.1 Synthesis of the binuclear complexes

The complexes used in this chapter were synthesised and supplied by Mr. A. J. Wood of The University of Bristol where he worked under the supervision of Prof. N. G. Connelly.

4.2.2 *In-situ* IR spectroelectrochemistry of 1

Compound 1 (5.8 mg; 4.29×10^{-6} mol) was made up to 2 cm^3 (2.14×10^{-3} M) in a standard flask using a solution of 0.1 M $[N^nBu_4][BF_4]$ in acetonitrile which had been degassed with argon. This solution was degassed with argon and the cell filled, constructed and placed in the cavity of the IR spectrometer. An initial spectrum was recorded then the potential was set to +0.45 V. IR spectra were recorded every two minutes. When the current decreased to almost zero, the potential was changed to –0.10 V to regenerate the starting material. The spectrum did not return to that of the original compound. Thus decomposition must have taken place.

4.2.3 *Ex-situ* spectroelectrochemistry of 1, 2, and 3

An H-cell was set up using a 0.4 M solution of $[N^nBu_4][BF_4]$ in THF or DCM. To this compound **N** (N = 1, 2, or 3; see Table 4.1) was added. The whole cell was immersed in a dry ice/acetone bath and cooled to 233 K. The solution was then electrogenerated at a potential sufficient to induce oxidation or reduction and samples were taken using a gas tight syringe every ten minutes originally then every thirty minutes as the coulometry slowed. The IR spectrum of each sample was recorded as quickly as possible using solution cells.

Table 4.1 Experimental details of the *ex situ* spectroelectrochemical experiments performed.

Compound	Weight / mg	Solvent
1 : $[(NH_3)_5Ru(\mu\text{-}NC)Mn(CO)(\eta^2\text{-}PPh_2CH_2PPh_2)_2][PF_6]_2$	33.4	THF
2 : *cis*-$(NH_3)_5Ru(\mu\text{-}NC)Mn(CO)_2(\eta^2\text{-}PPh_2CH_2PPh_2)(P\{OEt\}_3)][PF_6]_3$	30.3	DCM
	32.3	THF
3 : *trans*-$(NH_3)_5Ru(\mu\text{-}NC)Mn(CO)_2(\eta^2\text{-}PPh_2CH_2PPh_2)(P\{OEt\}_3)][PF_6]_3$	35.4	DCM
	31.5	THF

4.2.4 UV/Vis spectroelectrochemistry

The compound being analysed (Table 4.2) was made up to 2 cm^3 in a volumetric flask using a solution of $[N^nBu_4][BF_4]$ in the required solvent which had been degassed with argon. This solution was also degassed. The cell was then filled and assembled and placed in the cavity of the UV/Vis spectrophotometer. The temperature was reduced to the required level and the potential set to a value that induced reduction or oxidation. During this process spectra were recorded every 5 minutes.

Table 4.2 Experimental details of the UV/Vis spectroelectrochemical experiments performed.

Compound	Amount / mg	Concentration / M	Concentration of $[N^nBu_4][BF_4]$ / solvent	Temperature / K
1	5.5	2.03×10^{-3}	0.1 M / DMF	228
	6.0	2.22×10^{-3}	0.1 M / acetonitrile	238
2	6.6	2.52×10^{-3}	0.1 M / DMF	228
	6.2	2.37×10^{-3}	0.1 M / DMF	228
	7.0	2.67×10^{-3}	0.5 M / DCM	238
3	3.1	1.19×10^{-3}	0.5 M / DCM	233

During an electrochemical investigation of **3**, it was found that some of the compound had converted to the cis isomer in the solid phase. In order to get the spectroelectrochemistry of the pure *trans* isomer, the experiment was set up as outlined above using **2** (7.0mg; 2.67×10^{-3} M) in 0.5 M DCM. The temperature was reduced to 238 K and the potential set at +1.5 V to produce the oxidised species. Following complete oxidation the temperature was allowed to increase to 253 K to

allow the conversion of $[2]^{4+}$ to the *trans* isomer, $[3]^{4+}$. Once this isomerisation reaction was complete the temperature was reduced to 238 K and the experiment continued as normal.

4.3 Results and Discussion

4.3.1 $[(NH_3)_5Ru(\mu\text{-}NC)Mn(CO)(\eta^2\text{-}PPh_2CH_2PPh_2)_2]^{2+}$: $[1]^{2+}$

Figure 4.7 Structure of $[(NH_3)_5Ru(\mu\text{-}NC)Mn(CO)(\eta^2\text{-}PPh_2CH_2PPh_2)_2]^{2+}$ $[1]^{2+}$

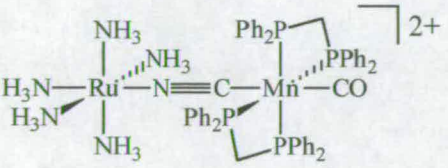

The cyclic voltammogram of compound 1 (Figure 4.7) is given in Figure 4.8. It shows two one-electron oxidations (confirmed using bulk electrolysis). The first oxidation, $E_{½}$ = +0.173 V (ΔE = 84 mV) displays a linear relationship between i_p and $\nu^{½}$ indicating this process is electrochemically reversible. The ratio of peak currents (i_{pa}/i_{pc}) was found to be 0.93 indicating that this oxidation is probably fully chemically reversible, however due to the difficulty in measuring the i_p values of two closely spaced couples it appears less so. (These values were recorded at a scan rate (ν) of 100 mV s^{-1}.) This process is thought to be based primarily on the ruthenium centre.

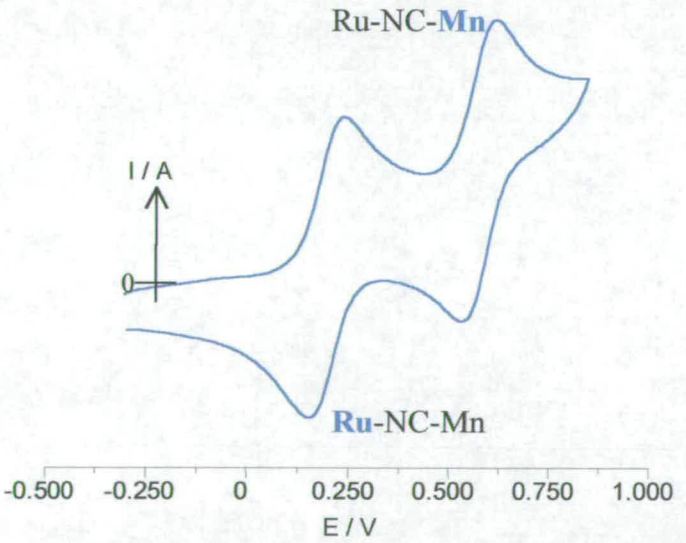

Figure 4.8 Cyclic voltammogram of $[1]^{2+}$ in 0.4 M $[N^nBu_4][BF_4]$ / THF at 298 K.

The second oxidation, $E_{½}$ = +0.552 V (ΔE = 85 mV) also displays a linear relationship between i_p and $\nu^{½}$ and thus is electrochemically reversible. For this oxidation, the ratio of peak currents was found to be 0.83, an indication of some

chemical instability of the oxidised species. This process is thought to be located primarily on the manganese centre, as labelled. (It should be noted that under the conditions that this cyclic voltammogram was recorded the ferrocinium/ferrocene couple was found to be at +0.55 V (ΔE = 93mV).)

The electrochemistry of the mononuclear complex *trans*-[Mn(CN)(CO)(dppm)$_2$] has been investigated previously.[55] A fully reversible one-electron oxidation was observed at +0.15 V in DCM. This is considerably less positive than the oxidation of the manganese centre in the binuclear complex at +0.552 V (in THF). (Both of these values have been adjusted to give the ferrocene couple at +0.55 V.) This implies that the manganese centre in the binuclear complex has less electron density than in the mononuclear analogue. This illustrates the ability of the $[Ru(NH_3)_5]^{3+}$ to pull electron density through the CN bridge from the manganese centre *i.e.* the $[Ru(NH_3)_5]^{3+}$ fragment is acting as a π-acceptor.[56, 57] Ru(III) (d^5 electronic configuration) has a vacancy in its t_{2g} orbital which can account for this behaviour.

This reduction in electron density at the manganese centre is also reflected in the IR spectroscopy of this compound (see later). The CO stretching vibration, ν_{CO}, for the Ru^{III}/Mn^{I} binuclear complex is observed at 1885 cm^{-1} (in THF), while in the mononuclear compound (Mn(I)) it is measured at 1865 cm^{-1} (in DCM). Thus the CO bond is stronger in the binuclear complex, indicating that the amount of back-bonding from the manganese to the CO anti-bonding orbital is smaller. This implies that the manganese in the binuclear complex has less electron density available for back-donation than found in the mononuclear case.

The mononuclear ruthenium complex $[Ru(NH_3)_5NCMe]^{3+}$ has also been studied. This compound is chosen for comparison over $[Ru(NH_3)_5NC]^{n+}$ since complexes with N-bound cyanides coordinated as a terminal ligand are extremely unstable. Cyclic voltammetry of $[Ru(NH_3)_5NCMe]^{3+}$ in acetonitrile revealed a one-electron reduction with a half-wave potential of +0.558 V.[58] This is somewhat more positive than the ruthenium couple in the binuclear complex (+0.173 V). That is, on

formation of the binuclear complex, the ruthenium centre becomes easier to oxidise (by 385 mV), which would imply that the manganese centre must be acting as a π-donor. It should be pointed out that this comparison has not taken account of the negative charge on the cyanide which will stabilise the higher oxidation state. Thus the half-wave potential of the CH_3CN monomer may be higher than that expected for the N bound cyanide monomer.

In the binuclear complex, **1**, the 2+ state formally gives a Ru(II) (d^6) and a Mn(I) (d^6) metal centre. When the compound is oxidised by one electron, the mixed-valence state, Ru(III)/Mn(I) (d^5/d^6) is formed. Further oxidation by one electron will generate the Ru(III)/Mn(II) (d^5/d^5) state. The purpose of the following experiments is to investigate all possible species, and to study the effect these redox processes have on the carbonyl function. Also, to determine the amount of communication between the ruthenium and manganese metal centres.

4.3.1.1 IR Spectroelectrochemistry of **1**

The first step is to oxidise the compound by one electron while studying the accompanying IR spectral changes, then oxidise by a second electron to investigate the fully oxidised species. The next step is the reduction by one electron back to the mixed-valence species, and then finally the reduction by a second electron to regenerate the starting material and prove the couples are fully reversible at the experimental temperature.

Since this compound has only one CO group, only one carbonyl band is expected in this region of the IR spectrum (Figure 4.9). The CO band is observed at 1865 cm^{-1}.

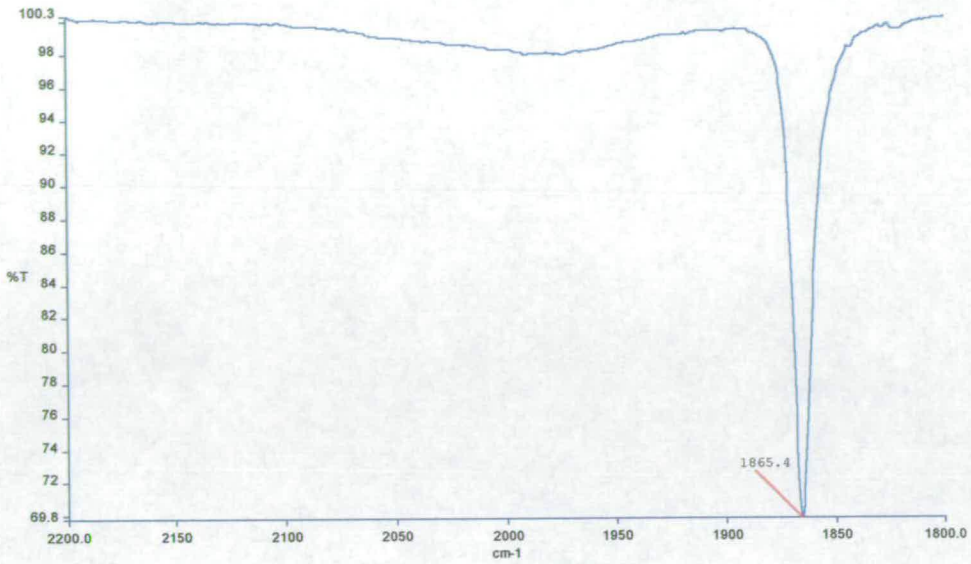

Figure 4.9 IR spectrum of $[\mathbf{1}]^{2+}$ in 0.1 M $[N^nBu_4][BF_4]$ / acetonitrile at 298 K.

The spectroelectrochemical oxidation experiment was first attempted at room temperature. The potential was set to +0.3V (between the two peak anodic potentials) to induce the oxidation of the compound by a single electron. The spectra obtained are shown in Figure 4.10 below. On examining the first few spectra from this experiment (blue-red-green-magenta-cyan-dark red) two new bands grow in at approx. 1880 cm^{-1} and 2000 cm^{-1}.

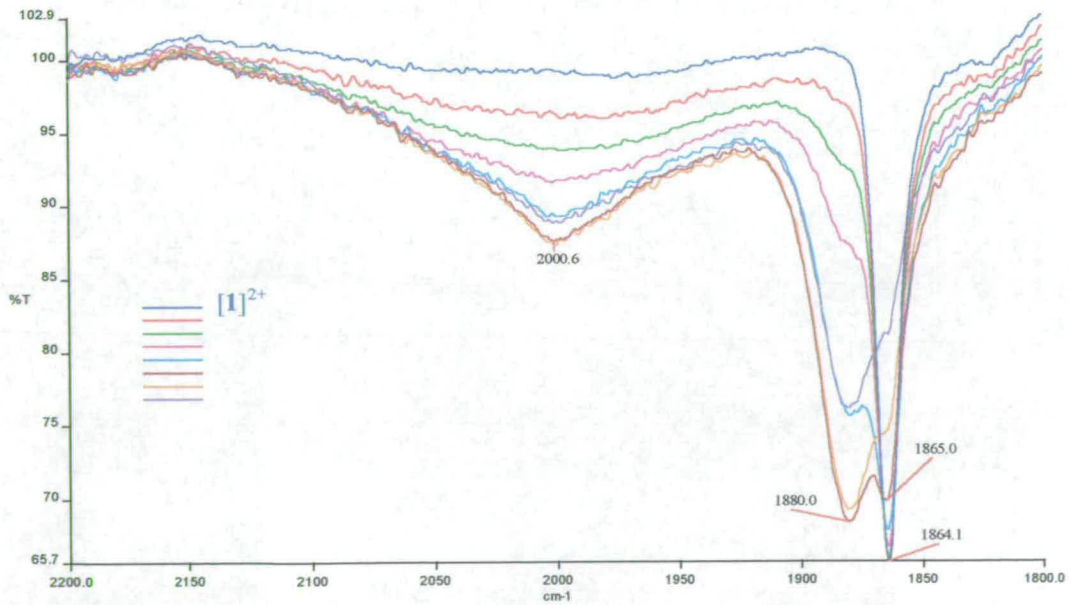

Figure 4.10 *In Situ* oxidation of $[\mathbf{1}]^{2+}$ in 0.1 M $[N^nBu_4][BF_4]$ / acetonitrile at 298 K. E_{app} = +0.30 V.

The spectra produced after the dark red line merely show the decomposition of the initial material and the oxidised species, until the carbonyl region is completely featureless. Only two of these decomposition spectra (orange and purple) have been shown for clarity purposes. The main conclusion from this experiment is that the compound (and its redox product) is not stable at room temperature and as a result, all future experiments had be performed at reduced temperatures. It is assumed from these results that upon one-electron oxidation, the carbonyl band of the new species, $[\mathbf{1}]^{3+}$, will be at approximately 1880 cm^{-1}.

Through a number of bulk electrolysis trials, it was found that the temperature needed to suppress the decomposition of the oxidised species was 233 K. All of the IR experiments reported hereafter were performed at 233 K.

The spectra recorded during electrogeneration to produce the one-electron oxidised species are shown in Figure 4.11. From these, it can be seen that on going from $[\mathbf{1}]^{2+}$ to $[\mathbf{1}]^{3+}$ the carbonyl band moves to 1885 cm^{-1}, a shift to higher energy of 20 cm^{-1}. The band at 2000 cm^{-1} is as yet unassigned, but is definitely real (not a decomposition product) since it collapses on re-reduction to $[\mathbf{1}]^{2+}$.

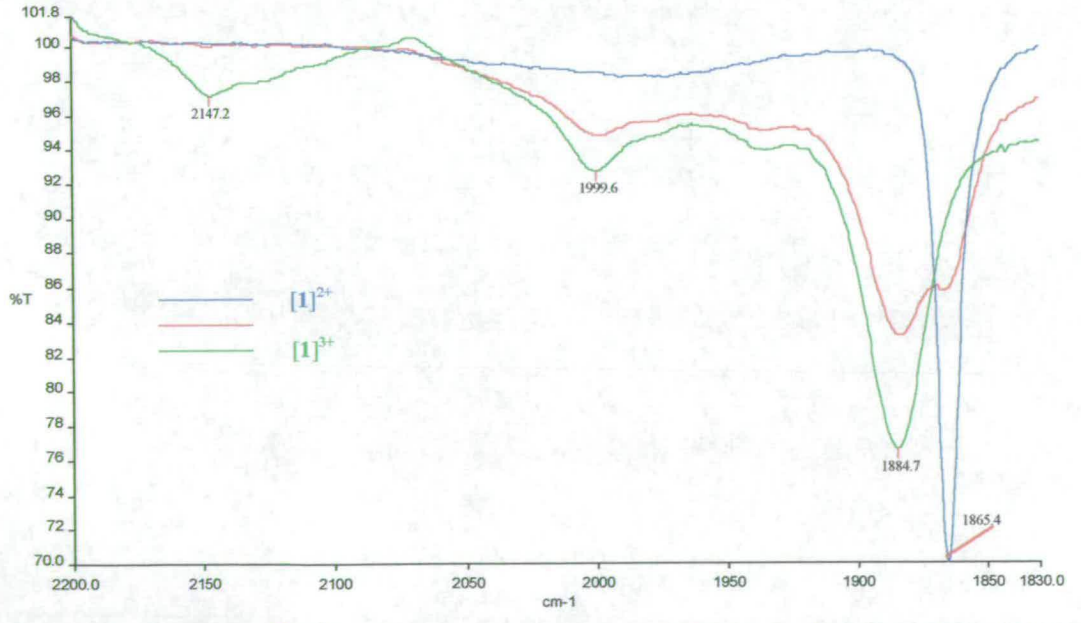

Figure 4.11 IR spectra of $[\mathbf{1}]^{2+}$ during electrogeneration at +0.30 V in 0.1 M $[N^nBu_4][BF]_4$ / THF at 233 K.

Figure 4.12 shows the spectra obtained on electrogeneration at +0.8 V to produce the fully oxidised species, $[\mathbf{1}]^{4+}$. The effect of this oxidation on the position of the carbonyl band is greater than for the first oxidation. The band again moves to higher energy, this time by 73 cm^{-1} to 1958 cm^{-1}. This is very similar to the change observed during the oxidation of the mononuclear complex *trans*-$[Mn(CN)(CO)(dppm)_2]$. The Mn(I) species shows a single CO band at 1865 cm^{-1}, on oxidation to the Mn(II) species this band moves to 1941 cm^{-1}, a change of 76 cm^{-1}.[55]

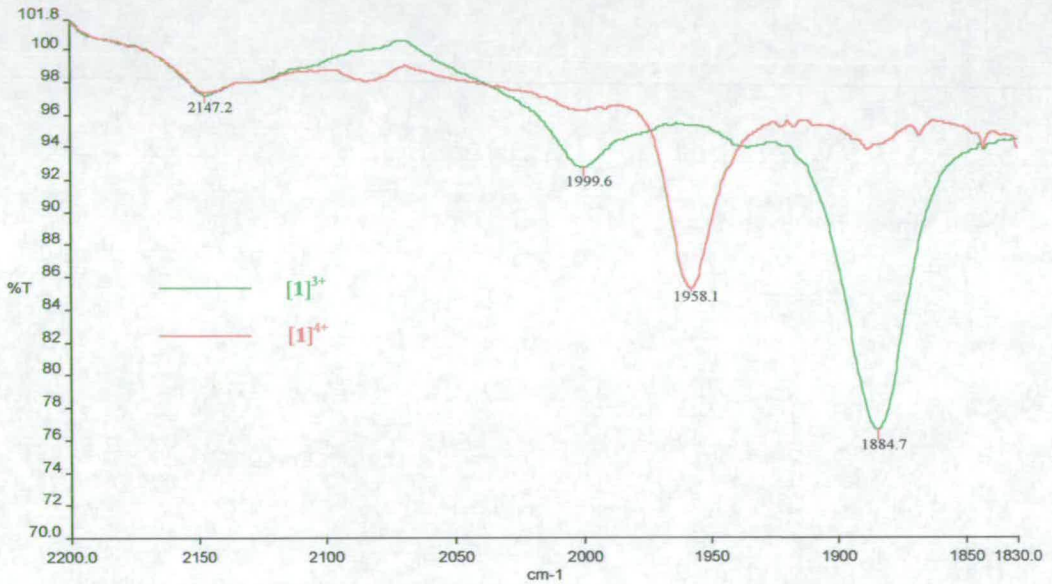

Figure 4.12 IR spectra of $[\mathbf{1}]^{3+}$ during electrogeneration at +0.80 V in 0.1 M $[N^nBu_4][BF]_4$ / THF at 233 K.

The band always moves to a higher energy upon oxidation of the compound. This is due to the bonding nature of the M-CO fragment. By removing an electron from the system, the electron density on the metal centre is decreased. This in turn will decrease the amount of back-bonding from the metal to the anti-bonding orbital of the CO unit. This will have the effect of strengthening the CO bond, and hence the CO stretch should become more difficult and so move to a higher energy. The CO band moves during both oxidations. However, it is expected only to move when the manganese is oxidised (since the manganese is directly bonded to the CO). This implies that there must be some delocalisation of the electron density through the bridge, and thus oxidation of the ruthenium centre has an effect on the distant CO fragment. This is an early indication of some ruthenium-manganese communication.

These results provide evidence that the electrochemical assignment made at the beginning of this section is correct. The first oxidation produces a 20 cm^{-1} change in ν_{CO} while the second produces a 73 cm^{-1} change. Since the manganese centre is directly bonded to the carbonyl unit, oxidation here should have the largest effect on ν_{CO} and indeed in the mononuclear Mn complex ν_{CO} moves 76 cm^{-1} upon oxidation. Thus, the second oxidation is based primarily on the manganese centre, and hence the first is based mainly on the ruthenium.

To investigate the amount of communication between the metal centres further, a UV/Vis spectroelectrochemical experiment must be performed.

4.3.1.2 Uv/Vis Spectroelectrochemistry of **1**

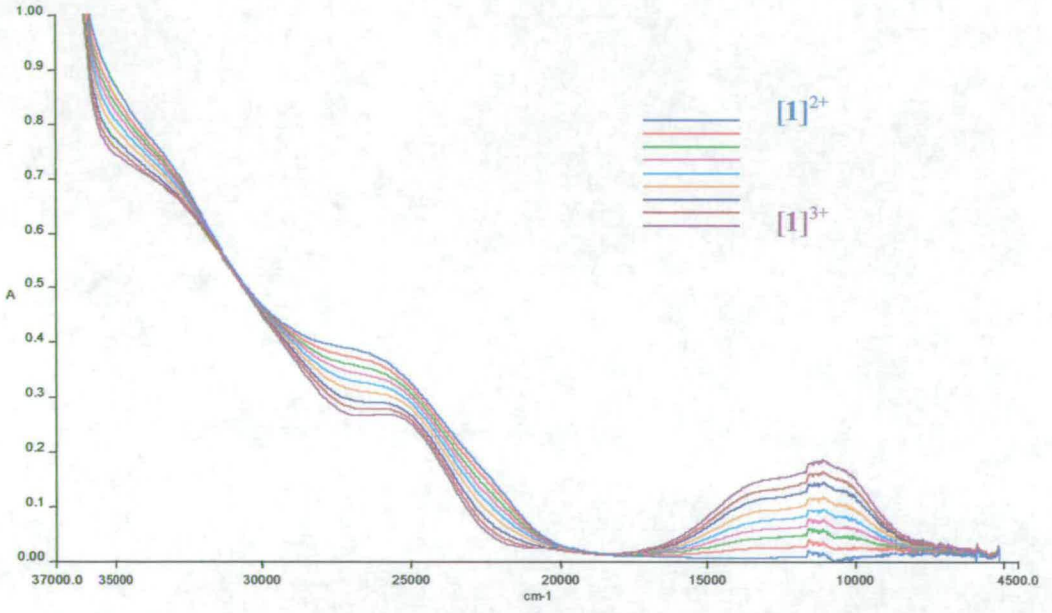

Figure 4.13 UV/Vis spectroelectrochemistry of $[\mathbf{1}]^{2+}$ in 0.1 M $[N^nBu_4][BF_4]$ / DMF at 228 K. E_{app} = +0.40 V.

The spectra recorded during the first one-electron oxidation of **1** are shown Figure 4.13. The spectrum of the fully reduced species (2+) is featureless in the low energy region (>20000 cm^{-1}). In the higher energy region only poorly defined bands are observed at approximately 26000 and 34000 cm^{-1}. As the compound is oxidised by one electron, two new bands grow in at low energy. These bands are overlapping but

are roughly centred at 10800 and 12950 cm^{-1}. An isosbestic point is observed at 18450 cm^{-1} illustrating that the conversion to the trication is clean. The measurement of the band positions is made more difficult by the strange feature in the low energy region. This is caused by the solvent/electrolyte system chosen. In order for more accurate band positions to be attained, the spectrum of the fully reduced species (which is featureless in the low energy region) was subtracted from each spectrum. The difference spectra produced are shown in Figure 4.14. From this it is clear that the low energy feature is made up of two overlapping bands, with the most prominent band centred at 10850 cm^{-1} (ε = 1600 M^{-1} cm^{-1}).

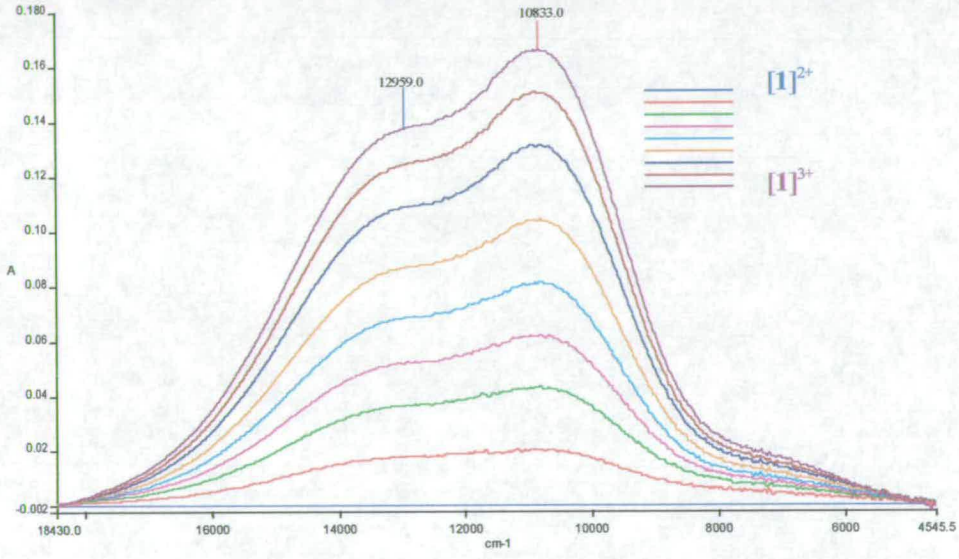

Figure 4.14 Difference spectra calculated by subtracting the spectrum of $[1]^{2+}$ from those recorded during the one electron oxidation of $[1]^{2+}$.

The spectra recorded during the second one electron step are shown in Figure 4.15. Upon oxidation to the fully oxidised species (4+) the two bands observed for the 3+ species collapse and two corresponding bands grow in at higher energy, at approximately 18250 and 19400 cm^{-1}. Two isosbestic points are observed at 15500 and 24050 cm^{-1} indicating that clean conversion to the fully oxidised species takes place.

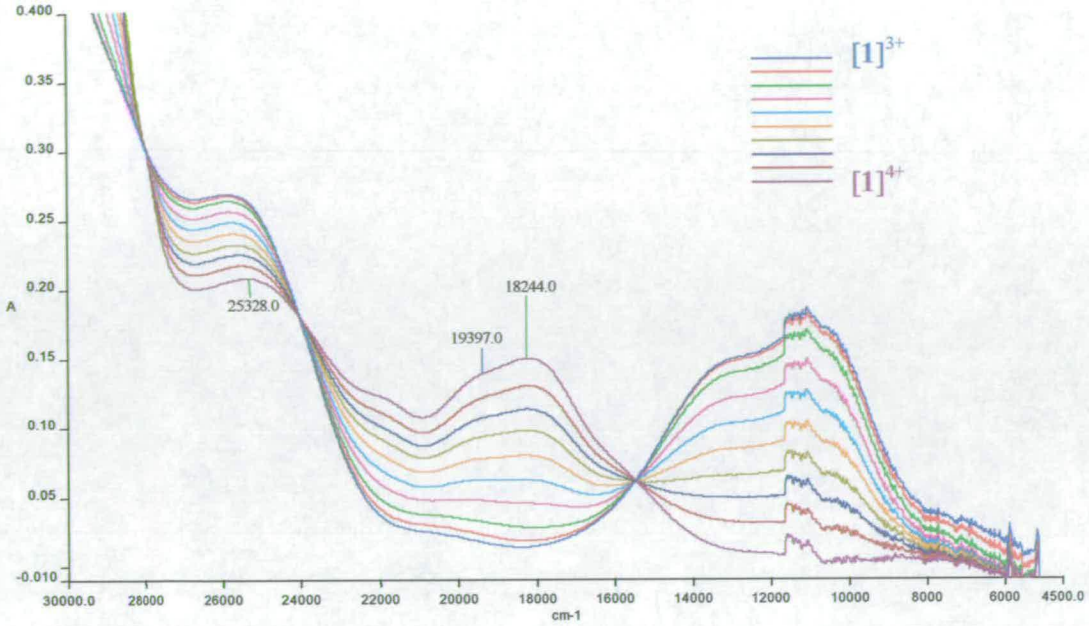

Figure 4.15 UV/Vis spectroelectrochemistry of $[1]^{3+}$ in 0.1 M $[N^nBu_4][BF_4]$ / DMF at 228 K. E_{app} = +1.30 V.

4.3.2 $[cis\text{-}(NH_3)_5Ru(\mu\text{-}NC)Mn(CO)_2(\eta^2\text{-}PPh_2CH_2PPh_2)(P\{OEt\}_3)]^{3+}$: $[2]^{3+}$

Figure 4.16 Structure of $[cis\text{-}(NH_3)_5Ru(\mu\text{-}NC)Mn(CO)_2(\eta^2\text{-}PPh_2CH_2PPh_2)(P\{OEt\}_3)]^{3+}$ $[2]^{3+}$

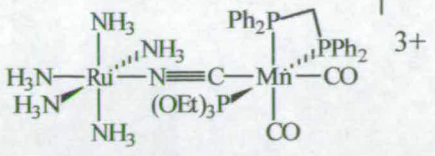

The cyclic voltammogram of compound 2 (Figure 4.16) at room temperature is given in Figure 4.17. This shows a one-electron reduction and an irreversible one-electron oxidation (the number of electrons involved was confirmed using bulk electrolysis). The reduction, $E_{½} = +0.284$ V ($\Delta E = 84$ mV), displays a linear relationship between i_p and $\nu^{½}$ indicating that this process is electrochemically reversible. The ratio of peak currents was found to be 0.94, an indication of some chemical instability of the reduced species. (These values were recorded at a scan rate (ν) of 100 mVs^{-1}.) This process is thought to be based primarily on the ruthenium centre.

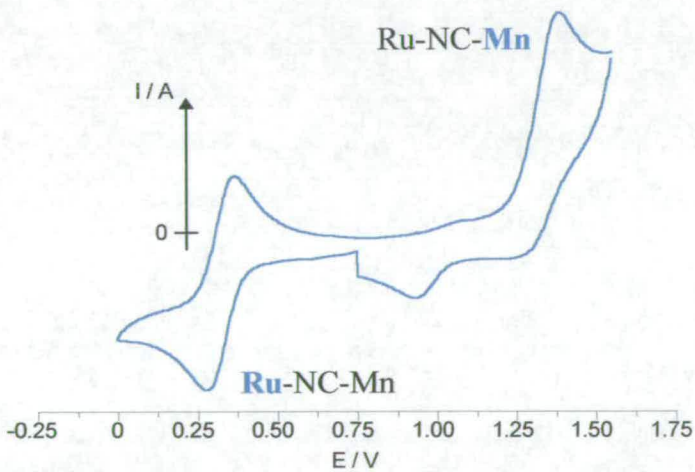

Figure 4.17 Cyclic voltammogram of **2** in 0.4 M $[N^nBu_4][BF_4]$ / DCM at 298 K.

The oxidation, $E_{pa} = +1.345$ V, is associated with a daughter peak at $E_{pc} = +0.896$ V. A linear relationship between i_p and $\nu^{½}$ indicates that, although this process is obviously chemically irreversible, it is electrochemically reversible. These values were recorded at a scan rate of 100 mVs^{-1}. At faster scan rates (500 mVs^{-1} to 1 Vs^{-1}) this couple could be made more reversible and a reduction peak could be observed at $E_{pc} = +1.246$ V (at $\nu = 1$ Vs^{-1}) giving a half-wave potential of +1.309 V. This process

is thought to be located primarily on the manganese centre, as labelled. On cooling to 233 K this couple remained largely irreversible. It should be noted that under the conditions that the cyclic voltammogram in Figure 4.17 was recorded, the ferrocinium/ferrocene couple was found to be at +0.55 V (ΔE = 81 mV).

The electrochemistry of the mononuclear complex *cis*-Mn(CN)(CO)$_2$dppm{P(OEt)$_3$} in DCM shows an irreversible one-electron oxidation with a peak potential of +1.03 V and a daughter peak with a cathodic peak potential of +0.54 V.[39] As found for **1**, the manganese centre in the binuclear complex is more difficult to oxidise (E_{pa} = +1.345 V) than in the mononuclear equivalent (by 315 mV). This is explained by the π-accepting nature of the $[Ru(NH_3)_5]^{3+}$ fragment when it is bonded to the nitrogen of the cyanide. Comparison of the IR spectra of the two complexes, ν_{CO}(mono) = 1955, 1896 cm^{-1} (in DCM) and ν_{CO}(bi-Ru^{III}/Mn^{I}) = 1960, 1918 cm^{-1} (in DCM), strengthens this argument. These results indicate a reduced amount of electron density on the Mn(I) in the binuclear complex compared to the mononuclear equivalent.

When the ruthenium couple of the binuclear complex ($E_{½}$ = +0.284 V) is compared to $[Ru(NH_3)_5NCMe]^{2+/3+}$ ($E_{½}$ = +0.558 V), as observed in **1**, the ruthenium centre in the binuclear complex is more easily oxidised (by 274 mV). Thus the manganese (I) fragment must be acting as a π-donor thereby increasing the electron density on the ruthenium, making it easier to oxidise.

In the binuclear complex, **2**, the 3+ state formally gives a Ru(III) (d^5) and a Mn (I) (d^6) metal centre, a mixed-valence species. This can be reduced to give the d^6/d^6 species, or oxidised to give the d^5/d^5 species. All of these oxidation states will be investigated using IR and UV/Vis spectroelectrochemistry, to study the effect these redox processes have on the carbonyl groups of this compound and to determine whether there is any communication between the two metal centres.

4.3.2.1 IR Spectroelectrochemistry of **2**

Compound 2 has two carbonyl groups in the *cis* position. The carbonyl groups are inequivalent, therefore, two absorptions in the carbonyl region of the IR spectrum are expected. The actual spectrum obtained for $[\mathbf{2}]^{2+}$ is shown in Figure 4.18, and clearly shows the two CO bands observed. DCM was used as the solvent in the blue spectrum, and THF in the red spectrum. This demonstrates that the bands are slightly solvent dependent. Hence IR spectroelectrochemical experiments were repeated in both solvents to study this effect.

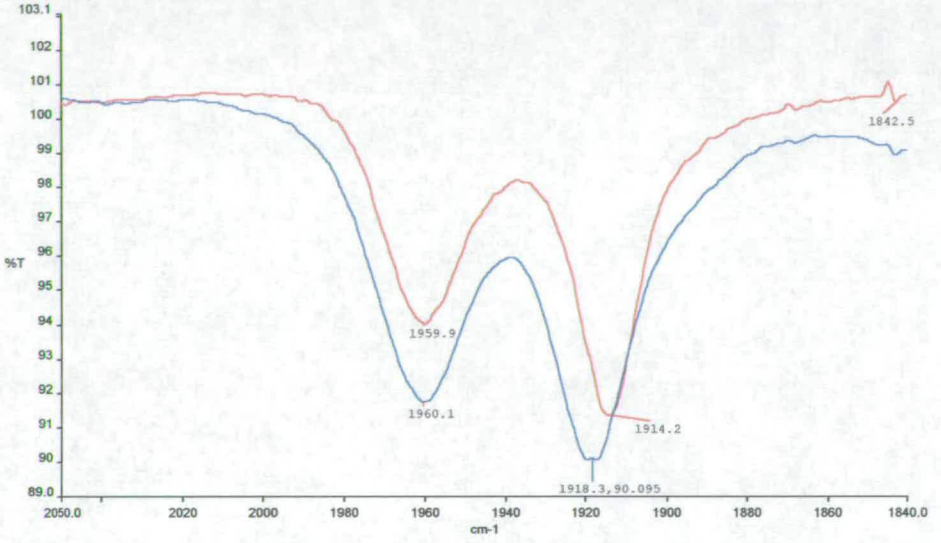

Figure 4.18 Carbonyl region of the IR spectra of $[\mathbf{2}]^{3+}$ in DCM (blue line) and THF (red line) at 298 K.

In the experiment, the compound is reduced to Ru(II)/Mn(I) and the spectral changes studied, then re-oxidised back to the mixed-valence species to check for reversibility. The compound is then oxidised to the Ru(III)/Mn(II) species and the spectral changes studied, and finally re-reduced back to the starting material, again to check the reversibility of the couple. These experiments will be performed at 233 K to avoid decomposition of the species, already identified for the similar system, compound 1.

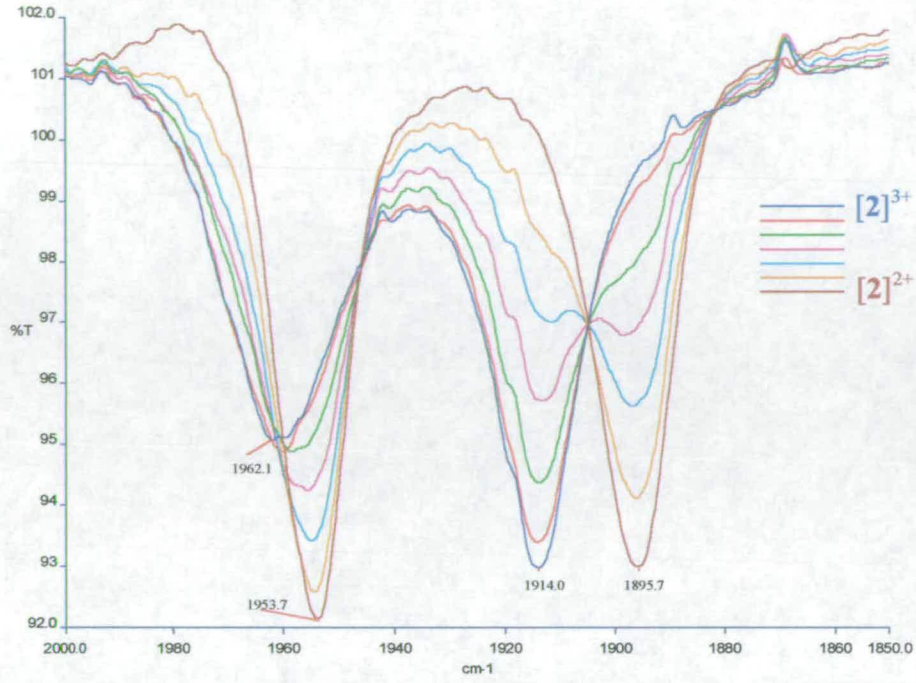

Figure 4.19 IR spectra of $[2]^{3+}$ during electrogeneration at –0.25 V in 0.1 M $[N^nBu_4][BF_4]$ / THF at 233 K.

Figure 4.19 shows the IR spectra recorded during the reduction of $[2]^{3+}$ to $[2]^{2+}$. On reduction, both carbonyl bands move to lower energy (this time, on reduction the amount of donation into the CO anti-bonding orbital is increased, making the bond weaker). The band at lower energy moves by a greater amount (18 cm^{-1}) than that at higher energy (6 cm^{-1}). This implies that the SOMO of the compound must have a better overlap with one of the CO anti-bonding orbitals. The isosbestic point at 1905 cm^{-1} shows that the conversion from the starting material to the reduced form proceeds without decomposition. The compound was then re-oxidised back to the mixed-valence species, which was regenerated at 100%.

Figure 4.20 shows the IR spectra obtained during the oxidation of $[2]^{3+}$ to $[2]^{4+}$. Note that these spectra were recorded in DCM since the solvent threshold for THF does not allow the oxidation to be studied. The reaction was not complete when the experiment was stopped. It was expected that, upon oxidation, the CO bands due to the $[2]^{3+}$ complex would collapse, and two new bands due to the CO fragments of $[2]^{4+}$ would grow in at higher energy. What was actually observed was the collapse of the two bands due the $[2]^{3+}$ and only one band growing in at 2010 cm^{-1}.

Since this was not as expected and bearing in mind the irreversible nature of the redox process, it was assumed that the compound was decomposing and therefore the experiment was stopped. It was only following the investigation of the *trans* isomer that the spectra obtained were explained. In fact, oxidation of the *cis* isomer ($[\mathbf{2}]^{3+} \rightarrow [\mathbf{2}]^{4+}$) is accompanied by a fast isomerisation reaction to produce the *trans* isomer ($[\mathbf{3}]^{4+}$) which has a single CO band at 2010 cm^{-1}. Indeed, the potential of the daughter peak observed growing in on the return scan (E_{pc} = +0.896 V) of the cyclic voltammogram (+1.5 V to 0.75V) is identical to E_{pc} for the oxidation of the *trans* isomer (+0.895 V) within experimental error.

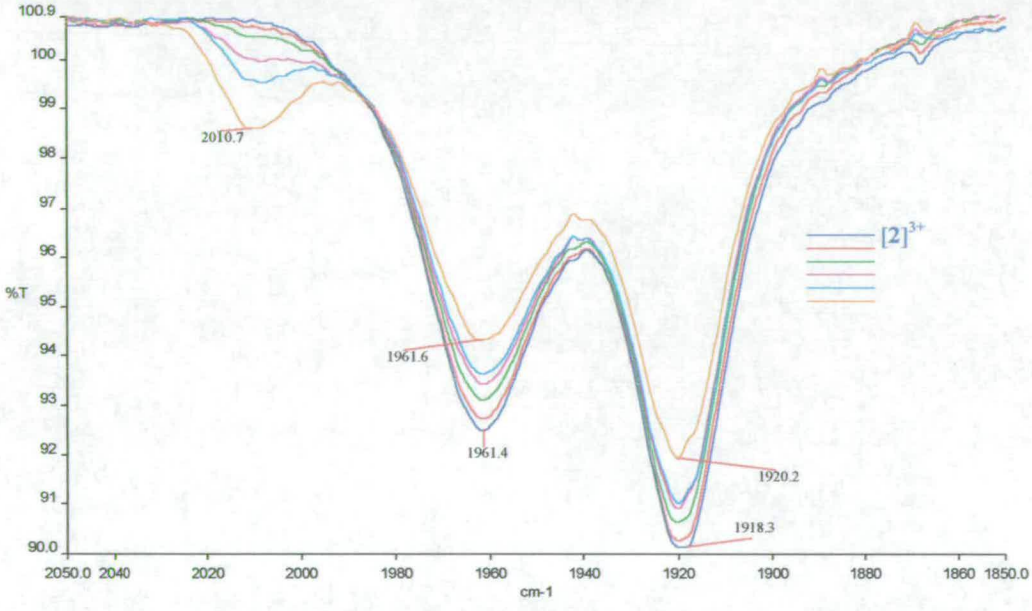

Figure 4.20 IR spectra recorded during electrogeneration of $[\mathbf{2}]^{3+}$ at +1.50 V in 0.4 M $[N^nBu_4][BF_4]$ / DCM at 233 K.

This is not a new phenomenon, the mononuclear complexes *cis,cis*-$[Mn(CO)_2\{P(OPh)_3\}(dppm)L]^z$ (z = 0 or 1; L = a variety of monodentate ligands), amongst others were found to undergo oxidative isomerisation to the *trans*-dicarbonylmanganese(II) analogues.[59] The cyclic voltammograms of these compounds showed a partially reversible oxidation wave in the range 0.8-1.8 V with an associated product wave at a more negative potential. The reversibility of this oxidation varies with L. By performing two scans back to back, this product wave was found to be reversible, and a half-wave potential could be determined.

In a bid to confirm the isomerisation theory, the *trans*-dicarbonyl analogues, *trans*-$[Mn(CO)_2\{P(OPh)_3\}(dppm)L]^z$ (z = 0 or 1; L = a variety of ligands), were investigated. These showed a fully reversible one-electron oxidation at potentials identical to the product wave observed in the *cis* equivalent. Controlled potential oxidation of orange *cis*-$[Mn(CO)_2\{P(OPh)_3\}(dppm)Br]$ ($E_{½}$ = 0.86 V) resulted in the formation of a dark red solution showing a one-electron reduction at 0.31 V which is identical to the potential of the oxidation of *trans*-$[Mn(CO)_2\{P(OPh)_3\}(dppm)Br]$.

This *cis* complex was chemically oxidised and the product isolated. One carbonyl band was observed in the infrared spectrum, at the same position as that in the oxidised *trans* complex. A cyclic voltammogram of the isolated product showed a fully reversible oxidation wave at a potential identical to that of the *trans* analogue. The square scheme shown below was proposed to explain this. The mechanism of the isomerisation is thought to be a non-dissociative twist mechanism, as was proposed by Bond *et al.*[60]

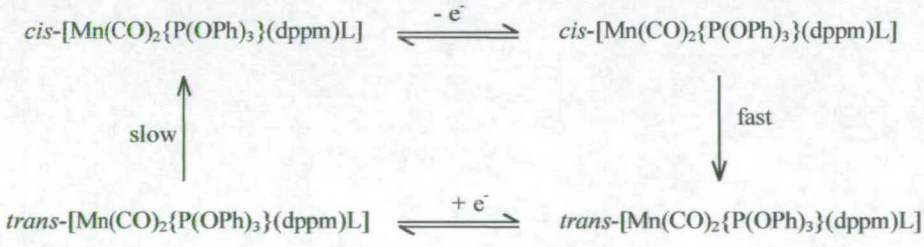

Scheme 4.2 'Square-scheme' for the oxidative isomerisation of *cis*-dicarbonylmanganese(II) compounds to *trans*-dicarbonylmanganese compounds.

Bond and co-workers[60] were investigating the oxidative isomerisation of the complexes *fac*-$Mn(CO)_3(L\text{-}L')X$ (L-L' = dppm, dppe; X = Cl, Br) to *mer*-$[Mn(CO)_3(L\text{-}L')X]^+$. Using electrochemical and spectrophotomeric methods, the kinetics and thermodynamics of the reaction were partially quantified. This resulted in the conclusion that a twist mechanism was most likely.

Thus, the oxidative isomerisation observed during the investigation of **2** is not unexpected, and on the ground of previous publications discussed above, is attributed to a non-dissociative twist mechanism.

Table 4.3 shows a summary of the results obtained during all of the IR spectroelectrochemical experiments for compound 2. Note that there is a small but real variation of CO stretching vibrations with solvent.

Table 4.3 Summary of CO stretch positions in the IR spectra of $[2]^{n+}$.

Solvent	Charge on compound	ν_{CO} / cm^{-1} (high energy)	ν_{CO} / cm^{-1} (low energy)
THF	2+	1954	1896
			+18 cm^{-1}
	3+	1960 (+6 cm^{-1})	1914
DCM	2+	1957	1898
			+22 cm^{-1}
	3+	1961 (+4 cm^{-1})	1920
	4+	Conversion to trans ν_{CO} = 2010 cm^{-1}	

On oxidation from $[2]^{2+}$ to $[2]^{3+}$, the carbonyl bands move by between 4 and 22 cm^{-1}. From the analysis of **1**, it is expected that oxidation at the ruthenium centre will change ν_{CO} by approximately 20 cm^{-1} and oxidation at the manganese centre will cause a 70 cm^{-1} shift. Therefore, the process $[2]^{2+}$ to $[2]^{3+}$ is based on the ruthenium centre. Thus, the electrochemical assignment given at the beginning of this section, that is, the reduction is based mainly on the ruthenium and the oxidation on the manganese centre, is corroborated.

As observed with **1**, an electronic change at the ruthenium centre is being communicated through the molecule and affecting the carbonyl functions which are bonded to the manganese centre. To investigate the amount communication between the two metal centres in this compound, a UV/Vis spectroelectrochemical experiment must be performed.

4.3.2.2 Uv/Vis Spectroelectrochemistry of **2**

The spectra recorded during the reduction of $[2]^{3+}$ are shown in Figure 4.21. The spectrum of the fully reduced (2+) species is, as found for $[1]^{2+}$ essentially

featureless. Upon one electron oxidation two new bands grow in at 17000 cm^{-1} (ε = 1400 M^{-1} cm^{-1}) and 9000 cm^{-1} (ε = 300 M^{-1} cm^{-1}). An isosbestic point is observed at 21600 cm^{-1} indicating clean conversion from $[\mathbf{2}]^{2+}$ to $[\mathbf{2}]^{3+}$.

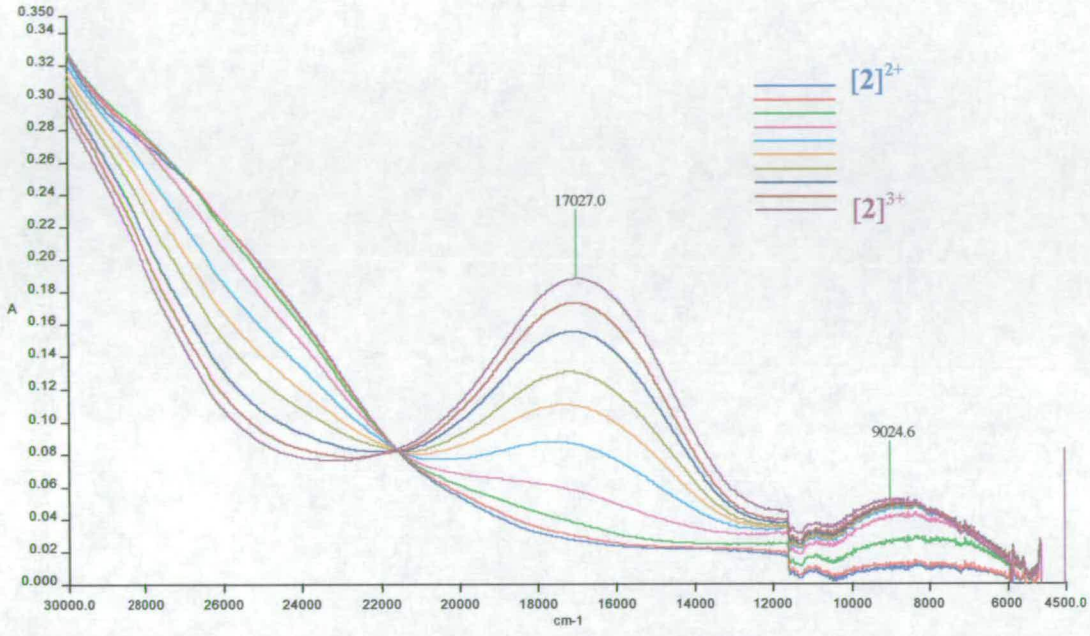

Figure 4.21 UV/Vis spectroelectrochemistry of $[\mathbf{2}]^{3+}$ in 0.1 M $[N^nBu_4][BF_4]$ / DMF at 228 K. E_{app} = -0.40 V.

The spectra recorded during the oxidation of $[\mathbf{2}]^{3+}$ are shown in Figure 4.22. Upon oxidation to the 4+ species the band at lower energy (9000 cm^{-1}) collapses and the band at 17000 cm^{-1} moves to a slightly lower energy (16750 cm^{-1}). The temperature at which this experiment was performed was low enough to prevent the isomerisation reaction (*cis* → *trans*) occurring. In fact, this experiment was repeated in DCM and following the oxidation of $[\mathbf{2}]^{3+}$ to $[\mathbf{2}]^{4+}$ (at 238 K) the temperature was allowed to rise to 253 K and the conversion of $[\mathbf{2}]^{4+}$ to $[\mathbf{3}]^{4+}$ could be followed using UV/Vis spectroscopy. These results are shown in Figure 4.23. The isosbestic point at 16000 cm^{-1} indicates that clean conversion is taking place. The UV/Vis spectroelectrochemistry of the *trans* species (**3**) could then be investigated (see chapter 4.3.3.2).

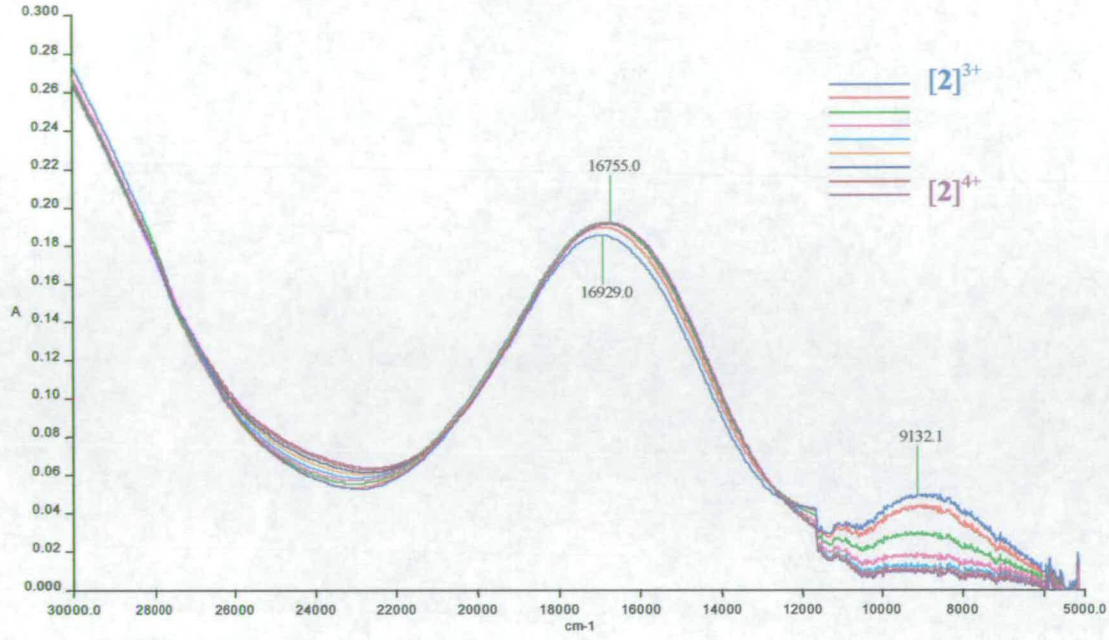

Figure 4.22 UV/Vis spectroelectrochemistry of $[2]^{3+}$ in 0.1 M $[N^nBu_4][BF_4]$ / DMF at 228 K. E_{app} = +1.40 V.

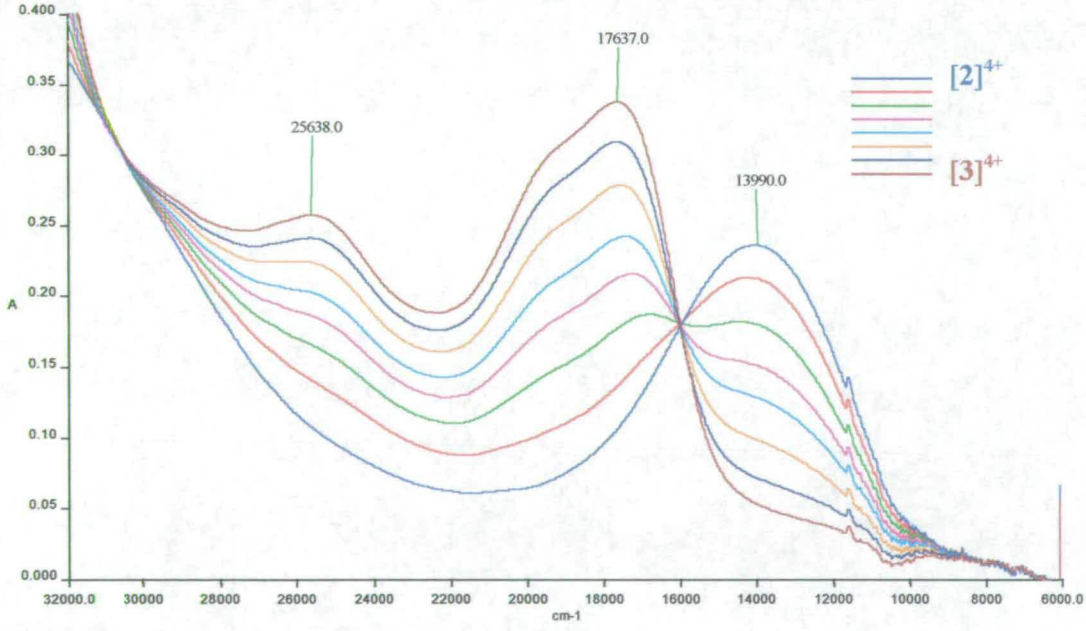

Figure 4.23 UV/Vis spectra following the conversion of $[2]^{4+}$ (blue line) to $[3]^{4+}$ (dark red line) in 0.5 M $[N^nBu_4][BF_4]$ / DCM at 253 K.

When the spectrum of $[\mathbf{2}]^{4+}$ in DMF is compared to that in DCM, a large difference in ν_{max} is observed (2750 cm^{-1}). Indicating that the position of this band is strongly dependent on the solvent. Similarly, the spectrum of $[\mathbf{2}]^{3+}$ in DCM showed two bands of similar intensity to those observed in DMF but with different ν_{max}, the higher energy band is centred at 14250 cm^{-1} (16950 cm^{-1} in DMF)and the lower energy band at 8650 cm^{-1} (9150 cm^{-1} in DMF).

4.3.3 [*trans*-$(NH_3)_5Ru(\mu\text{-}NC)Mn(CO)_2(\eta^2\text{-}PPh_2CH_2PPh_2)(P\{OEt\}_3)]^{3+}$: $[3]^{3+}$

Figure 4.24 Structure of [*trans*-$(NH_3)_5Ru(\mu$-NC)$Mn(CO)_2(\eta^2$-$PPh_2CH_2PPh_2)(P\{OEt\}_3)]^{3+}$ $[3]^{3+}$

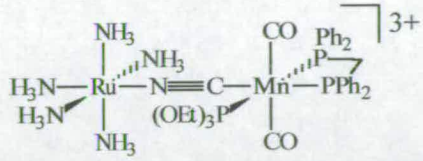

The cyclic voltammogram of $[3]^{3+}$ (Figure 4.24) is given in Figure 4.25. It shows a one-electron reduction and also a one-electron oxidation (the number of electrons in each process was determined using bulk electrolysis). The reduction, $E_{½}$ = +0.212 V (ΔE = 140 mV), displays a linear relationship between i_p and $\nu^{½}$ indicating that this process is electrochemically reversible. The ratio of peak currents was found to be 0.89, an indication of some chemical instability of the reduced species. (These values were recorded at a scan rate (ν) of 100 mVs^{-1}.) This process is thought to be based primarily on the ruthenium centre.

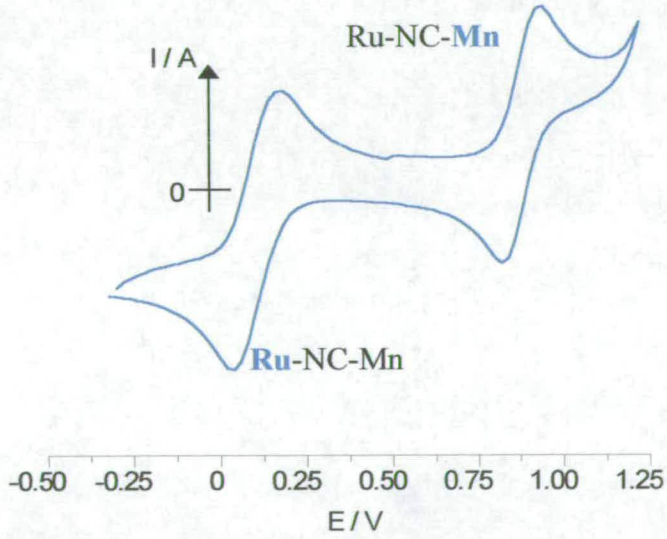

Figure 4.25 Cyclic voltammogram of $[3]^{3+}$ in 0.4 M $[N^nBu_4][BF_4]$ / THF at 298 K.

The oxidation, $E_{½}$ = +0.912 V (ΔE = 100 mV) also displays a linear relationship between i_p and $\nu^{½}$ thus is electrochemically reversible. For this oxidation, i_{pa}/i_{pc} = 0.76, again indicating that the oxidation is not fully chemically reversible. This process is thought to be located primarily on the manganese centre, as labelled. (It should be noted that under the conditions that this cyclic voltammogram was

recorded the ferrocinium/ferrocene couple was found to be at +0.55 V ($\Delta E = 93$ mV).)

The electrochemistry of the mononuclear complex *trans*-$Mn(CN)(CO)_2dppm\{P(OEt)_3\}$ in DCM shows a fully reversible one-electron oxidation at +0.58 V.[39] When this is compared to the manganese couple in the binuclear complex (+0.912 V), as for **1** and **2**, the oxidation of the mangenese centre in the binuclear complex is more difficult (by 330 mV). This is due to the $[Ru(NH_3)_5]^{3+}$ fragment removing electron density (through the CN bridge) from the manganese centre. This is supported by the IR spectra of these compounds, ν_{CO}(mono) = 1914 cm^{-1} (in DCM) and ν_{CO} (bi-Ru^{III}/Mn^{I}) = 1938 cm^{-1} (in DCM).

When the ruthenium couple of the binuclear complex ($E_{½}$ = +0.212 V) is compared to $[Ru(NH_3)_5NCMe]^{2+/3+}$ ($E_{½}$ = 0.558 V), as observed for **1** and **2**, the ruthenium centre in the binuclear complex is easier to oxidise (by 350 mV). This is due to the manganese (I) fragment acting as a π-donor.

In the binuclear complex, **3**, the 3+ state formally gives a Ru(III) (d^5) and a Mn(I) (d^6), a mixed-valence species. The compound can be reduced to give the d^6/d^6 species, or oxidised to give the d^5/d^5 species. All of these oxidation states will be investigated using IR and UV/Vis spectroelectrochemistry, to study the effect these redox processes have on the carbonyl groups of this compound and to determine whether there is any communication between the two metal centres.

4.3.3.1 IR Spectroelectrochemistry of **3**

Compound 3 has two carbonyl bands in the *trans* position (see Figure 4.24). Since these two carbonyls are equivalent, only one CO band is expected in the IR spectrum.

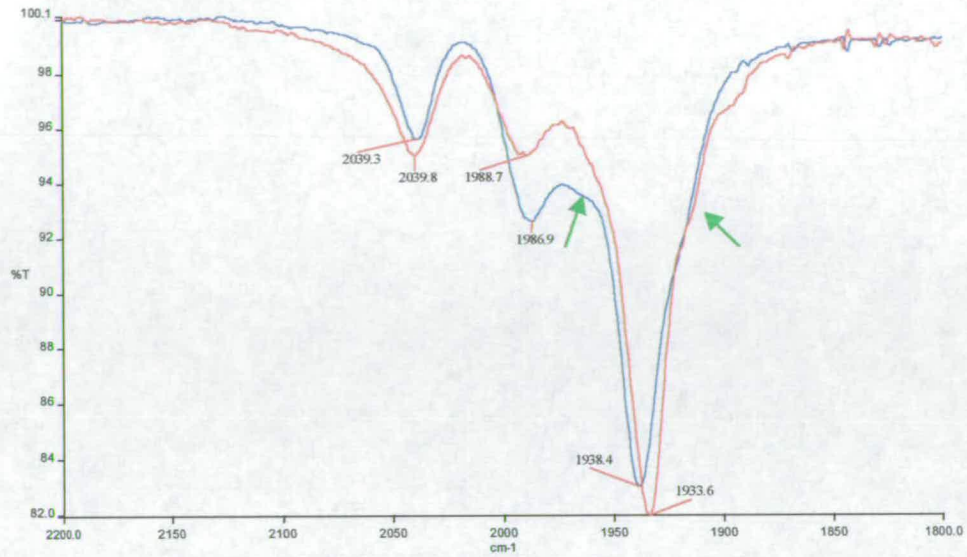

Figure 4.26 Carbonyl region of the IR spectra of $[\mathbf{3}]^{3+}$ in DCM (blue line) and THF (red line).

The actual spectrum obtained for $[\mathbf{3}]^{3+}$ is shown in Figure 4.26, the single CO band expected is the strong absorption at approx. 1935 cm^{-1}. Also observed however, are the less prominent bands at 2039 and 1988 cm^{-1}. The band at 2039 cm^{-1} is most likely due to the bridging cyanide. This has been observed previously in a mixed-valence dimanganese cyano-bridged compound where ν_{CN} was observed at 2043 cm^{-1}.[39] The remaining band at 1988 cm^{-1} is as yet unassigned. These weaker bands are only associated with this oxidation state of the compound, since they collapse on oxidation and reduction and then grow back in on returning to the 3+ state. The spectra of **3** are made more complicated by the presence of the *cis* isomer as an impurity. Although in the 3+ state, the bands due to **2** appear as shoulders, in the other oxidation states they will become more prominent. They will be marked by a green arrow throughout. As observed with compound 2, the bands are also slightly solvent dependent, both in position and in relative intensity.

The experimental procedure will be the same as that for **2**. The compound will be reduced, then re-oxidised back to the mixed-valence state. Then it will be oxidised, and re-reduced the back to its original state. These experiments were all performed at 233 K to avoid decomposition.

Figure 4.27 shows the IR spectra recorded during the reduction of $[\mathbf{3}]^{3+}$ to $[\mathbf{3}]^{2+}$. On reduction, the carbonyl band moves to lower energy as expected (from previous results), by 18 cm^{-1}. The two bands, which were assigned to ν_{CN} and an overtone or combination of overtones collapsed. The remaining two bands are due to $[\mathbf{2}]^{2+}$. The potential at which the bulk electrolysis was carried out was also sufficient to reduce the *cis* isomer. The compound was then re-oxidised to regenerate the mixed-valence system at 100%

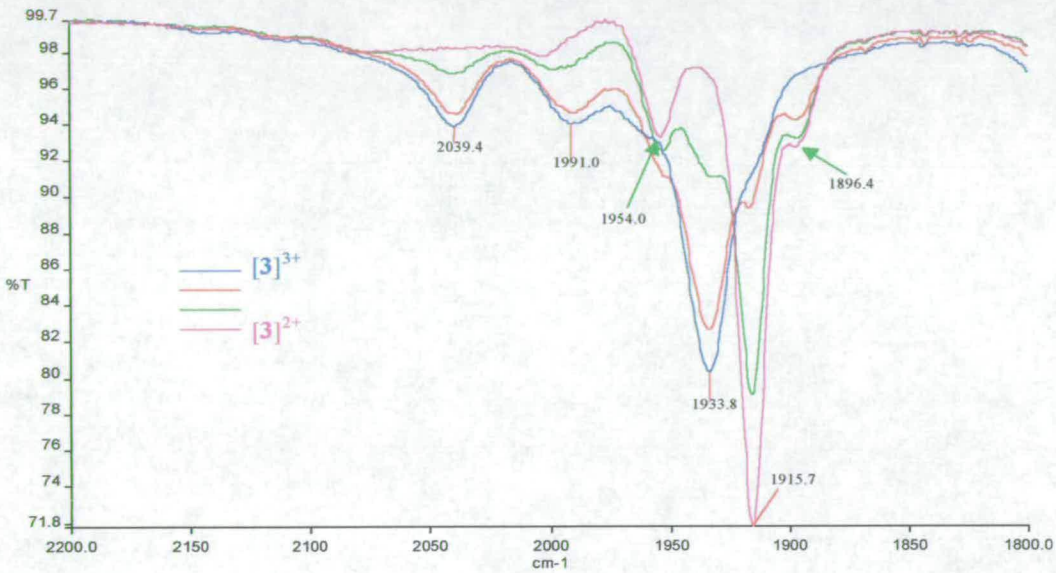

Figure 4.27 IR spectra of $[\mathbf{3}]^{3+}$ during electrogeneration at –0.25 V on 0.1 M $[N^nBu][BF_4]$ / THF at 233 K.

Figure 4.28 shows the IR spectra obtained during the oxidation of $[\mathbf{3}]^{3+}$to $[\mathbf{3}]^{4+}$. The band due to the 3+ species collapses, and the corresponding growth of a new band at 2010 cm^{-1}, (a change of 72 cm^{-1}) is observed. This is attributed to the CO of the 4+ species. The ν_{CN} band and the band thought to be due to an overtone also collapse. The two remaining (smaller) bands are due to $[\mathbf{2}]^{3+}$. (The potential at which the electrogeneration was performed (+1.15 V) was not positive enough to induce the oxidation of the *cis* isomer (E_{pa} = +1.383 V).) This oxidation was only successful when dichloromethane was used as the solvent. In THF, upon oxidation all of the bands in the carbonyl region collapsed, hence the compound $[\mathbf{3}]^{4+}$ is not stable in THF.

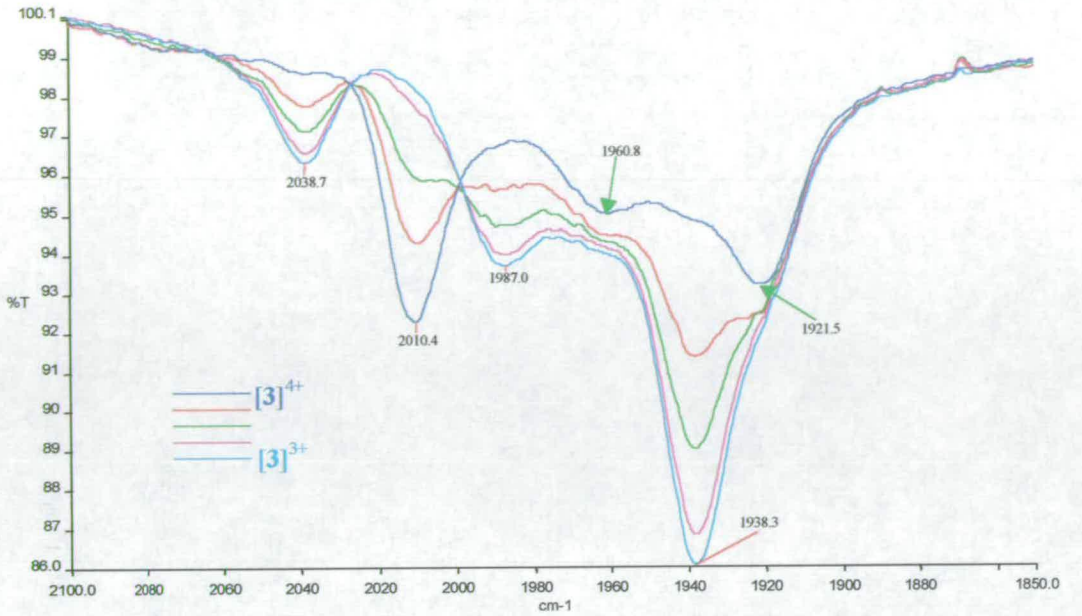

Figure 4.28 IR spectra of $[3]^{4+}$ during electrogeneration at +0.50 V in 0.4 M $[N^nBu_4][BF_4]$ / DCM at 233 K.

The change produced in ν_{CO} upon oxidation is very similar to that observed during the investigation of the complex *trans*-$[Mn(CN)(CO)_2\{P(OPh)_3\}(dppm)]$. In the Mn(I) compound ν_{CO} is observed at 1930 cm^{-1}. Upon one-electron oxidation to Mn(II) ν_{CO} moves 72 cm^{-1} to 2002 cm^{-1}. These results also highlight the π-accepting nature of the Ru(III) fragment (discussed previously). If ν_{CO} for the binuclear and mononuclear Mn(I) species are compared, ν_{CO} in the binuclear species is 8 cm^{-1} higher in energy. The same difference is also noted in the Mn(II) species. Thus the CO bonds in the binuclear species are stronger than the mononuclear analogue *i.e.* there is less electron density on the manganese of the binuclear species to be delocalised into the π^* orbital of the CO group.

Table 4.4 shows a summary of the results obtained during all of the IR spectroelectrochemical experiments for compound 3.

Table 4.4 Summary of CO stretch positions in the IR spectra of $[\mathbf{3}]^{n+}$

Solvent	Charge on compound	ν_{CO} / cm^{-1}	
THF	2+	1916	+18 cm^{-1}
	3+	1934	
	4+	Decomposition	
DCM	2+	1916	+22 cm^{-1}
	3+	1938	+72 cm^{-1}
	4+	2010	

From these results, as with **1** and **2**, it is clear that an electronic change at the ruthenium centre is having an effect on the carbonyl fragment. Therefore some electronic communication between the two metals is assumed. In order to quantify the amount of communication a UV/Vis spectroelectrochemical investigation needs to be carried out.

4.3.3.2 UV/Vis Spectroelectrochemistry of **3**

The UV/Vis spectroelectrochemistry of **3** was investigated following the conversion of $[\mathbf{2}]^{4+}$ to $[\mathbf{3}]^{4+}$ (see previous section 4.3.2.2). Once formed, $[\mathbf{3}]^{4+}$ was then reduced in two separate steps to $[\mathbf{3}]^{2+}$ and finally brought back (again in two one-electron steps) to $[\mathbf{3}]^{4+}$ to check the reversibility of these reactions. The spectra recorded during the oxidation of $[\mathbf{3}]^{2+}$ are shown in Figure 4.29.

The spectrum of the fully reduced species (2+) is, as found for **1** and **2** previously, essentially featureless, with the exception of a weak band at 8650 cm^{-1} (ε = 400 M^{-1} cm^{-1}) which was not observed in $[\mathbf{1}]^{2+}$ or $[\mathbf{2}]^{2+}$. Upon one electron oxidation to the mixed-valence species two new bands grow in. These bands are overlapping but are roughly centred at 9600 (ε = 3300 M^{-1} cm^{-1}) and 14000 cm^{-1} (ε = 1300 M^{-1} cm^{-1}). One isosbestic point is observed at 21000 cm^{-1} illustrating that the oxidation takes place without significant decomposition.

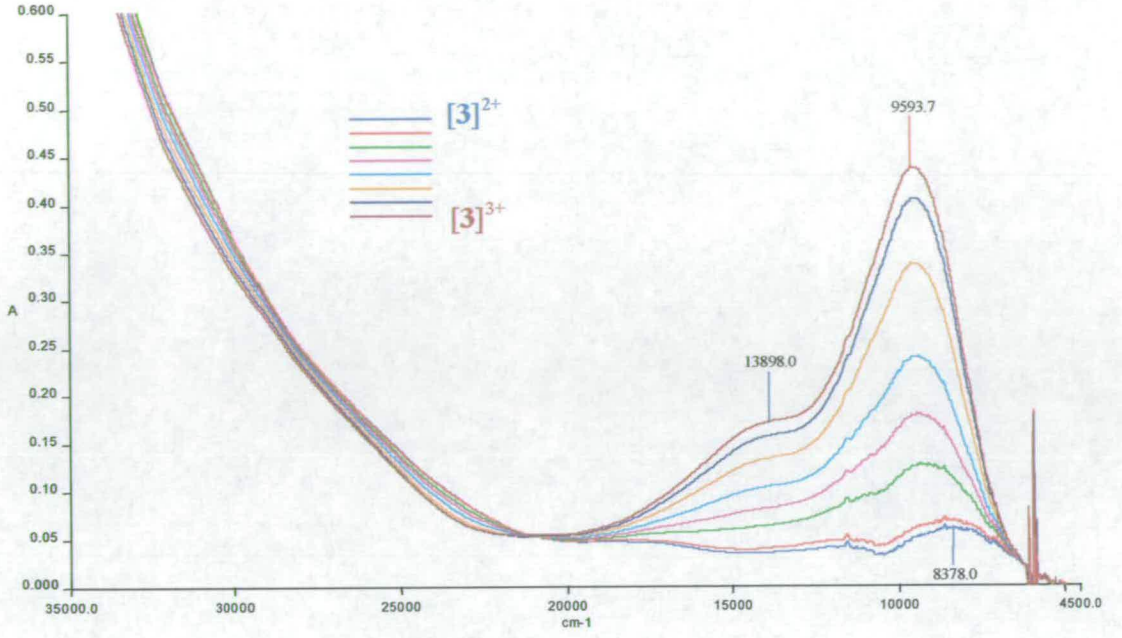

Figure 4.29 UV/Vis spectroelectrochemistry of $[3]^{2+}$ in 0.5 M $[N^nBu_4][BF_4]$ / DCM at 238 K. E_{app} = +0.40 V.

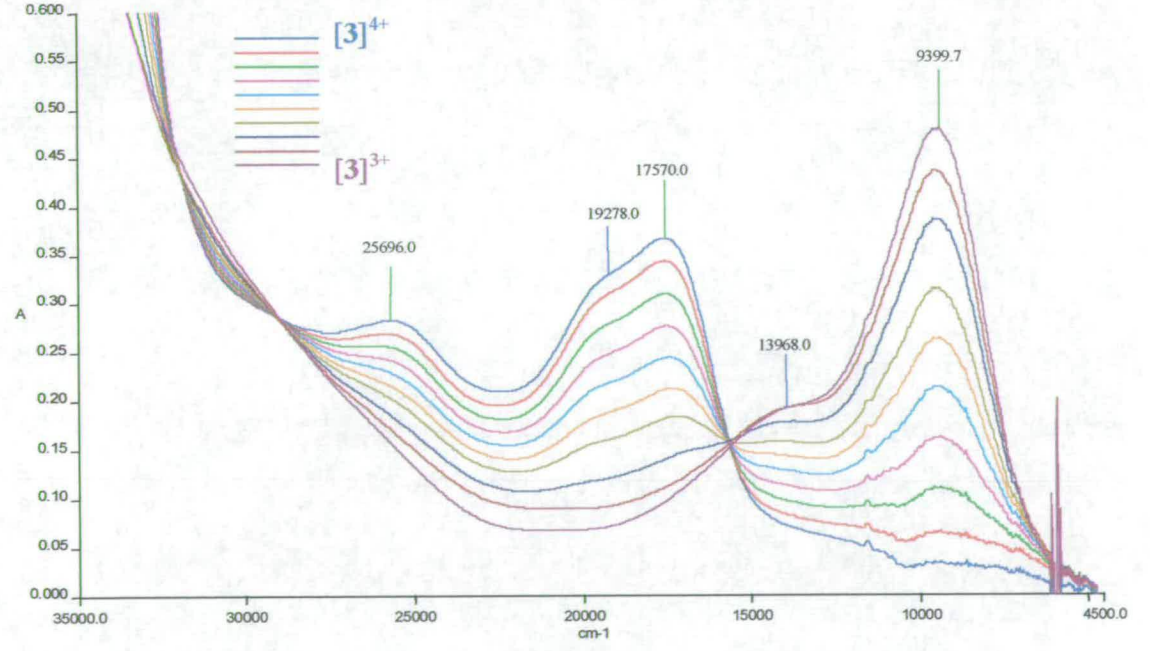

Figure 4.30 UV/Vis spectroelectrochemistry of $[3]^{4+}$ in 0.5 M $[N^nBu_4][BF_4]$ / DCM at 238 K. E_{app} = +0.45 V.

The spectra recorded during the oxidation of $[\mathbf{3}]^{3+}$ to the fully oxidised (4+) species are shown in Figure 4.30. Upon oxidation by one electron the two bands in the spectrum of the mixed-valence species collapse and two corresponding bands grow in at higher energy. Again these bands are overlapping, with the most prominent band (at lower energy) centred at 17550 cm^{-1} (ε = 2700 M^{-1} cm^{-1}) and the shoulder estimated at 19300 cm^{-1} (ε = 2400 M^{-1} cm^{-1}). An additional band is observed at 25700 cm^{-1} (ε = 2000 M^{-1} cm^{-1}). Three isosbestic points result at 31850, 29050 and 15700 cm^{-1}.

4.3.4 Comparison of 1, 2 and 3

4.3.4.1 Electrochemistry

Table 4.5 Summary of redox couples calculated for compounds 1, 2 and 3.

Compound	Redox Couple	$E_{½}$ / V
1	$Ru^{III} \rightarrow Ru^{II}$	+0.173
	$Mn^{II} \rightarrow Mn^{I}$	+0.552
2	$Ru^{III} \rightarrow Ru^{II}$	+0.284
	$Mn^{II} \rightarrow Mn^{I}$	+1.309
3	$Ru^{III} \rightarrow Ru^{II}$	+0.212
	$Mn^{II} \rightarrow Mn^{I}$	+0.912
$[Ru(NH_3)_5(NCMe)]^{3+/2+}$	$Ru^{III} \rightarrow Ru^{II}$	+0.558

Table 4.5 shows the half wave potentials for compounds 1, 2 and 3. These potentials have been corrected to the ferrocinium/ferrocene couple (+0.55 V). If the half-wave potentials for the $Ru^{III/II}$ couple are compared, the value remains relatively constant (varies by only 110 mV) and is always less positive than that in the mononuclear complex, $[Ru(NH_3)_5NCMe]^{3+/2+}$ (also given in Table 4.5). As explained previously, the reason for the half-wave potential being less positive in the binuclear compounds compared to the mononuclear compound is due to the π-donor ability of the Mn(I) centre when bonded to the nitrogen of the cyano group. The small variation in half-wave potential in **1**, **2**, and **3** is expected since the structure of the ruthenium centre is remaining unchanged, and any shift in the half-wave potential which is observed will be due to the communication between the two centres.

The $Mn^{II/I}$ couple of **1**, **2** and **3** on the other hand, is strongly dependent on both the number, and the position of the carbonyl groups. The structural change in **2** and **3** compared to **1** is the addition of a second carbonyl function. Carbonyl groups are commonly known as σ-donor, strong π-acceptors. On addition of a second carbonyl group, more electron density is pulled away from the metal centre. Therefore, it is

expected that the oxidation (removal of even more electron density) of that metal centre will become more difficult, and hence should move to a higher potential. This is observed, the $Mn^{II/I}$ couple moves from +0.552 V in **1** to +1.309 V in **2** (a variation of 760 mV).

One surprising aspect of the peak potential of the manganese couple is the difference between the *cis* and *trans* isomers. The manganese of the *cis* isomer is 400 mV more difficult to oxidise than the trans. This implies that the HOMO of the complex must have a better overlap with the π-acceptor orbitals of the *cis* CO arrangement than the *trans*. Thus, more electron density is being removed from the manganese centre making it more difficult to oxidise. This phenomenon was also noticed in the *cis* and *trans* isomers of the mononuclear complex $[Mn(CN)(CO)_2\{P(OEt)_3\}(dppm)]$. E_{pa} for the *cis* isomer was found to be +1.03 V while $E_{½}$ for the *trans* isomer was +0.58 V, a difference of 450 mV.

A simplistic explanation of this effect involves the consideration of the number of interactions between the dπ-orbitals of the manganese centre and the π* anti-bonding orbitals of the CO groups. Firstly, the structure of the *cis* isomer must be defined since there are 3 possible structures. The crystal structure of the complex *cis*-$[MnL(CO)_2\{P(OPh)_3\}(dppm)]$ (L = Br) has been determined and shows one CO group *trans* to L and the other *trans* to a phosphorus of the dppm ligand.[59] It is assumed that the complex where L is cyanide will have a similar structure, this is shown in Figure 4.31, also shown is the structure of the *trans* isomer.

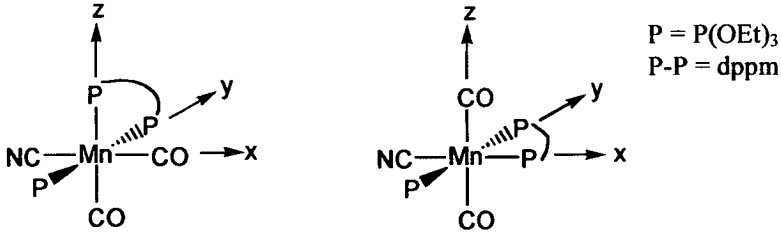

Cis isomer *Trans isomer*

Figure 4.31 Expected molecular structures of the isomers of $[Mn(CN)(CO)_2\{P(OEt)_3\}(dppm)]$.

Assuming the axis are labelled as shown in Figure 4.31 the dπ orbitals will be the d_{xz}, d_{yz}, and d_{xy} (the t_{2g} set in octahedral symmetry) in both cases. The interactions between the manganese dπ orbitals and the π* orbitals of the carbonyl groups can now be examined. In the *cis* isomer, the d_{xz} orbital can interact with the π*-orbitals of both CO groups, the d_{yz} can interact with the CO which is *trans* to the P, and the d_{xy} can interact with the CO which is *trans* to the cyanide. In the *trans* isomer, the d_{xz} orbital can interact with the π* orbitals of both CO groups, as can the d_{yz}, however, the d_{xy} cannot interact with either. This interaction of π-accepting orbitals with metal-based dπ orbitals will lower the energy of the interacting dπ orbitals with respect to the assumed t_{2g} set. This is demonstrated pictorially in Figure 4.32. Thus, since in the *cis* isomer all of the dπ orbitals have been stabilised by a π interaction, the energy of the HOMO will be lower (more stable) and hence the manganese will be more difficult to oxidise than the *trans* isomer. This simple argument will also be applicable to the manganese centre of the binuclear complex.

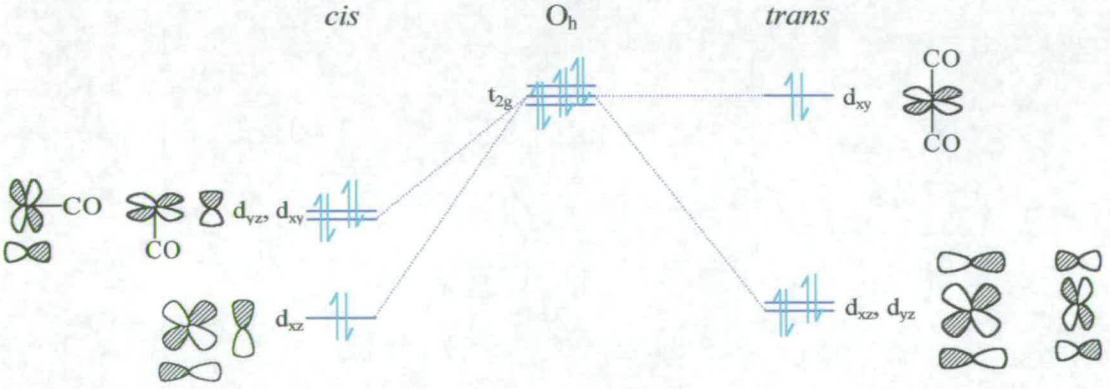

Figure 4.32 Simplified MO diagram demonstrating the effect of the dπ orbital interaction with the CO function for the isomers of $[Mn(CN)(CO)_2\{P(OEt)_3\}(dppm)]$.

The amount of electron density on the manganese centre is also reflected in the position of the ruthenium couple. The manganese(I) acts as a π-donor and thus, the half-wave potential of the ruthenium centre will be dependent on the electron density of manganese. In **1** (compared to **2** and **3**) the manganese has most electron density (is the easiest to oxidise since **1** has only a single CO ligand). Hence, through π-delocalisation of the electron density on to the ruthenium, this ruthenium centre is also the most easily oxidised. In **2** the manganese centre is the most difficult to

oxidise, *i.e.* it has less electron density to share with the ruthenium and so that ruthenium is also the most difficult to oxidise.

Thus the electrochemistry of these complexes has allowed the following conclusions to be made: (i) The Mn(I) moiety can function as a π-donor unit; (ii) the ruthenium (III) moiety can function as a π-acceptor; (iii) the half-wave potentials of the manganese centre depends strongly on the number and orientation of the carbonyl groups and to a much smaller effect so does the ruthenium centre. (iv) The cyanide bridge does allow some communication between the two metal centres.

4.3.4.2 IR Spectra

Table 4.6 Summary of the results from all of the IR experiments performed.

Compound	Solvent	Charge on Comound	ν_{CO} / cm^{-1}	ν_{CO} / cm^{-1}
1	THF	2+	1865	
		3+	1885	
		4+	1958	
2	THF	2+	1954	1896
		3+	1960	1914
	DCM	2+	1957	1898
		3+	1961	1920
		4+	Conversion to *trans*	
3	THF	2+	1916	
		3+	1934	
	DCM	2+	1916	
		3+	1938	
		4+	2010	

A summary of the CO band positions in all of the compounds is given in Table 4.6. Generally, on oxidation from 2+ to 3+, ν_{CO} moves 18-22 cm^{-1}, and on oxidation from

3+ to 4+, ν_{CO} moves 73-76 cm^{-1} except in **2** where on oxidation, an isomerisation reaction takes place. Since an electronic change at the manganese centre (which is directly bonded to the CO group) will have the largest effect on the ν_{CO} position, these results confirm the electrochemical assignment of the redox processes for all three compounds. That is, the redox couple at the lowest potential (3+/2+) is based primarily on the ruthenium metal centre, and the redox couple at the more positive potential (4+/3+) is based primarily on the manganese metal centre.

The IR spectra of the mononuclear manganese compounds have been studied previously, and upon oxidation of the manganese centre the CO band moves approximately 70 cm^{-1}. This helps to support the electrochemical assignment (discussed previously).

The energy of the CO stretch for **1** is consistently lower than that for **2** and **3**. The carbonyl groups are σ-donors, strong π-acceptors and any back-bonding from the manganese centre will serve to weaken the CO bond (thus its stretching frequency will move to lower energy). **2** and **3** show ν_{CO} at higher energy than **1**, that is, the CO bonds are stronger, this is due to the presence of two CO functions which have to compete for/share the electron density on the manganese centre. Whereas, in **1**, there is only one CO function, this eliminates the competition and so more electron density is available for back donation (compared to **2** and **3**), hence the CO band will be at lower energy.

For a more detailed comparison **3** must be considered separately since the CO band observed in this compound is due to the concerted motion of both CO groups (will be the asymmetric stretch). In order to use this value in a comparison, the amount of coupling between the two groups would have to be known. However, **1** and **2** can be compared, **1** has only one CO group hence ν_{CO} will be due to the symmetric stretch; **2** has two groups which are in very different environments and are orthogonal which does not permit strong coupling between the two groups, hence the two ν_{CO} will be due to the symmetric stretch of each separately. In **1** on oxidation from 2+ to 3+ the

CO band moves 20 cm^{-1}, in **2** (on oxidation from 2+ to 3+) one CO band moves 18 cm^{-1} and the other 6 cm^{-1}. From these results it can be inferred that the carbonyl group whose band moves 18 cm^{-1} in **2** must be in a very similar electronic environment to the CO group in **1**, that is, *trans* to the cyanide. Therefore the remaining band in **2** will be due to the CO group which is *trans* to the phosphorous of dppm. This argument is supported by the position of these bands, the band in **2** which is assigned to the carbonyl group *trans* to cyanide is at 1896 cm^{-1}, (the other band is at 1954 cm^{-1}) and in **1** ν_{CO} is at 1865 cm^{-1}.

Since in **2** the CO groups move by a differing amount upon oxidation from 2+ to 3+, this implies the interaction between the π-acceptor CO orbital and the HOMO (remember this is primarily ruthenium based) is different in each. The simplified MO diagram in Figure 4.32 shows that the d_{xy} and the d_{yz} orbital are equivalent in energy, however, this MO diagram does not take into account the effect of the *trans* ligands (only the interaction of the dπ orbitals with the CO groups). Oxidation at the ruthenium centre is communicated through the cyanide bridge (as discussed earlier), the dπ orbitals which can interact with this bridge are d_{xy} and d_{xz}. Any alteration of the electron density of the d_{xz} orbital should affect both CO groups in the same manner. On the other-hand, any change in the d_{xy} orbital will only affect the carbonyl *trans* to the cyanide, that is, a reduction in electron density here (upon oxidation) will result in a reduced amount of back-bonding into the π*-orbital of this CO only. Hence the stretching frequency for the carbonyl *trans* to the cyanide should move by a greater amount on oxidation of the ruthenium centre than that of the carbonyl *trans* to the phosphorous as found experimentally.

4.3.4.3 UV/Vis Spectroelectrochemistry

The assignment of the electronic transitions in these complexes has proved very difficult, and is discussed generally below.

In the fully reduced species (2+), formally there is a Ru(II) (d^6) metal centre and a Mn(I) (d^6) metal centre. Any significant bands (high ε) observed can only be due to

either intraligand ($\pi \rightarrow \pi^*$) or MLCT ($Ru \rightarrow \pi^*$) transitions. Any Mn(I) MLCT transitions are expected at much higher energies than Ru(II) MLCT transitions. Bands with small extinction coefficients can be explained by d-d transitions within the metal centres.

The mixed-valence species formally contains a Ru(III) (d^5) and a Mn(I) (d^6) metal centre. Spectral changes which occur upon formation of this compound from the 2+ species cannot be due to the Mn fragment exclusively since this moiety has not changed significantly. Since the ruthenium centre now has a d^5 configuration, LMCT transitions can occur. However, NH_3 is a σ-only donor and therefore cannot participate in this type of interaction, and the π-bonding orbitals of cyanide lie too far below the metal d orbitals for this transition to be observed in the visible region of the spectrum.[2] Thus the bands observed cannot be due to LMCT transitions.

This leaves either d-d transitions or $Mn \rightarrow Ru$ CT transitions. In all of the compounds, at least one of the bands observed has an extinction coefficient of $>1000\ M^{-1}\ cm^{-1}$, therefore they cannot all be accounted for by d-d transitions. Furthermore, increasing the oxidation state of ruthenium means that Δ_o increases and hence d-d transitions should occur at higher energy. The bands in question are at very low energy and therefore cannot be d-d transitions. Thus the bands with larger extinction coefficients are assigned as $Mn \rightarrow Ru$ charge transfer transitions which will be mediated by the cyanide bridging ligand. More than one of these bands can be explained by the non-degenerate nature of the $d\pi$-orbitals of the manganese centre (discussed above). The intensity of the band indicates that there is significant electronic communication between the two metal centres.

The spectra of the fully oxidised species tends to show the same features observed in the mixed-valence species (that is the two overlapping peaks) but moved to higher energy. Since in these complexes the two metal centres are very different (highly asymmetrical) the $Mn \rightarrow Ru$ charge transfer transition can still occur, but will be shifted to higher energy since the manganese centre involved is now Mn(II).

Given the difficulty in the assignment of the bands observed in the electronic spectra of these compounds, and the absence of the relevant information on the mononuclear fragments, a detailed comparison of the results could not be carried out.

In conclusion, the results from all of the experiments performed indicate that there is a degree of communication between the two metal centres in all three complexes. However, due to the highly asymmetrical nature of these complexes the level of this communication is difficult to determine.

The experiments here have proved that the oxidation from $[\mathbf{N}]^{2+}$ to $[\mathbf{N}]^{3+}$ is based primarily on the ruthenium centre and the $[\mathbf{N}]^{3+}$ to $[\mathbf{N}]^{4+}$ oxidation is based primarily on the manganese metal centre. The IR spectroelectrochemical experiments have allowed the assignment of the carbonyl absorptions in the *cis* isomer (**2**) to specific CO groups.

CHAPTER FIVE :

Diruthenium Mixed-Valence Complexes With A Variety of Nitrogen Donor Bridges

5 Diruthenium Complexes With A Variety of Nitrogen Donor Bridges

Reported here is a spectroelectrochemical and electrochemical investigation of the mononuclear and binuclear ruthenium compounds shown in Figure 5.1. All accessible oxidation states will be studied.

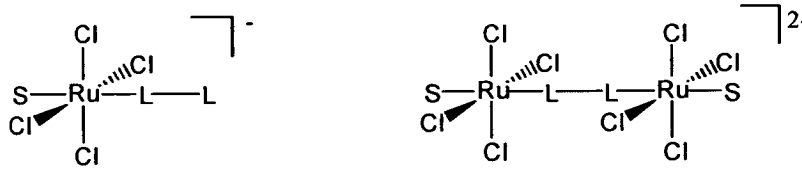

L-L =pyz, pym
S = S bound DMSO

L-L =pyz, pym, bipy, BPA, BPE
S = S bound DMSO

Figure 5.1 Ruthenium complexes to be studied.

5.1 Introduction

Symmetrical, molecule-bridged mixed-valence binuclear complexes have been the subject of much research since the discovery of the Creutz-Taube ion in 1969 (see Chapter 1.1.2).[9] The majority of this type of complex which have been studied to date involve the $M(NH_3)_5$ fragment bridged by a variety of organic ligands.[61,62] Other metal fragments which have been studied extensively are the $M(CN)_5$ and M(polypyridyl) moieties.

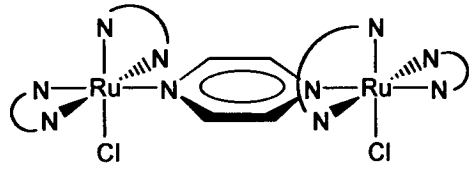

N-N = 2, 2' bipyridine

Figure 5.2 Representation of *cis*-$[\{Ru(bipy)_2Cl\}_2(\mu\text{-pyz})]^{n+}$.

The M(polypyridyl) moieties were investigated to study the effect of replacing the neutral and exclusively σ-donating ammine ligands (which permit a high degree of $d\pi \rightarrow \pi^*$ (pyz) back-bonding) with π-accepting polypyridyl units (such as bipy or py) which can compete for electron density from the metal centres. One of the first

polypyridyl complexes investigated was the complex *cis*-$[\{Ru(bipy)_2Cl\}_2(\mu\text{-pyz})]^{n+}$ (n = 2, 3 or 4) by Meyer and co-workers[63] shown in Figure 5.2. The electrochemistry of the n = 2 species showed two reversible one-electron oxidation processes with a difference in half-wave potential of 120 mV (in acetonitrile). This corresponds to a comproportionation constant of $K_c = 10^2$ and indicates a valence localised (Class II) situation. The Creutz-Taube ion exhibits a difference in half-wave potential of 430 mV and hence a K_c value of $10^{7.3}$ (also in acetonitrile).[64] Thus the polypyridyl binuclear compound has decreased metal-metal communication compared to the Creutz-Taube ion.

A good diagnostic tool often used in these symmetrical complexes is IR spectroscopy. In the isovalent species (M^n, M^n and M^{n+1}, M^{n+1}) the complex will be symmetrical, hence the stretching band of the pyrazine ligand will not induce a change in dipole and thus this band will not be observed in the IR spectrum. On the other hand in the mixed-valence species, if there are discrete M^n and M^{n+1} sites, bond lengths etc will be different for each metal fragment. Thus the local symmetry of the complex will be lost and a strong pyrazine stretching mode will be observed in the IR spectrum at around 1600 cm^{-1}. Therefore, the electron must be localised on the IR time-scale. An IR spectral study of the complex *cis*-$[\{Ru(bipy)_2Cl\}_2(\mu\text{-pyz})]^{n+}$ showed a band at 1599 cm^{-1} only in the mixed-valence (3+) state. The IR spectrum of the mononuclear complex, $[(bipy)_2Ru(pyz)Cl]^+$ also shows this band (at 1589 cm^{-1}) as expected since here the pyrazine is bonded through one nitrogen and hence will be asymmetric.[65] The band present in the mixed-valence species and in the mononuclear complex occurs in the region of aromatic six-membered ring vibrations. Hence it is ascribed to the pyrazine ring vibration. Thus, IR spectroscopy can be instructive in determining the class of the mixed-valence compounds, and in this case indicates that the mixed-valence species is valence localised (Class II).

Near-IR spectroscopy of *cis*-$[\{Ru(bipy)_2Cl\}_2(\mu\text{-pyz})]^{n+}$ revealed a band at 1300 nm which was only present in the mixed-valence ion and displayed a solvent

dependence. Thus it was assigned to an intervalence charge transfer transition. Band analysis suggested that the mixed-valence electron was localised.

These experimental results all support the classification of this polypyridyl mixed-valence complex as Class II, thus, the mixed-valence complex can be formulated as $[(bipy)_2ClRu^{III}(pyz)Ru^{II}Cl(bipy)_2]^{3+}$. That is, on replacement of the ammine ligands by bipy, the amount of metal-metal communication is reduced. This may be due to the π-acceptor bipyridine ligands competing with the pyrazine ligand for the electron density on the metal centre. The Ru(II) centre will be stabilised by the additional π-accepting ligands, and the Ru(III) destabilised although the π-donor chloride ligand will favour the Ru(III) oxidation state. Thus the molecular orbital formed which enables metal-metal interaction, that is, the π-symmetry orbitals on the pyrazine and the dπ orbitals of ruthenium, will have a smaller contribution from the ruthenium metal centres in the bipy complexes compared to the Creutz-Taube ion. The mixed-valence state must then have a smaller metal-metal communication in the bipy compound.

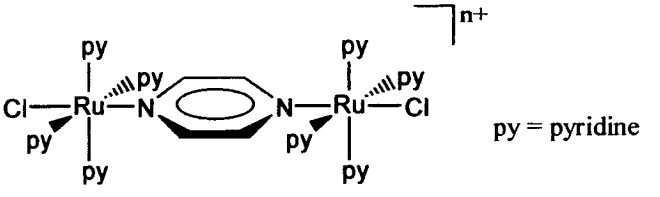

Figure 5.3 Structural representation of $[\{trans\text{-}RuCl(py)_4\}_2(\mu\text{-}pyz)]^{n+}$.

More recently, the complex $[\{trans\text{-}RuCl(py)_4\}_2(\mu\text{-}pyz)]^{2+}$ has been investigated.[66] A single crystal X-ray study confirmed the *trans* geometry about the ruthenium atoms and its structure is shown in Figure 5.3. The electrochemistry of this compound showed two reversible one-electron oxidations with a difference in the half-wave potentials of 280 mV (in acetonitrile). This corresponds to a comproportionation value, $K_c = 10^{4.7}$, a value intermediate between the Creutz-Taube ion and $[\{Ru(bipy)_2Cl\}_2(\mu\text{-}pyz)]^{3+}$.

Here it was stated that the terminal ligand which will have the greatest effect on the amount of metal-metal coupling will be the ligand which is *trans* to the pyrazine

bridge.[66] Although the $Ru(bipy)_2Cl$ and the $RuCl(py)_4$ fragments both contain a single chloride and pyridine based ligands, there is more communication permitted by the latter. This is attributed to the *trans* ligand in this fragment being a chloride which, as it is a strong σ-donor, π-donor ligand, permits a greater extent of $d\pi(Ru) \rightarrow \pi^*(pyz)$ back bonding than in the $Ru(bipy)_2Cl$ fragment, where the *trans* ligand is half of a π-accepting bipy, and as mentioned above, this will compete for back-bonding and hence the communication between the two metal centres will be reduced.

Another explanation is that the pyridine is a considerably weaker π-acceptor than bipy, hence less electron density will be withdrawn from the metal centre by four pyridine ligands than two bipy ligands. As a result the π-acceptor orbital of the bridging pyrazine ligand will have more metal character than that of the bipy complex. Therefore the metal-metal interaction in the compound with terminal pyridine ligands will be greater than in the complex with terminal bipy ligands.

The $M(CN)_5$ units were investigated to allow the effect of replacing ammine ligands by negatively charged and π-bonding cyanide ligands on the extent of metal-metal interaction to be studied. Recently the complex $[\{Os(CN)_5\}_2(\mu\text{-pyz})]^{n-}$ (n = 4, 5, 6) has been investigated[67] and compared to the Creutz-Taube ion and its osmium analogue (both of which are considered to be Class III compounds). The electrochemistry of the n = 6 species (in acetonitrile) showed two reversible one-electron oxidations with a half-wave potential difference of 340 mV. This corresponds to a comproportionation constant of $K_c = 10^{5.8}$ which is slightly lower than the value of $10^{7.3}$ reported for the Creutz-Taube ion in acetonitrile[64] and considerably smaller than the value of $10^{13.0}$ (determined in hydrochloric acid) which was reported for the osmium analogue of the Creutz-Taube ion.[68] However, it is larger than the value of $K_c = 50$ for the iron analogue, $[\{Fe(CN)_5\}_2(\mu\text{-pyz})]^{5-}$ (in aqueous solution)[69] which is typical of a Class II mixed-valence compound.

When the electrochemistry of the binuclear complex, $[\{Os(CN)_5\}_2(\mu\text{-pyz})]^{n-}$ is compared with that of the mononuclear $[Os(CN)_5(pyz)]^{3-/2-}$ species, the two redox potentials were found to lie at lower and higher potentials than the mononuclear value. This was also observed in the Creutz-Taube ion and its osmium analogue. In the electronic spectrum of $[\{Os(CN)_5\}_2(\mu\text{-pyz})]^{6-}$, the MLCT bands observed were found to be solvatochromic, and were found to vary linearly with the acceptor number (AN; Gutmann scale).[67] This was also the case for the mononuclear complex, $[Os(CN)_5pyz]^{3-}$.[70] On the other hand, for the complexes, $[M(NH_3)_5L]^{n+}$ (M = Ru, Os) the energy of the charge transfer bands correlate with donor number (DN).

Gutmann's scale[71] measures the electron-pair-donor ability or 'donicity' of a solvent relative to 1,2-dichloroethane. During an investigation into a series of ruthenium-polypyridyl-ammine complexes it was suggested that the solvent effect appears to arise from a hydrogen-bonding type of interaction involving electron pair donation from a solvent molecule (or molecules) to the NH bond.[52] The net effect of this 'H-bonding' between the solvent and the ammine proton will be an increase in the electron density of the metal centre. As a result, a MLCT transition should move to lower energy as DN increases, and a LMCT transition should move to higher energy. This was indeed found for $[Ru(NH_3)_5(py)]^{2+}$ where the changes in band maxima could not be correlated with intrinsic solvent properties such as $1/D_{op}$, $1/D_s$, or $1/D_{op}$-$1/D_s$. Also investigated was the complex $[Ru(bipy)_3]^{2+}$ where the changes in band position in varying solvents was negligible (compared to the ammine complexes). This will be due to there being no sites for specific interaction available on the periphery of this ligand. As the number of ammine ligands in the series was increased, the sensitivity of the band position on DN also increases.

Generally, in complexes where the periphery of the terminal ligands are capable of 'H-bonding' or accepting electron density the band maxima of the CT bands should correlate with DN. In complexes with ligands which are capable of donating electron density (lone-pairs *e.g.* Cl^-, CN^-) the CT bands should correlate with AN. In the complex discussed above, $[\{Os(CN)_5\}_2(\mu\text{-pyz})]^{n-}$, as expected the band position

correlates with AN, illustrating the important role of the 10 lone-pair containing cyanide ligands on the overall interaction of the complex with the solvent.

Upon one electron oxidation to the mixed-valence (5-) species, an intervalence transition is observed which disappears on further oxidation to the 4- species. The near-IR region of osmium(III/II) mixed-valence complexes is generally dominated by spin-orbit coupling transitions and for this reason the spectrum obtained is compared to the spectrum of the osmium analogue of the Creutz-Taube ion. The bands were all similar but appreciably lower in energy in the decacyano case.

The IR spectrum of $[\{Os(CN)_5\}_2(\mu\text{-pyz})]^{5-}$ showed a sharp strong band at 1582 cm^{-1} which is unique to the mixed-valence species (this is the region of aromatic six-membered ring vibrations). Thus, the band is attributed to a pyrazine ring vibration. Therefore, on the time-scale of vibrational spectroscopy, the complex can be described as $[(CN)_5Os^{III}(pyz)Os^{II}(CN)_5]^{5-}$.

In summary, the complex $[\{Os(CN)_5\}_2(\mu\text{-pyz})]^{5-}$ and the Creutz-Taube ion, if judged solely on the IVCT bandwidths and the K_c values, could be described as delocalised compounds. However, when the IR spectra were compared the Creutz-Taube ion shows averaged metal-ligand vibrations,[72] whereas this is not the case for $[\{Os(CN)_5\}_2(\mu\text{-pyz})]^{5-}$. Thus, there is reduced metal-metal interaction in the latter compound. This is attributed to the π-accepting effect of the cyanide ligands. The cyanide ligand will reduce the amount of electron density on the metal centre and thus decrease the metal-pyrazine interaction.

On comparison of this osmium complex with the iron analogue, the complex containing osmium metal centres shows an increased amount of metal-metal interaction (on the basis of the K_c values). However this comparison may be misleading. The osmium complex was studied in acetonitrile and the iron complex in an aqueous solution. Water has a much higher AN (54.8) compared to acetonitrile (18.9).[73] As a result, in water, the π-acceptor character of the cyanide ligands

(competitive with pyrazine) will be enhanced. Hence, the metal centre will be more deficient in electron density and the M-pyz-M interaction will be disfavoured and therefore there will be a lower degree of metal-metal communication. This report has highlighted that in addition to 'internal' factors, such as metal type and auxiliary ligands, second-sphere interactions can be important in influencing the electronic structure of mixed-valence compounds.

The examples given in this introduction highlight the complexity of the investigation of mixed-valence complexes and the factors which affect the degree of electronic communication between the two metal centres. The complexes to be investigated in this chapter involve the replacement of the ammine ligands in the Creutz-Taube ion by strong σ-donor, π-donor chloride ligands to assess the effect this has on the amount of delocalisation in the mixed-valence complex. The *trans* ligand in this case is a DMSO molecule bound through the sulfur atom. In addition, the bridging ligand has been varied to study the effect this has on metal-metal communication.

5.2 Experimental

5.2.1 Chemical Synthesis

These compounds were synthesised by the group of Dr Enzo Alessio in the chemistry department of the Universita' Degli Studi Di Trieste.

5.2.2 Electrochemistry

All complexes were studied using the techniques outlined in chapter 2. Following the electrochemical analysis of these compounds ferrocene was added to the solution as an internal standard. All half-wave potentials are therefore referenced against the ferrocinium/ferrocene couple at +0.55 V.

5.2.3 *Insitu* UV/Vis Spectroelectrochemistry

The compound being analysed (Table 5.1) was made up to 2 cm^3 in a volumetric flask using a solution of $[N^nBu_4][BF_4]$ in the required solvent which had been degassed with argon. This solution was also degassed. The cell was then filled and assembled and placed in the cavity of the UV/Vis spectrophotometer. The temperature was reduced to the required level and the potential set to a value that induced reduction or oxidation. During this process spectra were recorded every 5 minutes.

Table 5.1 Experimental details of the UV/Vis spectroelectrochemical experiments performed.

Compound	Amount / mg	Concentration / M	Concentration of $[N^nBu_4][BF_4]$ / solvent	Temperature / K
$Na[RuCl_4(DMSO)pyz]$	3.8	3.28×10^{-3}	0.1 M / DMF	224
$Na[RuCl_4(DMSO)pym]$	4.7	4.05×10^{-3}	0.1 M / DMF	232
$[N^nBu_4][RuCl_4(DMSO)bipy]$	4.7	3.26×10^{-3}	0.1 M / DMF	223
$Na_2[\{(DMSO)Cl_4Ru\}_2(\mu\text{-pyz})]$	4.1	2.01×10^{-3}	0.1 M / DMF	224
$[N^nBu_4]_2[\{(DMSO)Cl_4Ru\}_2(\mu\text{-pyz})]$	2.3	9.5×10^{-4}	0.4 M / DCM	217

$[N^nBu_4]_2[\{(DMSO)Cl_4Ru\}_2(\mu\text{-pyz})]$	2.1	8.7×10^{-4}	0.1 M / DMF	217
$[N^nBu_4]_2[\{(DMSO)Cl_4Ru\}_2(\mu\text{-pyz})]$	2.8	1.12×10^{-3}	0.5 M / chloroform	217
$[N^nBu_4]_2[\{(DMSO)Cl_4Ru\}_2(\mu\text{-pyz})]$	2.8	1.12×10^{-3}	0.2 M / proprionitrile	217
$[N^nBu_4]_2[\{(DMSO)Cl_4Ru\}_2(\mu\text{-pyz})]$	6.5	2.69×10^{-3}	0.1 M / acetonitrile	220
$[N^nBu_4]_2[\{(DMSO)Cl_4Ru\}_2(\mu\text{-pyz})]$	5.1	2.11×10^{-3}	0.1 M / pyridine	228
$[N^nBu_4]_2[\{(DMSO)Cl_4Ru\}_2(\mu\text{-pyz})]$	5.5	2.69×10^{-3}	0.1 M / benzonitrile	248
$[N^nBu_4]_2[\{(DMSO)Cl_4Ru\}_2(\mu\text{-pyz})]$	24.5	1.015×10^{-2}	0.2 M / proprionitrile	217
$Na_2[\{(DMSO)Cl_4Ru\}_2(\mu\text{-pym})]$	2.0	9.8×10^{-4}	0.1 M / DMF	220
$Na_2[\{(DMSO)Cl_4Ru\}_2(\mu\text{-bipy})]$	4.6	2.10×10^{-3}	0.1 M / DMF	217
$Na_2[\{(DMSO)Cl_4Ru\}_2(\mu\text{-BPA})]$	4.5	2.00×10^{-3}	0.1 M / DMF	217
$Na_2[\{(DMSO)Cl_4Ru\}_2(\mu\text{-BPE})]$	4.3	1.91×10^{-3}	0.1 M / DMF	217

5.2.4 *Exsitu* UV/Vis Spectroelectrochemistry of $Na_2[\{(DMSO)Cl_4Ru\}_2(\mu\text{-pyz})]$

An H-cell was set up using a 0.1 M solution of $[N^nBu_4][BF_4]$ in DMF and bubbled with argon. To this $Na_2[\{(DMSO)Cl_4Ru\}_2(\mu\text{-pyz})]$ (11.1 mg; 1.09×10^{-5} mol) was added. The whole cell was immersed in a dry ice/acetone bath and cooled to 223 K. The solution was then electrogenerated at a potential sufficient to induce reduction (-0.75 V) or re-oxidation (+0.5 V) and samples were taken using a gas tight syringe roughly every 0.2 coulombs. The spectrum of each sample was recorded as quickly as possible.

5.3 Results and Discussion

5.3.1 $[RuCl_4(DMSO)pyz]^{n-}$ (n = 1, 2)

The cyclic voltammogram of $Na[RuCl_4(DMSO)pyz]$ in DMF is shown in Figure 5.4. This shows a one-electron reduction. Bulk electrolysis confirmed the number of electrons involved in this step. The half-wave potential of this reduction was measured to be –0.22 V. The electron-transfer process displays a linear relationship between i_p and $\nu^{½}$ indicating this process is electrochemically reversible. The ratio of peak currents (i_{pc}/i_{pa}) in DMF at 100 mVs^{-1} was found to be 0.97 indicating that this reduction is fully chemically reversible.

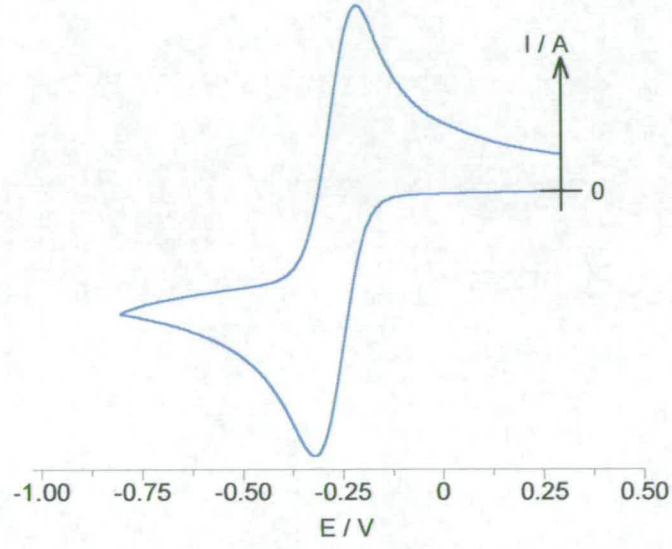

Figure 5.4 Cyclic voltammogram of $[RuCl_4(DMSO)pyz]^-$ in 0.1 M $[N^nBu_4][BF_4]$ / DMF at 298 K.

When the cyclic voltammetry was recorded at slower scan rates, the process became less chemically reversible and a shoulder could be seen on the positive potential side of the re-oxidation peak. Two irreversible oxidations are also observed, one at approximately +1.2 V and the other at +1.52 V. The oxidation at +1.2 V is very distended while the peak at +1.52 V is more defined. The peak at higher potential has been assigned to the Ru(III/IV) couple, but appears on the solvent background and so further analysis could not be undertaken to substantiate this claim.

The electrochemistry of this complex was also investigated in DMSO. Again a fully reversible (linear relationship between i_p and $\nu^{½}$; ratio of peak currents of 0.92), one-electron reduction was observed. The $E_{½}$ was calculated to be –0.204 V, making it 14 mV more positive than that in DMF.

Since the reduced species seemed relatively reactive (as shown by the peak current ratios at slow scan rates) the coulometry of this compound was carried out at a reduced temperature of 233 K in an attempt to suppress the chemical reaction following electron-transfer. On complete reduction of the compound a cyclic voltammogram was run to investigate the species which had formed. This cyclic voltammogram is shown in Figure 5.5. The main peak is due to the oxidation of the $[RuCl_4(DMSO)pyz]^{2-}$ species, however, a new reversible couple has appeared, albeit very small. The estimated half-wave potential of this new species is +0.048V. This is probably the same species that gave the shoulder observed in the cyclic voltammogram at slow scan rates.

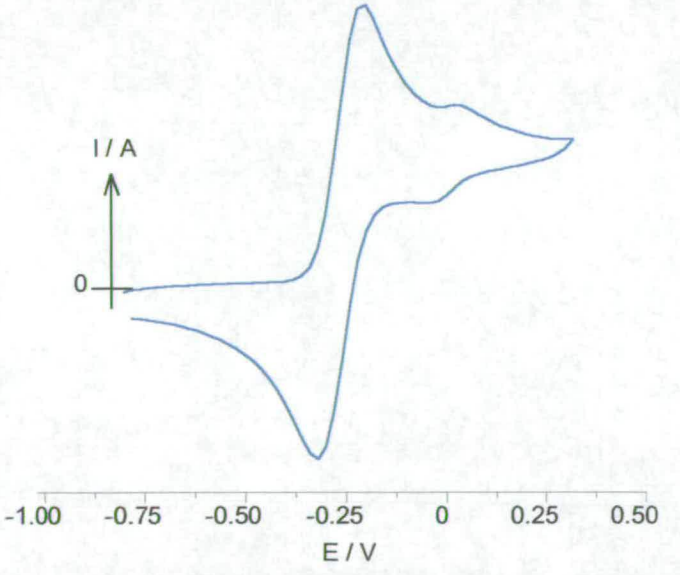

Figure 5.5 Cyclic voltammogram of $[RuCl_4(DMSO)pyz]^{2-}$ in 0.1 M $[N^nBu_4][BF_4]$ / DMF at 233 K.

Compounds very similar to this have been investigated previously.[74,75] The compound *trans*- $[Ru(DMSO)_2Cl_4]^-$ has recently been structurally characterised[74] following its synthesis in 1976.[76] The IR spectrum of this complex showed only one

SO stretching band at 1115 cm^{-1} suggesting a *trans* configuration. X-ray crystal structure analysis confirmed the *trans* geometry and also showed that the DMSO moieties are bound to the ruthenium centre through the sulfur atom.

The electrochemistry of this compound was reported separately.[75] In DMSO solution, the cyclic voltammogram showed a quasi-reversible one-electron reduction at –0.182 mV (referenced to the SCE electrode). In aqueous solutions on the other hand, the cyclic voltammetry was more complex. This was attributed to the loss of one of the S-bound DMSO moieties and its replacement with a water ligand immediately upon dissolution. This was confirmed by IR and NMR spectroscopy.[74] At slow scan rates (100 mVs^{-1}), a single reduction peak (due to the monoaquo complex) but two re-oxidation peaks are observed, the one at lower potential being the counterpart of the monoaquo species and the other was assigned as the oxidation of the bis-DMSO dianion. It is thought that on reduction, the monoaquo species is (partially) equilibrating with the free DMSO in solution.

If the monoaquo complex, $[RuCl_4(DMSO)(OH_2)]^-$ is left in solution, slow dissociation of a chloride ligand and replacement by a solvent molecule is observed. This reaction was confirmed by NMR studies, and was also found to take place for $[RuCl_4(DMSO)_2]^-$ in DMSO and methanol solutions.[74]

Also reported was the complex *trans*-$[RuCl_4(DMSO)(py)]^-$.[74] Hydrolysis of this complex is considerably slower compared to that discussed above, allowing its electrochemistry to be performed in water. This shows a reversible one electron reduction, the half-wave potential of which was found to be +0.065 V.

These highlight the considerations that were taken in trying to determine the nature of the electroactive species and its daughter product. Is the species in solution the same as the assigned solid state structure or is a DMSO ligand being replaced by the electrochemical solvent?

Following the investigation of the mononuclear complex with pyrimidine (see later) and since hydrolysis of the complex *trans*-[$RuCl_4$(DMSO)(py)]$^-$ was not significant, it was decided that on dissolution, no ligand replacement occurs. Thus the species in solution is [$RuCl_4$(DMSO)pyz]$^-$. This is in agreement with the minimal shift in Ru(III)/Ru(II) half-wave potential in DMF and DMSO.

The new electroactive species formed following the coulometry is thought to be due to the replacement of the DMSO ligand by a solvent molecule, in this case, DMF. The replacement of a chloride ligand by the solvent was ruled out as this would result in a much larger potential shift than that observed. The replacement of the pyrazine ligand is also excluded since the UV/Vis spectrum of the reduced complex shows a Ru $t_{2g}^6 \rightarrow \pi^*$(pyz) MLCT band.

This idea is supported by the electrochemistry of the complex in DMSO. As stated above, the cyclic voltammogram in DMF at slow scan rates shows a shoulder (due to the DMF species) on the positive potential side of the re-oxidation peak for the original complex. The cyclic voltammogram in DMSO does not show this phenomenon, even if the potential of the working electrode is held constant following the reduction for a few minutes and then the potential switched to investigate the anodic region, no daughter peak in this region is formed. Assuming the assignment of the daughter peak is correct, no daughter peak is expected to be formed when DMSO is used as the solvent. On extending the scan to a more anodic potential a reversible daughter peak was observed at a much higher potential (approx. +0.69 V). This daughter product will in all likelihood be due to the loss of chloride, which can be replaced by the solvent. In order to prove this conclusively the coulometry should be performed in DMSO, however, due to lack of sample this could not be carried out, it does however seem the most likely explanation. Furthermore, it seems that the DMSO ligand is more labile when bound to Ru(II) than to Ru(III).

This complex was also investigated using UV/Vis spectroelectrochemistry. The experiment was run at a reduced temperature to prevent the ligand substitution

reaction taking place on reduction of the compound. The spectra produced during this experiment are shown in Figure 5.6. The spectrum of the monoanion (formally containing a Ru(III) centre) is dominated by an intense band at 24050 cm^{-1} (ε = 7200 M^{-1} cm^{-1}) which is confidently assigned as a ligand to metal charge transfer transition, namely $Cl^- \rightarrow Ru\ t_{2g}^5$ (blue line). The much weaker band centred at 20650 cm^{-1} (ε = 600 M^{-1} cm^{-1}) is assigned as a d-d transition. On reduction of this complex the LMCT band collapses and a new band grows in at lower energy. This band in the spectrum of the Ru(II) complex (dark yellow line) cannot be assigned as a LMCT transition as the ruthenium centre now has a d^6 configuration. It is in fact assigned as a metal to ligand charge transfer transition from the Ru t_{2g} orbitals to the antibonding π^* orbital of the pyrazine ligand. An isosbestic point is observed at 23500 cm^{-1}, indicating that the conversion of the monoanion to the dianion is clean, that is, no DMSO-solvent exchange has occurred. Reversal of the applied potential to +0.50 V results in the complete regeneration of the starting spectrum.

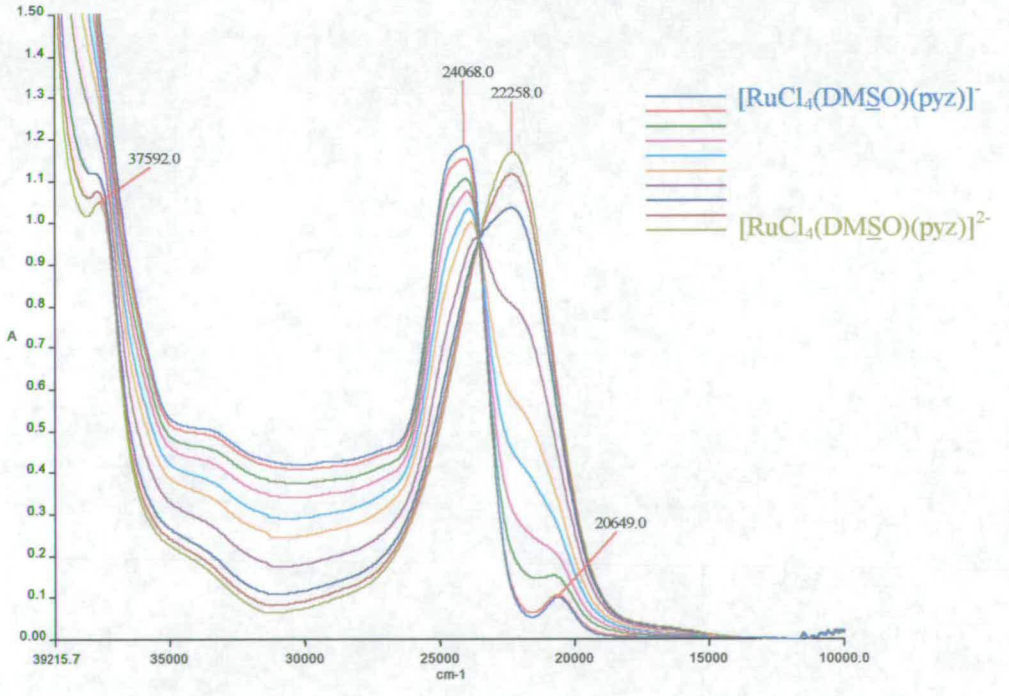

Figure 5.6 UV/Vis spectroelectrochemistry of Na[$RuCl_4$(DMSO)(pyz)] in 0.1 M [N^nBu_4][BF_4] / DMF at 224 K. E_{app} = –0.75 V.

From these results it can be concluded that the compound Na[$RuCl_4$(DMSO)(pyz)] undergoes an electrochemically reversible one-electron reduction, the half-wave

potential of which appears to be slightly solvent dependent. Upon bulk electrolysis to produce the Ru(II) species, the complex seems to become susceptible to attack by the solvent and it is thought that the DMSO is displaced by a solvent molecule. This chemical reaction can be suppressed at low temperatures as highlighted by the isosbestic point observed during the UV/Vis spectroelectrochemical experiment.

5.3.2 $[RuCl_4(DM\underline{S}O)(pym)]^{n-}$ (n = 1, 2)

The compound $Na[RuCl_4(DM\underline{S}O)(pym)]$ was investigated using cyclic voltammetry. It showed a fully reversible one-electron reduction (linear relationship between i_p and $v^{½}$; ratio of peak currents of 0.96). The electrochemistry was performed in DMF ($E_{½}$ = -0.255 V) and DMSO ($E_{½}$ = -0.215 V) showing a dependence of the half-wave potential on the electrochemical medium. Note the potentials are measured against the ferrocinium/ferrocene couple following the addition of ferrocene to the solution once the analysis was complete. In DMF at slow scan rates the process became less chemically reversible and a shoulder could be seen on the positive potential side of the re-oxidation peak as found for the pyrazine complex. The cyclic voltammogram in DMSO is shown in Figure 5.7. The potential was held following the reduction for three minutes then the anodic region was investigated. This shows a reversible daughter product with a half-wave potential of +0.725 V, which is associated with the reduction.

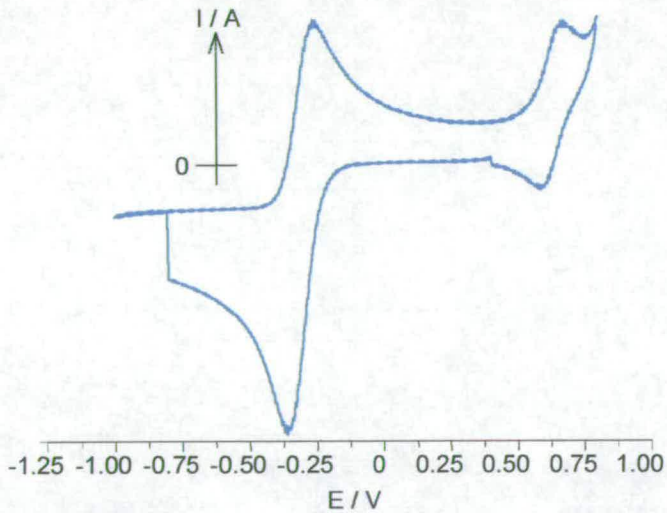

Figure 5.7 Cyclic voltammogram of $[RuCl_4(DM\underline{S}O)(pym)]^-$ in 0.1 M $[N^nBu_4][BF_4]$ /DMSO at 297 K where the potential was held at –0.8V for three minutes.

The most plausible reason for the dependence of the half-wave potential of the pyrazine and pyrimidine mononuclear complexes on the medium it is investigated in, is the nature of the counter ion. Due to the small sodium counterion, the complexes are only soluble in highly polar solvents. It is thought that on dissolution, the small

positively charged sodium ion is difficult to solvate and thus is remaining partially associated with the complex. The degree of association varies in the different solvents, thus the electrochemical properties are altered.

The bulk electrolysis of the pyrimidine compound was carried out in DMF at a reduced temperature of –40 °C. This confirmed the number of electrons involved in the reduction step. As also seen for the pyrazine complex, on reduction (even at the reduced temperature) a new electroactive species seems to be forming which shows a reversible oxidation at a more positive potential than that of the original complex. This is shown as the blue trace in Figure 5.8. The complex was then left in its reduced form to determine whether this new complex would form exclusively. After 4hrs (the temperature was not kept constant) the cyclic voltammogram shown in red in Figure 5.8 was recorded. The half-wave potential of this new species, thought to be $[RuCl_4(DMF)(pym)]^{2-}$, is +0.038 V (corrected to ferrocene at +0.55 V).

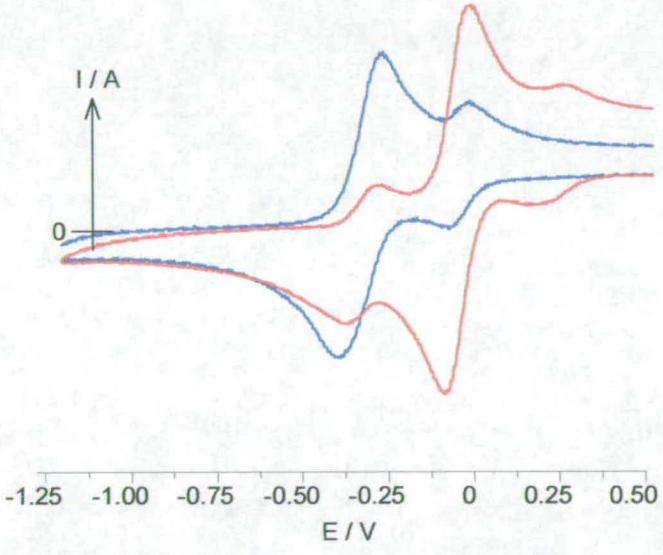

Figure 5.8 Cyclic voltammogram of $[RuCl_4(DMSO)(pym)]^{2-}$ in 0.1 M $[N^nBu_4][BF_4]$ /DMF at 233 K immediately following reduction – blue trace, and at 277 K after 4hrs – red trace.

The assignment of this daughter product is supported by the electrochemistry in DMSO. The half-wave potential of the daughter product observed in DMSO is much more positive than that observed in DMF (similar to the result with the pyrazine species). In DMF the daughter product is thought to be due to the substitution of the

weakly bound DMSO with a solvent molecule. Since this solvent replacement cannot take place in DMSO and considering the half-wave potential of the new species is at a much higher potential, (the separation between this and the half-wave potential of $[RuCl_4(DMSO)(pym)]^-$ is 950 mV), the daughter product here is thought to be due to the loss of chloride, which will be replaced by solvent molecules. Also, the further redox process at +0.31 V is also thought to be due to the replacement of chlorine by solvent.

In order to confirm that upon dissolution the complex remains intact *i.e.* none of the ligands are replaced by solvent molecules, the complex was dissolved in acetonitrile and allowed to stir for a few hours at room temperature. The solvent was then removed *in vacuo* and the solid formed was investigated using IR spectroscopy. If indeed the DMSO ligand had been replaced by an acetonitrile molecule, no SO stretch of bound DMSO would be observed. The SO region of the IR spectra of the compound initially and then after dissolution are shown in Figure 5.9. Since the initial spectrum and the spectrum after dissolution have similar band intensities and positions, it can be assumed that no replacement of a DMSO moiety occurs upon dissolution.

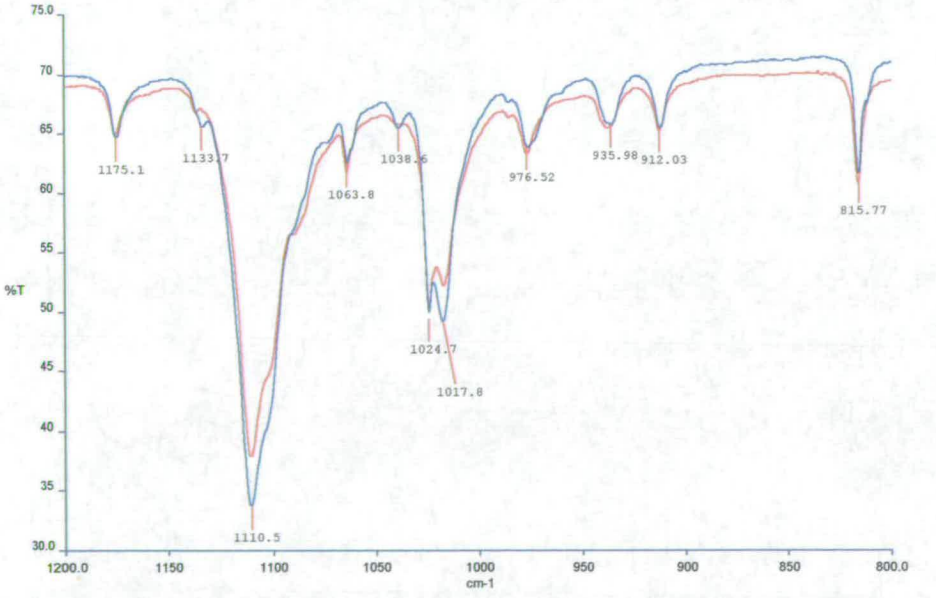

Figure 5.9 IR spectra, recorded as a KBr disc, of $[RuCl_4(DMSO)(pym)]^-$ (blue) and solid recovered following the dissolution of $[RuCl_4(DMSO)(pym)]^-$ in acetonitrile (red).

An absorption due to a sulfur bound DMSO unit appears at approx. 1100 cm^{-1}, an O bound DMSO unit at approx. 910 cm^{-1} and a free DMSO molecule at approx. 1015 cm^{-1}. Thus from these spectra it is clear that in this compound the DMSO unit is bound through the sulfur atom. Also observed in the IR spectrum is a strong peak at 1593 cm^{-1} which is attributed to the pyrimidine ring stretching vibration.

The UV/Vis spectroelectrochemistry of this compound was investigated. The experiment was run at a reduced temperature to prevent the ligand substitution reaction occurring on reduction of the compound. The spectra produced during this experiment are shown in Figure 5.10. The spectrum of the monoanion (formally containing a Ru(III) centre) is dominated by an intense band at 24200 cm^{-1} (ε = 6550 M^{-1} cm^{-1}) which is confidently assigned as a ligand to metal charge transfer transition, namely $Cl^- \rightarrow Ru\ t_{2g}^5$ (blue line). The much weaker band centred at 20750 cm^{-1} (ε = 500 M^{-1} cm^{-1}) is assigned as a d-d transition.

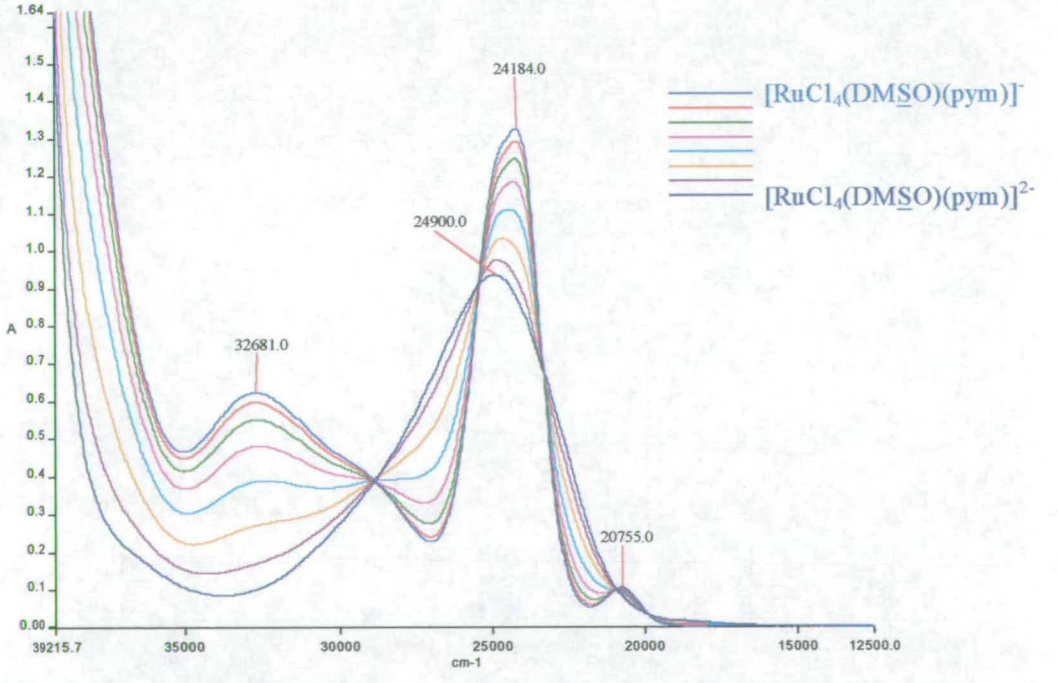

Figure 5.10 UV/Vis spectroelectrochemistry of Na[$RuCl_4$(DMSO)(pym)] in 0.1 M [N^nBu_4][BF_4] / DMF at 232 K. E_{app} = -0.75 V.

On reduction of this complex at –0.75 V the LMCT band collapses and a new band grows in at slightly higher energy (24900 cm^{-1}; ε = 4600 M^{-1} cm^{-1}). In a similar

argument to the pyrazine complex, the band in the spectrum of the Ru(II) complex (dark blue line) cannot be assigned as a LMCT transition since the ruthenium centre now has a d^6 configuration. Instead it is assigned as a metal to ligand charge transfer transition from the Ru t_{2g} orbitals to the antibonding π^* orbital of the pyrimidine ligand. Five isosbestic points at 28900, 25350, 23300, 20950, and 19900 cm^{-1} are observed, indicating that the conversion of the monoanion to the dianion is clean, thus no DMSO-solvent exchange has occurred.

From these results it can be concluded that the compound $Na[RuCl_4(DMSO)(pym)]$ undergoes an electrochemically reversible one-electron reduction, the half-wave potential of which appears to be solvent dependent. This solvent dependence is thought to be caused by the poor solvation of the Na counterion. IR spectroscopy has shown that upon dissolution no immediate ligand exchange occurs, thus in solution the species remains intact. Upon bulk electrolysis to produce the Ru(II) species, the complex seems to become susceptible to attack by the solvent and it is thought that the DMSO is displaced by a solvent molecule. The electrochemical investigation in DMSO showed that upon reduction the complex is also susceptible to loss of chloride. These chemical reactions can be suppressed at low temperatures as highlighted by the isosbestic points observed during the UV/Vis spectroelectrochemical experiment.

5.3.3 $[RuCl_4(DM\underline{S}O)(bipy)]^{n-}$ (n = 1, 2)

The compound TBA[$RuCl_4$(DM<u>S</u>O)(bipy)] was investigated using cyclic voltammetry. In DMF (see Figure 5.11) it shows a quasi-reversible one-electron reduction. A linear relationship between i_p and $\nu^{1/2}$ is observed at scan rates of 0.1 Vs^{-1} or above thus the process is considered electrochemically reversible. The ratio of peak currents was found to be 0.48, indicating that this process is highly chemically irreversible. The half-wave potential of the reduction attributed to $[RuCl_4(DM\underline{S}O)(bipy)]^-$ was measured to be –0.41 V.

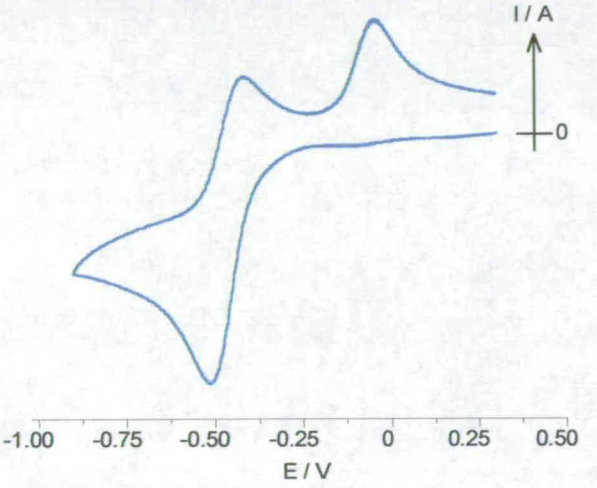

Figure 5.11 Cyclic voltammogram of $[RuCl_4(DM\underline{S}O)(bipy)]^-$ in 0.1 M $[N^nBu_4][BF_4]$ / DMF at 292 K.

As found for L = pyz and pym, the daughter peak is thought to be due to the replacement of the DMSO ligand by a solvent molecule upon reduction, by running two consecutive scans a return peak for the oxidation of $[RuCl_4(DMF)(bipy)]^{2-}$ could be observed, the half-wave potential of this couple was found to be –0.025 V. The couple for $[RuCl_4(DM\underline{S}O)(bipy)]^{-/2-}$ became more reversible as the scan rate was increased and at 0.8 Vs^{-1} was fully reversible. On cooling this couple also became more reversible and at 258 K with a scan rate of 0.1 Vs^{-1} it was fully reversible.

The counterion in this case is TBA, therefore the complex can now be studied in DCM (a non-coordinating solvent) where it shows a quasi-reversible one-electron reduction. A linear relationship between i_p and $\nu^{1/2}$ is observed at scan rates of 0.1

Vs^{-1} or above and indicates that the process is electrochemically reversible. The ratio of peak currents was found to be 0.79, indicating a level of chemical irreversibility of this process. The half-wave potential of this reduction was measured to be –0.28 V. No daughter peak was observed in dichloromethane.

Due to the non-coordinating nature of dichloromethane, it can be assumed that upon dissolution the complex will remain intact. It seems that in the reduced form the complex is unstable (hence the low peak current ratio, this was also found for the previous complexes at slow scan rates). Since no ligand substitution reaction can occur (in the reduced species) to produce a more stable compound, the compound must decompose to species which are not electroactive (at least in the solvent / electrolyte window).

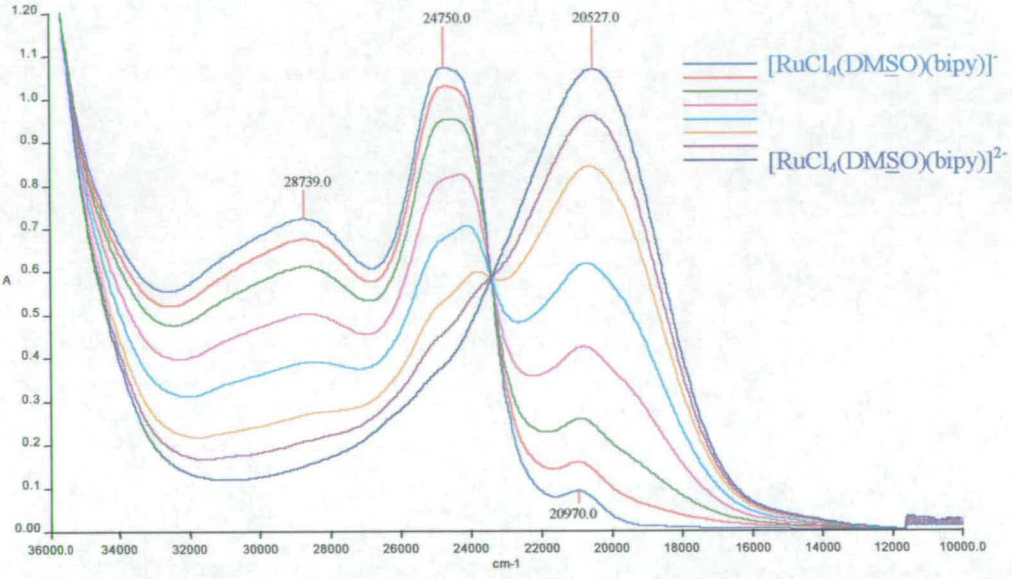

Figure 5.12 UV/Vis spectroelectrochemistry of $[N^nBu_4][RuCl_4(DMSO)(bipy)]$ in 0.1 M $[N^nBu_4][BF_4]$ / DMF at 223 K. E_{app} = -0.50 V.

This complex was also investigated using UV/Vis spectroelectrochemistry and the spectra recorded are shown in Figure 5.12. As with the previous mononuclear complexes, the spectrum of the monoanion (formally containing a Ru(III) centre) is dominated by an intense band at 24750 cm^{-1} (ε = 6550 M^{-1} cm^{-1}) which is assigned as a ligand to metal charge transfer transition, namely $Cl^- \rightarrow Ru\ t_{2g}^5$ (blue line). The

much weaker band centred at 20950 cm^{-1} (ε = 550 M^{-1} cm^{-1}) is assigned as a d-d transition.

On reduction of this complex the LMCT band collapses and a new band grows in at lower energy (20550 cm^{-1}; ε = 6550 M^{-1} cm^{-1}). In a similar fashion to the other mononuclear complexes, the band in the spectrum of the Ru(II) complex (dark blue line) cannot be assigned as a LMCT transition and is instead assigned as a metal to ligand charge transfer transition from the Ru t_{2g} orbitals to the antibonding π^* orbital of the bipyridine ligand. A single isosbestic point at 23400 cm^{-1} is observed which indicates that the conversion of the monoanion to the dianion is clean, that is, no DMSO-solvent exchange has occurred.

Thus it can be concluded from these results that the compound $[N^nBu_4]$ $[RuCl_4(DMSO)(bipy)]$ undergoes an quasi-reversible one-electron reduction, that is, the process is electrochemically reversible but partially chemically irreversible (due to a ligand exchange reaction (DMF for DMSO) which occurs upon reduction in a coordinating solvent). The Ru(III)/Ru(II) couple could be made completely reversible at fast scan rates (less time for the species to react) and also at low temperatures (suppresses the rate of chemical reaction following reduction). The half-wave potential of this complex appears to be solvent dependent, which is likely to be due to an interaction between the solvent and the complex since the TBA counterion is expected to be significantly less associated with the complex than its sodium counterpart. The chloride ligands have lone pairs which are available for donation to the solvent molecules, thus the half-wave potentials are expected to correlate with Gutmanns acceptor number of the solvent. DCM (AN = 20.4) has a higher acceptor number than DMF (AN = 16.0), thus the metal centre in DCM will be more electron deficient and as a result the half-wave potential for the reduction will be more positive. Indeed, the half-wave potential was found to be more positive in DCM than in DMF.

From the investigation of the previous mononuclear complexes, it is thought that upon reduction a ligand substitution reaction can occur where a solvent molecule replaces the weakly bound DMSO ligand. This is supported by the electrochemical results. In DMF, the Ru(III)/Ru(II) couple is almost completely irreversible and shows a daughter product. Whereas, in DCM, the couple is largely reversible, as expected since DCM cannot coordinate, thus no ligand exchange can occur. The chemical reaction, which follows reduction, can be suppressed at low temperatures as highlighted by the isosbestic points observed during the UV/Vis spectroelectrochemical experiment.

5.3.4 Comparison of [$RuCl_4$(DMSO)(L)], L = pyz, pym, bipy

The half-wave potentials of the L = pyz, pym and bipy species (in DMF) are –0.218, –0.257, and –0.412 V respectively. Since it is thought that the counter ion is having an effect on the electrochemistry, the complex with bipy is not comparable to the others, hence only those with pyrazine and pyrimidine will be compared.

The pyrazine complex is the most easily reduced. This indicates that the amount of electron density on the ruthenium centre here is less than the ruthenium centre in $[RuCl_4(DMSO)pym]^{-1}$. This may be due to two factors; (i) pyrazine is a poorer σ-donor than pyrimidine and/or (ii) pyrazine is a better π-acceptor than pyrimidine. The two ligands were modelled using the molecular modelling program CAChe 3.2, which allowed an electron density calculation to be performed. The amount of electron density on the nitrogen of pyrazine was 5.04 compared to 5.12 for the pyrimidine nitrogen. This would imply that since there is more electron density on the donating atoms of pyrimidine that this ligand will be a stronger σ-donor. On comparison of the pK_a for these ligands, this result is substantiated. The pK_a for pyrazine (0.6) is lower than the pK_a of pyrimidine (1.3). Thus, pyrimidine is a better base, and as such will be a better σ-donor than pyrazine.

The small shift in absorption band maxima in the Ru(III) containing complexes with the various ligands (100-700 cm^{-1}) is further evidence that this band can be assigned to a LMCT transition involving the chloride ligands, namely $Cl^- \rightarrow Ru\ t_{2g}^5$. Additionally, the electrochemistry states that the complex with pyrazine is easier to reduce than with pyrimidine, that is, there is less electron density on the ruthenium centre which is bound to the pyrazine. This will result in an easier (lower energy) LMCT in this case, which is as observed (24050 cm^{-1} for pyz and 24200 cm^{-1} for pym).

The dramatic shift in absorption band maxima observed for the lowest energy band in the Ru(II) containing compounds (1700-4350 cm^{-1}) confirms that this peak is

correctly assigned as a Ru $d\pi \rightarrow \pi^*$ (pyz, pym or bipy) MLCT transition. In the Ru(II) species π-effects are thought to be more significant due to the increased electron density of the metal centre. Bipyridine is expected to be the best π-acceptor (due to delocalisation of electron density onto the rings) and pyrazine is expected to be a better π-acceptor than pyrimidine, (due to the delocalisation of the additional electron density on to the *para*-nitrogen). Hence, the MLCT in the bipy complex is expected to be at the highest energy, followed by the pyrazine complex and finally the pyrimidine complex. However, the difficulty in comparing the results for these complexes arises from the fact that there will be an inherent difference in the energy of the lowest π^* molecular orbital of bipyridine, pyrazine and pyrimidine which cannot be accounted for. Experimentally it is observed that the MLCT band in the bipy complex lies at a significantly lower energy (1700 cm^{-1}) than the pyrazine complex which is at a lower energy (2650 cm^{-1}) than the pyrimidine complex. This suggests that the energy of the π^* orbitals vary according to bipy < pyz < pym. It is unfortunate that the reduction potential of the bound ligand to Ru(II) cannot be measured for these complexes.

Molecular orbital (CNDO and INDO) calculations have been performed on the free pyrazine and pyrimidine ligands. These showed that for pyrazine, the lowest π^* orbital is at lower energy compared to pyridine,[77] thus supporting the above argument.

The large difference in the π-accepting capability of pyrazine and pyrimidine when coordinated to Ru(II) was highlighted during an investigation into their basicity.[29] When a $Ru(NH_3)_5$ fragment is bound to one of the nitrogen atoms in pyrazine, the basicity at the unbound nitrogen atom is greatly enhanced (from 0.6 in the free ligand[78] to 2.5 when complexed with Ru(II)). In contrast, on binding this metal fragment to the nitrogen of pyrimidine there is a decrease in basicity at the free nitrogen atom (from 1.3 in the free ligand to 0.0). If the ligand is capable of π-accepting, the amount of electron density on that ligand will increase, as a result the basicity of the free nitrogen may increase, as found for pyrazine. If π-effects are not

significant, the amount of electron density on the ligand will be reduced (due to σ-donation to the metal centre). This and the electrostatic effect of the co-ordination to the positively charged ruthenium will result in the basicity of the free nitrogen being reduced. Additionally the basicity of the free nitrogen may also be reduced if the π-accepting orbital of the ligand does not have any 'free nitrogen' character (*i.e.* the coefficient at the *meta* position is very small).

It must also be borne in mind that the molecular orbital of the complex probed using electrochemistry will be different from that investigated by the MLCT in the UV/Vis spectroscopy. A simplistic investigation into the effect π-bonding will have on the t_{2g} orbitals can be performed. Assuming the z-axis lies along the (L)N-Ru-S(DMSO) bonds and the x- and y-axis along the Cl-Ru-Cl bonds, the d_{xy} orbital will experience the π-donation from four Cl^- ligands and the d_{xz} and d_{yz} only two , therefore the d_{xy} orbital will be pushed higher in energy than the others. A π-accepting interaction by the pyrazine or pyrimidine will effect only the d_{xz} and the d_{yz} orbitals and thus they will be stabilised further (with respect to the d_{xy}). From this, the SOMO of the complex (the orbital which is probed by the electrochemistry) will be the d_{xy}. This will also be the orbital investigated by the LMCT in the Ru(III) complex. Hence these two results correlate. The intense MLCT band on the other hand will not be due to the $d_{xy} \rightarrow \pi^*$ transition since there is no direct overlap between these orbitals. Here the transition will be a d_{xz} or $d_{yz} \rightarrow \pi^*$ transition.

On comparison of the position of the daughter peaks (with respect to the original complex) for these two compounds in DMF, when L = pyrazine the difference in half-wave potential is +270 mV, and when L = pyrimidine the difference is +300 mV. These two values are too small to signify the replacement of a chloride by a solvent molecule, chloride is a σ-donor, strong π-donor thus in the Ru(II) species (where the ligand replacement occurs) the oxidation of a complex which has lost a chlorine will occur at a much higher potential (greater than 300 mV). It is therefore concluded that the daughter peak is due to the replacement of the DMSO ligand by a solvent molecule. Since this replacement occurs only in the Ru(II) species this would

imply that the sulfur atom is acting mainly as a σ-donor. On reduction, the ruthenium centre will have increased electron density, if sulfur was acting as a π-acceptor it would stabilise this oxidation state, therefore ligand exchange would become very unlikely.

In conclusion, both the electrochemical and IR spectroscopic results of these complexes show that the species in solution is the same as that found in the solid phase. When the complex is reduced however, the weakly bound DMSO ligand can be replaced by a solvent molecule to produce a more stable compound (with respect to re-oxidation). This ligand replacement reaction can be suppressed at temperatures more negative than 233 K.

Through the electrochemical investigation, both the solvent and the nature of the counterion were found to have an effect on the electronic nature of the complex under study. The counter ion can remain associated with the complex to a varying degree in different solvents thus the half-wave potential will be altered. The solvent itself can have an effect also, this manifested itself during the study of the bipy complex. The counterion this time was TBA, which (being the same as the electrolyte) should be completely dissociated in solution and still a large change in the half-wave potential (130 mV) was observed in different solvents. It can be envisioned that the chloride ligands, which have lone pairs, can donate some of its electron density to the solvent. Gutmann introduced the concept of donor and acceptor numbers for solvents to quantify this effect.[71] For complexes with chlorides, acceptor number will be important, a solvent with a high acceptor number will reduced the amount of electron density on the ruthenium centre and thus the compound will be more easily oxidised. The acceptor number for DCM is 20.4 and for DMF is 16.0, thus the half-wave potential for the complex should be more positive in DCM. This is as observed.

5.3.5 $[\{(DM\underline{S}O)Cl_4Ru\}_2(\mu\text{-pyz})]^{n-}$ (n = 2, 3, 4)

Both the TBA salt and the sodium salt of this compound were investigated. The cyclic voltammogram of the sodium salt in DMF is shown in Figure 5.13. It shows two closely spaced reversible reduction couples. The presence of two waves becomes clear when differential pulse voltammetry is used (Figure 5.13). The half-wave potentials of these reductions, measured from the differential pulse voltammogram, were found to be –0.16 V and –0.24 V (a separation of 80 mV). A plot of i_p (for the prominent peak) versus $\nu^{1/2}$ showed a linear relationship indicating these processes are both electrochemically reversible. The ratio of peak currents was found to be 0.96 indicating that the reductions are fully chemically reversible. Bulk electrolysis at –0.6 V confirmed that the number of electrons involved overall is two.

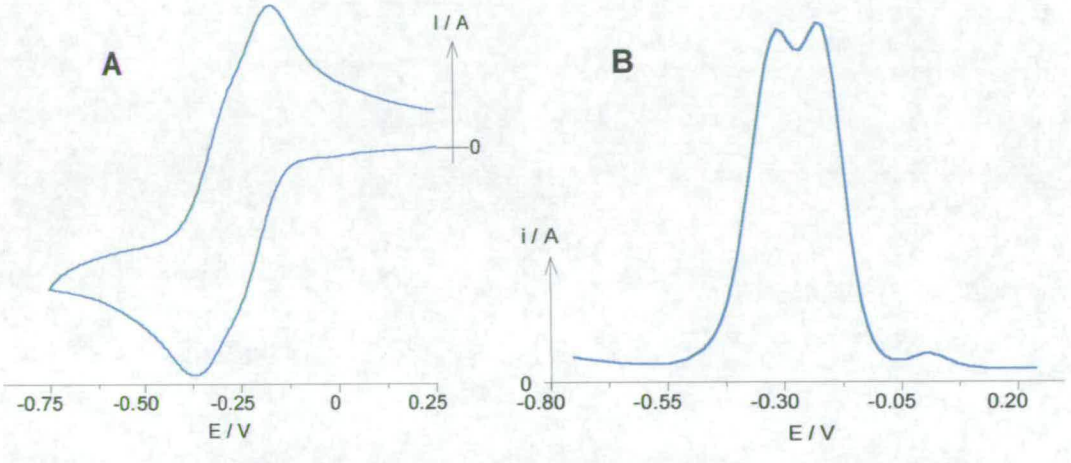

Figure 5.13 A, Cyclic voltammogram and **B**, differential pulse voltammogram of Na $[\{(DM\underline{S}O)Cl_4Ru\}_2(\mu\text{-pyz})]$ in 0.1 M $[N^nBu_4][BF_4]$ / DMF at 298 K.

An electrochemical investigation of the TBA salt was performed in DMF and DCM and the measured half-wave potentials are shown in Table 5.2. The cyclic voltammograms recorded in these solvents are shown in Figure 5.14. Both cyclic voltammograms are referenced to the ferrocinium/ferrocene couple and hence there is a significant dependence of the half-wave potentials on solvent. In DMF the difference in peak-to-peak potentials is 100 mV for the first reduction whereas for the second it is 140 mV. The second reduction/re-oxidation is more sluggish than the

first. The phenomenon was not observed for the cyclic voltammogram in DCM. Here the peak-to-peak potentials were similar for both couples (70 mV).

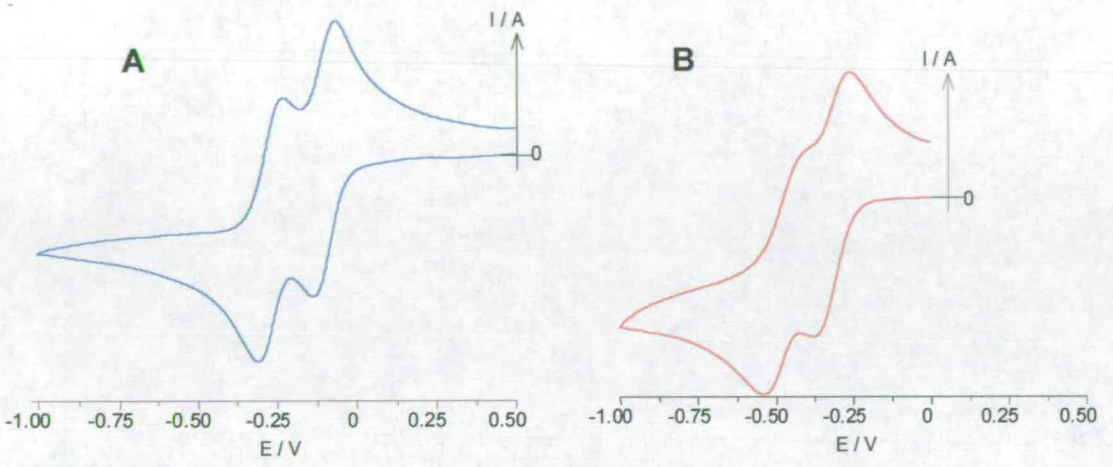

Figure 5.14 Cyclic voltammogram of $[N^nBu_4]_2[\{(DM\underline{S}O)Cl_4Ru\}_2(\mu\text{-pyz})]$ **A** in 0.4 M $[N^nBu_4]BF_4$ / DCM at 298 K and **B** in 0.1 M $[N^nBu_4]BF_4$ / DMF at 298 K.

Table 5.2 Calculated half-wave potentials for $[\{(DM\underline{S}O)Cl_4Ru\}_2(\mu\text{-pyz})]^{n-}$, n- = 2-, 3-, 4-.

Complex	Solvent	E_1 / V	E_2 / V	$E_1 - E_2$ / mV	K_c
$Na_2[\{(DM\underline{S}O)Cl_4Ru\}_2(\mu\text{-pyz})]$	DMF	-0.16	-0.24	80	20
$[N^nBu_4]_2[\{(DM\underline{S}O)Cl_4Ru\}_2(\mu\text{-pyz})]$	DMF	-0.28	-0.43	150	340
	DCM	-0.15	-0.32	170	750

The half-wave potentials show similar trends to those observed for the mononuclear species. That is they are dependent on both the counterion and the solvent. The shift of the redox couples to more positive potentials, in DMF, on replacing the TBA counterion with Na^+ can be rationalised on electrostatic grounds. If the sodium salt is not fully dissociated on dissolution then the presence of the positive charge will result in the reduction potentials shifting to lower energy. Upon reduction the overall negative charge of the binuclear complex increases thereby increasing the association of the complex and the sodium ion. Thus the second reduction potential will shift to more positive potentials (compared to the TBA salt in the same solvent) and hence the E_1-E_2 separation is smaller for the sodium salt as observed. When the counterion is TBA, the half-wave potentials for the reductions in DCM are more positive than

those in DMF (also observed for the mononuclear complex with L = bipy), this is attributed again to the higher acceptor number of DCM.

If the electrochemistry of the sodium salt is compared to the mononuclear species $Na[RuCl_4(DMSO)(pyz)]$ ($E_{½}$ = -0.22 V), the half-wave potential for the mononuclear complex lies between those of the binuclear complex. That is, the first reduction of the binuclear complex is easier than the mononuclear complex and the second reduction is more difficult. This is indicative of some communication between the two metal centres (discussed in chapter 1). Additionally, this is a symmetrical binuclear complex, and the presence of two distinct redox couples is also indicative of a level of delocalisation of the unpaired electron. The comproprotionation constant (K_c) can be calculated for this separation in redox couples, and the values are shown in Table 5.2. These values correspond to the system being a Class II complex. Thus a solvent dependent intervalence charge transfer band is expected in the UV/Vis spectrum of the mixed-valence complex.

It should also be noted that it appears from the electrochemistry that this binuclear species is less susceptible to ligand substitution (no chemical reaction following reduction was observed). From a solution of the TBA salt in proprionitrile, crystals suitable for X-ray analysis were formed. The structure is shown in Figure 5.15.

Crystal data

Data was collected on a Bruker AXS SMART diffractometer equipped with a CCD area detector, Oxford Cryosystems cryostream and graphite monochromated Mo-K_α radiation using ϕ and ω scans in the range $0.88 \leq \theta \leq 26.40$ °. The crystal was a red plate of dimensions 0.08 × 0.08 ×0.03 mm. Of a total of 43410 reflections collected, 26050 were found to be independent. The final difference map extrema were 1.097 and –0.811 e $Å^{-3}$ with a final R of 8.38% for 8787 parameters. An empirical absorption coefficient was applied (T_{min} = 0.9320, T_{max} = 0.9737).

Table 5.3 Crystallographic data for $[N^nBu_4]_2[\{(DM\underline{S}O)Cl_4Ru\}_2(\mu\text{-pyz})]$.

Empirical formula	$C_{44.5}H_{95.5}Cl_8N_{5.5}O_2Ru_2S_2$	γ / °	113.666(4)
Formula weight	1289.62	Volume / $Å^3$	6497(3)
Crystal system	Triclinic	Z	4
Space group	P-1	Temperature	150(2) K
a / Å	16.193(4)	Wavelength / Å	0.71073
b / Å	18.907(4)	Density calc. / Mg m^{-3}	1.318
c / Å	23.258(6)	μ(Mo-K_α) / mm^{-1}	0.893
α / °	94.146(4)	$R_1[F>4\sigma F]$	0.0838
β / °	90.866(4)	wR_2 (all data)	0.2160

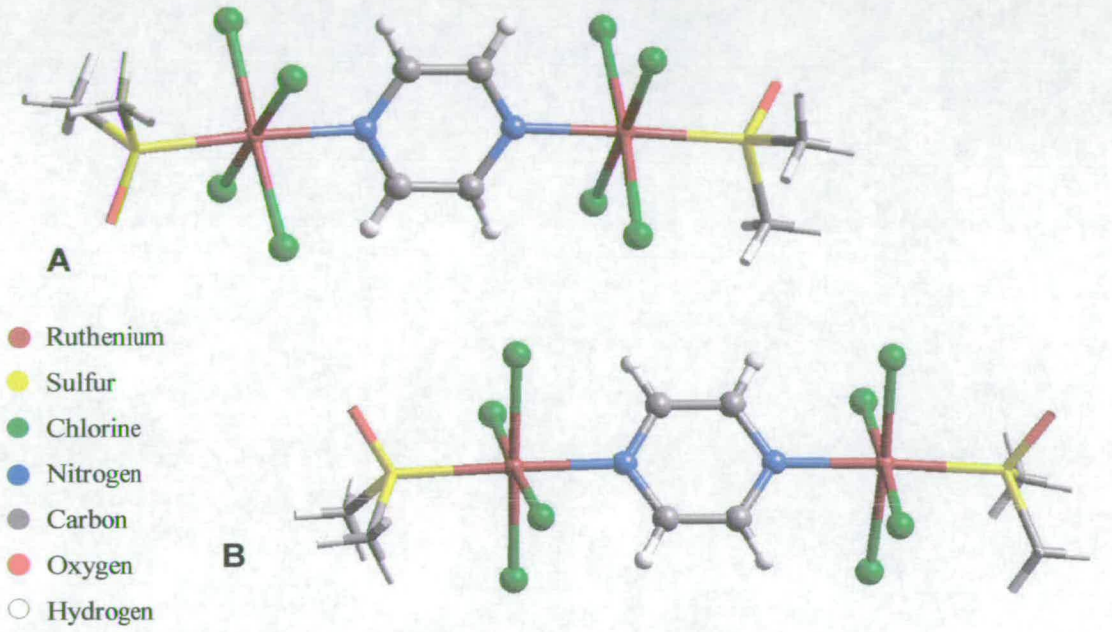

Figure 5.15 Crystal structure of $[N^nBu_4]_2[\{(DM\underline{S}O)Cl_4Ru\}_2(\mu\text{-pyz})]$. **A** shows the *'trans'* configuration of the DMSO ligands and **B** shows the *'cis'* configuration.

There are in fact two molecules of the binuclear complex per unit cell (also four TBA counterions and three proprionitrile solvent molecules). The two molecules differ in the orientation of the DMSO ligands. The best way to describe this difference is that in one molecule, both oxygens are pointing *'trans'* to each other and in the other they are *'cis'* (they are not true *cis* and *trans*, in fact the torsion angles are 26.2° and 143.1° respectively). Nevertheless, since proprionitrile is a solvent which is capable of co-ordination, this proves conclusively that upon dissolution, no ligand replacement reaction occurs.

The crystal structure of this, and the pym and bipy bridged complexes have been published previously with sodium as the counter ion.[79] Here, all of these complexes were found to lie on crystallographic inversion centres located on the mass centre of the bridging ligands. If the two structures with pyrazine are compared, the one presented in this thesis has a slightly better refinement, however only small variations in the molecular parameters are observed.

In order to allow the study of this complex in a number of solvents, the TBA salt of the species was investigated. The UV/Vis spectroelectrochemistry showing the complete reduction in DMF (for comparison with mononuclear complex) is shown in Figure 5.16. From this it can be clearly seen that two reduction steps are involved, this is indicated by the presence of two separate isosbestic points at 22000 cm^{-1} initially and then 23350 cm^{-1} nearer the end of the reaction. Thus, these spectra can be separated into the first one electron reduction and then the second one electron reduction (isosbestic regions are shown in Figure 5.17 and Figure 5.18 respectively – note solvent change to highlight the solvent dependence of the band maxima).

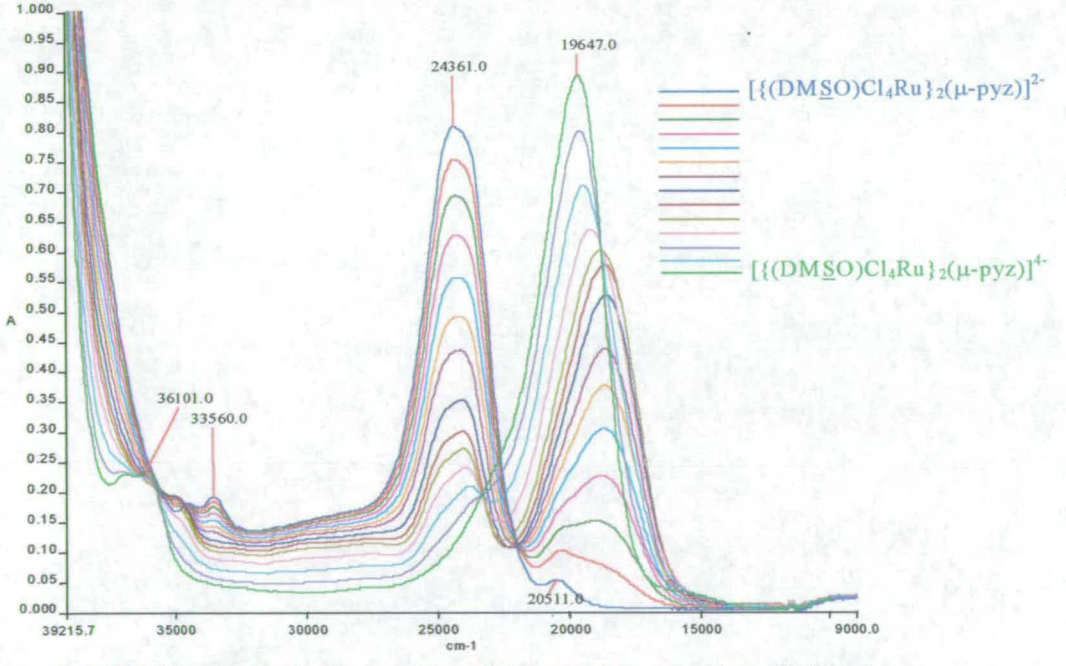

Figure 5.16 UV/Vis spectroelectrochemistry of the complete reduction of $[N^nBu_4]_2$ [{(DMSO)Cl_4Ru}$_2$(μ-pyz)] in 0.1 M $[N^nBu_4]BF_4$ / DMF at 217 K. E_{app} = -0.60 V.

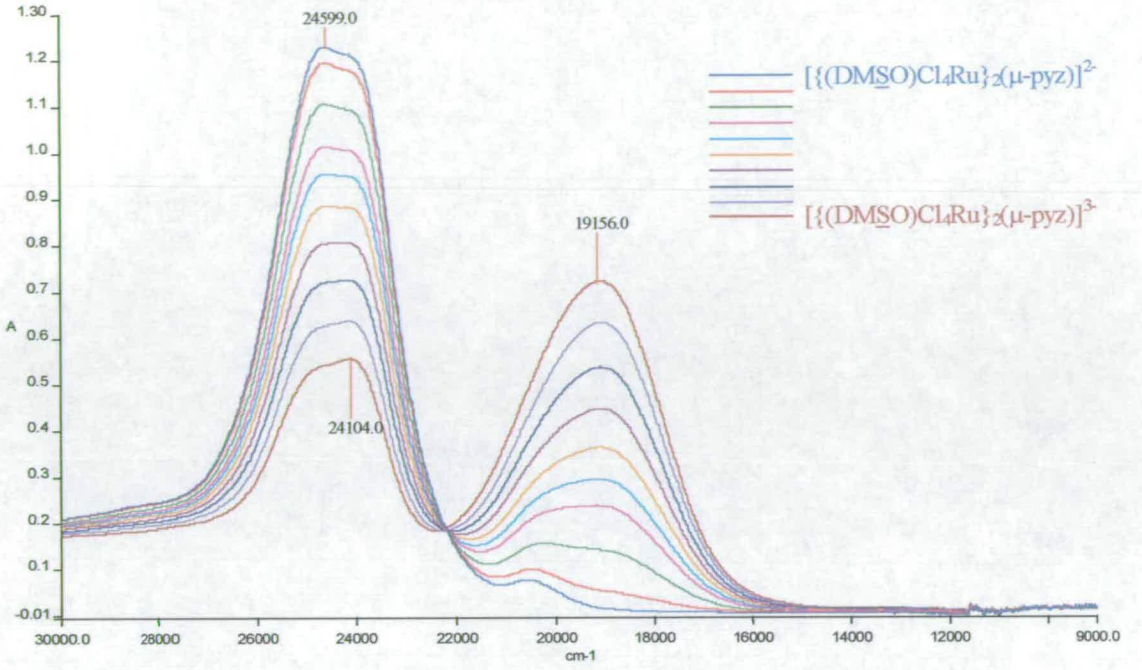

Figure 5.17 Uv/Vis spectroelectrochemistry of the first one electron reduction of $[N^nBu_4]_2$ $[\{(DMSO)Cl_4Ru\}_2(\mu\text{-pyz})]$ in 0.1 M $[N^nBu_4]BF_4$ / proprionitrile at 217 K. E_{app} = -0.6 V.

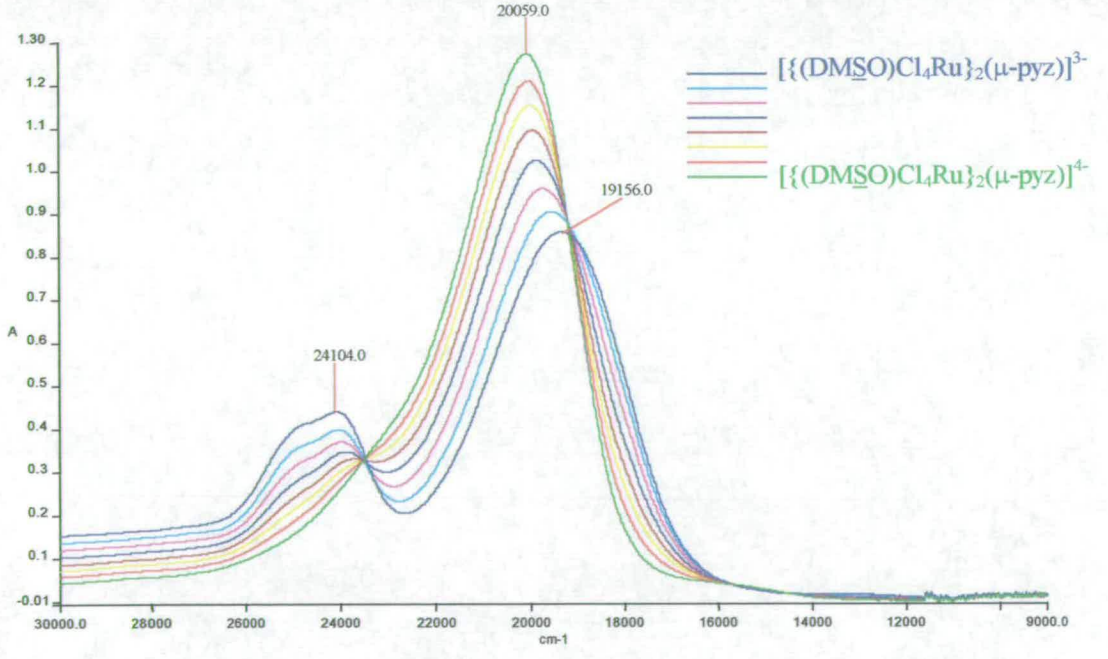

Figure 5.18 UV/Vis spectroelectrochemistry of the second one electron reduction of $[N^nBu_4]_2$ $[\{(DMSO)Cl_4Ru\}_2(\mu\text{-pyz})]$ in 0.1 M $[N^nBu_4]BF_4$ / Proprionitrile at 217 K. E_{app} = -0.60 V.

The UV/Vis spectrum of the fully oxidised species (formally Ru(III)/Ru(III)) is very similar to that of the mononuclear Ru(III) complex, and is dominated by a $Cl^- \rightarrow Ru$ t_{2g}^5 LMCT transition at 24350 cm^{-1} (ε = 18600 M^{-1} cm^{-1}) compared to 24050 cm^{-1} (ε = 7200 M^{-1} cm^{-1}) in the mononuclear complex. These bands appear to be at slightly different positions, however in both the mono- and binuclear compounds they are actually due to two (or more) bands very close together in energy and hence produce a rather wide absorption and a different band is more intense in each compound. If the spectra of the mononuclear and binuclear complex are overlaid the intense bands are in exactly the same position. The extinction coefficient of the band in the binuclear complex is much larger than that of the mononuclear complex. This is to be expected since in the binuclear complex there are two metal centres (in identical environments) contributing to the absorption, compared to one in the mononuclear species. Thus the extinction coefficient of the absorption in the binuclear complex is expected to be approximately double that of the mononuclear complex.

The UV/Vis spectrum of the fully reduced species (formally Ru(II)/Ru(II)) resembles closely that of the dianionic (Ru(II)) mononuclear species. It is dominated by a MLCT, from the Ru t_{2g} orbital to the antibonding π^* orbital of the pyrazine ligand, at 19650 cm^{-1} (ε = 20600 M^{-1} cm^{-1}), compared to 22300 cm^{-1} (ε = 7150 M^{-1} cm^{-1}) in the mononuclear complex. This transition is at lower energy in the binuclear complex, which is due to the π^* orbital in the pyrazine ligand being unable to satisfy (remove enough electron density from) both ruthenium centres, hence the energy of the ruthenium based MO's will be higher. As a result the orbital gap will be lower, and thus the transition will appear at lower energy.

The two separate isosbestic points observed during the two-electron reduction, as mentioned previously, indicate that the reduction takes place in two one electron steps; Ru(III)/Ru(III) $\rightarrow$ Ru(III)/Ru(II) $\rightarrow$ Ru(II)/Ru(II). This was confirmed using an *ex situ* experiment. The compound was reduced by bulk electrolysis in a standard H-cell (see chapter 2.2.4) where the number of coulombs passed could be monitored. Samples were taken (and their electronic spectrum recorded) every 5 minutes or so.

The spectrum that corresponded to the addition of one electron was almost identical to the dark blue spectrum shown above.

The spectrum of the mixed-valence species is a combination of the spectrum of the individual Ru(II) and Ru(III) species with slightly perturbed features. One explanation for the appearance of the spectrum could be the disproprotionation reaction:

$$2\ \text{Ru(III)/Ru(II)} \rightleftharpoons \text{Ru(II)/Ru(II)} + \text{Ru(III)/Ru(III)}$$

If this was the case, the spectrum observed would be the sum of that of the fully reduced and fully oxidised species divided by two. The software used to control the spectrophotometer allows this calculation to be performed and the spectrum produced, along with the others for comparison, is shown in Figure 5.19.

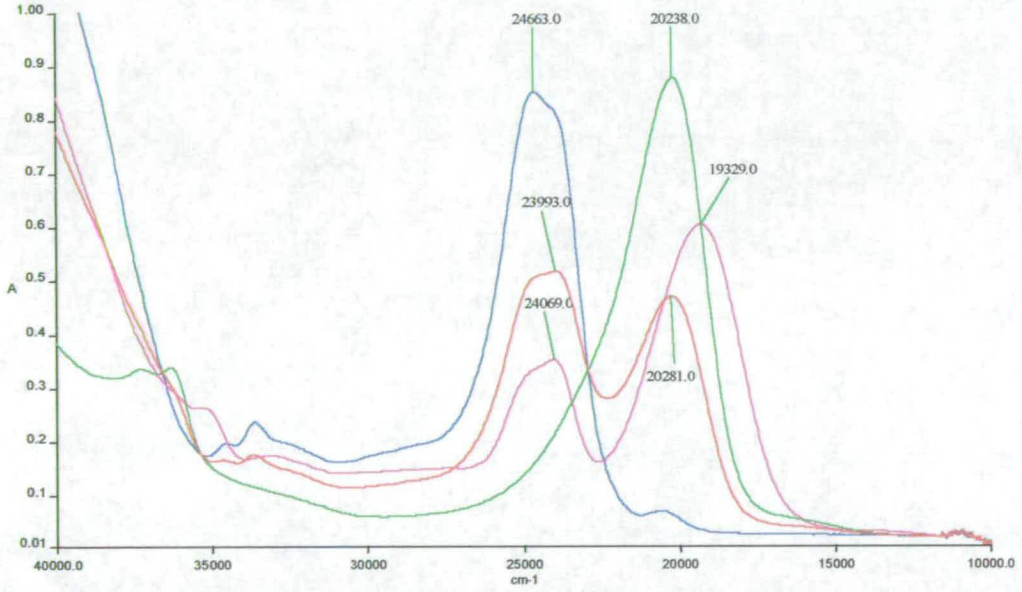

Figure 5.19 UV/Vis spectrum of $[\{(DMSO)Cl_4Ru\}_2(\mu\text{-pyz})]^{2-}$ - blue line; $[\{(DMSO)Cl_4Ru\}_2(\mu\text{-pyz})]^{3-}$ - pink line; $[\{(DMSO)Cl_4Ru\}_2(\mu\text{-pyz})]^{4-}$ - green line in 0.4 M $[N^nBu_4][BF_4]$ / DCM at 217 K and predicted spectrum of the disproportionation reaction – red line.

If the actual spectrum (pink line) is compared to that of the product of the disproprotionation reaction (red line), then it is obvious that disproprotionation does not account for the observed spectrum. Clearly the band due to the MLCT is shifted to lower energy than predicted, and disproportionation would imply that only one isosbestic point should be observed. Thus, it can be concluded that

disproportionation is not significant and the spectrum observed is indeed that of the mixed-valence species.

Since the spectra are slightly perturbed from those of the constituent ions then this would imply that the binuclear species is a Class II mixed-valence species (as also implied by the electrochemistry). If this is the case, an intervalence charge transfer transition should be observed. On closer inspection of the low energy region, a very weak band which exists only in the mixed-valence species is noticed. In order to study this band further a more concentrated solution was used, and the spectra produced are shown in Figure 5.20. This band has been attributed to the IVCT transition from the Ru(II) metal centre to the Ru(III) end. Note the isosbestic points which are observed at 15700 and 14700 cm^{-1} during the second one electron reduction.

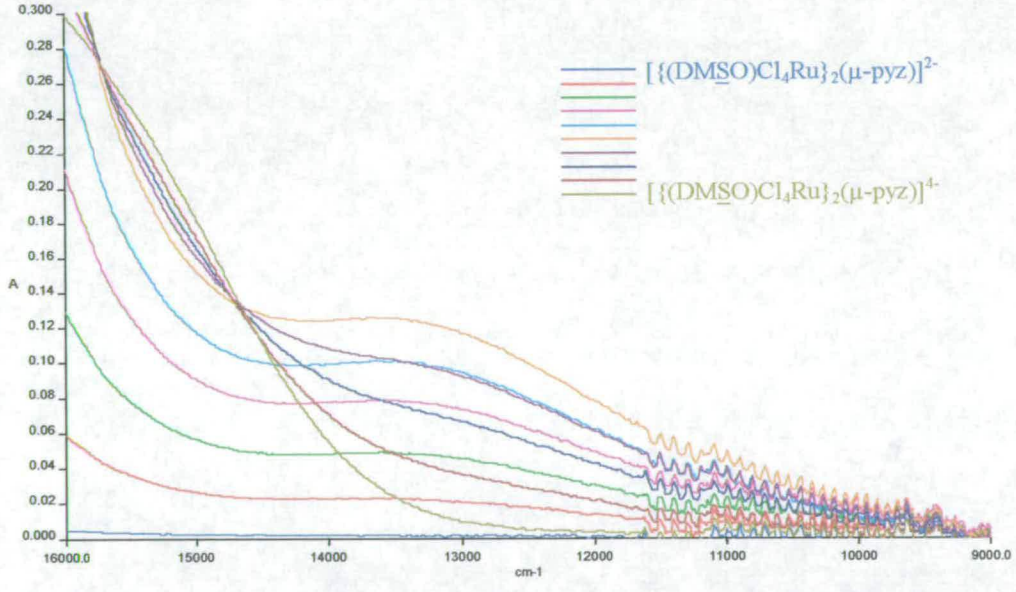

Figure 5.20 UV/Vis spectroelectrochemistry of the complete reduction of a more concentrated solution of $[N^nBu_4]_2[\{DMSO)Cl_4Ru\}_2(\mu\text{-pyz})]$ in 0.1 M $[N^nBu_4][BF_4]$ / Proprionitrile at 217 K. E_{app} = -0.75 V.

The UV/Vis spectroelectrochemistry experiment was repeated in a number of different solvents to investigate the effect this has on the band position. Table 5.4 shows the band position in the experiments performed. It should be noted that the band positions given were calculated from difference spectra where the spectrum of

the mixed-valence compound was subtracted from that of the fully reduced compound.

Table 5.4 Position of IVCT transition in various solvents.

Solvent	Acceptor Number	IVCT position / cm^{-1}
Pyridine	14.2	12300
Benzonitrile	15.5	12700
Dimethylformamide	16.0	12500
Acetonitrile	18.9	13100
Dichloromethane	20.4	13200
Chloroform	23.1	13400

It was expected that the position of the IVCT band should correlate with $1/D_{op} - 1/D_s$ for the solvent as predicted by Hush. However, this was not the case. Instead, the results were found to correlate with Gutmann acceptor number,[73] and the plot obtained is shown in Figure 5.21. The acceptor number reflects the ability of the solvent to accept electron density from the lone pairs on the chloride ligands.

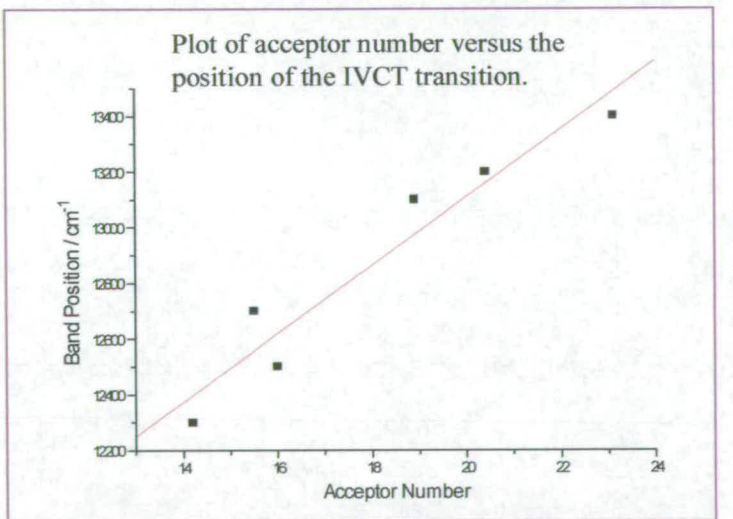

Figure 5.21 Plot of Gutmann acceptor number versus the position of the IVCT transition in various solvents.

Thus it can be concluded from these results that the compound $[\{(DMSO)Cl_4Ru\}_2(\mu\text{-pyz})]^{2-}$ undergoes two separate reversible one electron reductions. The separation between these two couples depends on both the solvent and the nature of the

counterion. The mixed-valence species produced following reduction by a single electron exhibits the behaviour of a Class II mixed-valence complex. That is, the separation of the two redox couples indicate a K_c of 10^2. Furthermore, the electronic spectrum produced is a combination of the constituent ions with slightly perturbed features, and shows the presence of a weak, solvent dependent IVCT transition, all indicating the complex is best defined as a Class II mixed-valence species.

5.3.6 $[\{(DM\underline{S}O)Cl_4Ru\}_2(\mu\text{-}L)]^{n-}$ (L = pym, bipy, BPA or BPE; n = 2, 3, 4)

The complexes $[\{(DM\underline{S}O)Cl_4Ru\}_2(\mu\text{-}L)]^{n-}$ (L = pym, bipy, BPA or BPE) have also been investigated using electrochemical and spectroelectrochemical techniques. In all cases, the interaction between the two metal centres was reduced compared to that experienced with pyrazine as the bridging ligand. This manifested itself in the inability to separate the redox couples. Bulk electrolysis confirmed two electrons were involved in the reduction step. For L = pym and bipy there still seems to be two separate isosbestic points in the spectroelectrochemistry during the complete reduction of the species, indicating that the process still occurs in two one electron steps.

These complexes were not investigated as intensively as the pyrazine bridged complex since the counterion is sodium. That is, any interaction between the two metal centres will be reduced due to ion pairing (as discussed previously), and as such cannot be compared to the results for the binuclear pyrazine complex. An added complication of the sodium salts is that, due to their solubilities, they cannot be investigated in a wide range of solvents. Table 5.5 shows the half-wave potentials for all of the binuclear complexes investigated.

Table 5.5 Half-wave potentials of the binuclear complexes investigated. Measured from their cyclic voltammetry in 0.1 M $[N^nBu_4][BF_4]$ / dmf at 298 K.

Compound	$E_{½}$ / V
$Na_2[\{(DM\underline{S}O)Cl_4Ru\}_2(\mu\text{-}\mathbf{pyz})]$	-0.161; -0.243
$Na_2[\{(DM\underline{S}O)Cl_4Ru\}_2(\mu\text{-}\mathbf{pym})]$	-0.28
$Na_2[\{(DM\underline{S}O)Cl_4Ru\}_2(\mu\text{-}\mathbf{bipy})]$	-0.30
$Na_2[\{(DM\underline{S}O)Cl_4Ru\}_2(\mu\text{-}\mathbf{BPA})]$	-0.32
$Na_2[\{(DM\underline{S}O)Cl_4Ru\}_2(\mu\text{-}\mathbf{BPE})]$	-0.28

When the mono-and binuclear complexes with pyrazine were compared the first reduction of the binuclear species was more positive than the mononuclear complex and the second more negative. However, on comparison of the mono- and binuclear

complexes with pyrimidine, a single couple is observed, the half-wave potential of which is 20 mV more negative than the mononuclear complex. This implies that on formation of the binuclear complex no stabilisation of the Ru(III) centre is observed (due to electron density being pushed through the system) and hence no communication between the metal centres is predicted. Although the difference in potential between the mono- and binuclear complexes is not significant, the binuclear complexes are expected to be slightly more difficult to reduce due to the additional negative charge on the complex.

The mono- and binuclear complexes with bipyridine cannot be compared due to the fact that they have different counterions. However, the same effect as discussed above would be expected.

If the sodium salts of all the binuclear complexes are compared, only the pyrazine bridged complex shows some evidence of the splitting of the two couples and even in this case it was only by 80 mV (compared to 150-170 mV when the TBA salt was used). The half-wave potentials of the other complexes are all quite similar, with differences arising from increased/decreased σ-donor and/or π-acceptor properties. A similar result was found during the investigation of the fragment $(bipy)_2ClRu$ with the same bridging ligands. When the bridging ligand was pyz and pym, two redox couples were observed. For bipy, BPA and BPE bridged complexes only a single redox process could be observed.[80]

If the results for the two isomers, where L is pyrazine and pyrimidine are compared, they point to their being less communication between the metal centres when the bridging ligand is pyrimidine. The electrochemistry has been discussed above, and the absence of two redox couples for the pyrimidine complex supports this. Figure 5.22 shows the spectroelectrochemistry of the binuclear complex with pyrimidine. From this it can be seen that two different sets of isosbestic points are observed during the complete reduction. These have been separated and the spectra generated during the first one-electron step with isosbestic points at 28350, 25600 and 23150

cm^{-1} are shown in Figure 5.23 and the second one-electron step with isosbestic points at 29700, 25600, 22850 and 21750 cm^{-1} in Figure 5.24.

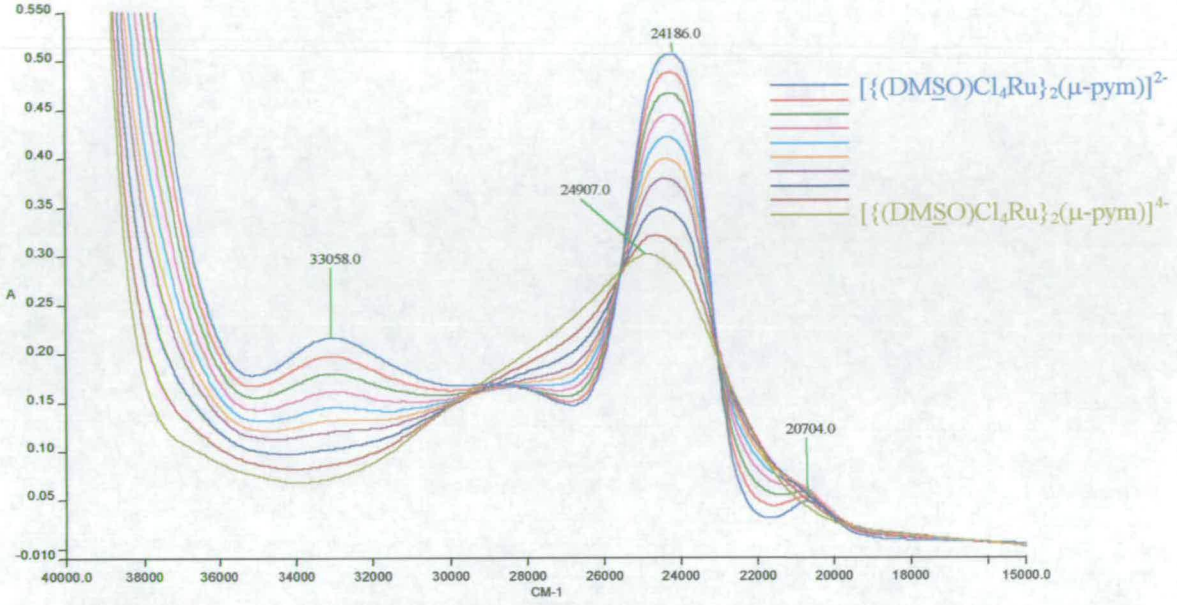

Figure 5.22 UV/Vis spectroelectrochemistry of the complete reduction of $Na_2[\{(DMSO)Cl_4Ru\}_2(\mu\text{-pym})]$ in 0.1 M $[N^nBu_4]BF_4$ / DMF at 217 K. E_{app} = -0.75 V.

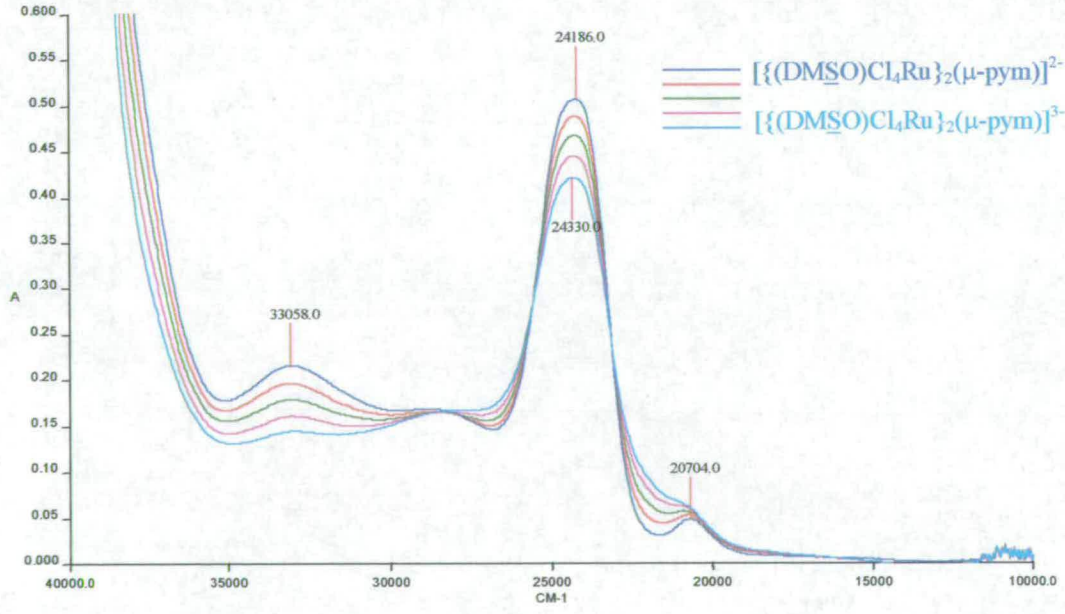

Figure 5.23 UV/Vis spectroelectrochemistry of the first one-electron reduction of $Na_2[\{(DMSO)Cl_4Ru\}_2(\mu\text{-pym})]$ in 0.1 M $[N^nBu_4]BF_4$ / DMF at 217 K.

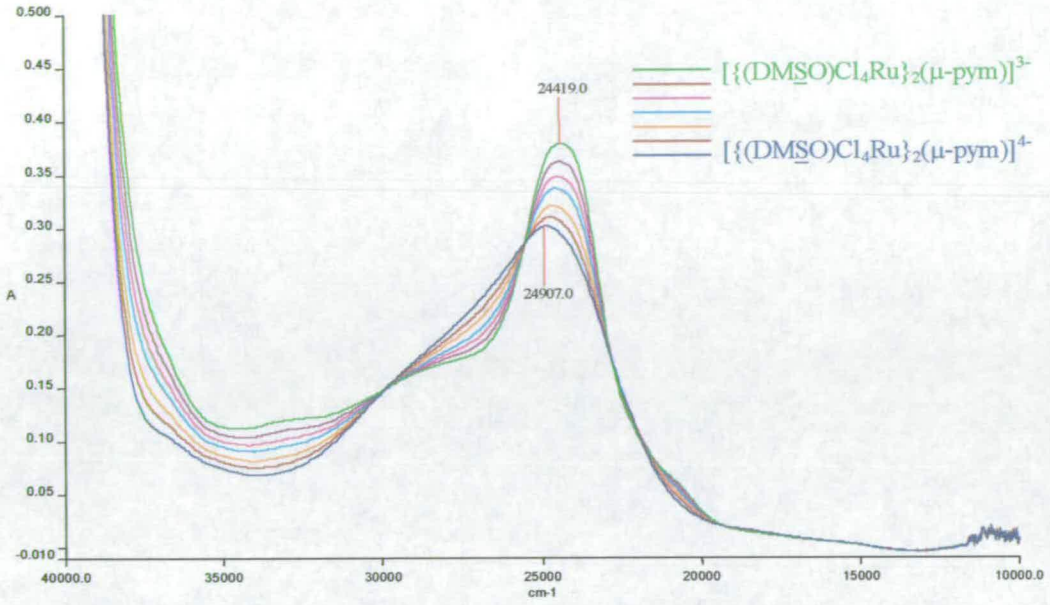

Figure 5.24 UV/Vis spectroelectrochemistry of the second one-electron reduction of $Na_2[\{(DMSO)Cl_4Ru\}_2(\mu\text{-pym})]$ in 0.1 M $[N^nBu_4]BF_4$ / DMF at 217 K.

The UV/Vis spectrum of the fully oxidised species (formally Ru(III)/Ru(III)) is very similar to that of the mononuclear Ru(III) complex, and is dominated by a $Cl^- \rightarrow Ru$ t_{2g}^5 LMCT transition at 24190 cm^{-1} (ε = 10350 M^{-1} cm^{-1}) compared to 24180 cm^{-1} (ε= 6540 M^{-1} cm^{-1}) in the mononuclear complex. As expected the extinction coefficient for the band in the binuclear complex is much larger since there are two equivalent ruthenium centres contributing to the band in this case.

The spectrum of the fully reduced species is also very similar to the spectrum of the reduced mononuclear complex. It has a MLCT (Ru $\rightarrow$ π^* (pym)) centred at 24900 cm^{-1} (ε = 6150 M^{-1} cm^{-1}) the same position as that found in the mononuclear complex (ε = 4600 M^{-1} cm^{-1}). This would imply that the ruthenium based molecular orbitals in the mono- and binuclear complexes are at similar energies. This at first seems counter intuitive, it is expected that on formation of the binuclear complex the π^*-orbital would not be able to withdraw enough electron density from both ruthenium centres to make the orbital equivalent in energy to the ruthenium based orbitals of the mononuclear complex. On further investigation, one explanation would be that in fact two separate π^* orbitals are involved in the stabilisation of the Ru(II) oxidation state and hence a level equivalent to that of the mononuclear complex could be

reached. Another explanation may also be that the Ru-N bond in the mononuclear and binuclear complexes can be considered as primarily σ-only with minimal π-interactions.

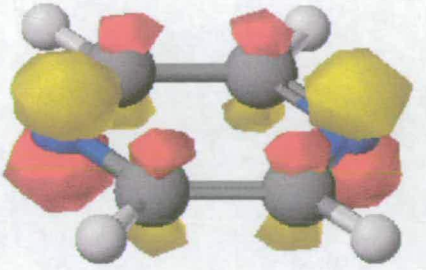

Figure 5.25 Pictorial representation of the molecular orbital of pyrazine which will interact with the two metal centres. Carbon atoms are shown in grey, and nitrogen atoms in blue.

In order to try and prove that the amount of communication between the metal centres is reduced when pyrazine is replaced by pyrimidine, the molecular modelling programme CAChe 3.2 was used to investigate the π* orbitals of the bridging ligands. In the case of the pyrazine ligand, the same π* orbital will interact with both ruthenium centres due to the nitrogen atoms being opposite one another. Figure 5.25 shows the LUMO +1 of the pyrazine (the LUMO was π* anti-bonding on the carbon atoms). On the other hand, as shown in Figure 5.26, the LUMO of pyrimidine is based on mainly on the carbon centres with only a small contribution from a single nitrogen atom. Hence there is no direct method of communication between the two metal centres with this orbital. The LUMO +1 does have a mediating effect with the metal centres (has a contribution from both nitrogen centres) but it can been seen from Figure 5.26 that this orbital is more skewed towards one nitrogen than the other. These results add support to the above argument.

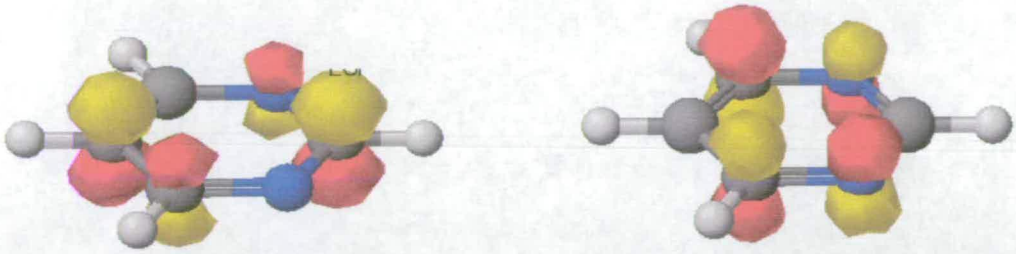

Figure 5.26 Pictorial representation of the two molecular orbitals in pyrimidine which may interact with the two metal centres. Carbon atoms are shown in grey, and nitrogen atoms in blue

In order to ascertain whether the mixed-valance species is forming, or if the spectra produced are due to disproportionation, the spectrum of the fully reduced and the fully oxidised species were added together and divided by two to produce the spectrum expected for the disproportionation product as was done for the pyrazine bridged species. This and the actual spectrum (and the fully reduced and oxidised for reference) are shown in Figure 5.27.

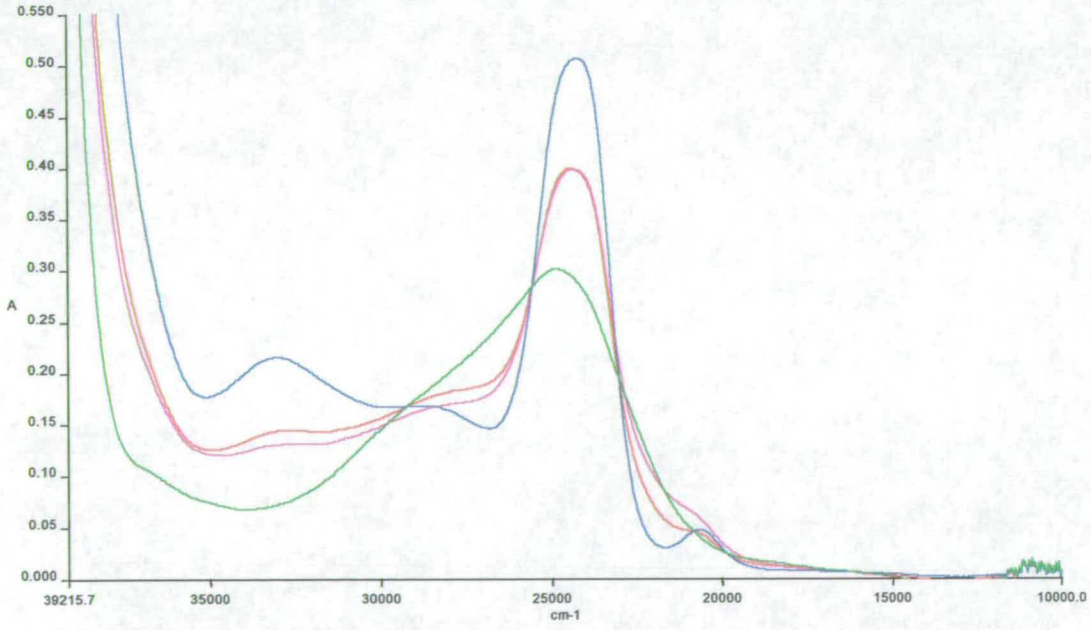

Figure 5.27 UV/Vis spectrum of $[\{(DM\underline{S}O)Cl_4Ru\}_2(\mu\text{-pym})]^{2-}$ - blue line; $[\{(DM\underline{S}O)Cl_4Ru\}_2(\mu\text{-pym})]^{3-}$ - pink line; $[\{(DM\underline{S}O)Cl_4Ru\}_2(\mu\text{-pym})]^{4-}$ - green line in 0.1 M $[N^nBu_4][BF_4]$ / DMF at 217 K and predicted spectrum of the disproportionation reaction – red line.

The spectrum of the mixed-valence species (pink line) is very similar to the spectrum expected for the disproportionation product, differing only in the low energy region.

This is indicative of only a very small degree of communication between the two ruthenium centres. Much smaller than if the bridging ligand is pyrazine.

Any communication between the two centres in systems such at these (two metals bridged by an organic ligand with accessible π orbitals) is known to occur through delocalisation of the electron density onto the ligand and correspondingly, onto the second metal centre. No communication can occur due to direct metal-metal orbital overlap because the distance between the two metals is too large (6.95 Å from crystal structure of the pyz complex). If the π^* orbital of pyrazine is considered then it is easy to see how this transfer of an electron can happen. On the other hand the π^* orbital of pyrimidine has no direct link between the two metal centres (the LUMO interacts greatly with one metal centre over the other) hence the likelihood of delocalisation of the mixed-valence electron is greatly reduced.

On comparison of the crystal structure of the complex bridged by pyrazine (reported here) and that bridged by pyrimidine[79] it is noticed that the RuN bond in the pyrazine complex is shorter than that in the pyrimidine complex, by 0.04Å. Although this difference is only slight, it would suggest that the π-interaction between the bridging ligand and the ruthenium is increased when pyrazine is used. As a result, the degree of communication is likely to be increased in this case also.

This effect has also been noted during the investigation of other metal fragments which are bridged with pyrazine or pyrimidine. Meyer and co-workers investigated the series $[\{Ru(bipy)_2Cl\}_2(\mu\text{-}L)]$ where L = pym, pyz, 4,4'-bipy, BPE and BPA[80] and found that the amount of communication between the metal centres when bridged by pyrazine is much greater than when bridged by pyrimidine. IT band analysis allowed the calculation of α^2 using Equation 5.1,[3] where ε_{max} is the extinction coefficient at ν_{max}, d is the internuclear separation between the metal centres, and $\Delta\nu_{½}$ is the bandwidth at half height.

$$\alpha^2 = \frac{(4.2 \times 10^{-4})\, \varepsilon_{max}\, \Delta\bar{\nu}_{½}}{\bar{\nu}_{max} d^2} \qquad \textbf{Equation 5.1}$$

For mixed-valence ions which have localised valences, α^2 gives an estimate of the extent of delocalisation of the odd electron. For the pyrazine bridged complex, α^2 was calculated to be 2.6×10^{-3} and for the pyrimidine bridged complex it was calculated at 3.0×10^{-4} indicating that the metal-metal interaction is considerably diminished in this case.[81] The delocalisation coefficient, α^2, can be calculated for [{(DMSO)$RuCl_4$}$_2$(μ-pyz)] and is found to be 6×10^{-4} indicating that the amount of delocalisation with the $RuCl_4$DMSO moiety is less than with the Ru(bipy)$_2$Cl moiety.

The binuclear complexes with ruthenium pentaammine fragments have also been investigated. Again, the degree of delocalistion of the odd electron is considerably reduced when the bridging ligand is pyrimidine compared to pyrazine. Through an electrochemical investigation the comproportionation constants were calculated. The Creutz-Taube ion in aqueous solution has a K_c value of 4×10^6, while the pyrimidine bridged equivalent has a K_c of 300 in the same medium.[82]

The UV/Vis spectroelectrochemistry of the bipy, BPA and BPE bridged complexes are shown below. They will not be discussed in great detail since it appears that the extent of metal-metal communication is greatly diminished and furthermore, the use of sodium as the counter ion does not permit the study of these complexes in a large number of solvents.

Figure 5.28 shows the spectra recorded during the complete reduction of the bipy bridged binuclear complex. Close inspection of the isosbestic region shows that two different isosbestic points can be observed. During the first one-electron reduction an isosbestic point is observed at 23500 cm^{-1}, and during the second one-electron reduction the isosbestic point is observed at 23700 cm^{-1}. The orange spectrum passes between both of these isosbestic points and is therefore the spectrum of the mixed-valence species.

The spectrum of the fully oxidised species (formally Ru(III)/Ru(III)) is very similar to that of the mononuclear Ru(III) complex, and is dominated by a $Cl^- \rightarrow Ru\ t_{2g}^5$ LMCT transition at 24800 cm^{-1} (ε = 12000 $M^{-1}\ cm^{-1}$) compared to 24750 cm^{-1} (ε = 6600 $M^{-1}\ cm^{-1}$) in the mononuclear complex. A band attributed to a d-d transition is observed at 20950 cm^{-1} (ε = 900 $M^{-1}\ cm^{-1}$), this was also observed in the mononuclear complex (at 20950 cm^{-1}; ε = 550 $M^{-1}\ cm^{-1}$). As expected the extinction coefficient for the transitions in the binuclear complex are much larger since there are two equivalent ruthenium centres contributing to the bands in this case.

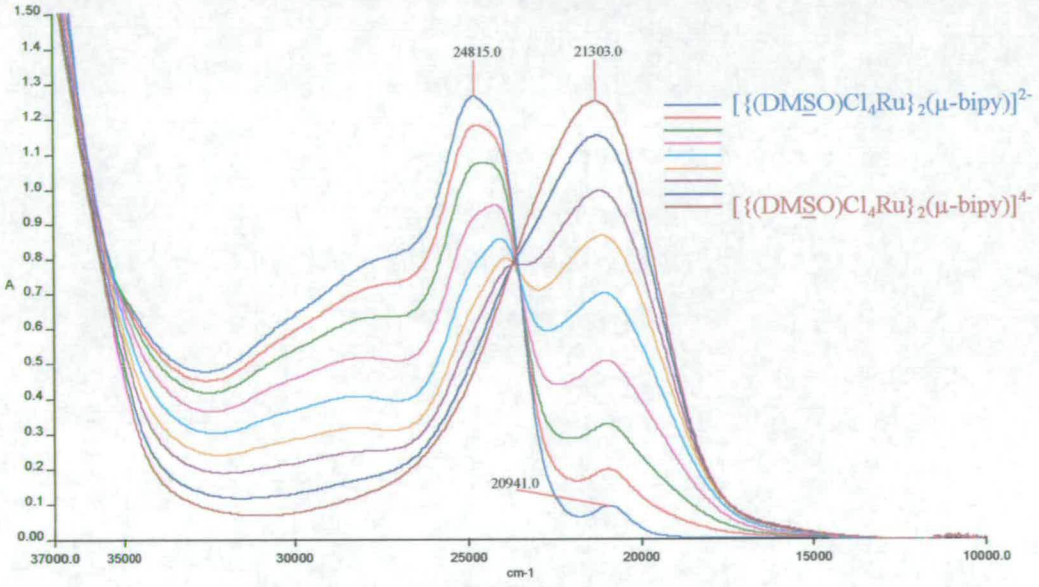

Figure 5.28 UV/Vis spectroelectrochemistry of the complete reduction of $Na_2[\{DMSO)Cl_4Ru\}_2(\mu\text{-bipy})]$ in 0.1 M $[N^nBu_4][BF_4]$ / DMF at 217 K. E_{app} = -0.80V.

The spectrum of the fully reduced species (formally Ru(II)/Ru(II)) resembles closely that of the dianionic mononuclear complex. It has a MLCT (Ru $\rightarrow$ π^* (bipy)) centred at 21300 cm^{-1} (ε = 11900 $M^{-1}\ cm^{-1}$) compared to 20550 cm^{-1} (ε = 6550 $M^{-1}\ cm^{-1}$) in the mononuclear complex.

The UV/Vis spectroelectrochemistry of the complete reduction of the BPA bridged binuclear compound is shown in Figure 5.29. Here only single isosbestic points are observed during the complete reduction of the complex. This is indicative of little or no communication between the two ruthenium centres. Isosbestic points were

observed at 30900, 25550, 22700 and 21700 cm^{-1} and highlight the clean conversion from the fully oxidised species to the fully reduced species.

The spectrum of the fully oxidised species (Ru(III)/Ru(III)) shows the features that have been observed previously for all of the binuclear and mononuclear complexes, that is, a $Cl^- \rightarrow Ru\ t_{2g}^5$ transition (at 24400 cm^{-1}; ε = 11000 $M^{-1}\ cm^{-1}$) and d-d transition (at 21000 cm^{-1}; ε = 800 $M^{-1}\ cm^{-1}$). This species has an additional band at 33350 cm^{-1} (ε = 8900 $M^{-1}\ cm^{-1}$) which has not been observed in the previous complexes investigated. This is attributed to a LMCT transition, namely π(BPA) $\rightarrow$ Ru(III). It is thought that the π-bonding orbital of BPA is closer in energy to the Ru dπ orbitals than that of the other bridging ligands. Upon reduction to Ru(II), which has a d^6 electronic configuration, this transition can no longer occur, and hence the band collapses.

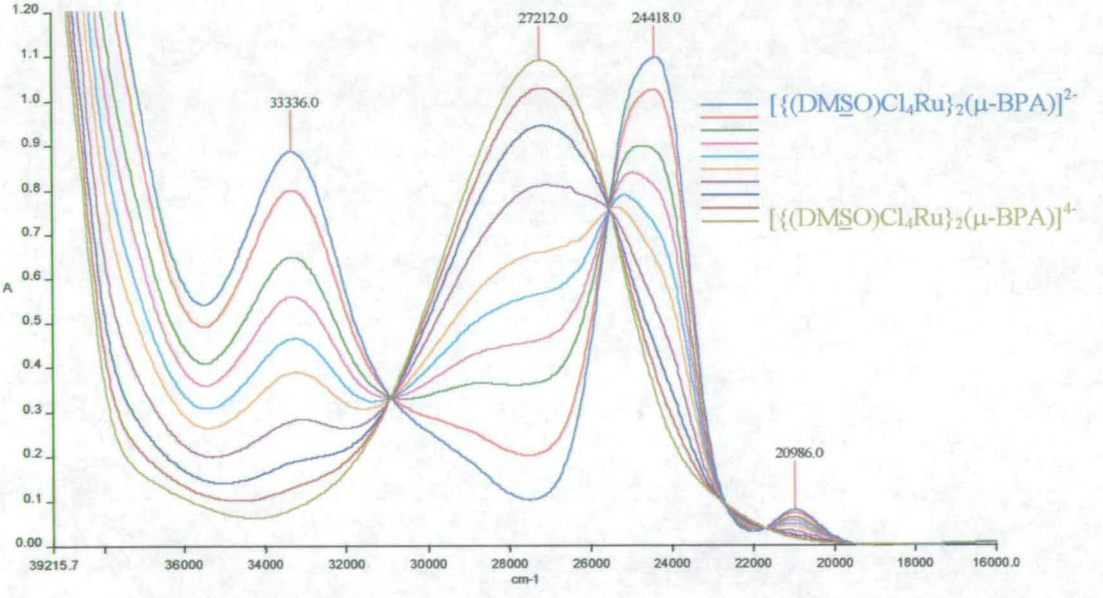

Figure 5.29 UV/Vis spectroelectrochemistry of the complete reduction of $Na_2[\{DMSO)Cl_4Ru\}_2(\mu$-BPA)] in 0.1 M $[N^nBu_4][BF_4]$ / DMF at 217 K. E_{app} = -0.75 V.

The spectrum of the fully reduced species (formally containing Ru(II)/Ru(II)) is as observed previously dominated by a MLCT (Ru $\rightarrow$ π^*(BPA)) transition centred at 27200 cm^{-1} (ε = 10900 $M^{-1}\ cm^{-1}$). The MLCT transition observed in this complex lies at a much higher energy than that of the previous compounds. This is in accordance

with assignment of the high energy band in the Ru(III)/Ru(III) spectrum as a LMCT transition. That is, if the π-bonding orbitals are higher in energy than shown previously (thus can donate to the Ru centre), then the π*-orbitals will correspondingly be at higher energy, thus the MLCT transition will become more difficult.

Figure 5.30 shows the spectra recorded during the complete reduction of the binuclear complex bridged by BPE. As found for the BPA bridged complex, only one set of isosbestic points are observed during the complete reduction of the complex. This indicates that there is little or no communication between the two ruthenium centres. Isosbestic points were observed at 32550, 31950 and 23150 cm^{-1} and highlight the clean conversion from the fully oxidised species to the fully reduced species.

The spectrum of the fully oxidised species (Ru(III)/Ru(III)) again shows the features that have been observed previously for all of the binuclear and mononuclear complexes, that is, a $Cl^- \rightarrow Ru\ t_{2g}^5$ transition (at 25150 cm^{-1}; ε = 12300 $M^{-1}\ cm^{-1}$) and d-d transition (at 21050 cm^{-1}; ε = 650 $M^{-1}\ cm^{-1}$). This species has an additional band at 33000 cm^{-1} (ε = 16400 $M^{-1}\ cm^{-1}$) which is attributed to the intraligand transition, $\pi \rightarrow \pi^*$(BPE).

The spectrum of the fully reduced species (formally containing Ru(II)/Ru(II)) shows a MLCT (Ru $\rightarrow \pi^*$(BPE)) centred at 19800 cm^{-1} (ε = 7300 $M^{-1}\ cm^{-1}$) and intraligand ($\pi \rightarrow \pi^*$(BPE)) transitions at 33450 (ε = 16000 $M^{-1}\ cm^{-1}$) and 32400 cm^{-1} (ε = 15800 $M^{-1}\ cm^{-1}$).

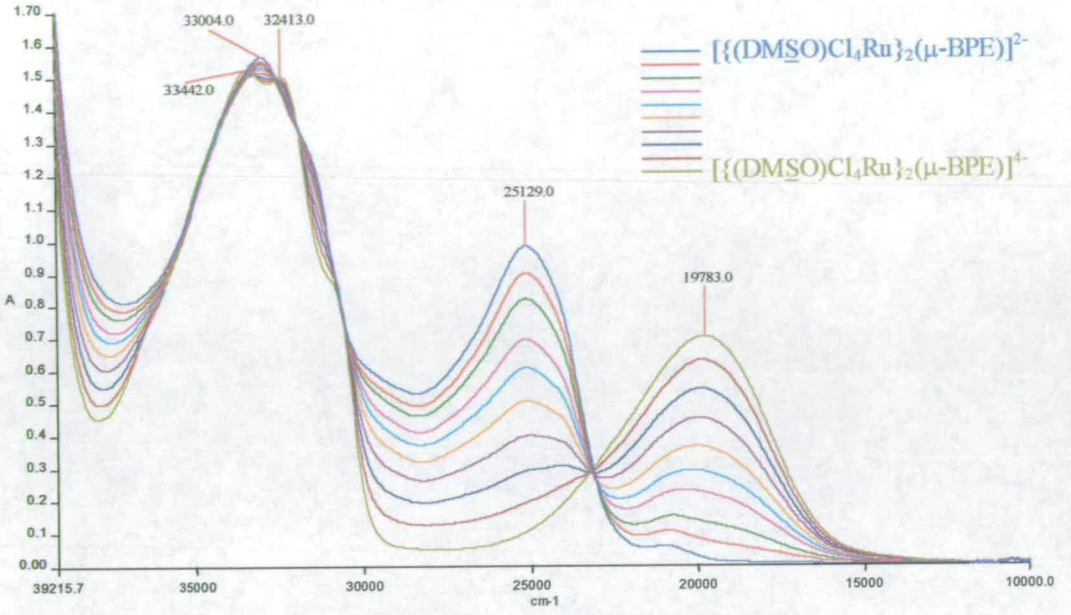

Figure 5.30 UV/Vis spectroelectrochemistry of the complete reduction of $Na_2[\{DMSO)Cl_4Ru\}_2(\mu$-BPE)] in 0.1 M $[N^nBu_4][BF_4]$ / DMF at 217 K. E_{app} = -0.9 V.

5.4 Conclusions

The experiments which have been carried out on the pyrazine bridged $RuCl_4(DMSO)$ fragment indicate that the amount of coupling between the two ruthenium centres is reduced compared to the Creutz-Taube ion. Certainly the difference in the redox potential (and hence the K_c value) is much smaller in the species discussed in this chapter compared to the Creutz-Taube ion. Thus on replacement of the σ-only donor NH_3 ligands by π-donating chloride ligands and a sulfur bound DMSO unit, the metal-metal coupling is reduced. These results can also be compared to the pyrazine bridged $Ru(py)_4Cl$ and $Ru(bipy)_2Cl$ fragments. Table 5.6 shows a summary of the results for these compounds.

Table 5.6 Separation between the two redox couples ($\Delta E = E_1-E_2$) and corresponding K_c values for the pyrazine bridged metal fragments. [a] measured in acetonitrile. [b] measured in dichloromethane.

Fragment	ΔE / mV	K_c
$Ru(NH_3)_5$	430[a]	$10^{7.3}$
$Ru(bipy)_2Cl$	120[a]	10^2
$Ru(py)_4Cl$	280[a]	$10^{4.7}$
$RuCl_4(DMSO)$	150[b]	10^2

Of the complexes described above, the one which is most readily comparable to $RuCl_4(DMSO)$ is the $Ru(py)_4Cl$ fragment since they have the most closely related structures. Both of these fragments showed diminished metal-metal communication than the Creutz-Taube ion. Following the observation that the degree of communication between the metal centres is reduced when the σ-only NH_3 ligands are replaced by π-accepting ligands (such as py and bipy), it was expected that on exchanging the NH_3 ligands for π-donating Cl^- ligands the degree of communication would be enhanced. This was not observed experimentally. Upon further consideration, this can be explained by considering the dπ orbitals of the $RuCl_4(DMSO)$ fragment.

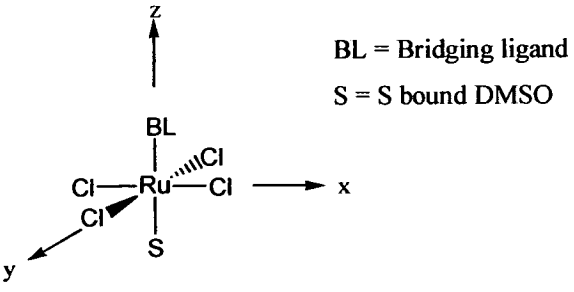

Figure 5.31 Labelling scheme for the molecular fragment $RuCl_4(DMSO)L$.

If it is assumed that the axis of the ruthenium fragment are labelled as shown Figure 5.31, then the d_{xz} and the d_{yz} orbitals will interact with 2 Cl^- ligands (plus the bridging ligand and the DMSO), thus will be destabilised by some extent. The d_{xy} orbital will interact with 4 Cl^- ligands thus will be destabilised by an even larger amount. Therefore the SOMO / HOMO of the complex will be the d_{xy} orbital. In the mixed-valence complex (d^5/d^6) the odd electron will be in the d_{xy} orbital. This orbital has no direct overlap with the orbitals of the bridging ligand thus the reduced level of delocalisation observed experimentally is explained.

One of the main effects of having Cl^- ligands in the periphery of the complex is that the stable form of the complex (synthesised chemically) is the Ru(III)/Ru(III) species and subsequent to forming this, the complex is then reduced to generate the mixed-valence complex. For the other complexes mentioned in this chapter, they are synthesised in the Ru(II)/Ru(II) form and oxidised to give the mixed-valence complex. By using π-donor chloride ligands the Ru(III) oxidation state has been stabilised.

It can be concluded that through electrochemical and spectroelectrochemical investigations, the mixed-valence binuclear complex bridged by pyrazine investigated in this chapter, can be confidently assigned as a Class II mixed-valence complex.

Two sets of isosbestic points could be observed in the pyrimidine and bipyridine bridged complexes indicating some communication between the two ruthenium centres. The extent of this communication could not be quantified, but is less than that experienced with pyrazine as the bridging ligand.

The amount of communication between the two ruthenium centres appears to be reduced further when the bridging ligand employed is BPA and BPE. This manifested itself in the apparent presence of only a single set of isosbestic points.

Since the discovery of the Creutz-Taube ion, a large amount of research into the role of the bridging ligand has been carried out and similar trends to those found here have been observed. That is, for aromatic bridging ligands with isomers (eg. pyz/pym or the dicyanobenzenes) stronger interaction occurs with the *ortho* and *para* isomers. Thus the interaction will be greater for pyrazine than pyrimidine. Interaction is also expected to be stronger when the bridging ligand features strong π-donor or π-acceptor interactions.

It is also noted in general that the interaction between the two metal centres decreases exponentially as the bridging ligand increases in size. Thus the amount of communication is expected to be smaller for BPA and BPE compared to pyrazine, as observed.

6 References

[1] Robin, M. B; Day, P.; *Adv. Inorg. Radiochem.*;1967, **10**, 247
[2] Lever, A.B.P. *Inorganic Electronic Spectroscopy*; Elsevier, Amsterdam, 1968.
[3] Hush, N. S.; *Prog. Inorg. Chem.*, 1967, **8**, 391.
[4] Marcus, R. A.; *Annu. Rev. Phys. Chem.*, 1964, **15**, 155, and earlier papers.
[5] Hush, N. S.; *Trans. Faraday Soc.*, 1961, **57**, 557.
[6] Creutz, C.; *Prog. Inorg. Chem.*, 1983, **30**, 29.
[7] Ward, M. D.; *Chem. Soc. Rev.*, 1995. 121.
[8] Richardson, D. E.; Taube, H., *Coord. Chem. Rev.*, 1984, **60**, 107.
[9] Creutz, C.; Taube, H.; *J. Am. Chem. Soc.*; 1969, **91**, 3988.
[10] Creutz, C.; Taube, H.; *J. Am. Chem. Soc.*, 1973, **95**, 1086.
[11] Clark, R. J. H.; *Chem. Soc. Rev.*; 1984, **13**, 219.
[12] Elias, J. H.; Drago, R.; *Inorg. Chem.*, 1972, **11**, 415.
[13] Creutz, C.; Good, M. L.; Chandra, S.; *Inorg. Nucl. Chem. Lett.*, 1973, **9**, 171.
[14] Best, S. P.; Clark, R. J. H.; McQueen, R. C. S.; Joss, S.; *J. Am. Chem. Soc.*, 1989, **111**, 548.
[15] Ondrechen, M. J.; Ellis, D. E.; Ratner, M. A.; *Chem. Phys, Lett.* 1984, **109**, 50.
[16] Zhang, L-T; Ko, J.; Ondrechen, M. J.; *J. Am. Chem. Soc.*, 1987, **109**, 1666.
[17] Fürholz, U.; Bürgi, H-B.; Wagner, F. E.; Stebler, A.; Ammeter, J. H.; Krausz, E.; Clark, R. J. H.; Stead, M. J.; Ludi, A.; *J. Am. Chem. Soc.*, 1984, **106**, 121.
[18] Bockris, J.O'M.; Yang, B. *J. Electroanal. Chem.*, 1988, **252**, 209.
[19] Yao, C-L.; Capdevielle, F.J.; Kadish, K.M.; Bear, J.L. *ibid.*, 1989, **61**, 2805.
[20] Ashley, K. *Talanta*, 1991, **38**, 1209.
[21] Yao, C.-L.; Capdevielle, F. J.; Kadish, K. M.; Bear, J. L.; *Anal. Chem.*; 1989, **61**, 2805.
[22] Khoo, S. B.; Foley, J. F.; Korzeniewski, C.; Pons, S.; Marcott, C.; *J. Electroanal. Chem.*; 1987, **233**, 223.
[23] Flowers, P. A.; Mamantov, G.; *Anal. Chem.*; 1989, **61**, 190.
[24] Roe, K. K.; Sass, J. K.; Bethune, D. S.; Luntz, A. C.; *J. Electroanal. Chem.*; 1987, **216**, 293.
[25] Khatkale, M. S.; Devlin, J. P.; *J. Chem. Phys.*; 1979, **70**, 1851.
[26] Connelly, N.G.; Geiger, W.E.; *J. Am. Chem. Soc.; Chem. Rev.*; 1996, **96**, 877.
[27] Taylor, K.J.; Yellowlees, L.J. "Molecular Electrochemistry of Inorganic, Bioinorganic and Organometallic Compounds"; Edited by Pombeiro, A.J.L.; McCleverty, J.A.; Kluwer Academic; Netherlands; 1993; p69.
[28] Taylor, K. J.; Ph.D. Thesis, The University of Edinburgh, 1990.
[29] Ford, P.C.; Rudd, D.F.P.; Gaunder, R.G.; Taube, H.; *J. Am. Chem. Soc.*, 1968, **90**, 1187.
[30] Lim, H.S.; Barclay, J.; Anson, F.C.; *Inorg. Chem.*, 1972, **11**, 1460.
[31] Huang, H-Y.; Chen, W-J.; Yang, C-C.; Yeh, A.; *Inorg. Chem.*; 1991, **30**, 1862.
[32] Richardson, D.E.; Taube, H. *J. Am. Chem. Soc.* 1983, **105**, 40.
[33] Sen, J.; Taube, H.; *Acta. Chem. Scand, Ser. A*; 1979, **A33**, 125.
[34] Lay, P. A.; Magnuson, R. H.; Sen, J. Taube, H.; *J. Am. Chem. Soc.*, 1982, **104**, 7658.
[35] Callahan, R. W.; Brown, G. M.; Meyer, T. J. *Inorg. Chem.* 1975, **14**, 1443.
[36] Tonna, H.E.; Santos, P.S. *Can. J. Chem.* 1977, **55**, 3549.
[37] Yeh. A.;Haim, A.; Tanner, M.; Ludi, A. *Inorg. Chim. Acta* 1979, **33**, 51.
[38] Vogler, A.; Osman, A.H.; Kunkely, H. *Inorg. Chem.* 1987, **26**, 2337.
[39] Carriedo, G.A.; Connelly, N.G.; Crespo, M.C.; Quarmby, I.C.; Riera, V.;Worth, G.H. *J. Chem. Soc. Dalton Trans.* 1991, 315.
[40] Bignozzi, C.A.; Roffia, S.; Chiorboli, C.; Davila, J.; Indelli, M.T.; Scandola, F. *Inorg. Chem.* 1989, **28**, 4350.
[41] Zhu, N.; Vahrenkamp, H. *Chem. Ber.-Recl.* 1997, **130**, 1241.
[42] Bignozzi, C.A.; Scandola, F. *Inorg. Chem.* 1984, **23**, 1540.
[43] Dows, D.A.; Haim, A.; Wilmarth, W.K. *J. Inorg. Nucl. Chem.* 1961, **21**, 33.
[44] Shriver, D.F. *J. Am. Chem. Soc.* 1963, **85**, 1405.

[45] Bignozzi, C.A.; Argazzi, R.; Schoonover, J.R.; Gordon, K.C.; Dyer, R.B.; Scandola, F. *Inorg. Chem.* 1992, **31**, 5260.
[46] Diaz, C.; Aranchibia, A. *Inorg. Chim. Acta*, 1998, **269**, 246.
[47] Barrado, G. Carriedo, G.A. Diaz-Valenzuela, C.; Riera, V. *Inorg. Chem.*, 1991, **30**, 4416.
[48] Laidlaw, W.M.; Denning, R.G. *Polyhedron*, 1994, **13**, 2337.
[49] (a) Atkinson, F.L.; Christofides, A.; Connelly, N.G.; Lawson, H.J.; Loyns, A.C.; Orpen, A.G.; Rosair, M.; Worth, G.H. *J. Chem. Soc., Dalton Trans.* 1993, 1441; (b) Kennedy, V.O.; Stern, C.L.; Shriver, D.F. *Inorg. Chem.* 1994, **33**, 5967 (c) Feglhammer, W.P.; Frtiz, M. *Chem. Rev.* 1993, **93**, 1234 and references therein.
[50] Laidlaw, W.M.; Denning, R.G.; *J. Chem. Soc., Dalton Trans.* 1994, 1987.
[51] Laidlaw, W.M.; Denning, R.G.; *J.Organomet. Chem.* 1993, **463**, 199.
[52] Curtis, J.C.; Sullivan, B.P.; Meyer, T.J.; *Inorg. Chem.* 1983, **22**, 224.
[53] Saleh, A.A.; Crutchley, R.J.; *Inorg. Chem.* 1990, **29**, 2132.
[54] Gutmann, V.; *Electrochim. Acta;* 1976, **21**, 661.
[55] Carriedo, G.A.; Riera, V.; Connelly, N.G.; Raven, S.J.; *J. Chem. Soc., Dalton Trans.* 1987, 1769.
[56] Ford, P.C.; *Inorg. Chem.* 1971, **10**, 2153.
[57] Zanella, A.; Ford, P.C.; *Inorg. Chem.* 1975, **12**, 42.
[58] Endicott, J.F.; Song, X.; Watzky, M.A.; Buranda, T.; Lei, Y.; *Chem. Phys.* 1993, **176**, 427.
[59] Connelly, N.G.; Keeley, A.H.; Dunne, B.J.; Orpen, A.G.; Raven, S.J.; Carriedo, G.A.; Riera, V. *J. Chem. Soc., Dalton Trans.* 1988. 1623.
[60] Bond, A.M.; Grabaric, B.S.; Garbaric, *Z. Inorg. Chem.*, 1978, **17**, 1013.
[61] Richardson, D. E.; Taube, H.; *J. Am. Chem. Soc.* 1983, **105**, 40.
[62] Sutton, J. E.; Taube, H.; *Inorg. Chem.* 1981, **20**, 3125.
[63] Callahan, R. W.; Keene, F. R.; Meyer, T. J.; Salmon, D. J.; *J. Am. Chem. Soc.* 1977, **99**, 1064.
[64] Creutz, C.; Chou, M. H.; *Inorg. Chem.* 1987, **26**, 2995.
[65] Callahan, R.W.; Ph.D. Dissertation, University of North Carolina, Chapel Hill, 1975.
[66] Coe, B. J.; Meyer, T. J.; White, P. S.; *Inorg. Chem.* 1995, **34**, 593.
[67] Hornung, F. M.; Baumann, F.; Kaim, W.; Olabe, J.A.; Slep, L. D.; Fiedler, J.; *Inorg. Chem.* 1998, **37**, 311.
[68] Lay, P. A.; Magnuson, R. H.; Taube, H.; *Inorg. Chem.* 1988, **27**, 2364.
[69] Felix, F.; Hauser, U.; Siegenthaler, H.; Wenk, F.; Ludi, A.; *Inorg. Chim. Acta,* 1975, **15**, L7.
[70] Slep, L. D.; Baraldo, L. M.; Olabe, J. A.; *Inorg. Chem.*
[71] Gutmann, V.; "The Donor-Acceptor Approach to Molecular Interactions"; Plenum Press : New York, 1980.
[72] Taube, H.; *Ann. N. Y. Acad. Sci.* 1978, **313**, 481.
[73] Gutmann, V.; Resch, G.; Linert, W.; *Coord. Chem. Rev.*; 1982, **43**, 133.
[74] Alessio, E.; Balducci, G.; Calligaris, M.; Costa, G.; Attia, W. M.; Mestroni, G.; *Inorg. Chem.*;1991, **30**, 609.
[75] Balducci, G.; Mestroni, G.; Alessio, E.; *Current Topics in Electrochemistry*, 1993, **2**, 323.
[76] Bora, M.; Singh, M. M.; *Inorg. Nucl. Chem.* 1976. **38**, 1815
[77] Kober, E.; Unpublished results (ref 15 in Powers, M. J.; Meyer, T. J.; *Inorg. Chem.*; 1978, **17**, 2955.
[78] Acheson, R. M.; "An introduction to the Chemistry of Heterocyclic Compounds", Interscience Publishers, Inc., New York, N. Y., 1960, p289 and p299.
[79] Iengo, E.; Mestroni, G.; Geremia, S.; Calligaris, M; Alessio; *J. Chem. Soc., Dalton Trans.*, 1999, 3361.
[80] Powers, M. J.; Meyer, T. J.; *J. Am. Chem. Soc.*; 1980, **102**, 1289.
[81] Powers, M. J.; Meyer, T. J.; *Inorg. Chem.*; 1978, **17**, 2955.
[82] Richardson, D. E.; Taube, H.; *Inorg. Chem.*; 1981, **20**, 1278.

APPENDICES

Crystal Data of $[N^nBu_4][OsCl_5(4\text{-cypy})]$

Table 1. Crystal data and structure refinement for osme63.

A. CRYSTAL DATA

Empirical formula	C22 H40 Cl5 N3 Os [NBu4][OsCl5(4CN-Pyridine)]
Formula weight	714.02
Wavelength	0.71073Å
Temperature	150(2) K
Crystal system	Triclinic
Space group	P-1
Unit cell dimensions	a = 11.214(2)Å alpha = 112.341(2) ° b = 11.460(2)Å beta = 101.414(2) ° c = 13.378(3)Å gamma = 106.780(2) °
Volume	1427.6(5) A^3
Number of reflections for cell	8259 (2.5 < theta < 26.5 °.)
Z	2
Density (calculated)	1.661 Mg/m^3
Absorption coefficient	4.949 mm^{-1}
F(000)	708

B. DATA COLLECTION

Crystal description	Brown plate
Crystal size	0.28 x 0.18 x 0.05 mm
Instrument	CCD area detector
Theta range for data collection	1.76 to 26.50 °.
Index ranges	-13<=h<=14, -14<=k<=14, -16<=l<=16
Reflections collected	11573
Independent reflections	5765 [R(int) = 0.0515]
Scan type	phi and omega scans

Absorption correction	Sadabs (Tmin= 0.385, Tmax=0.801)

C. SOLUTION AND REFINEMENT.

Solution	Patterson (DIRDIF)
Refinement type	Full-matrix least-squares on F^2
Program used for refinement	SHELXL-97
Hydrogen atom placement	geometric
Hydrogen atom treatment	riding
Data / restraints / parameters	5765/0/280
Goodness-of-fit on F^2	0.837
Conventional R [F>4sigma(F)]	R1 = 0.0347 [4391 data]
Weighted R (F^2 and all data)	wR2 = 0.0733
Final maximum delta/sigma	0.002
Weighting scheme calc w=1/[\s^2^(Fo^2^)+(0.0195P)^2^+0.0000P] where P=(Fo^2^+2Fc^2^)/3	
Largest diff. peak and hole	2.343 and -1.795 $e.A^{-3}$

Table 2. Atomic coordinates (x 10^4) and equivalent isotropic displacement parameters (A^2 x 10^3) for osme63. U(eq) is defined as one third of the trace of the orthogonalized Uij tensor.

	x	y	z	U(eq)
Os(1)	2163(1)	3324(1)	1755(1)	29(1)
Cl(1)	3365(2)	3988(2)	3635(1)	40(1)
Cl(2)	4021(2)	4632(2)	1552(1)	41(1)
Cl(3)	1511(2)	5155(2)	2360(1)	42(1)
Cl(4)	254(1)	1970(2)	1875(1)	36(1)
Cl(5)	2684(1)	1407(1)	1034(1)	33(1)
N(1)	1053(4)	2752(5)	32(4)	28(1)
C(2)	1190(6)	3704(6)	-338(5)	34(1)
C(3)	483(6)	3359(6)	-1458(5)	36(1)
C(4)	-383(5)	2001(6)	-2212(5)	30(1)
C(5)	-506(5)	1033(6)	-1821(5)	33(1)
C(6)	218(5)	1431(6)	-703(5)	31(1)
C(7)	-1098(6)	1610(6)	-3378(5)	35(1)
N(8)	-1663(5)	1281(5)	-4318(5)	48(1)
N(11)	6895(4)	2689(4)	3083(4)	28(1)
C(11)	5741(5)	2430(6)	3521(5)	31(1)
C(12)	6009(5)	2293(6)	4612(5)	32(1)
C(13)	4752(6)	1992(7)	4918(5)	45(2)
C(14)	4952(7)	1794(6)	5994(5)	47(2)
C(21)	7972(5)	4122(5)	3887(5)	31(1)
C(22)	7675(6)	5335(6)	3892(5)	36(1)
C(23)	8875(6)	6667(6)	4780(5)	40(2)
C(24)	8671(6)	7947(6)	4871(6)	53(2)
C(31)	6310(5)	2531(6)	1890(4)	32(1)
C(32)	7285(5)	2676(6)	1248(5)	33(1)
C(33)	6641(6)	2759(6)	178(5)	38(2)
C(34)	7366(6)	2525(7)	-672(5)	46(2)
C(41)	7534(5)	1688(5)	3044(5)	31(1)
C(42)	6658(5)	173(5)	2286(5)	34(1)
C(43)	7444(6)	-674(6)	2426(5)	38(2)
C(44)	6663(6)	-2215(6)	1651(5)	46(2)

Table 3. Bond lengths Å and angles [°] for osme63.

Os(1)-N(1)	2.129(4)
Os(1)-Cl(1)	2.3088(15)
Os(1)-Cl(2)	2.3218(14)
Os(1)-Cl(4)	2.3283(14)
Os(1)-Cl(3)	2.3284(15)
Os(1)-Cl(5)	2.3349(14)
N(1)-C(2)	1.343(6)
N(1)-C(6)	1.350(7)
C(2)-C(3)	1.389(7)
C(3)-C(4)	1.389(7)
C(4)-C(5)	1.380(7)
C(4)-C(7)	1.430(8)
C(5)-C(6)	1.376(7)
C(7)-N(8)	1.144(7)
N(11)-C(41)	1.509(6)
N(11)-C(31)	1.520(6)
N(11)-C(21)	1.520(6)
N(11)-C(11)	1.521(6)
C(11)-C(12)	1.508(7)
C(12)-C(13)	1.526(7)
C(13)-C(14)	1.525(8)
C(21)-C(22)	1.518(7)
C(22)-C(23)	1.535(7)
C(23)-C(24)	1.513(8)
C(31)-C(32)	1.528(7)
C(32)-C(33)	1.522(7)
C(33)-C(34)	1.511(7)
C(41)-C(42)	1.513(7)
C(42)-C(43)	1.523(8)
C(43)-C(44)	1.522(8)
N(1)-Os(1)-Cl(1)	178.87(13)
N(1)-Os(1)-Cl(2)	88.69(12)
Cl(1)-Os(1)-Cl(2)	91.02(6)
N(1)-Os(1)-Cl(4)	88.92(12)
Cl(1)-Os(1)-Cl(4)	91.38(5)
Cl(2)-Os(1)-Cl(4)	177.56(6)
N(1)-Os(1)-Cl(3)	87.82(12)
Cl(1)-Os(1)-Cl(3)	91.10(5)
Cl(2)-Os(1)-Cl(3)	91.71(6)
Cl(4)-Os(1)-Cl(3)	88.69(5)
N(1)-Os(1)-Cl(5)	88.57(12)
Cl(1)-Os(1)-Cl(5)	92.52(5)
Cl(2)-Os(1)-Cl(5)	89.92(5)
Cl(4)-Os(1)-Cl(5)	89.52(5)
Cl(3)-Os(1)-Cl(5)	176.00(5)
C(2)-N(1)-C(6)	119.2(5)
C(2)-N(1)-Os(1)	120.2(4)
C(6)-N(1)-Os(1)	120.6(4)
N(1)-C(2)-C(3)	121.4(5)
C(4)-C(3)-C(2)	119.3(5)
C(5)-C(4)-C(3)	118.6(5)
C(5)-C(4)-C(7)	120.8(5)
C(3)-C(4)-C(7)	120.5(5)

C(6)-C(5)-C(4)	119.7(5)
N(1)-C(6)-C(5)	121.7(5)
N(8)-C(7)-C(4)	178.9(7)
C(41)-N(11)-C(31)	111.4(4)
C(41)-N(11)-C(21)	106.5(4)
C(31)-N(11)-C(21)	111.3(4)
C(41)-N(11)-C(11)	111.3(4)
C(31)-N(11)-C(11)	105.8(4)
C(21)-N(11)-C(11)	110.5(4)
C(12)-C(11)-N(11)	116.4(4)
C(11)-C(12)-C(13)	110.2(5)
C(14)-C(13)-C(12)	112.4(5)
C(22)-C(21)-N(11)	117.3(4)
C(21)-C(22)-C(23)	108.4(5)
C(24)-C(23)-C(22)	112.7(5)
N(11)-C(31)-C(32)	115.2(4)
C(33)-C(32)-C(31)	109.3(4)
C(34)-C(33)-C(32)	113.0(5)
N(11)-C(41)-C(42)	116.9(4)
C(41)-C(42)-C(43)	109.2(5)
C(44)-C(43)-C(42)	113.1(5)

Symmetry transformations used to generate equivalent atoms:

Table 4. Anisotropic displacement parameters (A^2 x 10^3) for osme63. The anisotropic displacement factor exponent takes the form: -2 pi^2 [h^2 a*^2 U11 + ... + 2 h k a* b* U12]

	U11	U22	U33	U23	U13	U12
Os(1)	30(1)	29(1)	22(1)	10(1)	5(1)	10(1)
Cl(1)	42(1)	48(1)	25(1)	13(1)	5(1)	20(1)
Cl(2)	37(1)	36(1)	38(1)	15(1)	8(1)	6(1)
Cl(3)	50(1)	35(1)	32(1)	9(1)	5(1)	20(1)
Cl(4)	32(1)	41(1)	36(1)	19(1)	14(1)	14(1)
Cl(5)	30(1)	32(1)	30(1)	13(1)	7(1)	12(1)
N(1)	28(3)	32(3)	24(3)	13(2)	7(2)	12(2)
C(2)	37(4)	29(3)	32(4)	15(3)	8(3)	9(3)
C(3)	36(4)	38(4)	40(4)	23(3)	13(3)	16(3)
C(4)	28(3)	32(3)	24(3)	11(3)	4(3)	8(3)
C(5)	31(3)	30(3)	28(3)	9(3)	7(3)	8(3)
C(6)	32(3)	27(3)	28(3)	12(3)	7(3)	8(3)
C(7)	36(4)	35(4)	31(4)	16(3)	8(3)	13(3)
N(8)	52(4)	49(4)	33(3)	15(3)	7(3)	19(3)
N(11)	22(2)	35(3)	18(3)	11(2)	4(2)	6(2)
C(11)	24(3)	39(3)	32(3)	17(3)	12(3)	11(3)
C(12)	29(3)	38(3)	24(3)	12(3)	8(3)	12(3)
C(13)	47(4)	53(4)	46(4)	30(4)	23(4)	20(3)
C(14)	62(5)	44(4)	37(4)	20(3)	25(4)	16(4)
C(21)	25(3)	34(3)	26(3)	12(3)	5(3)	6(3)
C(22)	34(3)	40(4)	29(3)	14(3)	9(3)	13(3)
C(23)	36(4)	37(4)	35(4)	13(3)	10(3)	8(3)
C(24)	38(4)	44(4)	60(5)	14(4)	13(4)	9(3)
C(31)	33(3)	37(3)	23(3)	14(3)	5(3)	11(3)
C(32)	26(3)	42(4)	27(3)	15(3)	5(3)	9(3)
C(33)	31(3)	49(4)	30(4)	20(3)	7(3)	11(3)
C(34)	53(4)	53(4)	34(4)	24(3)	17(4)	21(4)
C(41)	28(3)	39(3)	23(3)	13(3)	8(3)	13(3)
C(42)	29(3)	32(3)	30(3)	9(3)	10(3)	5(3)
C(43)	37(4)	38(4)	32(4)	14(3)	8(3)	10(3)
C(44)	53(4)	40(4)	44(4)	16(3)	19(4)	22(3)

Table 5. Hydrogen coordinates (x 10^4) and isotropic displacement parameters (A^2 x 10^3) for osme63.

	x	y	z	U(eq)
H(2)	1782	4633	177	41
H(3)	590	4046	-1706	43
H(5)	-1087	97	-2322	39
H(6)	127	757	-441	37
H(11A)	5450	3197	3651	38
H(11B)	4992	1576	2906	38
H(12A)	6723	3157	5251	38
H(12B)	6310	1537	4505	38
H(13A)	4470	2765	5044	54
H(13B)	4032	1150	4262	54
H(14A)	4123	1610	6159	70
H(14B)	5655	2631	6649	70
H(14C)	5207	1014	5866	70
H(21A)	8182	4236	4682	37
H(21B)	8782	4170	3686	37
H(22A)	6871	5321	4097	43
H(22B)	7511	5280	3118	43
H(23A)	9046	6691	5544	47
H(23B)	9669	6666	4563	47
H(24A)	9459	8766	5451	80
H(24B)	7893	7960	5096	80
H(24C)	8528	7943	4122	80
H(31A)	5937	3232	1963	39
H(31B)	5566	1614	1417	39
H(32A)	8104	3518	1757	40
H(32B)	7530	1873	1024	40
H(33A)	5714	2062	-208	46
H(33B)	6613	3678	414	46
H(34A)	6912	2596	-1339	68
H(34B)	7374	1606	-927	68
H(34C)	8280	3222	-301	68
H(41A)	7898	1836	3840	37
H(41B)	8293	1918	2780	37
H(42A)	6352	-22	1471	41
H(42B)	5867	-78	2509	41
H(43A)	8261	-371	2249	46
H(43B)	7716	-493	3239	46
H(44A)	7212	-2706	1784	69
H(44B)	6416	-2406	843	69
H(44C)	5858	-2525	1828	69

Crystal Data of $[N^nBu_4][OsCl_5(3\text{-cypy})]$

Table 1. Crystal data and structure refinement for osmecn.

A. CRYSTAL DATA

Empirical formula	C22 H40 Cl5 N3 Os [NBu4]+[OsCl5(3Cyano-pyridine)]-
Formula weight	714.02
Wavelength	0.71073Å
Temperature	220(2) K
Crystal system	Triclinic
Space group	P-1
Unit cell dimensions	a = 11.262(2)Å alpha = 112.992(10)° b = 11.767(2)Å beta = 108.836(10)° c = 12.736(3)Å gamma = 90.407(13)°
Volume	1453.2(5) A^3
Number of reflections for cell	36 (14 < theta < 15 °.)
Z	2
Density (calculated)	1.632 Mg/m^3
Absorption coefficient	4.862 mm^{-1}
F(000)	708

B. DATA COLLECTION

Crystal description	Yellow block
Crystal size	0.31 x 0.23 x 0.12 mm
Theta range for data collection	2.54 to 25.09 °.
Index ranges	-13<=h<=12, -14<=k<=12, 0<=l<=15
Reflections collected	5227
Independent reflections	5147 [R(int) = 0.0784]
Scan type	Omega-theta with learnt-profile (Clegg)
Absorption correction	Optimised numerical (Tmin= 0.394, Tmax=0.583)

C. SOLUTION AND REFINEMENT.

Solution	direct methods (SIR92)
Refinement type	Full-matrix least-squares on F^2
Program used for refinement	SHELXL-97
Hydrogen atom placement	geometric
Hydrogen atom treatment	riding
Data / restraints / parameters	5147/0/281
Goodness-of-fit on F^2	1.058
Conventional R [F>4sigma(F)]	R1 = 0.0305 [4531 data]
Weighted R (F^2 and all data)	wR2 = 0.0594
Extinction coefficient	0.00150(14)
Final maximum delta/sigma	0.001
Weighting scheme calc w=1/[\s^2^(Fo^2^)+(0.0151P)^2^+2.0191P] where P=(Fo^2^+2Fc^2^)/3	
Largest diff. peak and hole	0.562 and -0.604 $e.A^{-3}$

Table 2. Atomic coordinates (x 10^4) and equivalent isotropic displacement parameters (A^2 x 10^3) for osmecn. U(eq) is defined as one third of the trace of the orthogonalized Uij tensor.

	x	y	z	U(eq)
Os(1)	7311(1)	6994(1)	8797(1)	32(1)
Cl(1)	7666(2)	8114(1)	10822(1)	64(1)
Cl(2)	8961(1)	8229(1)	8849(1)	49(1)
Cl(3)	5918(1)	8270(1)	8220(1)	46(1)
Cl(4)	5581(1)	5716(1)	8606(1)	42(1)
Cl(5)	8665(1)	5623(1)	9217(1)	42(1)
N(1)	6974(4)	5893(4)	6909(3)	33(1)
C(2)	6699(4)	4650(5)	6469(4)	37(1)
C(3)	6388(5)	3877(5)	5246(5)	40(1)
C(4)	6370(5)	4409(6)	4442(5)	49(1)
C(5)	6699(5)	5675(5)	4902(5)	48(1)
C(6)	6986(5)	6392(5)	6123(5)	42(1)
C(7)	6040(6)	2557(6)	4864(5)	56(2)
N(8)	5760(6)	1539(5)	4621(5)	82(2)
N(10)	7172(3)	2381(3)	9737(3)	29(1)
C(11)	8164(4)	3540(4)	10586(4)	34(1)
C(12)	7770(5)	4569(5)	11505(5)	47(1)
C(13)	8889(5)	5593(5)	12405(5)	53(2)
C(14)	9820(6)	5235(7)	13326(6)	77(2)
C(21)	6730(5)	1806(5)	10451(5)	38(1)
C(22)	7785(6)	1512(5)	11360(5)	52(2)
C(23)	7478(7)	1458(7)	12370(6)	74(2)
C(24)	8591(7)	1362(7)	13353(6)	76(2)
C(31)	6057(4)	2782(4)	8983(4)	35(1)
C(32)	5050(5)	1763(5)	7925(5)	51(1)
C(33)	4076(5)	2335(5)	7223(5)	59(2)
C(34)	3033(6)	1435(6)	6153(6)	81(2)
C(41)	7769(5)	1427(4)	8935(4)	34(1)
C(42)	8221(5)	1813(5)	8112(4)	39(1)
C(43)	8674(5)	737(5)	7290(5)	46(1)
C(44)	9170(6)	1097(6)	6464(5)	55(2)

Table 3. Bond lengths Å and angles [°] for osmecn.

Os(1)-N(1)	2.138(4)
Os(1)-Cl(1)	2.2842(16)
Os(1)-Cl(2)	2.3180(14)
Os(1)-Cl(5)	2.3236(12)
Os(1)-Cl(3)	2.3248(13)
Os(1)-Cl(4)	2.3423(13)
N(1)-C(2)	1.337(6)
N(1)-C(6)	1.347(6)
C(2)-C(3)	1.384(7)
C(3)-C(4)	1.388(7)
C(3)-C(7)	1.442(8)
C(4)-C(5)	1.368(7)
C(5)-C(6)	1.372(7)
C(7)-N(8)	1.128(7)
N(10)-C(21)	1.518(5)
N(10)-C(31)	1.519(5)
N(10)-C(41)	1.521(5)
N(10)-C(11)	1.524(6)
C(11)-C(12)	1.507(6)
C(12)-C(13)	1.524(7)
C(13)-C(14)	1.501(8)
C(21)-C(22)	1.517(7)
C(22)-C(23)	1.460(7)
C(23)-C(24)	1.500(8)
C(31)-C(32)	1.507(7)
C(32)-C(33)	1.517(7)
C(33)-C(34)	1.476(8)
C(41)-C(42)	1.509(6)
C(42)-C(43)	1.510(6)
C(43)-C(44)	1.523(7)
N(1)-Os(1)-Cl(1)	178.16(11)
N(1)-Os(1)-Cl(2)	88.62(11)
Cl(1)-Os(1)-Cl(2)	92.66(6)
N(1)-Os(1)-Cl(5)	87.21(10)
Cl(1)-Os(1)-Cl(5)	91.44(5)
Cl(2)-Os(1)-Cl(5)	90.90(5)
N(1)-Os(1)-Cl(3)	88.44(10)
Cl(1)-Os(1)-Cl(3)	92.89(6)
Cl(2)-Os(1)-Cl(3)	89.28(5)
Cl(5)-Os(1)-Cl(3)	175.64(5)
N(1)-Os(1)-Cl(4)	88.00(11)
Cl(1)-Os(1)-Cl(4)	90.76(6)
Cl(2)-Os(1)-Cl(4)	176.21(5)
Cl(5)-Os(1)-Cl(4)	90.65(5)
Cl(3)-Os(1)-Cl(4)	88.91(5)
C(2)-N(1)-C(6)	117.8(4)
C(2)-N(1)-Os(1)	119.0(3)
C(6)-N(1)-Os(1)	123.1(3)
N(1)-C(2)-C(3)	122.6(5)
C(2)-C(3)-C(4)	118.8(5)
C(2)-C(3)-C(7)	117.8(5)
C(4)-C(3)-C(7)	123.3(5)
C(5)-C(4)-C(3)	118.4(5)
C(4)-C(5)-C(6)	119.9(5)

N(1)-C(6)-C(5)	122.3(5)
N(8)-C(7)-C(3)	176.5(7)
C(21)-N(10)-C(31)	109.7(3)
C(21)-N(10)-C(41)	108.6(3)
C(31)-N(10)-C(41)	111.5(3)
C(21)-N(10)-C(11)	111.2(4)
C(31)-N(10)-C(11)	107.5(3)
C(41)-N(10)-C(11)	108.4(3)
C(12)-C(11)-N(10)	116.2(4)
C(11)-C(12)-C(13)	111.2(4)
C(14)-C(13)-C(12)	113.8(5)
C(22)-C(21)-N(10)	114.7(4)
C(23)-C(22)-C(21)	115.0(5)
C(22)-C(23)-C(24)	114.0(6)
C(32)-C(31)-N(10)	117.2(4)
C(31)-C(32)-C(33)	109.6(4)
C(34)-C(33)-C(32)	115.3(5)
C(42)-C(41)-N(10)	116.4(4)
C(41)-C(42)-C(43)	110.5(4)
C(42)-C(43)-C(44)	112.2(4)

Symmetry transformations used to generate equivalent atoms:

Table 4. Anisotropic displacement parameters (A^2 x 10^3) for osmecn. The anisotropic displacement factor exponent takes the form: $-2\ pi^2\ [\ h^2\ a^{*2}\ U11 + ... + 2\ h\ k\ a^*\ b^*\ U12\ ]$

	U11	U22	U33	U23	U13	U12
Os(1)	29(1)	29(1)	38(1)	14(1)	11(1)	4(1)
Cl(1)	75(1)	57(1)	47(1)	11(1)	17(1)	8(1)
Cl(2)	32(1)	46(1)	69(1)	32(1)	10(1)	0(1)
Cl(3)	37(1)	35(1)	62(1)	21(1)	12(1)	11(1)
Cl(4)	37(1)	39(1)	56(1)	19(1)	24(1)	3(1)
Cl(5)	38(1)	45(1)	52(1)	29(1)	15(1)	12(1)
N(1)	30(2)	34(2)	36(2)	16(2)	11(2)	7(2)
C(2)	32(3)	41(3)	41(3)	19(3)	12(2)	12(2)
C(3)	42(3)	37(3)	40(3)	12(2)	18(2)	17(2)
C(4)	42(3)	66(4)	33(3)	15(3)	14(3)	22(3)
C(5)	50(3)	61(4)	44(3)	31(3)	20(3)	16(3)
C(6)	39(3)	43(3)	49(3)	26(3)	15(3)	9(2)
C(7)	64(4)	52(4)	45(4)	16(3)	14(3)	28(3)
N(8)	111(5)	43(3)	80(4)	19(3)	26(4)	22(3)
N(10)	29(2)	28(2)	34(2)	15(2)	12(2)	7(2)
C(11)	30(3)	29(3)	40(3)	13(2)	12(2)	2(2)
C(12)	43(3)	36(3)	50(3)	8(3)	14(3)	4(2)
C(13)	49(3)	46(3)	51(4)	3(3)	21(3)	0(3)
C(14)	60(4)	89(5)	51(4)	7(4)	7(3)	0(4)
C(21)	43(3)	34(3)	48(3)	22(2)	24(3)	10(2)
C(22)	62(4)	61(4)	59(4)	43(3)	33(3)	31(3)
C(23)	93(5)	104(6)	65(4)	55(4)	52(4)	61(5)
C(24)	97(6)	91(5)	52(4)	44(4)	25(4)	39(4)
C(31)	38(3)	33(3)	38(3)	19(2)	12(2)	9(2)
C(32)	43(3)	51(3)	48(3)	17(3)	8(3)	11(3)
C(33)	47(4)	57(4)	55(4)	18(3)	1(3)	10(3)
C(34)	70(5)	62(4)	72(5)	14(4)	-4(4)	5(4)
C(41)	38(3)	28(3)	37(3)	11(2)	17(2)	7(2)
C(42)	48(3)	38(3)	38(3)	16(2)	23(3)	9(2)
C(43)	58(4)	47(3)	44(3)	22(3)	29(3)	15(3)
C(44)	62(4)	68(4)	42(3)	23(3)	28(3)	15(3)

Table 5. Hydrogen coordinates (x 10^4) and isotropic displacement parameters (A^2 x 10^3) for osmecn.

	x	y	z	U(eq)
H(2)	6718	4288	7013	44
H(4)	6139	3910	3602	58
H(5)	6729	6054	4381	57
H(6)	7198	7262	6423	50
H(11A)	8919	3281	11029	40
H(11B)	8413	3882	10086	40
H(12A)	7424	4222	11950	56
H(12B)	7099	4927	11079	56
H(13A)	9334	5815	11949	64
H(13B)	8564	6337	12837	64
H(14A)	10508	5923	13862	116
H(14B)	10158	4507	12908	116
H(14C)	9396	5042	13802	116
H(21A)	6255	2381	10892	46
H(21B)	6144	1033	9874	46
H(22A)	8016	706	10923	62
H(22B)	8532	2149	11695	62
H(23A)	6822	735	12049	89
H(23B)	7122	2210	12731	89
H(24A)	8312	1304	13978	114
H(24B)	9226	2097	13711	114
H(24C)	8954	622	13006	114
H(31A)	5648	3316	9529	42
H(31B)	6391	3298	8665	42
H(32A)	4633	1288	8227	61
H(32B)	5441	1188	7385	61
H(33A)	3707	2915	7782	71
H(33B)	4515	2823	6949	71
H(34A)	2470	1882	5756	121
H(34B)	2562	972	6415	121
H(34C)	3383	859	5586	121
H(41A)	8494	1217	9465	41
H(41B)	7147	664	8426	41
H(42A)	8915	2517	8608	47
H(42B)	7525	2086	7615	47
H(43A)	7971	42	6785	55
H(43B)	9351	450	7791	55
H(44A)	9449	381	5952	82
H(44B)	9879	1772	6960	82
H(44C)	8498	1367	5955	82

Crystal Data of $[N^nBu_4][OsCl_5(pyz)]$

Table 1. Crystal data and structure refinement for OSME17.

Identification code	osme17
Empirical formula	C20 H40 Cl5 N3 Os
Formula weight	690.00
Temperature	220(2) K
Wavelength	0.71073 Å
Crystal system, space group	Monoclinic, P2(1)/c
Unit cell dimensions	a = 10.761(3)Å alpha = 90 b = 32.755(13)Å beta = 112.36(2)° c = 8.659(2)Å gamma = 90 °
Volume	2822.6(15) A^3
Z, Calculated density	4, 1.624 Mg/m^3
Absorption coefficient	5.003 mm^{-1}
F(000)	1368
Crystal size	0.35 x 0.27 x 0.12 mm
Theta range for data collection	2.62 to 25.07 °.
Index ranges	0<=h<=12, -39<=k<=0, -10<=l<=9
Reflections collected / unique	5749 / 4985 [R(int) = 0.1126]
Completeness to theta = 25.07	97.7%
Absorption correction	PSI SCANS
Max. and min. transmission	1.00 and 0.307
Refinement method	Full-matrix least-squares on F^2
Data / restraints / parameters	4985 / 0 / 267
Goodness-of-fit on F^2	0.958
Final R index [I>2sigma(I)]	R1 = 0.0580, [for 3045 data]
R indices (all data)	R1 = 0.1199, wR2 = 0.1199
Extinction coefficient	0.00030(15)
Largest diff. peak and hole	2.034 and -1.400 $e.A^{-3}$

Table 2. Atomic coordinates (x 10^4) and equivalent isotropic displacement parameters (A^2 x 10^3) for OSME17.
U(eq) is defined as one third of the trace of the orthogonalized Uij tensor.

	x	y	z	U(eq)
Os(1)	6926(1)	1297(1)	3522(1)	25(1)
Cl(4)	8885(3)	1584(1)	5451(4)	36(1)
Cl(5)	4972(3)	1042(1)	1493(4)	40(1)
Cl(6)	8136(3)	774(1)	2943(4)	39(1)
Cl(7)	5688(3)	1825(1)	4015(4)	45(1)
Cl(8)	6642(3)	909(1)	5586(4)	44(1)
N(1)	7234(9)	1647(3)	1663(11)	28(2)
C(2)	7523(11)	2045(4)	1876(15)	36(3)
C(3)	7787(13)	2277(4)	694(18)	52(4)
N(4)	7713(12)	2123(4)	-762(14)	52(3)
C(5)	7389(12)	1733(4)	-989(15)	45(4)
C(6)	7173(10)	1494(4)	186(14)	34(3)
N(1A)	12674(7)	992(3)	6045(11)	26(2)
C(1A)	13546(10)	644(3)	5917(14)	31(3)
C(2A)	14647(10)	512(3)	7550(13)	30(3)
C(3A)	15275(12)	113(4)	7353(17)	44(3)
C(4A)	16467(12)	8(4)	8934(16)	48(4)
C(5A)	11908(10)	877(4)	7174(13)	33(3)
C(6A)	11155(11)	483(4)	6838(15)	34(3)
C(7A)	10294(12)	458(4)	7878(15)	39(3)
C(8A)	9504(13)	63(4)	7564(18)	55(4)
C(9A)	11630(10)	1085(4)	4342(13)	31(3)
C(10A)	12135(11)	1259(4)	3097(13)	43(3)
C(11A)	10947(14)	1390(6)	1534(18)	87(6)
C(12A)	11295(14)	1590(5)	261(18)	79(5)
C(13A)	13542(10)	1356(3)	6785(14)	31(3)
C(14A)	12836(12)	1740(4)	6828(18)	49(4)
C(15A)	13747(14)	2070(4)	7960(2)	82(6)
C(16A)	12988(19)	2426(5)	8120(3)	136(9)

Table 3. Bond lengths Å and bond and torsion angles [°] for OSME17.

Os(1)-N(1)	2.102(9)
Os(1)-Cl(8)	2.306(3)
Os(1)-Cl(6)	2.319(3)
Os(1)-Cl(7)	2.320(3)
Os(1)-Cl(5)	2.323(3)
Os(1)-Cl(4)	2.332(3)
N(1)-C(2)	1.337(14)
N(1)-C(6)	1.351(13)
C(2)-C(3)	1.388(16)
C(3)-N(4)	1.332(16)
N(4)-C(5)	1.318(15)
C(5)-C(6)	1.372(15)
N(1A)-C(13A)	1.501(12)
N(1A)-C(9A)	1.506(12)
N(1A)-C(1A)	1.508(13)
N(1A)-C(5A)	1.545(12)
C(1A)-C(2A)	1.521(14)
C(2A)-C(3A)	1.510(15)
C(3A)-C(4A)	1.517(16)
C(5A)-C(6A)	1.492(15)
C(6A)-C(7A)	1.520(14)
C(7A)-C(8A)	1.516(16)
C(9A)-C(10A)	1.492(14)
C(10A)-C(11A)	1.527(16)
C(11A)-C(12A)	1.448(17)
C(13A)-C(14A)	1.477(15)
C(14A)-C(15A)	1.535(17)
C(15A)-C(16A)	1.46(2)
N(1)-Os(1)-Cl(8)	178.6(3)
N(1)-Os(1)-Cl(6)	88.4(3)
Cl(8)-Os(1)-Cl(6)	90.66(12)
N(1)-Os(1)-Cl(7)	90.2(3)
Cl(8)-Os(1)-Cl(7)	90.75(12)
Cl(6)-Os(1)-Cl(7)	178.25(12)
N(1)-Os(1)-Cl(5)	88.7(2)
Cl(8)-Os(1)-Cl(5)	92.25(11)
Cl(6)-Os(1)-Cl(5)	89.52(11)
Cl(7)-Os(1)-Cl(5)	89.38(11)
N(1)-Os(1)-Cl(4)	88.1(2)
Cl(8)-Os(1)-Cl(4)	90.97(11)
Cl(6)-Os(1)-Cl(4)	91.38(11)
Cl(7)-Os(1)-Cl(4)	89.64(11)
Cl(5)-Os(1)-Cl(4)	176.65(11)
C(2)-N(1)-C(6)	114.6(10)
C(2)-N(1)-Os(1)	121.5(8)
C(6)-N(1)-Os(1)	123.9(8)
N(1)-C(2)-C(3)	122.3(12)
N(4)-C(3)-C(2)	122.4(13)
C(5)-N(4)-C(3)	115.1(12)
N(4)-C(5)-C(6)	123.5(12)
N(1)-C(6)-C(5)	122.0(12)
C(13A)-N(1A)-C(9A)	111.6(9)
C(13A)-N(1A)-C(1A)	109.2(8)

C(9A)-N(1A)-C(1A)	109.5(8)
C(13A)-N(1A)-C(5A)	108.6(8)
C(9A)-N(1A)-C(5A)	106.9(7)
C(1A)-N(1A)-C(5A)	111.0(9)
N(1A)-C(1A)-C(2A)	115.6(9)
C(3A)-C(2A)-C(1A)	111.3(10)
C(2A)-C(3A)-C(4A)	110.8(11)
C(6A)-C(5A)-N(1A)	117.9(9)
C(5A)-C(6A)-C(7A)	109.9(9)
C(8A)-C(7A)-C(6A)	111.5(10)
C(10A)-C(9A)-N(1A)	116.4(9)
C(9A)-C(10A)-C(11A)	109.6(10)
C(12A)-C(11A)-C(10A)	115.5(12)
C(14A)-C(13A)-N(1A)	116.5(9)
C(13A)-C(14A)-C(15A)	113.9(11)
C(16A)-C(15A)-C(14A)	112.2(13)

Cl(8)-Os(1)-N(1)-C(2)	-92(11)
Cl(6)-Os(1)-N(1)-C(2)	-139.1(8)
Cl(7)-Os(1)-N(1)-C(2)	41.9(8)
Cl(5)-Os(1)-N(1)-C(2)	131.3(8)
Cl(4)-Os(1)-N(1)-C(2)	-47.7(8)
Cl(8)-Os(1)-N(1)-C(6)	88(11)
Cl(6)-Os(1)-N(1)-C(6)	40.2(8)
Cl(7)-Os(1)-N(1)-C(6)	-138.7(8)
Cl(5)-Os(1)-N(1)-C(6)	-49.3(8)
Cl(4)-Os(1)-N(1)-C(6)	131.7(8)
C(6)-N(1)-C(2)-C(3)	-2.3(16)
Os(1)-N(1)-C(2)-C(3)	177.1(9)
N(1)-C(2)-C(3)-N(4)	3(2)
C(2)-C(3)-N(4)-C(5)	-1(2)
C(3)-N(4)-C(5)-C(6)	-2(2)
C(2)-N(1)-C(6)-C(5)	-0.2(16)
Os(1)-N(1)-C(6)-C(5)	-179.6(8)
N(4)-C(5)-C(6)-N(1)	2(2)
C(13A)-N(1A)-C(1A)-C(2A)	58.0(12)
C(9A)-N(1A)-C(1A)-C(2A)	-179.5(9)
C(5A)-N(1A)-C(1A)-C(2A)	-61.7(11)
N(1A)-C(1A)-C(2A)-C(3A)	168.6(9)
C(1A)-C(2A)-C(3A)-C(4A)	173.9(10)
C(13A)-N(1A)-C(5A)-C(6A)	-170.2(9)
C(9A)-N(1A)-C(5A)-C(6A)	69.3(12)
C(1A)-N(1A)-C(5A)-C(6A)	-50.1(12)
N(1A)-C(5A)-C(6A)-C(7A)	-170.8(9)
C(5A)-C(6A)-C(7A)-C(8A)	179.6(10)
C(13A)-N(1A)-C(9A)-C(10A)	53.4(13)
C(1A)-N(1A)-C(9A)-C(10A)	-67.7(13)
C(5A)-N(1A)-C(9A)-C(10A)	171.9(10)
N(1A)-C(9A)-C(10A)-C(11A)	-172.2(12)
C(9A)-C(10A)-C(11A)-C(12A)	176.0(14)
C(9A)-N(1A)-C(13A)-C(14A)	52.2(13)
C(1A)-N(1A)-C(13A)-C(14A)	173.4(10)
C(5A)-N(1A)-C(13A)-C(14A)	-65.4(13)
N(1A)-C(13A)-C(14A)-C(15A)	165.9(11)
C(13A)-C(14A)-C(15A)-C(16A)	-173.3(15)

Table 4. Anisotropic displacement parameters (A^2 x 10^3) for OSME17. The anisotropic displacement factor exponent takes the form: $-2\ pi^2\ [\ h^2\ a^{*2}\ U11 + ... + 2\ h\ k\ a^*\ b^*\ U12\ ]$

	U11	U22	U33	U23	U13	U12
Os(1)	22(1)	26(1)	27(1)	0(1)	8(1)	0(1)
Cl(4)	28(2)	43(2)	31(2)	-6(2)	4(1)	-2(1)
Cl(5)	27(1)	49(2)	37(2)	-7(2)	5(1)	-8(2)
Cl(6)	36(2)	30(2)	51(2)	0(2)	17(2)	6(1)
Cl(7)	38(2)	42(2)	58(2)	-5(2)	23(2)	7(2)
Cl(8)	44(2)	46(2)	45(2)	10(2)	21(2)	-7(2)
N(1)	39(5)	12(5)	28(6)	-1(5)	6(5)	-8(4)
C(2)	41(7)	34(8)	32(7)	9(7)	12(6)	14(6)
C(3)	66(10)	28(8)	58(10)	8(8)	19(8)	-9(7)
N(4)	72(8)	41(8)	43(8)	7(6)	22(6)	-5(6)
C(5)	58(9)	53(10)	25(7)	-1(7)	18(6)	-14(7)
C(6)	34(6)	45(8)	22(7)	0(6)	7(5)	3(6)
N(1A)	14(4)	32(6)	27(6)	-10(5)	3(4)	-6(4)
C(1A)	20(5)	38(8)	37(7)	-8(6)	14(5)	-2(5)
C(2A)	30(6)	38(8)	20(6)	7(6)	9(5)	6(6)
C(3A)	45(7)	37(8)	54(9)	10(7)	21(7)	-2(6)
C(4A)	50(8)	37(8)	62(10)	17(8)	25(8)	1(7)
C(5A)	21(6)	53(9)	24(7)	7(6)	9(5)	2(6)
C(6A)	34(6)	39(8)	35(7)	-7(6)	19(6)	-2(6)
C(7A)	39(7)	44(8)	36(8)	1(7)	16(6)	2(6)
C(8A)	53(8)	52(10)	78(11)	-1(9)	44(8)	-23(7)
C(9A)	30(6)	34(7)	23(6)	7(6)	3(5)	3(6)
C(10A)	48(7)	51(9)	28(7)	9(7)	12(6)	-8(7)
C(11A)	58(9)	148(19)	45(9)	44(11)	8(8)	-29(11)
C(12A)	55(10)	119(16)	53(10)	17(11)	8(8)	0(10)
C(13A)	35(6)	19(7)	35(7)	-8(6)	7(5)	-6(5)
C(14A)	50(8)	24(8)	73(11)	-14(8)	25(8)	-2(6)
C(15A)	58(10)	32(9)	155(19)	-37(11)	38(11)	-8(8)
C(16A)	121(18)	71(15)	240(3)	-67(17)	99(19)	-49(13)

Table 5. Hydrogen coordinates (x 10^4) and isotropic displacement parameters (A^2 x 10^3) for OSME17.

	x	y	z	U(eq)
H(2)	7548	2172	2861	44
H(3)	8027	2553	930	62
H(5)	7301	1613	-2011	54
H(6)	6977	1216	-44	41
H(1A1)	13967	722	5137	37
H(1A2)	12968	408	5436	37
H(2A1)	15341	724	7923	35
H(2A2)	14266	481	8408	35
H(3A1)	15571	134	6416	53
H(3A2)	14605	-105	7100	53
H(4A1)	17165	212	9128	72
H(4A2)	16813	-258	8811	72
H(4A3)	16186	3	9873	72
H(5A1)	12559	871	8331	39
H(5A2)	11269	1096	7095	39
H(6A1)	11790	254	7118	41
H(6A2)	10582	464	5649	41
H(7A1)	10872	477	9064	47
H(7A2)	9670	690	7603	47
H(8A1)	8939	42	6388	83
H(8A2)	8946	60	8219	83
H(8A3)	10121	-166	7885	83
H(9A1)	11144	832	3880	37
H(9A2)	10982	1277	4478	37
H(10A)	12669	1054	2801	52
H(10B)	12712	1495	3581	52
H(11A)	10409	1148	1040	105
H(11B)	10381	1575	1871	105
H(12A)	11423	1880	506	119
H(12B)	10575	1552	-820	119
H(12C)	12118	1473	246	119
H(13A)	14136	1288	7931	38
H(13B)	14112	1405	6151	38
H(14A)	12109	1680	7213	58
H(14B)	12427	1849	5690	58
H(15A)	14237	1953	9071	99
H(15B)	14409	2156	7502	99
H(16A)	12173	2336	8253	204
H(16B)	12754	2593	7129	204
H(16C)	13531	2583	9093	204

Crystal Data of $[N^nBu_4][OsCl_5(NC_5H_4(CONH)]$

Table 1. Crystal data and structure refinement for osme46.

A. CRYSTAL DATA

Empirical formula	C22 H41 Cl4 N3 O Os [NBu4][OsCl4(C5H4N(CONH))]
Formula weight	695.58
Wavelength	0.71073Å
Temperature	123(2) K
Crystal system	Orthorhombic
Space group	Pbca
Unit cell dimensions	a = 18.090(3)Å alpha = 90 °. b = 16.779(3)Å beta = 90 °. c = 18.466(3)Å gamma = 90 °.
Volume	5604.9(18) A^3
Number of reflections for cell	72 (12 < theta < 14 °.)
Z	8
Density (calculated)	1.649 Mg/m^3
Absorption coefficient	4.950 mm^{-1}
F(000)	2768

B. DATA COLLECTION

Crystal description	Orange block
Crystal size	0.19 x 0.19 x 0.12 mm
Instrument	Stoe Stadi-4 diffractometer
Theta range for data collection	2.56 to 25.06 °.
Index ranges	0<=h<=21, 0<=k<=20, -21<=l<=0
Reflections collected	6248
Independent reflections	4959 [R(int) = 0.0481]
Scan type	omega-theta
Absorption correction	Psi-scans (Tmin= 0.217, Tmax=0.254)

C. SOLUTION AND REFINEMENT.

Solution	Patterson (DIRDIF)
Refinement type	Full-matrix least-squares on F^2
Program used for refinement	SHELXL-97
Hydrogen atom placement	geometric
Hydrogen atom treatment	riding
Data / restraints / parameters	4959/0/280
Goodness-of-fit on F^2	1.030
Conventional R [F>4sigma(F)]	R1 = 0.0592 [2898 data]
Weighted R (F^2 and all data)	wR2 = 0.1198
Final maximum delta/sigma	0.006
Weighting scheme calc w=1/[\s^2^(Fo^2^)+(0.0291P)^2^+27.5562P] where P=(Fo^2^+2Fc^2^)/3	
Largest diff. peak and hole	1.588 and -0.811 $e.A^{-3}$

Table 2. Atomic coordinates (x 10^4) and equivalent isotropic displacement parameters (A^2 x 10^3) for osme46. U(eq) is defined as one third of the trace of the orthogonalized Uij tensor.

	x	y	z	U(eq)
Os(1)	1558(1)	949(1)	1051(1)	27(1)
N(1)	2130(5)	-120(5)	942(5)	25(2)
C(2)	1754(6)	-690(7)	568(6)	31(3)
C(2')	1007(6)	-434(7)	302(6)	28(3)
N(2)	844(5)	321(6)	470(5)	30(2)
O(2)	608(4)	-920(5)	-18(4)	40(2)
C(3)	2029(7)	-1435(7)	488(6)	35(3)
C(4)	2737(6)	-1597(7)	765(7)	35(3)
C(5)	3115(7)	-1016(8)	1116(7)	42(3)
C(6)	2806(7)	-283(7)	1207(6)	33(3)
Cl(1)	2479(2)	1586(2)	1744(2)	41(1)
Cl(2)	1028(2)	420(2)	2095(2)	41(1)
Cl(3)	784(2)	2063(2)	1070(2)	38(1)
Cl(4)	2161(2)	1378(2)	2(2)	35(1)
N(10)	269(5)	2487(6)	-1490(5)	30(2)
C(11)	-148(7)	2803(8)	-837(6)	41(4)
C(12)	-406(8)	3663(8)	-868(7)	51(4)
C(13)	-780(7)	3907(9)	-167(8)	64(5)
C(14)	-253(9)	3991(9)	458(7)	73(5)
C(21)	-218(6)	2519(7)	-2156(6)	36(3)
C(22)	-928(7)	2035(7)	-2148(7)	42(3)
C(23)	-1291(7)	2072(9)	-2887(7)	50(4)
C(24)	-1999(7)	1590(8)	-2894(7)	50(4)
C(31)	488(6)	1648(6)	-1301(6)	28(3)
C(32)	833(6)	1129(7)	-1880(6)	35(3)
C(33)	965(8)	315(8)	-1553(7)	47(4)
C(34)	1238(7)	-274(8)	-2090(7)	54(4)
C(41)	943(6)	2986(7)	-1659(6)	26(3)
C(42)	1540(7)	3029(7)	-1072(7)	44(3)
C(43)	2103(7)	3672(9)	-1237(6)	46(4)
C(44)	1857(7)	4477(8)	-1030(7)	49(4)

Table 3. Bond lengths Å and angles [°] for osme46.

Os(1)-N(2)	1.983(9)
Os(1)-N(1)	2.080(9)
Os(1)-Cl(2)	2.329(3)
Os(1)-Cl(3)	2.336(3)
Os(1)-Cl(4)	2.336(3)
Os(1)-Cl(1)	2.357(3)
N(1)-C(6)	1.346(13)
N(1)-C(2)	1.362(13)
C(2)-C(3)	1.354(16)
C(2)-C(2')	1.499(16)
C(2')-O(2)	1.240(13)
C(2')-N(2)	1.336(14)
C(3)-C(4)	1.404(16)
C(4)-C(5)	1.356(16)
C(5)-C(6)	1.361(16)
N(10)-C(31)	1.504(14)
N(10)-C(41)	1.511(13)
N(10)-C(21)	1.513(13)
N(10)-C(11)	1.518(14)
C(11)-C(12)	1.517(16)
C(12)-C(13)	1.517(17)
C(13)-C(14)	1.504(18)
C(21)-C(22)	1.520(16)
C(22)-C(23)	1.516(16)
C(23)-C(24)	1.515(16)
C(31)-C(32)	1.513(15)
C(32)-C(33)	1.513(16)
C(33)-C(34)	1.484(16)
C(41)-C(42)	1.532(15)
C(42)-C(43)	1.515(16)
C(43)-C(44)	1.473(16)
N(2)-Os(1)-N(1)	79.2(4)
N(2)-Os(1)-Cl(2)	88.6(3)
N(1)-Os(1)-Cl(2)	87.5(2)
N(2)-Os(1)-Cl(3)	92.5(3)
N(1)-Os(1)-Cl(3)	171.7(3)
Cl(2)-Os(1)-Cl(3)	92.65(12)
N(2)-Os(1)-Cl(4)	91.1(3)
N(1)-Os(1)-Cl(4)	87.3(2)
Cl(2)-Os(1)-Cl(4)	174.74(11)
Cl(3)-Os(1)-Cl(4)	92.61(11)
N(2)-Os(1)-Cl(1)	174.5(3)
N(1)-Os(1)-Cl(1)	95.3(3)
Cl(2)-Os(1)-Cl(1)	90.81(12)
Cl(3)-Os(1)-Cl(1)	93.02(12)
Cl(4)-Os(1)-Cl(1)	88.92(11)
C(6)-N(1)-C(2)	119.8(10)
C(6)-N(1)-Os(1)	126.3(8)
C(2)-N(1)-Os(1)	113.9(7)
C(3)-C(2)-N(1)	121.3(11)
C(3)-C(2)-C(2')	124.1(12)
N(1)-C(2)-C(2')	114.5(11)
O(2)-C(2')-N(2)	127.3(11)
O(2)-C(2')-C(2)	119.4(11)

N(2)-C(2')-C(2)	113.2(11)
C(2')-N(2)-Os(1)	119.0(8)
C(2)-C(3)-C(4)	118.3(12)
C(5)-C(4)-C(3)	119.6(11)
C(4)-C(5)-C(6)	120.1(11)
N(1)-C(6)-C(5)	120.8(11)
C(31)-N(10)-C(41)	110.8(8)
C(31)-N(10)-C(21)	112.0(9)
C(41)-N(10)-C(21)	106.4(8)
C(31)-N(10)-C(11)	105.9(9)
C(41)-N(10)-C(11)	111.8(9)
C(21)-N(10)-C(11)	110.1(8)
C(12)-C(11)-N(10)	117.1(10)
C(13)-C(12)-C(11)	111.3(11)
C(14)-C(13)-C(12)	113.3(11)
N(10)-C(21)-C(22)	117.8(10)
C(23)-C(22)-C(21)	109.6(11)
C(24)-C(23)-C(22)	110.6(11)
N(10)-C(31)-C(32)	118.9(9)
C(33)-C(32)-C(31)	107.6(9)
C(34)-C(33)-C(32)	112.8(11)
N(10)-C(41)-C(42)	116.6(9)
C(43)-C(42)-C(41)	111.4(10)
C(44)-C(43)-C(42)	113.4(11)

Symmetry transformations used to generate equivalent atoms:

Table 4. Anisotropic displacement parameters (A^2 x 10^3) for osme46. The anisotropic displacement factor exponent takes the form: $-2\ pi^2\ [\ h^2\ a^{*2}\ U11 + ... + 2\ h\ k\ a^*\ b^*\ U12\ ]$

	U11	U22	U33	U23	U13	U12
Os(1)	30(1)	22(1)	30(1)	-1(1)	-1(1)	1(1)
N(1)	28(5)	25(5)	21(5)	0(5)	3(4)	-7(5)
C(2)	40(8)	34(7)	20(6)	2(6)	9(5)	-7(6)
C(2')	17(6)	36(8)	31(7)	-3(6)	12(5)	2(6)
N(2)	32(6)	26(6)	32(6)	1(5)	7(5)	5(5)
O(2)	34(4)	33(5)	54(5)	-11(5)	-5(4)	-16(5)
C(3)	50(9)	21(7)	36(8)	3(6)	8(7)	-9(7)
C(4)	39(8)	18(7)	48(8)	14(6)	16(6)	13(7)
C(5)	45(7)	41(8)	38(7)	1(8)	-10(7)	9(7)
C(6)	51(8)	27(7)	21(7)	-6(6)	-9(6)	-5(7)
Cl(1)	47(2)	34(2)	42(2)	-5(2)	-13(2)	-4(2)
Cl(2)	57(2)	34(2)	33(2)	-1(2)	8(2)	-1(2)
Cl(3)	37(2)	28(2)	51(2)	0(2)	2(2)	6(1)
Cl(4)	36(2)	30(2)	40(2)	5(2)	2(2)	0(2)
N(10)	24(5)	30(5)	36(5)	10(5)	3(5)	-2(6)
C(11)	35(7)	49(9)	38(8)	-5(7)	8(6)	-19(7)
C(12)	65(10)	34(8)	53(9)	7(7)	-4(8)	11(8)
C(13)	33(8)	59(11)	100(13)	-23(10)	-1(8)	1(8)
C(14)	110(14)	53(10)	58(9)	-8(9)	12(10)	47(12)
C(21)	46(8)	27(7)	36(7)	-6(6)	-16(6)	6(7)
C(22)	49(8)	24(7)	52(8)	4(7)	-11(7)	0(7)
C(23)	46(8)	60(10)	45(8)	-8(8)	-7(7)	-2(8)
C(24)	45(9)	50(9)	56(9)	-20(8)	-9(7)	10(8)
C(31)	28(6)	17(6)	41(7)	5(6)	-10(5)	-1(6)
C(32)	27(6)	42(9)	37(7)	-5(7)	-4(6)	-4(6)
C(33)	64(9)	33(8)	44(8)	-9(7)	9(8)	
15(8)						
C(34)	64(10)	48(9)	51(9)	3(8)	0(8)	-9(8)
C(41)	31(6)	21(7)	27(6)	11(5)	4(5)	-8(6)
C(42)	39(7)	49(8)	45(7)	11(8)	7(8)	0(8)
C(43)	43(8)	71(10)	24(7)	-7(7)	1(6)	-7(8)
C(44)	51(8)	48(9)	47(8)	-10(8)	-4(8)	-3(7)

Table 5. Hydrogen coordinates (x 10^4) and isotropic displacement parameters (A^2 x 10^3) for osme46.

	x	y	z	U(eq)
H(2)	425	535	325	36
H(3)	1751	-1838	252	42
H(4)	2950	-2110	705	42
H(5)	3596	-1121	1300	50
H(6)	3071	119	1460	40
H(11A)	-587	2461	-761	49
H(11B)	174	2741	-407	49
H(12A)	24	4014	-957	61
H(12B)	-756	3729	-1275	61
H(13A)	-1036	4422	-243	77
H(13B)	-1160	3505	-42	77
H(14A)	-528	4139	895	110
H(14B)	112	4404	347	110
H(14C)	0	3482	539	110
H(21A)	81	2340	-2575	43
H(21B)	-351	3083	-2242	43
H(22A)	-817	1474	-2023	50
H(22B)	-1269	2251	-1777	50
H(23A)	-1403	2634	-3010	60
H(23B)	-947	1861	-3257	60
H(24A)	-2226	1620	-3375	75
H(24B)	-2342	1805	-2532	75
H(24C)	-1887	1033	-2778	75
H(31A)	41	1371	-1123	34
H(31B)	840	1676	-892	34
H(32A)	497	1086	-2302	42
H(32B)	1305	1364	-2045	42
H(33A)	1332	364	-1157	56
H(33B)	498	117	-1340	56
H(34A)	1312	-790	-1852	81
H(34B)	1708	-89	-2293	81
H(34C)	874	-331	-2480	81
H(41A)	776	3536	-1765	31
H(41B)	1172	2774	-2106	31
H(42A)	1305	3141	-598	53
H(42B)	1794	2508	-1037	53
H(43A)	2568	3548	-977	55
H(43B)	2212	3666	-1763	55
H(44A)	2241	4865	-1154	73
H(44B)	1764	4493	-507	73
H(44C)	1401	4608	-1291	73

Crystal Data of $[N^nBu_4]_2[\{(DMSO)Cl_4Ru\}_2(\mu\text{-pyz})]$. 1.5 CH_3CH_2CN

Table 1. Crystal data and structure refinement for wotsit.

A. CRYSTAL DATA

Empirical formula	C44.50 H95.50 Cl8 N5.50 O2 Ru2 S2 [dmsoRuCl4N2C4H4RuCl4dmso][NBu4]2.1.5CH3CH2CN
Formula weight	1289.62
Wavelength	0.71073Å
Temperature	150(2) K
Crystal system	Triclinic
Space group	P-1
Unit cell dimensions	a = 16.193(4)Å alpha = 94.146(4)° b = 18.907(4)Å beta = 90.866(4)° c = 23.258(6)Å gamma = 113.666(4)°
Volume	6497(3) A^3
Number of reflections for cell	1742 (4 < theta < 41 °.)
Z	4
Density (calculated)	1.318 Mg/m^3
Absorption coefficient	0.893 mm^{-1}
F(000)	2692

B. DATA COLLECTION

Crystal description	Red Plate
Crystal size	0.08 x 0.08 x 0.03 mm
Theta range for data collection	0.88 to 26.40 °.
Index ranges	-20<=h<=19, -23<=k<=21, -29<=l<=28
Reflections collected	43410
Independent reflections	26050 [R(int) = 0.0970]
Scan type	phi and omega scans
Absorption correction	Empirical (Tmin= 0.9320, Tmax=0.9737)

C. SOLUTION AND REFINEMENT.

Solution	direct (SHELXS-97 (Sheldrick, 1990))
Refinement type	Full-matrix least-squares on F^2
Program used for refinement	SHELXL-97
Hydrogen atom placement	geom
Hydrogen atom treatment	riding, some rotating groups me
Data / restraints / parameters	26050/400/1172
Goodness-of-fit on F^2	0.869
Conventional R [F>4sigma(F)]	R1 = 0.0838 [8787 data]
Weighted R (F^2 and all data)	wR2 = 0.2160
Extinction coefficient	0.00033(7)
Final maximum delta/sigma	0.005
Weighting scheme	calc w=1/[\s^2^(Fo^2^)+(0.0858P)^2^+0.0000P] where P=(Fo^2^+2Fc^2^)/3
Largest diff. peak and hole	1.097 and -0.811 $e.A^{-3}$

Table 2. Atomic coordinates (x 10^4), equivalent isotropic displacement parameters (A^2 x 10^3) and site occupancies for wotsit. U(eq) is defined as one third of the trace of the orthogonalized Uij tensor.

	x	y	z	U(eq)	Occ
Ru(1)	2028(1)	874(1)	3621(1)	36(1)	1
N(1A)	2962(6)	1283(5)	2993(4)	43(2)	1
C(1A)	3863(7)	1695(6)	3115(4)	36(3)	1
C(2A)	4478(7)	1936(6)	2688(5)	42(3)	1
N(2A)	4210(5)	1801(5)	2132(3)	30(2)	1
C(3A)	3331(7)	1430(6)	2016(5)	39(3)	1
C(4A)	2720(7)	1173(6)	2430(4)	41(3)	1
Cl(1A)	1390(2)	-315(2)	3051(1)	46(1)	1
Cl(2A)	1051(2)	1291(2)	3135(1)	53(1)	1
Cl(3A)	2703(2)	2089(2)	4135(1)	50(1)	1
Cl(4A)	3050(2)	480(2)	4078(1)	43(1)	1
S(1A)	965(2)	374(2)	4288(1)	38(1)	1
C(5A)	-138(7)	-19(8)	3953(5)	65(4)	1
C(6A)	1019(7)	-476(6)	4524(5)	55(3)	1
O(1A)	959(4)	883(4)	4800(3)	41(2)	1
Ru(2)	5105(1)	2181(1)	1468(1)	39(1)	1
Cl(5A)	4273(2)	992(2)	938(1)	52(1)	1
Cl(6A)	4116(2)	2687(2)	1106(1)	49(1)	1
Cl(7A)	5911(2)	3349(2)	2019(1)	47(1)	1
Cl(8A)	6063(2)	1672(2)	1887(1)	51(1)	1
S(2A)	6052(2)	2574(2)	731(1)	50(1)	1
C(7A)	6332(8)	1811(8)	424(5)	72(4)	1
C(8A)	5525(8)	2713(8)	123(5)	74(4)	1
O(2A)	6938(5)	3227(6)	857(4)	82(3)	1
Ru(3)	-7712(1)	-3928(1)	1341(1)	34(1)	1
N(1B)	-6630(5)	-3497(5)	1947(4)	39(2)	1
C(1B)	-6708(7)	-3531(6)	2514(4)	37(3)	1
C(2B)	-5986(7)	-3231(6)	2894(5)	39(3)	1
N(2B)	-5134(5)	-2871(5)	2723(3)	35(2)	1
C(3B)	-5055(7)	-2872(6)	2146(5)	41(3)	1
C(4B)	-5769(7)	-3160(6)	1764(5)	39(3)	1
Cl(1B)	-8532(2)	-3459(2)	1975(1)	44(1)	1
Cl(2B)	-8195(2)	-5085(2)	1785(1)	49(1)	1
Cl(3B)	-6856(2)	-4369(2)	731(1)	46(1)	1
Cl(4B)	-7138(2)	-2735(2)	932(1)	43(1)	1
S(1B)	-8874(2)	-4371(2)	665(1)	39(1)	1
C(5B)	-8469(7)	-4291(6)	-45(4)	43(3)	1
C(6B)	-9449(7)	-3761(7)	672(5)	54(3)	1
O(1B)	-9548(5)	-5178(4)	678(3)	50(2)	1
Ru(4)	-3993(1)	-2330(1)	3278(1)	41(1)	1
Cl(5B)	-4823(2)	-1755(2)	3802(1)	53(1)	1
Cl(6B)	-4534(2)	-3350(2)	3876(1)	52(1)	1
Cl(7B)	-3257(2)	-2972(2)	2732(1)	48(1)	1
Cl(8B)	-3520(2)	-1296(2)	2686(1)	52(1)	1
S(2B)	-2711(2)	-1708(2)	3841(1)	55(1)	1
C(7B)	-2890(9)	-1210(9)	4448(5)	90(5)	1
C(8B)	-2380(9)	-2360(8)	4184(6)	94(5)	1

O(2B)	-1916(5)	-1191(6)	3560(4)	105(4)	1
N(1C)	-6059(7)	-773(6)	2432(4)	56(3)	1
C(1C)	-5511(8)	-1014(7)	2027(6)	64(4)	1
C(2C)	-4962(9)	-435(8)	1613(7)	87(5)	1
C(3C)	-4460(11)	-808(9)	1204(7)	102(6)	1
C(4C)	-3926(12)	-275(11)	766(7)	128(7)	1
C(5C)	-5479(9)	-36(6)	2816(5)	61(4)	1
C(6C)	-4726(10)	-73(9)	3187(7)	88(5)	1
C(7C)	-4200(11)	706(9)	3511(8)	112(6)	1
C(8C)	-3454(12)	609(11)	3912(9)	161(9)	1
C(9C)	-6519(8)	-1458(7)	2805(5)	57(3)	1
C(10C)	-7098(8)	-1360(8)	3268(6)	68(4)	1
C(11C)	-7482(9)	-2106(7)	3556(6)	78(4)	1
C(12C)	-8115(10)	-2071(10)	4024(7)	118(6)	1
C(13C)	-6734(10)	-544(7)	2143(6)	78(5)	1
C(14C)	-7399(10)	-1163(9)	1719(6)	79(4)	1
C(15C)	-8016(10)	-876(9)	1414(6)	77(5)	1
C(16C)	-8617(11)	-1414(11)	999(7)	123(7)	1
N(1D)	5797(7)	5635(6)	7122(4)	57(3)	1
C(1D)	6125(8)	5292(7)	6613(6)	63(4)	1
C(2D)	6308(11)	5715(8)	6074(6)	86(5)	1
C(3D)	6642(13)	5306(10)	5612(7)	131(7)	1
C(4D)	6750(19)	5665(15)	5045(7)	243(15)	1
C(5D)	4971(9)	5738(8)	6940(5)	64(4)	1
C(6D)	4130(9)	4994(8)	6764(7)	83(5)	1
C(7D)	3327(10)	5169(9)	6568(6)	86(5)	1
C(8D)	2496(10)	4448(10)	6450(7)	101(6)	1
C(9D)	5629(9)	5099(7)	7579(6)	69(4)	1
C(10D)	5309(8)	5361(7)	8139(5)	63(4)	1
C(11D)	5012(9)	4736(8)	8570(5)	69(4)	1
C(12D)	4770(10)	5044(9)	9137(6)	97(5)	1
C(13D)	6498(8)	6421(7)	7321(5)	59(4)	1
C(14D)	7445(9)	6481(7)	7479(5)	62(4)	1
C(15D)	8007(8)	7259(7)	7826(6)	67(4)	1
C(16D)	8968(9)	7361(8)	7917(6)	84(5)	1
N(1E)	8942(7)	4117(6)	2298(5)	67(2)	1
C(1E)	9658(9)	4783(8)	2656(6)	84(4)	1
C(2E)	10288(12)	4699(12)	3010(8)	146(6)	1
C(3E)	10847(13)	5501(12)	3387(8)	166(8)	1
C(4E)	11653(13)	5416(14)	3659(8)	192(10)	1
C(5E)	8290(9)	4407(9)	2026(6)	87(4)	1
C(6E)	8669(10)	5041(9)	1650(6)	90(4)	1
C(7E)	7940(11)	5261(10)	1367(7)	103(5)	1
C(8E)	7653(11)	5672(12)	1761(9)	154(8)	1
C(9E)	9384(9)	3778(9)	1853(6)	85(3)	1
C(10E)	8779(9)	3078(9)	1409(6)	91(4)	1
C(11E)	9308(11)	2839(10)	989(7)	106(5)	1
C(12E)	8809(12)	2170(12)	584(7)	146(7)	1
C(13E)	8443(10)	3489(8)	2630(6)	103(4)	1
C(14E)	7989(13)	3620(9)	3171(7)	169(7)	1
C(15E)	7624(11)	2981(12)	3605(7)	195(9)	1
C(16E)	8254(16)	2830(16)	4029(11)	266(13)	1
N(1F)	8930(6)	9115(6)	1800(5)	88(3)	1
C(1F)	9534(13)	8713(13)	1860(9)	98(4)	0.56(1)
C(1FA)	9053(19)	8802(13)	2340(7)	96(4)	0.44(1)
C(2F)	9262(8)	8105(7)	2299(6)	104(4)	1
C(3F)	9804(9)	7755(9)	2578(8)	155(6)	1
C(4F)	9704(11)	7119(9)	2937(8)	149(7)	1

C(5F)	8988(15)	9499(11)	2367(7)	90(4)	0.56(1)
C(5FA)	8284(15)	9489(14)	1797(11)	108(5)	0.44(1)
C(6F)	8672(9)	10137(8)	2236(6)	113(4)	1
C(7F)	8431(11)	10636(8)	2661(6)	140(6)	1
C(8F)	8116(12)	11270(10)	2579(9)	169(7)	1
C(9F)	9249(11)	9477(12)	1272(7)	94(4)	0.56(1)
C(9FA)	9877(10)	9577(15)	1670(11)	97(4)	0.44(1)
C(10F)	10126(9)	10231(8)	1304(6)	121(4)	1
C(11F)	10706(11)	10503(8)	797(6)	161(6)	1
C(12F)	11471(10)	11275(8)	729(8)	158(7)	1
C(13F)	8000(11)	8535(13)	1703(11)	103(4)	0.56(1)
C(13A)	8510(20)	8760(20)	1181(15)	98(4)	0.44(1)
C(14F)	7776(10)	8020(11)	1252(7)	130(4)	1
C(15F)	6887(13)	7385(12)	940(9)	169(6)	1
C(16F)	6235(10)	7133(12)	646(8)	167(8)	1
N(1S)	792(10)	2607(10)	-388(8)	154(7)	1
C(1S)	1179(12)	3054(11)	-38(8)	105(5)	1
C(2S)	1722(10)	3632(10)	376(7)	105(5)	1
C(3S)	2467(11)	3538(8)	638(7)	103(5)	1
N(2S)	697(19)	3356(15)	3673(10)	250(10)	1
C(4S)	628(18)	2889(15)	3998(11)	176(7)	1
C(5S)	625(15)	2405(13)	4374(9)	160(7)	1
C(6S)	402(14)	2665(13)	4955(9)	173(8)	1

Table 3. Bond lengths Å and angles [°] for wotsit.

Ru(1)-N(1A)	2.074(8)
Ru(1)-S(1A)	2.291(3)
Ru(1)-Cl(3A)	2.335(3)
Ru(1)-Cl(2A)	2.340(3)
Ru(1)-Cl(4A)	2.340(3)
Ru(1)-Cl(1A)	2.353(3)
N(1A)-C(4A)	1.338(12)
N(1A)-C(1A)	1.364(12)
C(1A)-C(2A)	1.387(13)
C(2A)-N(2A)	1.330(12)
N(2A)-C(3A)	1.324(11)
N(2A)-Ru(2)	2.096(7)
C(3A)-C(4A)	1.361(13)
S(1A)-O(1A)	1.478(7)
S(1A)-C(6A)	1.769(11)
S(1A)-C(5A)	1.777(10)
Ru(2)-S(2A)	2.277(3)
Ru(2)-Cl(7A)	2.334(3)
Ru(2)-Cl(6A)	2.345(3)
Ru(2)-Cl(5A)	2.346(3)
Ru(2)-Cl(8A)	2.359(3)
S(2A)-O(2A)	1.477(9)
S(2A)-C(8A)	1.731(11)
S(2A)-C(7A)	1.785(13)
Ru(3)-N(1B)	2.081(8)
Ru(3)-S(1B)	2.275(3)
Ru(3)-Cl(2B)	2.333(3)
Ru(3)-Cl(3B)	2.333(3)
Ru(3)-Cl(4B)	2.349(3)
Ru(3)-Cl(1B)	2.353(3)
N(1B)-C(1B)	1.331(11)
N(1B)-C(4B)	1.369(12)
C(1B)-C(2B)	1.353(13)
C(2B)-N(2B)	1.352(12)
N(2B)-C(3B)	1.349(12)
N(2B)-Ru(4)	2.085(8)
C(3B)-C(4B)	1.347(13)
S(1B)-O(1B)	1.480(8)
S(1B)-C(6B)	1.749(11)
S(1B)-C(5B)	1.780(9)
Ru(4)-S(2B)	2.268(3)
Ru(4)-Cl(7B)	2.343(3)
Ru(4)-Cl(6B)	2.343(3)
Ru(4)-Cl(5B)	2.346(3)
Ru(4)-Cl(8B)	2.351(3)
S(2B)-O(2B)	1.467(8)
S(2B)-C(7B)	1.733(13)
S(2B)-C(8B)	1.760(12)
N(1C)-C(1C)	1.475(13)
N(1C)-C(13C)	1.495(15)
N(1C)-C(5C)	1.538(14)
N(1C)-C(9C)	1.547(14)
C(1C)-C(2C)	1.520(16)
C(2C)-C(3C)	1.566(17)
C(3C)-C(4C)	1.510(19)

C(5C)-C(6C)	1.509(16)
C(6C)-C(7C)	1.509(18)
C(7C)-C(8C)	1.59(2)
C(9C)-C(10C)	1.487(15)
C(10C)-C(11C)	1.507(15)
C(11C)-C(12C)	1.522(16)
C(13C)-C(14C)	1.513(17)
C(14C)-C(15C)	1.504(16)
C(15C)-C(16C)	1.396(17)
N(1D)-C(9D)	1.472(14)
N(1D)-C(5D)	1.488(14)
N(1D)-C(13D)	1.497(14)
N(1D)-C(1D)	1.513(14)
C(1D)-C(2D)	1.504(16)
C(2D)-C(3D)	1.510(18)
C(3D)-C(4D)	1.51(2)
C(5D)-C(6D)	1.537(17)
C(6D)-C(7D)	1.535(16)
C(7D)-C(8D)	1.486(19)
C(9D)-C(10D)	1.532(16)
C(10D)-C(11D)	1.536(15)
C(11D)-C(12D)	1.524(17)
C(13D)-C(14D)	1.530(15)
C(14D)-C(15D)	1.540(16)
C(15D)-C(16D)	1.500(16)
N(1E)-C(13E)	1.428(14)
N(1E)-C(1E)	1.506(16)
N(1E)-C(9E)	1.513(16)
N(1E)-C(5E)	1.520(15)
C(1E)-C(2E)	1.368(18)
C(2E)-C(3E)	1.60(2)
C(3E)-C(4E)	1.51(2)
C(5E)-C(6E)	1.469(17)
C(6E)-C(7E)	1.552(17)
C(7E)-C(8E)	1.364(19)
C(9E)-C(10E)	1.584(18)
C(10E)-C(11E)	1.470(18)
C(11E)-C(12E)	1.46(2)
C(13E)-C(14E)	1.521(9)
C(14E)-C(15E)	1.566(9)
C(15E)-C(16E)	1.530(10)
N(1F)-C(5F)	1.441(9)
N(1F)-C(9F)	1.449(9)
N(1F)-C(13F)	1.466(9)
N(1F)-C(1FA)	1.470(9)
N(1F)-C(1F)	1.470(8)
N(1F)-C(9FA)	1.478(9)
N(1F)-C(5FA)	1.479(9)
N(1F)-C(13A)	1.57(4)
C(1F)-C(2F)	1.529(8)
C(1FA)-C(2F)	1.484(8)
C(2F)-C(3F)	1.461(7)
C(3F)-C(4F)	1.471(8)
C(5F)-C(6F)	1.534(9)
C(5FA)-C(6F)	1.456(9)
C(6F)-C(7F)	1.480(8)
C(7F)-C(8F)	1.501(9)
C(9F)-C(10F)	1.553(9)

C(9FA)-C(10F)	1.476(9)
C(10F)-C(11F)	1.507(7)
C(11F)-C(12F)	1.511(7)
C(13F)-C(14F)	1.32(2)
C(13A)-C(14F)	1.45(4)
C(14F)-C(15F)	1.580(17)
C(15F)-C(16F)	1.157(17)
N(1S)-C(1S)	1.109(17)
C(1S)-C(2S)	1.394(19)
C(2S)-C(3S)	1.421(17)
N(2S)-C(4S)	1.18(2)
C(4S)-C(5S)	1.31(2)
C(5S)-C(6S)	1.50(2)

N(1A)-Ru(1)-S(1A)	177.5(3)
N(1A)-Ru(1)-Cl(3A)	88.6(3)
S(1A)-Ru(1)-Cl(3A)	93.93(10)
N(1A)-Ru(1)-Cl(2A)	89.8(3)
S(1A)-Ru(1)-Cl(2A)	89.88(10)
Cl(3A)-Ru(1)-Cl(2A)	89.91(12)
N(1A)-Ru(1)-Cl(4A)	87.7(3)
S(1A)-Ru(1)-Cl(4A)	92.55(10)
Cl(3A)-Ru(1)-Cl(4A)	89.88(11)
Cl(2A)-Ru(1)-Cl(4A)	177.57(10)
N(1A)-Ru(1)-Cl(1A)	88.1(3)
S(1A)-Ru(1)-Cl(1A)	89.41(10)
Cl(3A)-Ru(1)-Cl(1A)	176.47(10)
Cl(2A)-Ru(1)-Cl(1A)	88.96(11)
Cl(4A)-Ru(1)-Cl(1A)	91.10(11)
C(4A)-N(1A)-C(1A)	114.3(9)
C(4A)-N(1A)-Ru(1)	122.2(7)
C(1A)-N(1A)-Ru(1)	123.5(7)
N(1A)-C(1A)-C(2A)	122.4(9)
N(2A)-C(2A)-C(1A)	121.2(10)
C(3A)-N(2A)-C(2A)	116.2(8)
C(3A)-N(2A)-Ru(2)	120.9(7)
C(2A)-N(2A)-Ru(2)	122.9(7)
N(2A)-C(3A)-C(4A)	123.3(10)
N(1A)-C(4A)-C(3A)	122.5(10)
O(1A)-S(1A)-C(6A)	108.6(5)
O(1A)-S(1A)-C(5A)	107.4(5)
C(6A)-S(1A)-C(5A)	100.3(6)
O(1A)-S(1A)-Ru(1)	118.6(3)
C(6A)-S(1A)-Ru(1)	109.9(3)
C(5A)-S(1A)-Ru(1)	110.5(4)
N(2A)-Ru(2)-S(2A)	178.7(3)
N(2A)-Ru(2)-Cl(7A)	90.2(2)
S(2A)-Ru(2)-Cl(7A)	91.02(11)
N(2A)-Ru(2)-Cl(6A)	86.6(2)
S(2A)-Ru(2)-Cl(6A)	92.91(11)
Cl(7A)-Ru(2)-Cl(6A)	90.44(11)
N(2A)-Ru(2)-Cl(5A)	88.1(2)
S(2A)-Ru(2)-Cl(5A)	90.66(11)
Cl(7A)-Ru(2)-Cl(5A)	178.28(10)
Cl(6A)-Ru(2)-Cl(5A)	89.84(11)
N(2A)-Ru(2)-Cl(8A)	90.2(2)
S(2A)-Ru(2)-Cl(8A)	90.34(11)
Cl(7A)-Ru(2)-Cl(8A)	88.30(11)

Cl(6A)-Ru(2)-Cl(8A)	176.54(10)
Cl(5A)-Ru(2)-Cl(8A)	91.32(11)
O(2A)-S(2A)-C(8A)	110.3(6)
O(2A)-S(2A)-C(7A)	103.7(6)
C(8A)-S(2A)-C(7A)	98.0(6)
O(2A)-S(2A)-Ru(2)	118.4(4)
C(8A)-S(2A)-Ru(2)	112.7(4)
C(7A)-S(2A)-Ru(2)	111.5(4)
N(1B)-Ru(3)-S(1B)	178.4(3)
N(1B)-Ru(3)-Cl(2B)	87.1(2)
S(1B)-Ru(3)-Cl(2B)	94.42(10)
N(1B)-Ru(3)-Cl(3B)	89.3(2)
S(1B)-Ru(3)-Cl(3B)	90.31(10)
Cl(2B)-Ru(3)-Cl(3B)	89.64(11)
N(1B)-Ru(3)-Cl(4B)	89.3(2)
S(1B)-Ru(3)-Cl(4B)	89.23(10)
Cl(2B)-Ru(3)-Cl(4B)	176.29(10)
Cl(3B)-Ru(3)-Cl(4B)	89.72(10)
N(1B)-Ru(3)-Cl(1B)	88.9(2)
S(1B)-Ru(3)-Cl(1B)	91.49(10)
Cl(2B)-Ru(3)-Cl(1B)	90.68(10)
Cl(3B)-Ru(3)-Cl(1B)	178.14(11)
Cl(4B)-Ru(3)-Cl(1B)	89.84(10)
C(1B)-N(1B)-C(4B)	116.1(9)
C(1B)-N(1B)-Ru(3)	124.4(7)
C(4B)-N(1B)-Ru(3)	119.5(7)
N(1B)-C(1B)-C(2B)	122.5(9)
N(2B)-C(2B)-C(1B)	122.2(10)
C(3B)-N(2B)-C(2B)	115.0(8)
C(3B)-N(2B)-Ru(4)	120.2(7)
C(2B)-N(2B)-Ru(4)	124.8(7)
C(4B)-C(3B)-N(2B)	123.3(9)
C(3B)-C(4B)-N(1B)	120.8(10)
O(1B)-S(1B)-C(6B)	108.2(5)
O(1B)-S(1B)-C(5B)	106.3(5)
C(6B)-S(1B)-C(5B)	101.1(5)
O(1B)-S(1B)-Ru(3)	117.7(3)
C(6B)-S(1B)-Ru(3)	111.0(4)
C(5B)-S(1B)-Ru(3)	111.1(3)
N(2B)-Ru(4)-S(2B)	176.9(2)
N(2B)-Ru(4)-Cl(7B)	89.4(2)
S(2B)-Ru(4)-Cl(7B)	89.26(11)
N(2B)-Ru(4)-Cl(6B)	90.6(2)
S(2B)-Ru(4)-Cl(6B)	92.19(11)
Cl(7B)-Ru(4)-Cl(6B)	90.75(11)
N(2B)-Ru(4)-Cl(5B)	87.0(2)
S(2B)-Ru(4)-Cl(5B)	94.36(12)
Cl(7B)-Ru(4)-Cl(5B)	176.11(11)
Cl(6B)-Ru(4)-Cl(5B)	87.67(11)
N(2B)-Ru(4)-Cl(8B)	87.8(2)
S(2B)-Ru(4)-Cl(8B)	89.42(11)
Cl(7B)-Ru(4)-Cl(8B)	91.86(11)
Cl(6B)-Ru(4)-Cl(8B)	176.95(11)
Cl(5B)-Ru(4)-Cl(8B)	89.62(11)
O(2B)-S(2B)-C(7B)	109.2(7)
O(2B)-S(2B)-C(8B)	106.6(7)
C(7B)-S(2B)-C(8B)	99.0(7)
O(2B)-S(2B)-Ru(4)	116.8(4)

C(7B)-S(2B)-Ru(4)	111.8(4)
C(8B)-S(2B)-Ru(4)	112.0(4)
C(1C)-N(1C)-C(13C)	113.7(10)
C(1C)-N(1C)-C(5C)	111.8(9)
C(13C)-N(1C)-C(5C)	102.9(10)
C(1C)-N(1C)-C(9C)	106.4(9)
C(13C)-N(1C)-C(9C)	111.6(9)
C(5C)-N(1C)-C(9C)	110.4(9)
N(1C)-C(1C)-C(2C)	117.5(10)
C(1C)-C(2C)-C(3C)	109.9(11)
C(4C)-C(3C)-C(2C)	113.0(13)
C(6C)-C(5C)-N(1C)	116.9(10)
C(7C)-C(6C)-C(5C)	109.9(12)
C(6C)-C(7C)-C(8C)	106.9(14)
C(10C)-C(9C)-N(1C)	117.8(10)
C(9C)-C(10C)-C(11C)	107.6(10)
C(10C)-C(11C)-C(12C)	111.4(11)
N(1C)-C(13C)-C(14C)	115.0(10)
C(15C)-C(14C)-C(13C)	112.1(12)
C(16C)-C(15C)-C(14C)	114.5(13)
C(9D)-N(1D)-C(5D)	112.3(10)
C(9D)-N(1D)-C(13D)	111.2(10)
C(5D)-N(1D)-C(13D)	107.2(9)
C(9D)-N(1D)-C(1D)	107.0(9)
C(5D)-N(1D)-C(1D)	109.4(9)
C(13D)-N(1D)-C(1D)	109.8(10)
C(2D)-C(1D)-N(1D)	117.6(10)
C(1D)-C(2D)-C(3D)	111.0(12)
C(4D)-C(3D)-C(2D)	112.9(16)
N(1D)-C(5D)-C(6D)	116.4(11)
C(7D)-C(6D)-C(5D)	112.0(12)
C(8D)-C(7D)-C(6D)	111.6(12)
N(1D)-C(9D)-C(10D)	114.6(10)
C(9D)-C(10D)-C(11D)	112.9(11)
C(12D)-C(11D)-C(10D)	110.9(12)
N(1D)-C(13D)-C(14D)	117.3(10)
C(13D)-C(14D)-C(15D)	110.9(10)
C(16D)-C(15D)-C(14D)	110.9(11)
C(13E)-N(1E)-C(1E)	112.7(11)
C(13E)-N(1E)-C(9E)	105.0(11)
C(1E)-N(1E)-C(9E)	109.5(10)
C(13E)-N(1E)-C(5E)	108.6(10)
C(1E)-N(1E)-C(5E)	108.7(11)
C(9E)-N(1E)-C(5E)	112.4(11)
C(2E)-C(1E)-N(1E)	123.5(15)
C(1E)-C(2E)-C(3E)	109.6(18)
C(4E)-C(3E)-C(2E)	106.0(19)
C(6E)-C(5E)-N(1E)	117.1(11)
C(5E)-C(6E)-C(7E)	112.9(13)
C(8E)-C(7E)-C(6E)	110.3(15)
N(1E)-C(9E)-C(10E)	119.9(11)
C(11E)-C(10E)-C(9E)	113.2(12)
C(12E)-C(11E)-C(10E)	116.8(14)
N(1E)-C(13E)-C(14E)	121.0(12)
C(13E)-C(14E)-C(15E)	120.8(10)
C(16E)-C(15E)-C(14E)	121.9(11)
C(5F)-N(1F)-C(9F)	127.0(15)
C(5F)-N(1F)-C(13F)	106.8(15)

C(9F)-N(1F)-C(13F)	109.8(14)
C(5F)-N(1F)-C(1FA)	55.8(9)
C(9F)-N(1F)-C(1FA)	152.8(15)
C(13F)-N(1F)-C(1FA)	92.4(17)
C(5F)-N(1F)-C(1F)	103.3(13)
C(9F)-N(1F)-C(1F)	99.5(12)
C(13F)-N(1F)-C(1F)	108.9(17)
C(1FA)-N(1F)-C(1F)	57.3(10)
C(5F)-N(1F)-C(9FA)	95.3(16)
C(9F)-N(1F)-C(9FA)	53.2(13)
C(13F)-N(1F)-C(9FA)	157.9(19)
C(1FA)-N(1F)-C(9FA)	101.1(15)
C(1F)-N(1F)-C(9FA)	65.7(12)
C(5F)-N(1F)-C(5FA)	72.6(13)
C(9F)-N(1F)-C(5FA)	86.4(16)
C(13F)-N(1F)-C(5FA)	69.0(14)
C(1FA)-N(1F)-C(5FA)	117.0(15)
C(1F)-N(1F)-C(5FA)	174.1(15)
C(9FA)-N(1F)-C(5FA)	118.4(17)
C(5F)-N(1F)-C(13A)	156.4(16)
C(9F)-N(1F)-C(13A)	55.2(14)
C(13F)-N(1F)-C(13A)	57.8(15)
C(1FA)-N(1F)-C(13A)	135.5(18)
C(1F)-N(1F)-C(13A)	98.9(18)
C(9FA)-N(1F)-C(13A)	100.9(18)
C(5FA)-N(1F)-C(13A)	84.6(15)
N(1F)-C(1F)-C(2F)	115.2(9)
N(1F)-C(1FA)-C(2F)	118.1(10)
C(3F)-C(2F)-C(1FA)	142.3(13)
C(3F)-C(2F)-C(1F)	129.4(9)
C(1FA)-C(2F)-C(1F)	55.7(10)
C(2F)-C(3F)-C(4F)	140.6(12)
N(1F)-C(5F)-C(6F)	101.6(12)
C(6F)-C(5FA)-N(1F)	103.5(13)
C(5FA)-C(6F)-C(7F)	142.7(12)
C(5FA)-C(6F)-C(5F)	70.6(13)
C(7F)-C(6F)-C(5F)	126.8(10)
C(6F)-C(7F)-C(8F)	130.9(11)
N(1F)-C(9F)-C(10F)	118.7(13)
C(10F)-C(9FA)-N(1F)	122.0(13)
C(9FA)-C(10F)-C(11F)	137.0(13)
C(9FA)-C(10F)-C(9F)	51.2(12)
C(11F)-C(10F)-C(9F)	123.5(9)
C(10F)-C(11F)-C(12F)	129.6(10)
C(14F)-C(13F)-N(1F)	120(2)
C(14F)-C(13A)-N(1F)	106(2)
C(13F)-C(14F)-C(13A)	63.8(19)
C(13F)-C(14F)-C(15F)	138.0(17)
C(13A)-C(14F)-C(15F)	143(2)
C(16F)-C(15F)-C(14F)	158(2)
N(1S)-C(1S)-C(2S)	176(2)
C(1S)-C(2S)-C(3S)	117.9(15)
N(2S)-C(4S)-C(5S)	175(4)
C(4S)-C(5S)-C(6S)	109.8(18)

Symmetry transformations used to generate equivalent atoms:

Table 4. Anisotropic displacement parameters ($A^2 \times 10^3$) for wotsit. The anisotropic displacement factor exponent takes the form: $-2\ pi^2\ [\ h^2\ a^{*2}\ U11 + \ldots + 2\ h\ k\ a^*\ b^*\ U12\ ]$

	U11	U22	U33	U23	U13	U12
Ru(1)	27(1)	37(1)	38(1)	4(1)	9(1)	8(1)
N(1A)	47(6)	48(7)	32(5)	2(5)	19(5)	16(5)
C(1A)	28(6)	31(7)	40(6)	6(5)	4(5)	2(5)
C(2A)	30(6)	33(7)	50(7)	3(6)	5(6)	-3(6)
N(2A)	8(4)	42(6)	35(5)	4(4)	11(4)	5(4)
C(3A)	24(6)	51(8)	46(7)	4(6)	3(5)	18(6)
C(4A)	28(6)	60(8)	30(6)	8(6)	9(5)	12(6)
Cl(1A)	33(2)	51(2)	41(2)	-4(1)	4(1)	6(2)
Cl(2A)	40(2)	70(2)	53(2)	18(2)	10(1)	26(2)
Cl(3A)	49(2)	40(2)	53(2)	1(2)	16(2)	8(2)
Cl(4A)	35(2)	50(2)	44(2)	6(1)	1(1)	15(2)
S(1A)	27(2)	44(2)	40(2)	6(1)	8(1)	9(1)
C(5A)	19(6)	99(11)	55(8)	6(7)	-3(6)	1(7)
C(6A)	43(7)	58(9)	57(8)	23(7)	34(6)	9(7)
O(1A)	26(4)	41(5)	40(4)	-7(4)	5(3)	-2(4)
Ru(2)	29(1)	43(1)	40(1)	8(1)	11(1)	8(1)
Cl(5A)	47(2)	54(2)	44(2)	-2(2)	10(1)	9(2)
Cl(6A)	39(2)	57(2)	53(2)	15(2)	12(1)	19(2)
Cl(7A)	36(2)	42(2)	57(2)	1(2)	10(1)	9(2)
Cl(8A)	40(2)	57(2)	58(2)	14(2)	12(2)	19(2)
S(2A)	39(2)	57(2)	44(2)	10(2)	15(2)	8(2)
C(7A)	60(9)	99(12)	60(8)	7(8)	14(7)	33(9)
C(8A)	76(10)	127(13)	44(8)	31(8)	19(7)	61(10)
O(2A)	36(5)	108(8)	80(6)	23(6)	22(5)	1(5)
Ru(3)	21(1)	40(1)	38(1)	3(1)	1(1)	9(1)
N(1B)	24(5)	51(6)	36(5)	6(5)	-1(4)	10(5)
C(1B)	23(6)	51(8)	33(6)	-2(6)	-10(5)	11(6)
C(2B)	23(6)	43(8)	45(7)	8(6)	-1(5)	7(6)
N(2B)	32(5)	45(6)	24(5)	-8(4)	-9(4)	15(5)
C(3B)	16(6)	39(8)	61(8)	6(6)	2(6)	3(5)
C(4B)	28(7)	49(8)	42(7)	-2(6)	5(6)	17(6)
Cl(1B)	33(2)	53(2)	45(2)	6(1)	7(1)	16(2)
Cl(2B)	40(2)	46(2)	52(2)	6(2)	-8(1)	10(2)
Cl(3B)	33(2)	53(2)	45(2)	-10(1)	-3(1)	15(2)
Cl(4B)	31(2)	49(2)	42(2)	7(1)	6(1)	7(1)
S(1B)	23(2)	49(2)	40(2)	5(1)	-3(1)	10(2)
C(5B)	29(6)	48(8)	36(6)	13(6)	15(5)	-2(6)
C(6B)	40(7)	64(9)	58(8)	-4(7)	-1(6)	22(7)
O(1B)	38(5)	55(6)	50(5)	9(4)	-7(4)	10(4)
Ru(4)	25(1)	51(1)	39(1)	-4(1)	-2(1)	9(1)
Cl(5B)	41(2)	64(2)	48(2)	-11(2)	1(1)	18(2)
Cl(6B)	45(2)	61(2)	48(2)	6(2)	3(1)	19(2)
Cl(7B)	33(2)	62(2)	46(2)	-4(2)	-2(1)	19(2)
Cl(8B)	38(2)	53(2)	57(2)	2(2)	5(2)	10(2)
S(2B)	32(2)	68(2)	48(2)	-5(2)	-8(2)	4(2)
C(7B)	55(9)	115(13)	77(10)	-42(9)	-36(8)	20(9)
C(8B)	70(10)	79(11)	124(13)	-8(9)	-78(10)	25(9)
O(2B)	34(5)	136(9)	79(7)	23(6)	-19(5)	-36(6)

N(1C)	60(7)	49(7)	75(7)	10(6)	23(6)	37(6)
C(1C)	53(8)	35(8)	107(11)	-5(8)	15(8)	21(7)
C(2C)	69(10)	59(11)	124(13)	1(10)	29(10)	19(9)
C(3C)	103(13)	89(13)	112(13)	23(11)	58(11)	33(11)
C(4C)	126(16)	152(19)	123(15)	-13(14)	21(13)	77(15)
C(5C)	84(10)	15(7)	80(9)	-18(6)	9(8)	17(7)
C(6C)	73(11)	83(13)	117(13)	-10(10)	-10(10)	45(10)
C(7C)	81(12)	69(13)	153(16)	-28(11)	-33(12)	4(10)
C(8C)	89(14)	137(19)	200(20)	-38(16)	-48(15)	-1(13)
C(9C)	50(8)	42(8)	88(10)	3(7)	0(7)	26(7)
C(10C)	61(9)	60(10)	89(10)	-3(8)	21(8)	31(8)
C(11C)	90(11)	45(9)	105(11)	15(8)	46(9)	31(9)
C(12C)	106(14)	114(15)	141(15)	45(12)	70(12)	44(12)
C(13C)	98(12)	36(9)	117(12)	12(9)	55(10)	43(9)
C(14C)	93(12)	78(12)	82(10)	-2(9)	6(9)	53(10)
C(15C)	101(12)	95(13)	74(10)	21(9)	24(9)	77(11)
C(16C)	105(14)	166(19)	120(14)	-74(14)	-66(12)	95(14)
N(1D)	68(8)	61(8)	55(7)	2(6)	-3(6)	39(7)
C(1D)	60(9)	45(9)	86(10)	-15(8)	-6(8)	27(7)
C(2D)	135(14)	69(11)	65(9)	-12(8)	36(9)	53(10)
C(3D)	174(19)	103(15)	117(15)	21(12)	61(14)	54(14)
C(4D)	400(40)	250(30)	59(13)	46(16)	93(19)	100(30)
C(5D)	74(10)	65(10)	63(9)	9(7)	15(8)	37(9)
C(6D)	72(11)	60(11)	127(13)	6(9)	-4(10)	37(9)
C(7D)	97(13)	93(13)	95(12)	7(10)	15(10)	67(12)
C(8D)	60(11)	122(16)	134(14)	7(12)	1(10)	49(11)
C(9D)	74(10)	39(9)	111(12)	25(8)	19(9)	37(8)
C(10D)	54(9)	62(10)	76(9)	8(8)	10(7)	26(8)
C(11D)	57(9)	70(10)	70(9)	29(8)	-10(7)	10(8)
C(12D)	82(11)	95(13)	76(11)	9(9)	-19(9)	-4(10)
C(13D)	54(9)	58(10)	68(9)	7(7)	3(7)	24(8)
C(14D)	80(10)	47(9)	75(9)	4(7)	19(8)	41(8)
C(15D)	46(9)	47(9)	102(11)	17(8)	6(8)	13(7)
C(16D)	82(11)	60(11)	108(12)	13(9)	6(9)	23(9)
N(1E)	47(6)	53(6)	97(7)	25(4)	4(4)	13(4)
C(1E)	52(7)	75(8)	100(9)	34(6)	2(6)	-5(6)
C(2E)	103(11)	158(13)	128(12)	43(9)	-44(8)	-2(9)
C(3E)	118(13)	180(15)	113(12)	47(10)	-44(9)	-33(11)
C(4E)	143(16)	250(20)	110(15)	28(15)	-60(12)	8(14)
C(5E)	73(8)	89(9)	102(9)	20(6)	-4(6)	35(7)
C(6E)	109(10)	79(9)	96(10)	16(7)	-9(8)	52(8)
C(7E)	122(11)	100(11)	112(12)	14(8)	-2(9)	70(9)
C(8E)	87(13)	174(19)	210(20)	-56(15)	-12(13)	76(12)
C(9E)	59(8)	95(9)	100(8)	21(6)	7(6)	28(6)
C(10E)	67(9)	113(10)	102(10)	4(6)	-5(7)	46(8)
C(11E)	80(10)	128(12)	109(11)	-4(8)	9(8)	40(9)
C(12E)	93(13)	186(19)	127(15)	-48(11)	10(11)	35(12)
C(13E)	90(10)	75(8)	122(10)	37(7)	21(7)	7(7)
C(14E)	156(13)	149(13)	149(13)	38(10)	71(10)	0(11)
C(15E)	191(17)	162(15)	183(15)	75(12)	79(13)	9(14)
C(16E)	260(30)	240(30)	290(30)	110(20)	40(20)	70(20)
N(1F)	37(4)	113(6)	121(6)	19(5)	18(5)	36(4)
C(1F)	42(6)	112(8)	135(8)	2(7)	11(6)	28(6)
C(1FA)	43(6)	111(8)	133(8)	9(7)	12(6)	29(6)
C(2F)	40(6)	111(8)	158(8)	-15(7)	-10(6)	33(6)
C(3F)	92(9)	129(11)	180(11)	-5(9)	-31(9)	-18(9)
C(4F)	96(12)	110(14)	221(17)	-3(13)	-39(12)	25(11)
C(5F)	37(6)	110(8)	128(8)	12(7)	32(7)	33(6)

C(5FA)	57(7)	124(9)	132(8)	31(7)	23(7)	21(7)
C(6F)	54(6)	128(9)	143(8)	38(7)	42(6)	15(6)
C(7F)	72(8)	146(11)	158(10)	23(9)	43(8)	-4(8)
C(8F)	95(12)	173(17)	248(17)	36(15)	40(13)	57(12)
C(9F)	52(6)	109(8)	124(8)	15(7)	19(6)	35(6)
C(9FA)	49(6)	112(8)	128(8)	8(7)	19(6)	30(6)
C(10F)	76(7)	126(8)	142(8)	-10(7)	27(7)	22(6)
C(11F)	123(10)	148(11)	179(11)	-2(10)	31(9)	23(9)
C(12F)	109(13)	123(14)	211(16)	-55(13)	16(13)	26(11)
C(13F)	56(6)	120(8)	128(8)	22(7)	16(7)	29(6)
C(13A)	48(6)	120(8)	123(8)	18(7)	17(7)	28(6)
C(14F)	76(7)	146(9)	135(8)	23(7)	4(7)	9(7)
C(15F)	105(10)	187(11)	168(11)	-19(10)	-5(9)	17(10)
C(16F)	59(11)	232(17)	168(15)	29(14)	-59(11)	17(12)
N(1S)	82(11)	168(16)	202(17)	-111(11)	-42(10)	61(11)
C(1S)	83(11)	106(13)	136(13)	-65(8)	-18(8)	61(10)
C(2S)	58(9)	113(12)	138(13)	-56(9)	-12(7)	39(9)
C(3S)	118(12)	62(10)	117(12)	4(9)	-37(10)	26(10)
N(2S)	380(30)	240(20)	220(20)	103(15)	60(20)	200(20)
C(4S)	259(16)	187(19)	187(16)	71(12)	91(15)	188(15)
C(5S)	209(15)	194(17)	187(16)	68(12)	68(14)	184(14)
C(6S)	199(19)	230(20)	166(15)	59(16)	46(16)	155(18)

Table 5. Hydrogen coordinates (x 10^4) and isotropic displacement parameters (A^2 x 10^3) for wotsit.

	x	y	z	U(eq)
H(1AA)	4076	1822	3508	43
H(2AA)	5103	2203	2793	51
H(3AA)	3115	1338	1624	47
H(4AA)	2099	905	2315	49
H(5AA)	-578	-285	4233	98
H(5AB)	-168	-388	3627	98
H(5AC)	-276	401	3813	98
H(6AA)	505	-731	4762	83
H(6AB)	1583	-338	4753	83
H(6AC)	997	-828	4189	83
H(7AA)	6641	1648	719	109
H(7AB)	6730	1995	104	109
H(7AC)	5779	1370	279	109
H(8AA)	5929	2801	-198	111
H(8AB)	5378	3165	202	111
H(8AC)	4969	2252	21	111
H(1BA)	-7293	-3775	2658	45
H(2BA)	-6081	-3276	3294	46
H(3BA)	-4467	-2659	2002	49
H(4BA)	-5673	-3129	1363	47
H(5BA)	-8965	-4366	-323	64
H(5BB)	-8233	-4687	-135	64
H(5BC)	-7987	-3776	-68	64
H(6BA)	-9897	-3927	348	81
H(6BB)	-9018	-3227	638	81
H(6BC)	-9756	-3788	1036	81
H(7BA)	-2320	-937	4674	135
H(7BB)	-3332	-1576	4683	135
H(7BC)	-3121	-833	4328	135
H(8BA)	-1938	-2079	4501	142
H(8BB)	-2109	-2606	3904	142
H(8BC)	-2910	-2759	4337	142
H(1CA)	-5920	-1490	1795	77
H(1CB)	-5089	-1156	2256	77
H(2CA)	-4516	34	1835	104
H(2CB)	-5367	-277	1381	104
H(3CA)	-4046	-952	1440	122
H(3CB)	-4909	-1289	999	122
H(4CA)	-3606	-529	533	192
H(4CB)	-3487	207	966	192
H(4CC)	-4337	-158	514	192
H(5CA)	-5210	392	2564	74
H(5CB)	-5883	102	3073	74
H(6CA)	-4982	-471	3464	105
H(6CB)	-4319	-223	2940	105
H(7CA)	-4605	870	3748	134
H(7CB)	-3911	1102	3238	134
H(8CA)	-3736	146	4122	241
H(8CB)	-3181	1066	4188	241

H(8CC)	-2987	554	3673	241
H(9CA)	-6894	-1916	2544	69
H(9CB)	-6040	-1579	2988	69
H(10A)	-7592	-1245	3101	82
H(10B)	-6736	-925	3553	82
H(11A)	-6982	-2208	3729	94
H(11B)	-7815	-2540	3263	94
H(12A)	-8368	-2569	4194	177
H(12B)	-8606	-1963	3854	177
H(12C)	-7779	-1659	4324	177
H(13A)	-6406	-80	1936	93
H(13B)	-7076	-397	2443	93
H(14A)	-7063	-1337	1430	95
H(14B)	-7766	-1615	1928	95
H(15A)	-8366	-723	1705	92
H(15B)	-7642	-407	1225	92
H(16A)	-8282	-1503	675	184
H(16B)	-9049	-1213	861	184
H(16C)	-8943	-1903	1170	184
H(1DA)	6688	5249	6740	76
H(1DB)	5669	4759	6510	76
H(2DA)	6766	6250	6166	103
H(2DB)	5747	5747	5929	103
H(3DA)	7231	5318	5747	157
H(3DB)	6211	4756	5552	157
H(4DA)	7277	6162	5077	365
H(4DB)	6208	5750	4948	365
H(4DC)	6836	5317	4742	365
H(5DA)	5115	6064	6610	77
H(5DB)	4816	6029	7262	77
H(6DA)	4276	4693	6446	100
H(6DB)	3960	4673	7096	100
H(7DA)	3216	5510	6872	103
H(7DB)	3476	5448	6214	103
H(8DA)	2418	4118	6768	152
H(8DB)	2549	4169	6090	152
H(8DC)	1973	4580	6413	152
H(9DA)	6192	5033	7668	83
H(9DB)	5168	4587	7429	83
H(10C)	4797	5499	8047	76
H(10D)	5805	5832	8323	76
H(11C)	4482	4280	8402	83
H(11D)	5507	4568	8644	83
H(12D)	4637	4654	9417	146
H(12E)	4237	5157	9071	146
H(12F)	5278	5519	9288	146
H(13C)	6276	6622	7663	71
H(13D)	6548	6769	7013	71
H(14C)	7753	6436	7123	75
H(14D)	7400	6049	7711	75
H(15C)	7987	7690	7616	80
H(15D)	7742	7276	8205	80
H(16D)	9298	7834	8169	127
H(16E)	9251	7403	7544	127
H(16F)	8985	6914	8096	127
H(1E1)	9997	5164	2383	101
H(1E2)	9337	5031	2900	101
H(2E1)	10704	4545	2776	175

H(2E2)	9985	4286	3269	175
H(3E1)	11046	5938	3139	199
H(3E2)	10471	5599	3688	199
H(4E1)	12012	5889	3904	288
H(4E2)	12024	5331	3355	288
H(4E3)	11444	4973	3894	288
H(5E1)	7816	3963	1798	104
H(5E2)	7991	4580	2340	104
H(6E1)	8995	4886	1342	108
H(6E2)	9113	5503	1879	108
H(7E1)	8194	5575	1040	124
H(7E2)	7422	4783	1215	124
H(8E1)	7168	5780	1584	230
H(8E2)	8158	6161	1890	230
H(8E3)	7427	5369	2093	230
H(9E1)	9798	3609	2064	102
H(9E2)	9762	4205	1626	102
H(10E)	8424	2630	1625	110
H(10F)	8348	3230	1198	110
H(11E)	9638	3285	764	128
H(11F)	9765	2726	1206	128
H(12G)	9229	2066	328	218
H(12H)	8367	2278	354	218
H(12I)	8494	1717	798	218
H(13E)	8859	3252	2746	123
H(13F)	7967	3096	2368	123
H(14E)	7475	3738	3044	203
H(14F)	8425	4095	3391	203
H(15E)	7181	3100	3837	234
H(15F)	7281	2485	3372	234
H(16G)	7896	2422	4271	398
H(16H)	8598	3306	4274	398
H(16I)	8671	2665	3814	398
H(1F1)	10149	9105	1972	117
H(1F2)	9561	8457	1478	117
H(1F3)	8495	8678	2554	115
H(1F4)	9546	9219	2576	115
H(2A)	9023	8327	2621	124
H(2B)	8736	7662	2113	124
H(2C)	8651	7684	2295	124
H(2D)	9443	8093	1895	124
H(3F1)	10260	8208	2809	186
H(3F2)	10134	7650	2251	186
H(4F1)	10223	6980	2893	223
H(4F2)	9148	6668	2814	223
H(4F3)	9676	7286	3342	223
H(5F1)	9614	9721	2535	108
H(5F2)	8585	9143	2632	108
H(5F3)	8239	9672	1415	130
H(5F4)	7677	9127	1898	130
H(6A)	9150	10497	2010	136
H(6B)	8136	9882	1967	136
H(6C)	9124	10530	2015	136
H(6D)	9031	9950	2483	136
H(7F1)	8970	10881	2928	168
H(7F2)	7959	10268	2886	168
H(8F1)	8101	11532	2955	254
H(8F2)	7510	11047	2391	254

H(8F3)	8533	11645	2336	254
H(9F1)	8760	9591	1099	112
H(9F2)	9341	9089	1002	112
H(9F3)	10217	9785	2045	117
H(9F4)	10114	9210	1490	117
H(10A)	9954	10659	1441	146
H(10B)	10524	10186	1614	146
H(10C)	10365	10689	1589	146
H(10D)	9533	10204	1165	146
H(11G)	10274	10426	469	193
H(11H)	10966	10115	717	193
H(12J)	11501	11380	321	237
H(12K)	12042	11262	862	237
H(12L)	11368	11685	959	237
H(13E)	7842	8246	2051	123
H(13F)	7605	8820	1681	123
H(13G)	8277	9109	1000	118
H(13H)	8966	8692	934	118
H(14A)	8140	7720	1327	156
H(14B)	8072	8339	935	156
H(14C)	7548	8131	1626	156
H(14D)	8113	7704	1345	156
H(15E)	7165	7042	772	202
H(15F)	6612	7137	1290	202
H(16G)	5854	6611	748	250
H(16H)	6393	7107	242	250
H(16I)	5906	7467	697	250
H(2S1)	1332	3682	686	126
H(2S2)	1959	4128	194	126
H(3SA)	2652	3862	1005	154
H(3SB)	2971	3695	380	154
H(3SC)	2290	2994	710	154
H(5SA)	1225	2384	4401	192
H(5SB)	172	1879	4247	192
H(6SA)	588	2413	5254	259
H(6SB)	-249	2523	4963	259
H(6SC)	724	3228	5026	259

Courses and Conferences Attended

Inorganic Seminars and Colloquia.

Departmental Lecture Courses on Ligand Design and Using the CSD.

Scottish Dalton Meeting, Glasgow University, April 1998.

USIC, University of Strathclyde, Sept 1998, and Heriot-Watt University, Sept 1999.

Butler Electrochemistry Meeting, University of St. Andrews, July 1999.

The Chemistry of the Platinum Group Metals, University of Nottingham, July 1999.

ICCC, University of Edinburgh, July 2000.